Seismic Attenuation System (AEI-SAS) for the AEI 10 m Prototype

Von der Fakultät für Mathematik und Physik der
Gottfried Wilhelm Leibniz Universität Hannover
zur Erlangung des Grades

Doktor der Naturwissenschaften
- Dr. rer. nat -
genehmigte Dissertation

von
Dipl.-Phys. Alexander Wanner
geboren am 08. Dezember 1978 in Rudny

2013

Referent:	Prof. Karsten Danzmann (Universität Hannover)
Korreferent:	Dr. Stefan Hild (Universtity of Glasgow)
Tag der Promotion:	26. April 2013

Abstract

An interferometric measurement facility with 10 m arm length, called AEI 10 m Prototype, is being set up at the Albert-Einstein-Institute (AEI) in Hannover, Germany. It will use three optical tables to provide an experimental platform for developing and testing novel techniques for gravitational wave detectors. The experiments in the 10 m Prototype will be housed in a large-scale vacuum system to isolate them from environmental influences. The main optical components of interferometers will be suspended to isolate them from seismic motion. These suspensions isolate above their natural frequencies (around 1 Hz). To reduce the motion at their natural modes, the suspensions require further pre-isolation. For that, a six-degree-of-freedom pre-isolator is needed, with natural frequencies far below these suspension modes. The AEI 10 m Prototype facility will be equipped with three of these isolators, one for each optical table.

This thesis describes the assembly, performance measurements, and enhancement of a low-frequency Seismic Attenuation System (SAS) for the 10 m Prototype facility. The design of this system is derived from another SAS prototype, the LIGO HAM-SAS. The specific design for the AEI 10 m Prototype is called AEI-SAS. It is an optimal tool to provide the necessary seismic pre-isolation for the optical suspensions of the interferometer. The techniques described throughout this thesis can, however, be adapted to other applications where ground motion in the 1 Hz–10 Hz frequency range must be reduced.

The AEI-SAS provides seismic attenuation by means of mechanical low-frequency oscillators. A major design feature of the SAS is the spatial and mechanical decoupling of vertical and horizontal oscillations. The horizontal isolation is performed by a three-leg Inverted Pendulum (IP). The IP supports the vertical isolation component, composed of three Geometric Anti-Spring (GAS) filters, and the optical bench is then mounted on the GAS filters. The mechanical configuration of these isolation stages allows them to be tuned independently to low frequencies in the order of 0.1 Hz.

Two of three AEI-SAS were assembled and tested. Six GAS filters were individually assembled and tuned. The filters achieved a maximum isolation of an unprecedented −80 dB, or a vibration reduction by a factor of 10 000. The isolation performance was achieved with two Centre of Percussion compensators (so-called magic wands), for which a stiffer material (silicone carbide) was introduced. Fluorel™ (ultra-high vacuum compatible rubber) pads were introduced to decouple the optical table from the oscillations of various AEI-SAS components.

The fully assembled AEI-SAS reduced the motion of the optical table with respect to ground motion at the natural frequencies of the suspensions (around 1 Hz) by a factor of 10 (−20 dB) in the vertical direction and at least factor of 300 (−50 dB) in horizontal directions. At 4 Hz, the maximum isolation of the system was −50 dB in vertical and −80 dB in horizontal degrees of freedom.

The AEI-SAS is a mostly passive mechanical system. However, it is augmented with sensors and actuators for active feedback control of the table motion and damping at the natural modes of the system. The first successful tests of damping are shown. A plan for advancements to the feedback and control system is presented and many of these elements will be implemented in the coming year.

Keywords: AEI 10 m Prototype, passive seismic isolation, mechanical low-frequency oscillators

Zusammenfassung

Am Albert-Einstein-Institut (AEI) in Hannover wird derzeit eine Anlage zur Durchführung quantenlimitierter interferometrischer Messungen aufgebaut. Diser sogenannte AEI 10m Prototyp, mit einem Interferometer von 10 m Armlänge, wird drei optische Tische beinhalten, die zusammen eine Experimentierplattform für die Entwicklung neuartiger Techniken zur Verbesserung der Empfindlichkeit von Gravitationswellendetektoren bilden. Die Experimente im AEI 10 m Prototyp werden zum Schutz vor Umwelteinflüssen in einem großen Ultrahochvakuumsystem untergebracht. Die wichtigsten optischen Komponenten des Interferometers werden als Mehrfachpendel aufgehängt, um sie von Bodenbewegungen zu entkoppeln. Diese Pendelaufhängungen isolieren oberhalb ihrer Eigenfrequenzen von ca. 1 Hz. Um die Oszillationsamplituden bei den Frequenzen der Eigenmoden zu reduzieren, müssen die Aufhängungen zusätzlich vorisoliert werden. Dazu ist ein Vorisolator mit sechs Freiheitsgraden erforderlich, dessen Eigenfrequenzen weit unterhalb der Eigenmoden der Aufhängungen liegen. Die drei optischen Tische des AEI 10 m Prototyp sollen mit je einem solchen Isolator ausgestattet werden.

Diese Doktorarbeit beschreibt die Montage, Überprüfung der Spezifikationen und Weiterentwicklung eines solchen niederfrequenten Seismischen Abschwächungs-Systems (SAS) für die 10 m Prototyp-Anlage. Der konzeptionelle Aufbau des Systems wurde von einem ähnlichen Modell, dem LIGO HAM-SAS, abgeleitet. Die spezifische Konfiguration, die für den AEI 10 m Prototyp entwickelt wurde, wird AEI-SAS genannt und ist ein hervorragendes Instrument, um die Aufhängungen der optischen Komponenten des Interferometers seismisch vorzuisolieren. Die in dieser Doktorarbeit beschriebene Technologie lässt sich darüber hinaus an nahezu jede andere Anwendung anpassen, bei der Bodenbewegungen im Frequenzbereich von 1 Hz-10 Hz reduziert werden müssen.

Die seismische isolierung des AEI-SAS wird durch Verwendung niederfrequenter mechanischer Oszillatoren realisiert. Ein grundlegendes Konzept des SAS ist eine weitgehende räumliche Trennung und mechanische Entkopplung von vertikalen und horizontalen Bewegungen. Die horizontale Isolierung wird durch ein dreibeiniges Invertiertes Pendel (IP) erreicht. Die Beine des IP stützen eine vertikale Isolationsstufe, die aus drei Geometrischen Anti-Sprungfedern (GAS) Filtern besteht, die wiederum den optischen Tisch tragen. Aufgrund der mechanischen Konfiguration können beide Isolationsstufen auf sehr niedrige Eigenfrequenzen, in der Größenordnung von 0.1 Hz, eingestellt werden.

Zwei der drei AEI-SAS wurden im Rahmen dieser Arbeit aufgebaut und getestet. Sechs GAS Filter wurden vormontiert und deren Eigenfrequenz individuell eingestellt. Die Filter zeigten eine für diese Art Filter bisher unerreichte maximale Isolierung von -80 dB, was einer Schwingungsreduzierung um einen Faktor 10 000 entspricht. Die Isolierung wurde durch den Einsatz sogenannter *Centre of Percussion* Kompensatoren ermöglicht, für die ein besonders steifes Material (Siliciumcarbid) ausgewählt wurde. Puffer aus Fluorel™ (Ultrahochvakuum-kompatibles Gummi) wurden eingeführt, um den optischen Tisch von Schwingungen AEI-SAS-interner Komponenten zu entkoppeln. Das AEI-SAS verringert die Tischbewegung bezüglich der Bodenbewegung um einen

Faktor von 10 (−20 dB) in vertikaler und mindestens einen Faktor 300 (−50 dB) in horizontaler Richtung im Bereich von 1 Hz, was den Frequenzen der Eigenmoden der Pendelaufhängungen entspricht. Bei 4 Hz wurde die maximale Isolierung erreicht, die in der Größenordnung von −50 dB in vertikaler und −80 dB in horizontaler Richtung lag.
Das AEI-SAS ist ein hauptsächlich passives mechanisches System. Zusätzlich ist es jedoch mit Sensoren und Aktoren zur kontrollierten Steuerung der Tischbewegungen und Dämpfung der Eigenmoden des Systems ausgestattet. Erste erfolgreiche Dämpfungstests werden in dieser Arbeit vorgestellt und Weiterentwicklungen der Regelkreise sind für die nahe Zukunft geplant.

Schlüsselwörter: AEI 10 m Prototyp, passive seismische Isolierung, mechanische Niederfrequenz-Oscillatoren

Abbreviations

Abbreviation	Disambiguation
AEI	Max Planck Institute for Gravitational Physics (Albert Einstein Institute) with locations in Golm and Hannover, Germany
AIGO	Australian International Gravitational Observatory, ground-based interferometric GW detector with 80 meters arm length
AURIGA	*Antenna Ultracriogenica Risonante per l'Indagine Gravitazionale Astronomic* (engl.: Ultracryogenic Resonant Antenna for the Astronomical Gravitational Investigation) cryogenic resonant bar GW detector in Italy
ADC	Analogue-to-Digital Converter
BBO	Bib Bang Observer, next generation space-born GW observatory project
BOSEM	Birmingham Optical Sensor and Electro-Magnetic actuator
BSC	Basic Symmetric Chamber / Beam Splitter Chamber / Big Steel Chamber
CDS	Control and Data acquisition System
CLIO	Cryogenic Laser Interferometer Observatory prototype for KAGRA
CoM	Centre of Mass
CoP	Centre of Percussion
CW	Counter Weight
DAC	Digital-to-Analogue Converter
DECIGO	DECi-hertz Interferometer Gravitational wave Observatory, space-born GW observatory project
DFT	Discrete Fourier Transform
eLISA	Evolved Laser Interferometer Space Antenna, space-born GW observatory project, also known as NGO
ENBW	Equivalent Noise Bandwidth
ET	Einstein Telescope, third generation ground-based interferometric GW detector project
GAS	Geometric Anti-Spring, passive mechanical vertical isolator

GEO600	Ground-based interferometric GW detector with 600 meters arm length in Germany
GEO-HF	Current configuration of GEO600
GW	Gravitational Wave
HEPI	Hydraulic External Pre-Isolation system, used at LIGO
IP	Inverted Pendulum, horizontal seismic isolation stage
KAGRA	KAmioka, GRAvitational wave detector, underground cryogenic interferometric GW detector in Japan, in construction
LCGT	Large-scale Cryogenic GW Telescope, re-named to KAGRA
LIGO	Laser Interferometer Gravitational-Wave Observatory, ground-based interferometric GW detector with 4 km arm length in the USA, being upgraded to Advanced LIGO
LISA	Laser Interferometer Space Antenna, space-born GW observatory project
LS	Linear Spectrum
LSD	Linear Spectral Density
LVDT	Linear Variable Differential Transformer
MiniGRAIL	Mini Gravitational Radiation Antenna In Leiden, cryogenic resonant bar GW detector in the Netherlands
MIT	Massachusetts Institute of Technology, Cambridge MA, USA
NENBW	Normalized Equivalent Noise BandWidth
NGO	New Gravitational wave Observatory, space-born GW observatory project based on LISA
PEEK	PolyEther Ether Ketone, vacuum compatible organic polymer
PS	Power Spectrum
PSD	Power Spectral Density
R&D	Research and Development
RF	Radio Frequency
RMS	Root-Mean-Square
SA	Superattenuator, seismic pre-isolation system at Virgo
SAS	Seismic Attenuation System
TAMA300	ground-based interferometric GW detector with 300 meters arm length in Japan
Virgo	ground-based interferometric GW detector with 3 km arm length in Italy, being upgraded to Advanced Virgo

Contents

1. Motivation

When in 1887 Michelson and Morley attempted to detect the luminiferous aether, which was predicted by the undulatory (wave) theory of light [Michelson1881], they discovered that a major source of disturbance in their experiment was seismic perturbation. They tried hard to get rid of the troublesome noise: they moved into the basement of a building far outside of the city, and stiffened the construction by placing the experiment on a massive stone floating on mercury, as shown in figure 1.1. They even blocked the traffic and worked at night to benefit from the quiet environment. Still, the experiment was sensitive to motion coming from the ground [Michelson1887]. The final conclusion of the experiment was that the aether does not exist, proving with their experiment that the theory was wrong. Michelson and Morley pioneered the modern interferometry and laid the path for many future optical experiments. Michelson-like interferometers are used as the basic configuration for interferometric detectors for gravitational waves. However, just like Michelson and Morley, modern gravitational wave researchers still struggle with seismic noise. The reduction of seismic motion in optical experiments, such as gravitational wave detectors, is the focus of this thesis.

1.1. Gravitational waves and their detectors

Just like the aether was a necessity for a theory, the existence of gravitational waves is predicted as the consequence of Einstein's general theory of relativity, stated about a century ago. The concept of gravitational waves is even older. Although Maxwell and Poincaré are cited as being the first to mention gravitational waves [Kennefick1997, Damour1987, Havas1979], Einstein was the first to provide a concrete description in a relativistic field theory. Einstein proposed the general theory of relativity in 1916 [Einstein1916] and covered gravitational waves in separate publications [Einstein1918, Einstein1937]. According to this theory, gravitational radiation is caused by oscillating multipole moments of the mass distribution of a system. Monopole radiation cannot exist as a consequence of mass conservation, and gravitational dipole radiation is ruled out by the principles of linear and angular momentum conservation; thus, quadrupole radiation is the lowest possible form [Abbott2009a]. The quadrupole oscillations of space-time occur in directions orthogonal to the direction of propagation of the wave; the space-time contracts along one transverse dimension, while expanding along the orthogonal transverse dimension. Gravitational waves travel at the speed of light and propagate essentially unperturbed through space, as they interact very weakly with matter. Their amplitude falls off inversely with the distance from the source [Schutz1999], unlike electromagnetic radiation (light), whose intensity (amplitude) falls off with the inverse *square* of the distance.

Gravitational waves can carry information from objects that are unobservable with electromagnetic radiation. Relativistic binaries composed of compact objects, such

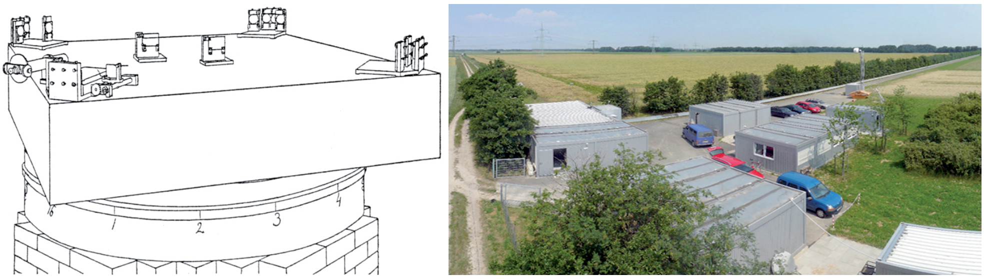

Figure 1.1.: The Michelson and Morley experiment (left) and the GEO600 gravitational wave interferometer (right). To reduce seismic motion, Michelson and Morley mounted their interferometer on a massive stone floating on mercury. The whole experiment rested on a bed of cement on a low brick pier built in the form of a hollow octagon. Image from [Michelson1887]. The GEO600 detector, attempting to detect gravitational waves, is based on a Michelson laser-interferometer with a physical arm-length of 600 m. The experiment is housed in a vacuum system, buried one meter into the soil. The interferometer mirrors are suspended from wires to isolate seismic motion.

as white dwarfs, neutron stars, and stellar-mass black holes, are strong sources of electromagnetic radiation. According to general relativity, black holes and compact binaries are also expected to be powerful sources of gravitational waves. These new signals will provide additional information about the behaviour, the structure and the history of the Universe, and will clarify several issues in fundamental physics [Amaro-Seoane2012].
Radio observations by Hulse and Taylor of the binary pulsar PSR 1913+16 published the first experimental evidence for the existence of gravitational waves, a discovery that won the authors the Nobel prize in 1993 [Hulse1974]. The results have shown that gravitational waves remove energy and momentum from the system, thus creating orbital decay between the two stellar bodies, causing them to spiral inwards with a decreasing period. The measurements of this effect at the radio telescope Arecibo continue to this day. The orbital decay is within $(0.13 \pm 0.21)\%$ of the general relativistic prediction for the emission of gravitational radiation [Weisberg2005]. The comparison of the observed and theoretical orbital decays are shown in figure 1.2.
The effect of gravitational waves on free falling masses is measurable as oscillations. One should be able to detect an incident gravitational wave by a measurement apparatus, which can be a group of test masses (suspended mirrors of an interferometer) or a single distributed-mass body (resonant mass detector), which would amplify the impinging oscillations at its resonance frequency.
The amplitude of the oscillations, measured by an interferometric detector on Earth, depends on the length of the measurement apparatus. The length change, dL, in the detector of length L is typically in the order of $dL/L \approx 10^{-21}$. As an example, a detector with length $L = 1000\,\mathrm{m}$ would need to detect length changes in the order of $10^{-18}\,\mathrm{m}$, an exa-meter, or 1000 times smaller than the diameter of a neutron ($\approx 1 \times 10^{-15}\,\mathrm{m}$). There are three classes of experiments currently in progress that aim to directly detect gravitational waves: resonant-mass detectors, interferometric detectors, and astronomical observations.

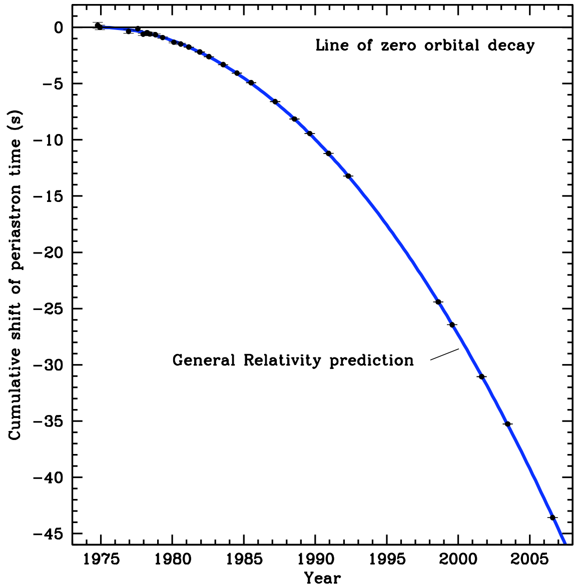

Figure 1.2: Orbital decay of the binary pulsar PSR 1913+16. The data points indicate the observed change in the periastron time. A periastron is the shortest distance between two stellar bodies, when one of them is orbiting on an elliptical orbit. The solid line illustrates the theoretically expected change for a system emitting gravitational radiation, according to general relativity. Picture taken from [Weisberg2010].

Resonant-mass detectors

The forefather of gravitational wave detection experiments principles was the Weber-bar, proposed by Joseph Weber in the late 1950s [Weber1960]. The Weber-bar evolved into resonant-mass detectors, several of which are still in operation. A resonant-mass detector consists of a massive test body isolated from environmental effects, such as temperature fluctuations and vibrations, and is equipped with sensors to detect deformations of the test mass excited by incident gravitational waves.

Weber's detector was an aluminium bar with sensors on the surface that would start *ringing* when a gravitational wave passed through. The oscillation in length and height caused by a sufficiently strong gravitational wave will cause the bar to ring-up to a measurable signal. The reliance on this resonant enhancement means that resonant-mass detectors are only sensitive in a narrow frequency band around the natural resonance frequency of the detector-mass. Weber claimed a positive detection of gravitational waves [Weber1968, Weber1969], but vigorous similar experiments by the scientific community were unable to make a repeat detection. More sensitive resonant detectors were built at different locations with different mass configurations and improved sensors.

Two still operational resonant-mass detectors are shown in figure 1.3. AURIGA, a cryogenic Webber-like bar detector in Legnaro, Italy [Bonaldi2009], and a spherical-mass detector MiniGRAIL [Gottardi2007] in Leiden, Netherlands. MiniGRAIL has a similar twin-detector MARIO SCHENBERG [Aguiar2008] in Brazil. Due to their inherently narrow-band and high-frequency operation, there are few gravitational wave sources observable with resonant-mass detectors. Even for these sources, the sensor noise limits the detection range to a dissatisfying level. These limitations triggered interest in alternative methods of detection.

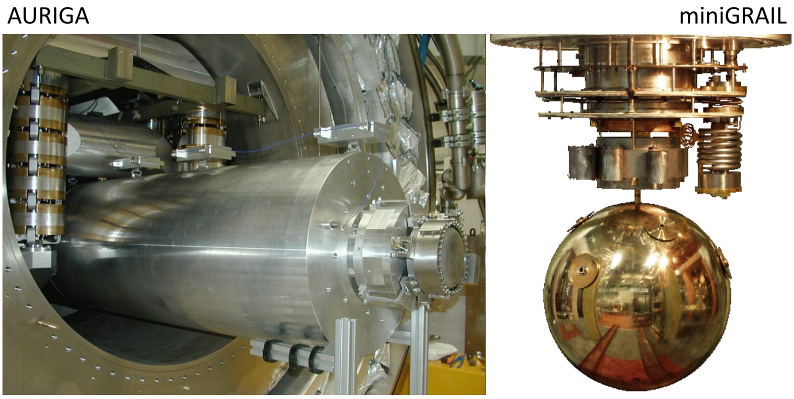

Figure 1.3.: Cryogenic resonant mass gravitational wave detectors: bar detector AURIGA (left) and spherical detector MiniGRAIL (right). Gravitational waves excite oscillations of the masses at their resonant frequency; the oscillations are measured by low-noise transducers. AURIGA is a 2.3 tons aluminium bar, 3 m long and 60 cm diameter, suspended from compressed blades for seismic isolation, with a resonance frequency of 920 Hz and a bandwidth of about 200 Hz. Picture taken from [Taffarello2005]. MiniGRAIL is a 68 cm diameter spherical gravitational wave antenna, made of CuAl(6%) alloy with a mass of 1400 kg, a resonance frequency of 2.9 kHz and a bandwidth around 230 Hz. Picture taken from [Minigrail].

Interferometric detectors

Interferometric detectors, in which laser ranging is used to monitor the position of suspended test-masses, make use of the Michelson interferometer with two orthogonal arms of (almost) identical length. An incident gravitational wave, that causes a differential phase change between the two light paths can be detected by a transient shift in the interference fringes. After interferometric gravitational wave detectors were proposed [Forward1969, Weiss1972, Drever1987], many prototype detectors were constructed, such as: the 2 m prototype interferometer at Hughes research laboratories, Malibu [Moss1971, Forward1978], the 5 m prototype at the MIT [1] [Benford1991, Lockerbie2011], the 10 m prototype in Glasgow [Drever1983, Edgar2009], the 30 m prototype in Garching, near Munich [Billing1983, Schnier1997], the 40 m prototype at Caltech [Drever1991, Ward2008], and the 80 m prototype AIGO in Gingin, Australia [Barriga2010]. The encouraging results of the prototypes triggered the development of large-scale gravitational wave detectors: TAMA300 in Japan [Takahashi2008], GEO600 in Germany [Lück2010], Virgo in Italy [Accadia2011], and LIGO in the USA [Abbott2009a].
The present-day detectors finished a joint science run (S6) in October 2010. No gravitational waves were detected, so far, even though the sensitivity of the detectors has reached the stage where they are, in principle, able to detect gravitational waves, as shown in figure 1.4. Furthermore, gravitational waves emanating from supernovae within the Milky Way should currently be detectable [Abadie2010a]. However, according to [Andersson2011], supernovae occur only a few times per century in a typical Milky Way type galaxy. Nevertheless, the results of previous science runs can set

[1] The meaning of all abbreviations can be found in the respective publications or in the abbreviations list on page vii

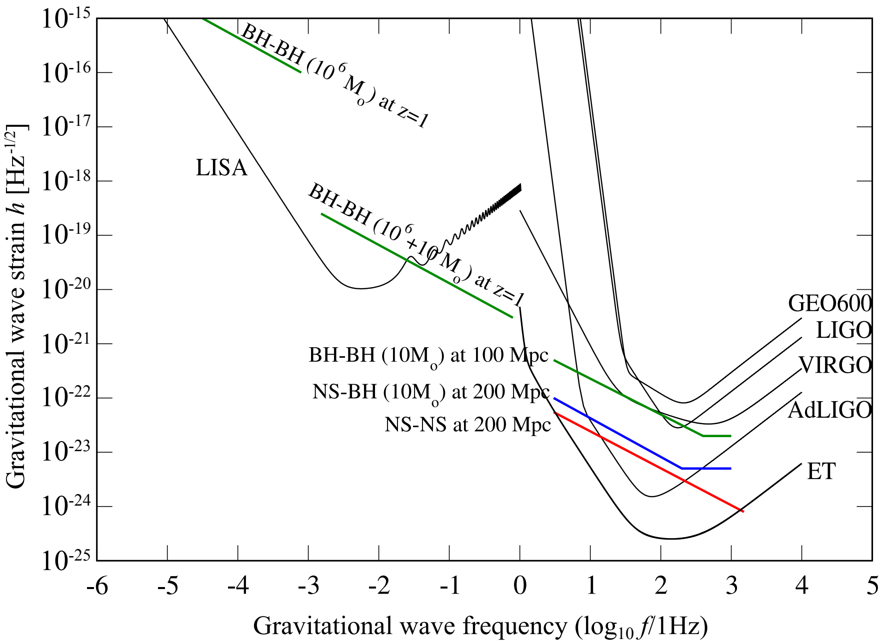

Figure 1.4.: Typical sensitivities of interferometric detectors compared to expected gravitational-wave strain of various sources. The sources are coalescing binary black holes (BH) and neutron stars (NS) at different distances of Megaparsec (Mpc) range. The current generation of ground-based detectors, GEO600, LIGO, and Virgo, which are sensitive above 10 Hz, is compared to the second generation of detectors, here shown Advanced LIGO (AdLIGO). Third generation detectors, like the Einstein Telescope (ET), would improve the sensitivity by another order of magnitude across a similar broad frequency range. The space-borne detector LISA is designed to operate at a lower frequency range, thus should be able to detect other sources than the ground-based detectors. Figure taken from [Andersson2011].

an upper limit, constraining the emission from a range of sources from inspiralling compact binaries [Abadie2010b] to (among others) rotating deformed neutron stars [Abbott2010] and from a stochastic gravitational-wave background originating in the early Universe [Abbott2009b].

The sensitivity of the detectors is limited by various noise sources, which are discussed in section 1.2. Just like in the original Michelson experiment, seismic noise is a key element which limits the performance of the detectors. Future generations of detectors aim to reduce their limiting noise levels and thereby increase their range.

After finishing the recent science run (S6), all detectors were shut down and are being upgraded; the only detector remaining operational is GEO600 in its current GEO-HF configuration [Willke2006]. The upgrade of the other detectors includes, among other advances, the installation of improved seismic isolation systems. A review focused on seismic isolation in major interferometric ground based gravitational wave detectors is given in section 2.5.

Future advanced gravitational wave detectors plan to mitigate thermal noise by cryogenic cooling of test-masses and their suspensions. Cryogenic cooling techniques were tested at CLIO [Yamamoto2008]; they are planned to be implemented in LCGT

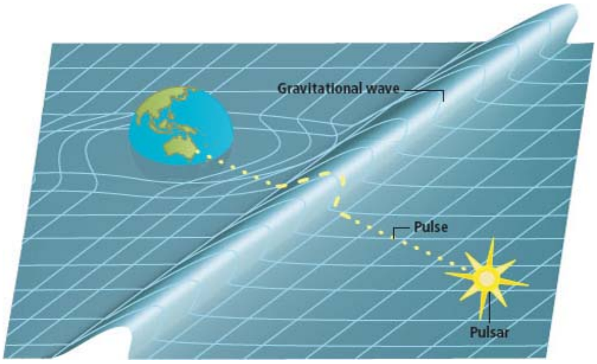

Figure 1.5: Pulsar timing is affected by gravitational waves. Artistic representation, showing a highly regular pulsed signal from a pulsar on its way to Earth. A gravitational wave causes deviations in arrival timing in the order of microseconds, which can be detected by radio telescopes. Picture from [Musser2007].

[Kuroda2010], recently renamed to KAGRA [KAGRA2012], and in the Einstein Telescope [Abernathy2011].
Several working groups investigate the possibility of using satellites, to detect gravitational waves in space. Space-based detectors are undisturbed by seismic noise, and are much longer than ground-based detectors. Hence, they are sensitive at lower frequencies. They can measure signals from sources which cannot be detected by earth-bound detectors. A number of projects investigate the feasibility of establishing a space mission: eLISA/NGO [Amaro-Seoane2012] (based on LISA [Hough1995]), BBO [Cutler2006, Harms2008], and DECIGO [Sato2009]. A nice review of interferometric gravitational wave detection is published in [Pitkin2011].

Pulsar timing

Astronomical observations, particularly pulsar timing measurements, can be used to detect gravitational waves. A pulsar is a rapidly rotating highly magnetized neutron star, a dense stellar object with a typical radius in the order of 10 km and a mass below 2.5 solar masses [Akmal1998]. Pulsars emit beams of electromagnetic radiation, which are only detectable when they sweep over Earth, like the beam of a lighthouse. These pulsar sweeps appear at very precise intervals, typically between milliseconds and seconds [Kaspi1994], and are as precise as early atomic clocks used to be [Backer1984]. Assuming that pulsars emit perfectly regular pulses, one should be able to see delays in the arrival time of the pulsar beam, when gravitational waves contract the space-time of the region in space where the beam passes through, as illustrated in figure 1.5.
Simultaneous observations of two or more pulsars can be used to detect long-period gravitational waves, requiring time-scales of several years in order to achieve the long-period stability of pulse arrival times. This method is suitable for sensing strong gravitational waves with periods of several years [Sathyaprakash2009]. Pulsar timing does not require special detector hardware, since pulsars are observed with radio telescopes. The detection of gravitational waves happens through extensive analysis of the data coming from radio telescopes. Pulsar timing observations for gravitational wave detection are currently under way at a number of radio observatories [Hobbs2010, Janssen2008, Oreshko2000].

Other proposals for gravitational wave detection

A rather exotic proposal for gravitational wave detection suggests observations of seismic activity on the Moon or the moons of Mars. There, gravitational waves are expected to excite quadrupole modes of the stellar body. The whole moon would perform oscillations with vibrational modes comparable to a spherical detector. Highly sensitive displacement sensors could be deployed on these planetary bodies to monitor the motion induced by gravitational waves. The Moon has no plate tectonics and its spin is locked to its revolution, thus is very quiet seismically. An alternative candidate is Martian moon Deimos, because of its small orbit eccentricity. Both celestial objects could be instrumented as sensitive resonant-mass gravitational wave antennas [Paik2009].
Another method proposes to measure gravitational waves by Doppler tracking of separated objects. Here, the test masses are Earth and an interplanetary space craft. Their relative positions are monitored by comparing a monochromatic microwave signal sent from a ground station with a coherently returned signal sent from the spacecraft [Estabrook1975].

1.2. Noise in interferometric ground based detectors

Noise sources

The measurement of gravitational waves requires substantial instrumental effort and extensive data analysis. The sensitivity curves of all interferometric ground-based detectors look rather similar. They have a plateau in the mid-frequency band, typically from 20 to 100 Hz, where the sensitivity is maximal. Towards larger and lower frequencies, the sensitivity decreases. The main limiting noise sources are discussed with reference to the GEO600 theoretical noise budget in figure 1.6.
Laser shot noise limits the sensitivity of the detector above several 100 Hz. Shot noise is caused by quantum fluctuations of the number of detected photons. Quantum fluctuations also cause back-action forces on the mirrors of the interferometer. The mirror position fluctuates with the irregularities in arrival times of impinging photons. Higher laser power increases the back-action forces on the mirror, the resulting displacement can be reduced by using larger optics, as in the case of Advanced LIGO. The laser power is increased from 10 W to 180 W while the initial 11 kg mirrors are being replaced by ∼40 kg mirrors [AdLIGO2011]. The higher laser power improves the shot-noise limited sensitivity of the detector. Further shot noise reduction techniques are discussed e.g. in [Tinto1999, Vahlbruch2008].
In the mid-frequency range, where the detector is most sensitive, the measurement is dominated by thermal noise. The noise is created by thermal fluctuations in mirror substrates, mirror coatings and suspensions. Thermal fluctuations can be reduced by, for example, cryogenic cooling or the use of low dissipation materials. However, cryogenic cooling requires new materials for substrates and suspension wires with better thermal properties.
Monolithic suspensions, first introduced in GEO600, replaced standard steel wire loops with low-dissipation fused silica fibres. The fibres were bonded to the sides of the mirrors. Monolithic suspensions will be used in all advanced detectors and in

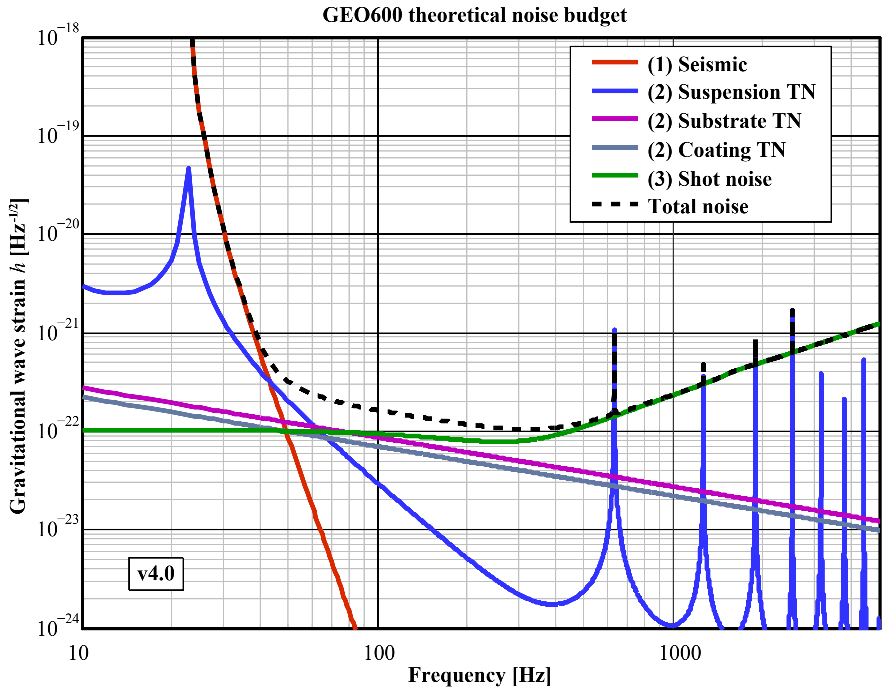

Figure 1.6.: Theoretical noise model of the interferometric gravitational wave detector GEO600. The total noise budget is defined by the sum of all incorporated noise sources: (1) seismic noise, (2) Thermal Noise (TN) of suspensions, substrate, and coating, and (3) laser shot noise. The gravitational wave strain, h, is a dimension-less quantity which gives the relative length change in the detector, proportional to the amplitude of gravitational waves, normalized by $\sqrt{\mathrm{Hz}}$ during LSD computation, as described in appendix C.2.3. Data taken from GEO600 homepage [GEO600].

the AEI 10 m Prototype. In GEO600, the wires were pulled in an H_2–O_2 flame. A fibre pulling machine was developed at the University of Glasgow for the Advanced LIGO detector. The machine heats the silica glass material with a CO_2 laser and pulls the fibres automated. The laser pulling machine creates fibres with better reproducible diameters than flame pulled fibres. The strength of the fibres is tested on samples by pulling them apart and measuring the maximal force that breaks them [Tokmakov2012]. Further thermal noise reduction techniques are discussed in, for example, [Cohadon1999, Mours2006].
At low frequencies below 50 Hz, the GEO600 detector is dominated by seismic noise. The isolation from seismic noise is discussed below and is the main focus of this thesis.

Methods for low frequency noise suppression

Figure 1.6 shows, that the lower frequency part of the detection band of interferometric ground-based gravitational wave detectors is limited by seismic noise. The simplest way of isolating the interferometer mirrors from seismic vibrations is suspending them with wires. The mirror mass and the wire form a pendulum which provides f^{-2} horizontal vibration isolation above the pendulums natural frequency. The isolation performance

of the pendulum can be improved by building a chain of several masses suspended from wires. The isolation improves according to f^{-2n}, where n is the number of isolation stages. Similarly, isolation can be achieved in the vertical direction by suspending the mirror from cantilever blade springs. The springs provide f^{-2} vertical isolation above their natural frequency.
The natural frequency of such a suspension pendulum is usually in the order of one hertz[2]. To improve the isolation performance, one can either reduce the natural frequency of the pendulum by increasing its length or use a chain of shorter pendulums. As will be shown in section 2.4, reducing the natural frequency is often difficult due to spatial restrictions or because the suspensions introduce additional noise at the bounce mode of the wires.
Alternatively, the mirror suspension can be pre-isolated. The Virgo gravitational wave detector uses a passive mechanical seismic pre-isolator called the Superattenuator. A small-scale passive pre-isolator, the TAMA Seismic Attenuation System (TAMA-SAS), was developed for TAMA300. LIGO uses a Hydraulic Active Pre-Isolation (HEPI) system for the actively isolated optical benches. All these pre-isolation systems are reviewed in section 2.5. Their common feature is their ability to isolate the mirror suspensions from ground motion at very low frequency. The effective isolation is given by the combined performance of pre-isolation and suspension. In a well designed system, the suspension resonances are in a frequency range where seismic motion is well attenuated by the pre-isolator.

Seismic isolation at the AEI 10 m Prototype

The work presented in this thesis was performed at the Albert Einstein Institute (AEI) in Hannover, where the AEI 10 m Prototype interferometer is being set up. The AEI 10 m prototype interferometer facility (in the following referred to as AEI 10 m Prototype) is a test bed for novel techniques for improving future generations of interferometric gravitational wave detectors. Like the large-scale detectors, the AEI 10 m Prototype uses an L-shaped vacuum system, as shown in figure 1.7, and a Michelson-type interferometer with suspended optics. However, the AEI 10 m Prototype is not intended as gravitational wave detector: its 10 m arm-length is simply too short to achieve the required sensitivity. A detailed review of the AEI 10 m Prototype facility is given in chapter 8.
A key feature of the AEI 10 m Prototype facility are seismically isolated optical tables, illustrated in figure 1.8. Each optical table is isolated from ground motion by means of a passive mechanical pre-isolator, the AEI Seismic Attenuation System (AEI-SAS). It uses the properties of mechanical oscillators to isolate the optical tables from ground motion. The isolating elements of the AEI-SAS are a three-leg Inverted Pendulum (IP) and curved blade springs that form the Geometric Anti-Spring (GAS) filters.
The optics will be suspended from multiple cascaded pendulums with a final all silica

[2] The unit *hertz*, abbreviated to Hz, is defined as one cycle per second, or the inverse of the period of an oscillation. The unit was named after Heinrich Rudolf Hertz, who was the first to prove the existence of electromagnetic waves. The *bureau international des poids et mesures* (BIPM) defining in the international system (SI) of units, regulates that the unit hertz is written with a lower-case (just like the units ampere, pascal and watt), although the abbreviation Hz (A, Pa, W) starts with a capital [BIPM]. This definition is maintained throughout this thesis.

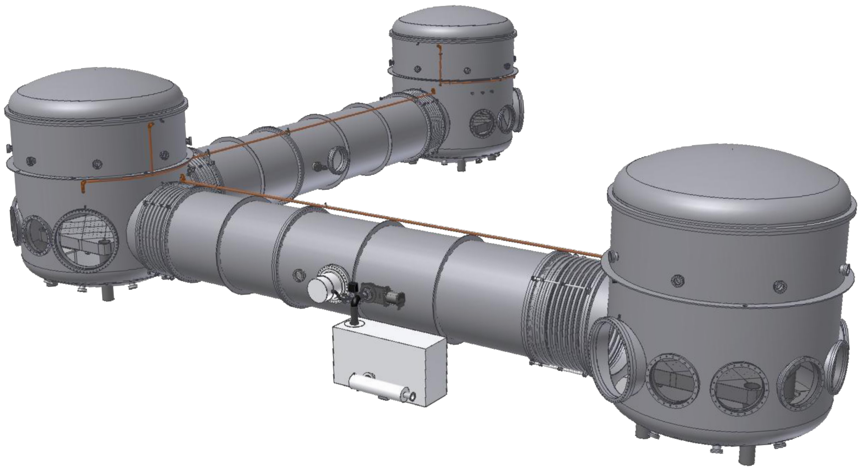

Figure 1.7.: A drawing of the L-shaped vacuum system of the AEI 10 m Prototype interferometer, consisting of three walk-in vacuum tanks. Each tank contains an optical table for the mirror suspensions. Each tables is passively isolated from ground motion by a mechanical Seismic Attenuation System (AEI-SAS).

monolithic stage. The multi-stage suspensions will be positioned on the three pre-isolated optical tables. The pre-isolation of the optics suspension reduces the large, low-frequency seismic motion near the suspension resonances, and provides a quieter platform at higher frequencies to improve the combined isolation performance.

1.3. The reader's guide to the thesis

Chapter 2 gives an introduction to the all pervasive seismic noise (section 2.1), its measurement, and instrumental and computational analysis (section 2.2). The subsequent sections give an introduction to seismic isolation by means of mechanical oscillators, such as harmonic oscillators (section 2.3) and a selection of low-frequency oscillators (section 2.4). Examples of low-frequency oscillators implemented as seismic isolators in gravitational wave detectors (section 2.5) are given.

Chapter 3 illustrates the AEI-SAS assembly (section 3.1). The design differences to the HAM-SAS prototype (section 3.2) and a review of the construction of the system (section 3.3) are provided.

Chapters 4 and 5 introduce the main isolating systems of the AEI-SAS: the IPs and GAS filters. The chapters are structured in a similar fashion: theoretical descriptions (sections 4.1 and 5.1) are followed by Centre of Percussion compensation methods (sections 4.2 and 5.2) and concluded with measurements of the independent performances (sections 4.3 and 5.3) of the horizontal and vertical isolators respectively.

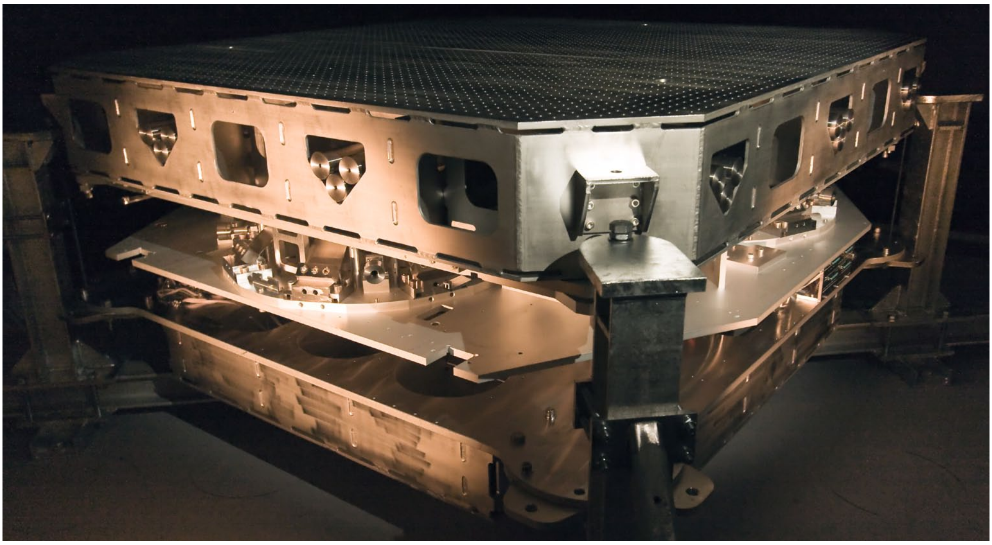

Figure 1.8.: A photograph of one of three identical AEI-SAS supporting an optical table.

Chapter 6 reviews the overall mechanical performance of the fully assembled AEI-SAS. The dependence of the system to temperature variations (section 6.1), force response measurements (section 6.2), and transfer function measurements (section 6.3) are shown.

Chapter 7 sketches the active feedback control strategy for the AEI-SAS, starting with an overview of the sensors and actuators for local control (section 7.1). Active damping of fundamental modes of the AEI-SAS are demonstrated (section 7.2). Tests of damping of the system's rigid-body modes by means of resonant mechanical dampers and active feedback controls (section 7.3) are presented. The implementation of Fluorel™ pads decoupling oscillations from the optical table (section 7.4) is introduced. The future control strategy (section 7.5) is sketched.

Chapter 8 provides a broader view of the importance of the AEI-SAS for the AEI 10 m Prototype. Major components of the facility (section 8.1) and first experiments for the 10 m Prototype interferometer (section 8.2) are described.

Chapter 9 concludes this thesis. A short summary and an outlook on future work on the AEI-SAS in the 10 m Prototype are provided.

2. Introduction to seismic noise, measurement, and isolation

Noise proves nothing.
Often a hen who has merely laid an egg cackles as if she has laid an asteroid.

Mark Twain

This chapter gives an overview of seismic noise. Various examples for seismic noise sources and measurement techniques are introduced in section 2.1. Signal analysis is briefly discussed in section 2.2. Since harmonic oscillators are used to isolate seismic noise, a selection of the most important properties of the harmonic oscillator is given in section 2.3. An overview of low-frequency pendulums, which can be used as isolators, is given in section 2.4. This chapter ends with a review of seismic isolators in gravitational wave observatories in section 2.5.

2.1. Seismic noise

The seismic noise discussed in this thesis refers not to short seismic events such as a temporary tremor caused by an earthquake, but rather the continuous background of seismic vibration. This continuous seismic noise has manifold causes and effects.
The low frequency noise sources are the reason, why seismic isolation is urgently required for optical experiments. The key goal for the Seismic Attenuation System is the reduction of the RMS motion (particularly near the suspension resonances), thereby offering a pre-isolation for the mirror suspension of the interferometer. To gain isolation at the lowest possible frequency and to provide a decent pre-isolation to the mirror suspensions, a seismically isolated table is required, as described in chapter 3.

New noise model

The lowest measurable vertical seismic noise level is indicated by the new low noise model (NLNM) published by [Peterson1993]. Peterson compares seismic noise signals from 75 seismic stations spread all over the world and derives the low- and high-noise models, both shown in figure 2.1. The models incorporate only noise without strong seismic events. The low noise model is widely used as a reference to evaluate the quality of seismic stations and to design new sensors for seismic measurements. The noise models are usually plotted as Power Spectral Density (PSD – see appendix C.1) of ground acceleration over time periods. Geologists often use the time axis to indicate the duration of the period of a certain seismic event. For our purposes it is easier to think in the frequency domain, so the period, T, is converted into frequency, f, with

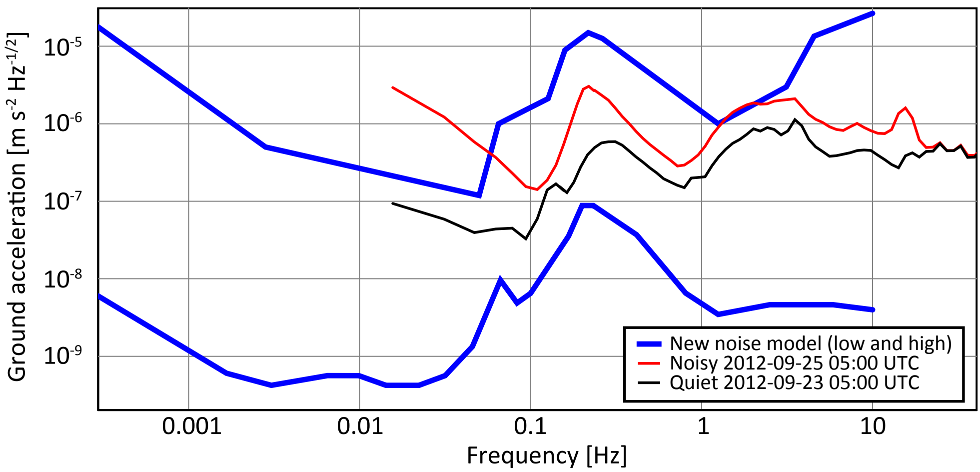

Figure 2.1.: The seismic linear acceleration spectral density of Peterson's New Low- and High- Noise Models (NLNM and NHNM indicated by blue thick curves) compared with seismic measurements at the AEI 10 m Prototype facility. The NLNM indicates the lowest possible seismic noise measurable on Earth [Peterson1993]. The two AEI seismic measurements were captured at quiet (black curve) and elevated seismic activities (red curve), labelled with A and B, respectively in figure 2.2. The peaks at 0.2 Hz are attributed to microseismic noise, caused by interaction of swells with the sea-floor near coastlines.

$T = 1/f$.

Figure 2.1 depicts the Linear Spectral Density (LSD – see chapter C.2.3) of the New Low Noise Model (NLNM) and New High Noise Model (NHNM) in units of ground acceleration, plotted over frequency. The noise models are compared with seismic measurements, performed in the Albert Einstein Institute (AEI) in close proximity to the vacuum tanks. The AEI is located a few kilometres from the city centre of Hannover, thus the plot in figure 2.1 shows characteristic attributes of a seismic spectrum recorded in an urban area: a broad bump around 3 Hz caused by human activity, that is also visible in figure 2.2.

	Date (UTC)	Magn. (M)	Depth [km]	Location
a	25 Sep 23:45	6.2	10.1	75km NNE of La Paz, Mexico
b	26 Sep 23:39	6.4	9.9	29km SSW of Tanaga Volcano, Alaska
c	27 Sep 23:53	6.0	10	112km SE of Gizo, Solomon Islands
d	30 Sep 16:31	7.3	168.3	9km WNW of San Agustin, Colombia
e	01 Oct 22:21	6.2	9.7	96km ENE of Miyako, Japan

Table 2.1.: Earthquakes, visible in the seismic spectrogram in figure 2.2, marked by letters (a)–(e). The earthquake information originates from [Volcanodiscovery].

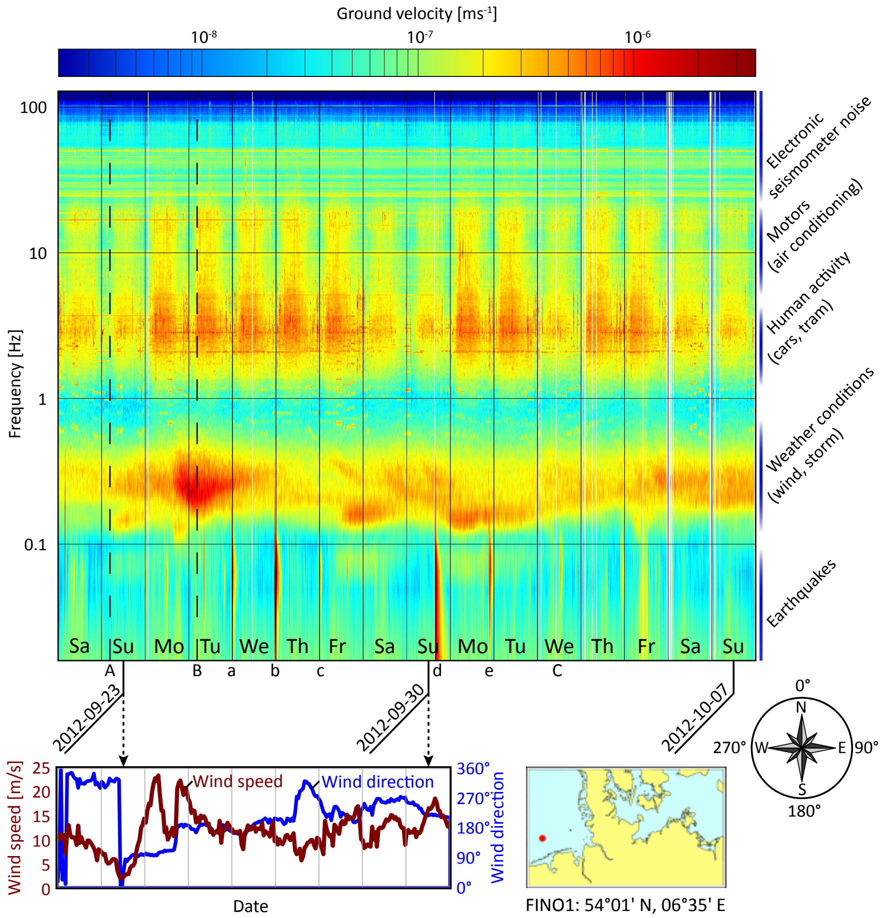

Figure 2.2.: Spectrogram of the vertical seismometer signal (Streckeisen STS-2), recorded over two weeks at the AEI 10 m Prototype in the basement of the institute. The spectrogram shows how the frequencies develop over time. The dashed lines (A and B) show the time when the quiet and noisy spectra for figure 2.1 were recorded. The frequency axis can be subdivided in several regions, in which different signals can be observed. Earthquakes are visible in the low frequency range, below 0.1 Hz. The letters (a)–(e) indicate earthquakes, identified and listed in table 2.1. Stormy weather conditions in the North Sea, especially waves interacting with the sea shore, are affecting the frequency region between 0.1 and 1 Hz. The plot below the spectrogram shows wind speed and wind direction over 9 days. The time when the wind speed rises and changes the direction (from East $\approx 90°$ to South $\approx 180°$) on Monday, 2012-09-24 correlates with the increase of seismic activity in the frequency range of the microseismic peak. The meteorological data was recorded by the offshore platform FINO1 in the North Sea [BSH]. The platform's position is indicated on the map, with GPS coordinates given below. The meteorological data is courtesy of the *Bundesministerium für Umwelt, Naturschutz und Reaktorsicherheit* (BMU) and the *Projektträger Jülich* (PtJ). Human activity increases the ground motion between 1 Hz and 30 Hz. Over weekends and during the holiday on Wednesday (German Unity Day, marked with C) human activity reduces, thus the seismic signal decreases. Above 30 Hz the seismometer sensitivity drops dramatically, as shown in figure F.5, and the data is dominated by the electronic noise of the seismometer.

Seismic noise sources

This section gives an overview of the main noise sources that cause ground vibrations like those depicted in figure 2.1. According to [Hillers2011], the noise below 0.002 Hz (corresponding periods longer than 500 s or ∼8 min) is usually attributed to long wavelength ground tilting caused by temperature fluctuations or large scale atmospheric pressure changes [Beauduin1996], which are correlated with seasonal climatic changes and result in larger noise amplitudes in horizontal components. The range between frequencies of 0.002 Hz and 0.025 Hz (corresponding periods of 500 s and 40 s) shows the lowest noise amplitudes. However, a small peak around 0.01 Hz (period of 100 s) consists of a series of distinct monochromatic oscillations, referred to as *Earth's hum* [Rhie2004, Tanimoto2005, Kurrle2008, Hillers2011].

The microseismic peak around 0.2 Hz is visible everywhere on Earth. It is considered to be related to the interaction of ocean swells with the seafloor near coastlines [Bormann1998]. Microseismic motion is typically observed in two distinct frequency bands. The generation mechanism of the primary microseism from 0.07–0.1 Hz (corresponding period 14–10 s) is not well understood, but is often accredited to direct interaction of the swell with a shallow seafloor or the shore [Yang2008]. Secondary microseisms are measured at double the swell frequency, typically 0.14–0.2 Hz. This signal with double the frequency is generated by non-linear interaction between two opposing wave fields, set up by reflection off a coastline. The amplitude of microseismic peaks varies with the location of the measurement site and is correlated to ocean wave heights [Schulte-Pelkum2004]. Figure 2.2 shows a spectrogram of a seismic measurement recorded at the AEI in correlation with wind measurements in the North Sea. It shows that the microseismic peak rises when the wind in the North Sea is oriented towards the coast. At frequencies above the microseismic peak, the amplitude of seismic noise has an f^{-2} slope. Signals produced by human activity, such as industrial facilities or traffic, usually appear around the 3 Hz [Webb1998] and can stretch over a wide frequency range.

Inertial sensors

Inertial sensors are often used to measure vibrational motion. Common inertial sensors are accelerometers, geophones, and seismometers. Their distinction is rather a commercial issue. All three types of sensors are available as single axis devices, sensitive in only one axis, or can be combined to make a bundle with more than one axis in a compact package. The natural frequency of the mechanics and the readout of the mechanical position makes them different from each other. There exist open-loop devices such as geophones and piezo-accelerometers or force-balanced devices, like the broadband seismometer Streckeisen STS-2 [Nakayama2004] or the AEI-accelerometers [Bertolini1999b].

Accelerometers, as the name suggests, are used to measure accelerations. The measurement principle is comparable to a damped mass on a spring. When the device is accelerated, the mass is displaced from its neutral position until the spring is able to accelerate the mass at the same rate as the casing. The displacement of the mass is proportional to the acceleration. Accelerometers are available with different sizes and working principles.

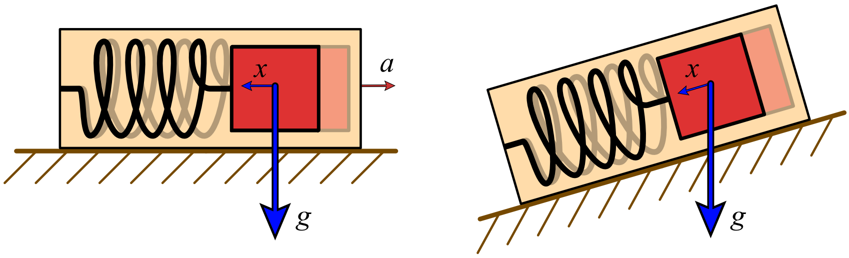

Figure 2.3.: Due to the equivalence principle, horizontal acceleration and tilt cannot be distinguished by horizontal accelerometer in Earth's gravity field [DeSalvo2009]. In both cases the test mass is displaced by the same amount, x and the devices measure an acceleration, a.

They are commonly used, for instance, for vibration monitoring of industrial machines [Honeywell], in modern mobile phones [Effa2009] and digital cameras [Wang2007], built as microscopic monolithic mass-spring systems. Accelerometers are also used to detect a car crash for airbag deployment, built as micro-accelerometers with piezo-resistive readout [Kim1995] or as thermal accelerometers without a solid proof mass [Mailly2003]. Monolithic horizontal accelerometers are used in the AEI-SAS to measure horizontal inertial motion and to monitor the vibration isolation performance. Details to the monolithic AEI-accelerometers are given in chapter 7.1.2.
Geophones are used to convert ground motion into voltage. They are robust and relatively cheap, usually composed of a coil and a magnetic mass suspended on springs. When the geophone body is displaced the mass tends to keep the resting position due to its inertia. The magnet induces a current in the coil. The induced current is proportional to the ground velocity above the natural frequency of the suspension. Geophones are usually designed to be used in harsh environmental conditions (increased humidity, dust) and are more robust to environmental effects than seismometers. Vertical geophones, L-22D by Mark Products, are used at the AEI 10 m Prototype to monitor the residual vertical motion of the optical table. A detailed description of their application is given in chapter 7.1.3.
Force balance seismometers are typically larger and more expensive and are more sensitive than geophones below 1 Hz, although at higher frequencies the geophones are more sensitive devices. Broadband seismometers, such as the Streckeisen STS-2, are designed for seismologists, who are normally interested in signals below 1 Hz. Seismometers are usually more fragile than geophones, due to more sophisticated mechanical design. They also are more sensitive to environmental deviations, so a careful installation (thermal and acoustic shielding, proper connection to the ground) is required. A Streckeisen STS-2 broadband seismometer is used at the AEI 10 m Prototype for seismic motion monitoring.

Environmental effects on the sensor output

Forces of non-inertial nature often superimpose the output of an inertial sensor. For example, the tilting of the sensor couples into the horizontal component of the signal. The horizontal degrees of freedom are by definition perpendicular to the direction

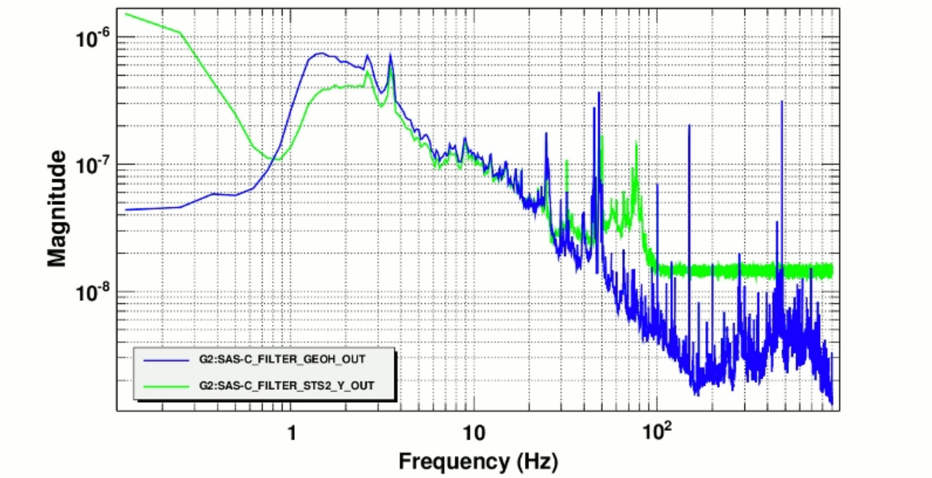

Figure 2.4.: Comparison of horizontal velocity spectral densities: geophone L-4C and broadband seismometer Streckeisen STS-2. The spectra (in units of $(\mathrm{m/s})/\sqrt{\mathrm{Hz}}$) agree within their common frequency range around $3-20\,\mathrm{Hz}$. The raise of the geophone signal above 200 Hz is attributed to acoustic noise picked up by the floor of the room and sensed by the geophone. The outputs of the devices are not calibrated with their corresponding responses, which are shown in figure F.5. Thus, a bump is visible in the geophone signal between $1-3\,\mathrm{Hz}$, and in the seismometer signal above 50 Hz. Above 100 Hz the seismometer signal is limited by ADC noise.

of the gravity. In a tilted mono-directional sensor the test mass is displaced due to gravity instead of acceleration, so the output indicates a permanent acceleration, as shown in figure 2.3. The tilt of the ground, which then is measured by the inertial sensor, is caused by moving or varying surface loads, such as walking people, driving cars, or changes of atmospheric pressure.

Seismic sensors are not only sensitive to inertial forces, but also to changes of environmental conditions. If one imagines the sensor to be a seismic mass suspended by spring blades, than the environmental influence becomes comprehensible. Temperature variations can change the spring's elasticity modulus. Fluctuations of air density and pressure can deform the seismometer's base, thereby causing tilt of the sensor, or generate buoyancy of the seismic mass. Furthermore, magnetic field variations can affect suspension springs, which often are ferromagnetic and magnetostrictive, so their modulus depends on magnetization. At high frequencies seismic sensors are sensitive to acoustic noise. Without a proper acoustic enclosure, the sensors work like a microphone, falsely showing the acoustically coupled signal as a seismic motion. In order to resolve low frequency signals, all these disturbing effects can be minimized by careful sensor installation.

A comparison of two different inertial sensors placed on one rigid plate is shown in figure 2.4. The broadband seismometer Streckeisen STS-2 and the geophone Mark Products L-4C agree within the range 3 Hz–20 Hz. Above 50 Hz the sensitivity of the STS-2 drops, and below 1 Hz the sensitivity of the L-4C drops, as shown in figure F.5 on page 162. The outputs of the devices were not calibrated with their corresponding responses, which are shown in figure F.5. Instead, constant values of the linear response plateau were used. Thus, a bump caused by sensor response is visible in the geophone signal between 1 Hz–3 Hz, and in in the seismometer signal above 50 Hz. Above 100 Hz the seismometer signal is limited by ADC noise, due to low pre-amplification of the signal. The sensors were not acoustically shielded during the test measurement, and the increased geophone signal above 200 Hz is attributed to acoustic noise picked up by the floor of the room and sensed by the geophone. An acoustic enclosure and proper connection to the ground, instead of placing the sensor on a platform, would have reduced the high frequency pick-up.

2.2. Seismic signal analysis

A signal measured in the time domain can be converted into the frequency domain. The representation of a signal in a different domain allows a deeper insight into the quality of the data. For instance, a noisy signal in the time domain may look more comprehensible in the frequency domain. A set of mathematical tools, including Fourier transform and interpretation of power spectral density plots, is presented in appendix C. The methods are required to analyse data from seismic sensors and to allow comparison of different records from different sites and times.
In an experimentalist's everyday life, it is unlikely to have a continuous function, $s(t)$, to be given to work with. Measured data is rather available as a sequence of sampled measurements, $s(t_k)$. Therefore a definition of the discrete Fourier transformation (DFT) is given in appendix C.2.1.
In signal analyses, data is usually presented as Linear Spectrum (LS) or as Power Spectrum (PS). Both LS and PS have the property that the noise level depends on the duration of the measurement. Therefore, the signal to noise ratio can be improved by using longer measurement times. In that case, the noise level reduces, while the peak level of the signal remains constant.
This thesis focuses on noise and its suppression. Since the noise level depends in both, LS and PS, on the measurement duration, a different type of spectrum analysis is required. The power spectral density (PSD) is defined as a PS normalized by the measurement resolution. The PSD is thus independent of the sampling frequency and additionally independent of the measurement duration. Therefore, plotting measurement data as PSD allows a comparison of measurements even if they were performed with different sampling rates and different measurement durations. PSDs are therefore a powerful tool to depict the power of the seismic noise. The definition of the PSD is given in appendix C.1. The relation between PSD and LS are shown in table 2.2.

2.3. Harmonic oscillators for seismic isolation

The focus of this thesis is achieving passive isolation from seismic noise using properties of harmonic oscillators. Therefore, major properties of harmonic oscillators are summarized in this section. The working principle of harmonic oscillators is discussed in appendix A.
There exist two major seismic isolation approaches: active and passive. Active isolation

Abbrev.	Name	Relation	Unit
PSD	power spectral density		V^2/Hz
PS	power spectrum	$\mathrm{PS} = \mathrm{PSD} \times \mathrm{ENBW}$	V^2
LSD	linear spectral density	$\mathrm{LSD} = \sqrt{\mathrm{PSD}}$	$\mathrm{V}/\sqrt{\mathrm{Hz}}$
LS	linear spectrum	$\mathrm{LS} = \sqrt{\mathrm{PS}} = \mathrm{LSD} \times \sqrt{\mathrm{ENBW}}$	V

Table 2.2.: Relation between the linear spectrum (LS), the power spectrum (PS), and their spectral densities (LSD and PSD) [Heinzel2002]. The ENBW is the equivalent noise bandwidth, defined in equation C.27.

uses feed-back and feed-forward techniques. In feed-back applications, motion of the payload, induced for example by the seismic, is measured and forces are applied to it to suppress the effect. In feed-forward applications, the ground motion is measured and forces are applied to the payload to cancel the anticipated effect. In contrast, a passive isolator uses the mechanical properties of a harmonic oscillator, which isolates at frequencies above its natural frequency.

Natural frequency of an harmonic oscillator

Harmonic oscillators, for instance a coil spring or a pendulum, as sketched in figure 2.5, require a mass. After being deflected from its resting position, it returns to its equilibrium position. The restoring force can, for instance, be a spring or gravity.
One simple harmonic oscillator consists of a linear spring with spring constant, κ, loaded with a mass, m. The natural frequency, f_n, of such an oscillator is defined as:

$$f_\mathrm{n} = \frac{1}{2\pi}\sqrt{\frac{\kappa}{m}}\,. \tag{2.1}$$

The force, F_κ, that is needed to deflect the spring by x is defined by Hooke's law as:

$$F_\kappa = -\kappa x\,. \tag{2.2}$$

This force can be applied, for example, by attaching a mass, m. The force is proportional to the acceleration of the mass, following Newton's second law of motion:

$$F_\mathrm{a} = mg\,, \tag{2.3}$$

with g, the gravitational acceleration on Earth. When the spring force and the gravity force are in balance, the sum of all forces in the system is zero. Thus, the spring constant of a spring can easily be determined by loading it with a mass and measuring its deflection:

$$\kappa = \frac{mg}{x}\,. \tag{2.4}$$

Hence, combining equations 2.1 and 2.4, the natural frequency of a spring is given by:

$$f_\mathrm{n} = \frac{1}{2\pi}\sqrt{\frac{g}{x}}\,. \tag{2.5}$$

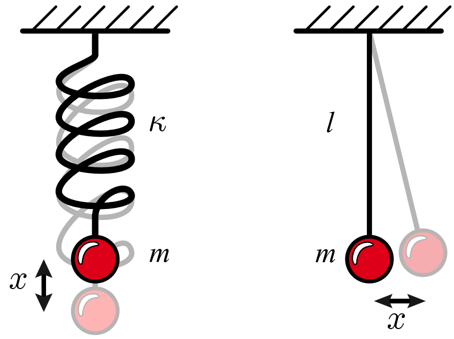

Figure 2.5: Two examples of ideal harmonic oscillators: a spring-mass oscillator and a pendulum. The masses are displaced by the distance, x, and perform oscillations at natural frequency, f_0. The restoring force is provided by the spring or gravity, respectively.

Thus, a spring contracted (or deflected) by 25 cm has a natural frequency of ∼1 Hz, and ∼5 Hz for 1 cm.
It is sometimes convenient to use the angular frequency, $\omega_\mathrm{n} = 2\pi f_\mathrm{n}$ to omit the 2π factor. The angular frequency, ${\omega_\mathrm{n}}^2 = \kappa/m$, is the outcome of the calculation of the equation of motion of the harmonic oscillator.
Alternatively, the natural frequency is determined by deflecting the oscillator, letting it oscillate freely, and measuring the period, T. The reciprocal of the period of a free oscillation is the natural frequency of the oscillator.

Damping

The damping, or loss, of an oscillator can be described by its quality factor, Q. The Q-factor is the energy stored in the oscillator divided by the energy dissipated per cycle, and is defined as:

$$Q = \frac{1}{2\zeta}\,, \tag{2.6}$$

and ζ is the damping ratio:

$$\zeta = \frac{c}{2\sqrt{m\kappa}} = \frac{c}{2m\omega_n}\,, \tag{2.7}$$

where c is the viscous linear damping coefficient proportional to velocity, and ω_n is the undamped natural frequency of the oscillator.
The natural frequency, ω_n^damp of a damped oscillator becomes:

$$\omega_n^\mathrm{damp} = \omega_n\sqrt{1-\zeta^2} \tag{2.8}$$

with the undamped natural frequency, ω_n, and the damping ratio, ζ, as defined in equation (2.7).
Damping quality of an oscillating system can be determined experimentally by measuring the logarithmic decrement, δ, defined as:

$$\delta = \frac{1}{n}\ln\frac{x_0}{x_n} = \frac{2\pi\zeta}{\sqrt{1-\zeta^2}}\,, \tag{2.9}$$

which is obtained by measuring the decaying amplitude of a damped oscillation, comparing an initial amplitude, x_0, to the amplitude x_n after n cycles. The damping

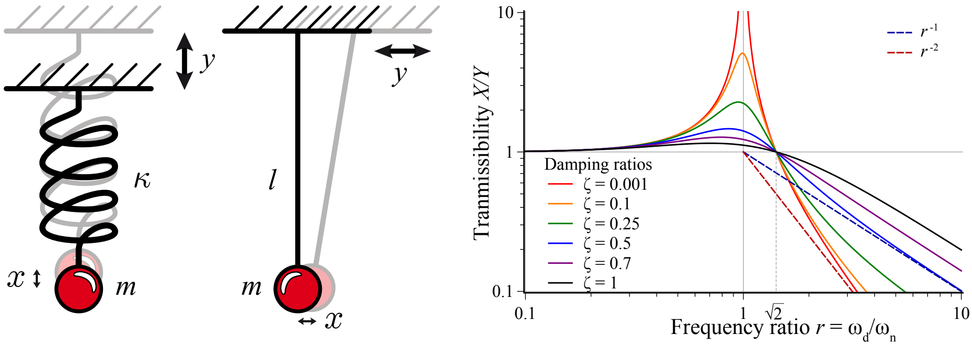

Figure 2.6.: Symbolic representation of ideal harmonic oscillators used as vibration isolators. When the ground is displaced sinusoidally with amplitude y the mass moves at the same frequency with amplitude x. The plot on the right-hand side shows transfer functions of a driven harmonic oscillator for different values of the quality factor, Q, as function of the frequency ratio $r = \frac{\omega_\mathrm{d}}{\omega_\mathrm{n}}$, where ω_d is the driving frequency of the ground and ω_n is natural frequency of the undamped oscillator. The isolation from ground motion starts above $\sqrt{2}$ of the resonance. The transmissibility of viscously damped oscillators rolls off with f^{-2} for large Q-factors, otherwise the transmissibility rolls off as f^{-1}.

ratio is then given as:

$$\zeta = \frac{1}{2Q} = \frac{\delta}{\sqrt{(2\pi)^2 + \delta^2}} \,. \tag{2.10}$$

There are further possibilities to define and compute the Q-factor. These are described in the subsequent section regarding transfer functions.

Transfer function

A transfer function is a mathematical description of the relation between the input and the output of a system. It is defined as the Fourier transform of the output amplitude, X, divided by the Fourier transform of the input amplitude, Y. Transfer functions are applicable to linear time-invariant systems. In simple words, a linear system responds at the same frequency with a certain magnitude and phase-angle relative to the input, when a sinusoidal signal is injected into the input at a certain frequency. In a time-invariant system, the output response does not depend on the particular time at which the input signal is applied, and the transfer function does not vary with time.
When vibrations are transmitted through an isolator, the transfer function is called the transmissibility. Both terms are used here interchangeably, since all transfer functions in this thesis depict isolation properties of mechanical isolators. In practice, transmissibilities of isolators are analysed by applying a sinusoidal input oscillation to the mounting point and comparing this movement to the output motion of the isolated mass, as shown in figure 2.6.
The displacement transmissibility of a single degree of freedom vibration isolator driven

from the ground is given by:

$$\frac{X}{Y} = \sqrt{\frac{1 + \left(\frac{r}{Q}\right)^2}{(1-r^2)^2 + \left(\frac{r}{Q}\right)^2}} . \tag{2.11}$$

The transfer function X/Y describes, how motion is transmitted from the ground to the mass as a function of the frequency ratio $r = \omega_\mathrm{d}/\omega_\mathrm{n}$, with the driving frequency, ω_d, of the ground.
Figure 2.6 shows transmissibility plots of a damped harmonic oscillator for different quality factors. It illustrates how the spring-damper system isolates the mass motion from ground oscillation. Below the natural frequency, the transmissibility is one, so that the mass moves with the same amplitude as the ground. The transfer function has a maximum at the resonance at ω_n^damp. At the resonance, the value of the transfer function is equal to the quality factor of the oscillator. The Q factor can also be defined by the width of the resonance peak:

$$Q = \frac{f_n}{\Delta f} , \tag{2.12}$$

with f_n, the resonance frequency and Δf, is the full-width at half-maximum power, where the amplitude is $\sqrt{2}$ smaller.
With insufficient damping, a mechanical system is prone to a so-called catastrophic resonance, leading to the destruction of the oscillator [Billah1991]. Without damping, the amplitude at the resonance frequency is calculated to be infinite.
Vibration isolation starts above $\sqrt{2}$, as computed in the appendix in equation A.35 and shown in figure 2.6. Above this point the transmissibility is less than 1, thus the oscillation amplitude of the mass is smaller than the amplitude of the ground oscillation. For small damping values the transmissibility rolls off as f^{-2}. As the damping becomes critical, the transmissibility rolls off as f^{-1}. See appendix A for more details on harmonic oscillators.

Bode diagram

Transfer functions are often depicted in a Bode diagram, as shown in figure 2.7. The Bode diagram consists of two plots in the frequency domain: a magnitude plot and a phase-angle plot. The magnitude plot is identical to the transmissibility plot, shown in figure 2.6. It depicts a quantitative measure of the output spectrum of the system per unit of input. The phase plot shows, for each frequency, the phase difference between a sinusoidal drive input and the output sinusoidal motion of the mass.
The equations for phase of a ground-driven harmonic oscillator is given as:

$$\theta_\mathrm{particular} = \tan^{-1}\left(\frac{2\zeta\omega_n\omega_d}{\omega_n^2 - \omega_d^2}\right) + \tan^{-1}\left(\frac{\omega_n}{2\zeta\omega_d}\right) , \tag{2.13}$$

where ω_n is the undamped natural frequency, ω_d is the driving frequency originating from the ground, and ζ the damping ratio. The phase-angle in the Bode diagram is at zero for frequencies below resonance. For a low damping factor, the phase angle is $-90°$

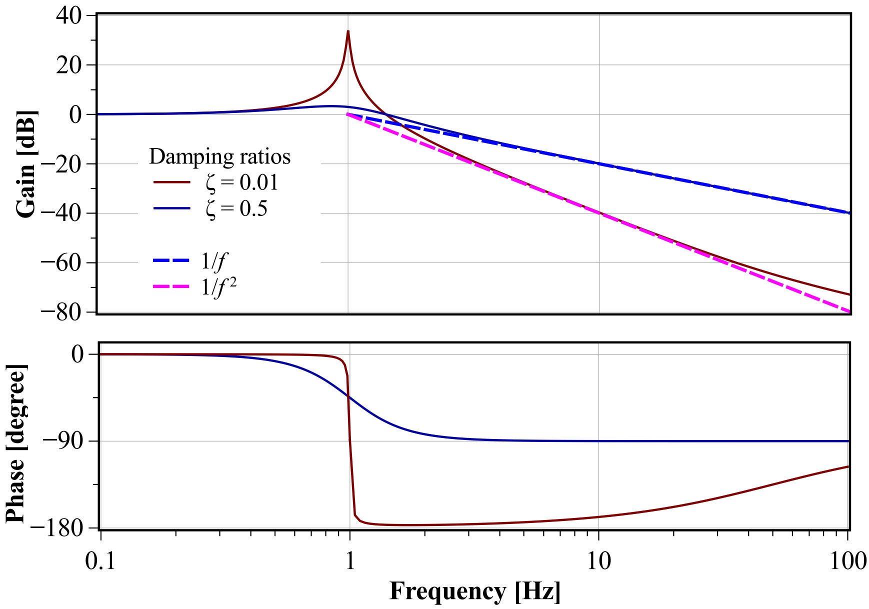

Figure 2.7.: Bode diagram of an harmonic oscillator driven from the ground, as illustrated in figure 2.6. The oscillator in this example has a resonance frequency of $f_{\mathrm{n}} = 1$. The magnitude plot shows the transfer function as Fourier transformed output amplitude divided by input in units of dB. The decibel is defined as $20\log_{10}(\mathrm{LSD}) = 10\log_{10}(\mathrm{PSD})$. Below the resonance, the transfer function is 0 dB, hence the mass follows the ground motion. The hight and width of the resonance peak depend on the damping. The gain plot in the Bode diagram is identical to the transmissibility plot in figure 2.6, except for the units and the additional phase information.
The second plot shows the phase of the oscillating system with respect to ground vibration. The phase angle indicates, how synchronous the output and input oscillate. At low frequencies, ground and mass oscillate in phase. At and above the resonance frequency, the phase depends on the damping. For low damping ($\zeta = 0.01$): directly at the resonance the phase is $-90°$ and above resonance the oscillations are out of phase at $-180°$. For rising frequency, the mass ketches-up to the ground oscillation, the phase diverges towards $-90°$. For high damping ($\zeta = 0.5$): the phase difference of the mass and the ground converge towards $-90°$.

at the resonance, at higher frequencies it drops to $-180°$ and increases again towards $-90°$. The equations for gain and phase are derived in appendix A in equation (A.31).

2.4. Low frequency isolation devices

The AEI-SAS uses the properties of low-frequency oscillators to provide seismic isolation. Examples for oscillators with very low (sub hertz) natural frequencies are reviewed in this section. Further examples can be found, for example, in [Suits2012, Winterflood-thesis]. Additionally, this section discusses the use of these low-frequency oscillators as passive isolation systems.

Mathematical pendulum

The natural frequency, f_n of a simple pendulum is given as

$$f_n = \frac{1}{2\pi}\sqrt{\frac{g}{l}},$$

assuming a massless suspension and omitting any losses. The natural frequency is independent of the mass, therefore, a pendulum with a length of 1 m has a natural frequency of about 0.5 Hz or a period of 2 s. To achieve lower frequencies the pendulum length needs to become significantly longer: roughly 100 m pendulum length are required for $f_n = 0.05$ Hz or 20 s period.
An intriguing example of, probably, the longest pendulum was built at the Michigan College (today's Michigan Technological University) in 1901 to explore a local vertical mine shaft with a length of more than 1 km. The length of the pendulum was about 1.3 km (4,250 ft.) and the frequency was assessed to be 0.014 Hz by measuring the pendulum's period of 70 s [Suits2006]. Unfortunately, such long pendulums are not practical, and simple pendulums are not an option for low frequency noise suppression in interferometric gravitational wave observatories.

Dumbbell pendulum configurations

A horizontally suspended dumbbell pendulum is known from its application in ancient weighing scales. Such a physical pendulum has a large moment of inertia but comparably small restoring forces. A pendulum with coinciding centre of mass and pivot point has no defined static rest position. However, if the centre of mass and the pivot point are slightly displaced, as shown in figure 2.8, the pendulum is be able to rest in a defined static equilibrium position. The tilting movement around the horizontal equilibrium position has a period depending on the distance between the rotation axis and the centre of mass. The smaller the displacement, the lower is the natural frequency. Optical experiments suffer from seismic motion around 100 mHz exerted by the microseismic peak, as shown in chapter 2. The dumbbell pendulum described in publication [Krylov1996] achieved oscillation frequencies as low as 2.7 Hz. The achieved natural frequency is not low enough to be used as a low frequency isolator, but the idea of displacing the pivot point from the centre of mass is applied to the next pendulum, which achieved a much lower natural frequency.

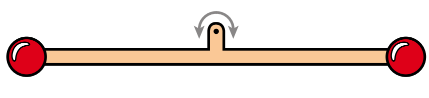

Figure 2.8.: A scales-like dumbbell pendulum, with long period due to the small distance between the rotation axis and the centre of mass.

A similar construction is presented by [Peters1990], with the difference that the dumbbell is oriented vertically, see figure 2.9a. The pivot point is again displaced from the centre of mass, but this time along the length of the pendulum. Thereby, the pendulum is pushed from a stable regime towards the verge of instability. This way,

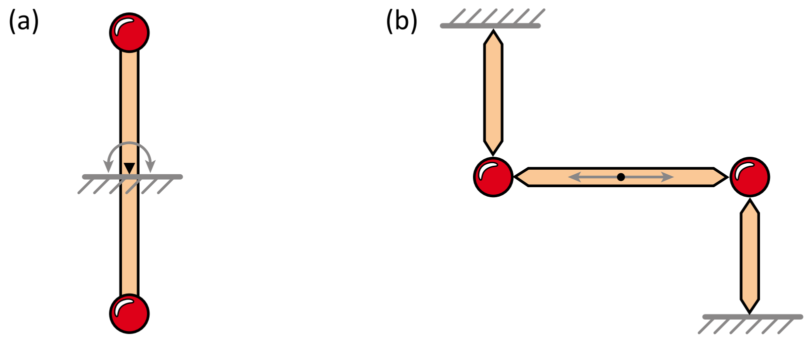

Figure 2.9.: Schematics of (a) a vertical dumbbell pendulum and (b) a folded pendulum. The vertical dumbbell pendulum achieves low natural frequencies by vertically displacing the rotation point (marked by a triangle). It consists of a stable regular pendulum and an unstable inverted pendulum. The folded pendulum, based on the Watt-Linkage design, is also a combination of a regular pendulum and an unstable inverted pendulum. The latter ads a negative restoring force to the system, thereby reducing the natural pendulum frequency. An interesting side effect of the Watt–linkage is that the central point of the connecting bar (marked by a dot) moves on a flat line for small oscillation amplitudes.

the pendulum consists of two linked pendulums: a stable regular pendulum and an unstable inverted pendulum. The inverted pendulum ads a negative restoring force to the positive restoring force of the pendulum, thereby reducing the natural frequency. The equilibrium position is disturbed by the unstable counterpart, which pushes the system to the verge of instability, thereby achieving longer oscillation periods. The lowest achieved natural frequency is 0.033 Hz (a period of 30 s). Tuning of the natural frequency by shifting the suspension point is tricky, because slight over-tuning leads to instability of the pendulum. The concept of one stable regular pendulum and one unstable inverted pendulum is found again in the folded pendulum design. A folded pendulum comprises a stable regular pendulum and an unstable inverted pendulum. The two legs of the folded pendulum are spatially separated linked by a massive connection, as shown in figure 2.9b. The folded pendulum was originally designed as linkage by J. Watt [Ferguson1963], and it is therefore referred to as Watt–linkage. The linkage can displace the central mass horizontally, while moving its centre of mass on a nearly straight line.

Folded pendulum

The folded pendulum linkage was proposed for horizontal seismic isolation systems [Blair1994, Liu1997]. The term *folded* refers to the trick of designing the two flexures of the IP arm in tension instead of the more standard compression. In this way extremely tiny flexures can be used without incurring in buckling.
The positive gravitational torque of the ordinary pendulum is balanced by the negative torque of the inverted pendulum. The residual elastic constant of the flexures is compensated by loading additional mass on the inverted pendulum leg side [Bertolini2006b]. Because of this design, the folded pendulum has a very low resonant frequency. As long as the negative return force of the inverted pendulum is smaller than the positive return

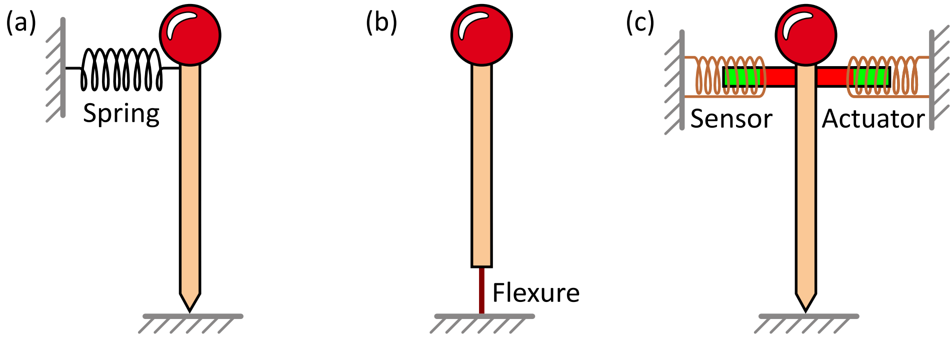

Figure 2.10.: Inverted pendulums, with external restoring forces from (a) an ancillary spring, (b) a flexure at the pivot, and (c) a voice-coil actuator in a feedback loop with a sensor.

force of the regular pendulum, the mass can oscillate, performing almost horizontal motion. The publications [Bertolini1999b, Bertolini2004, Bertolini2006c, Acernese2008] discuss the implementation of a folded pendulum as a concept for monolithic accelerometers.

Monolithic accelerometers with low-frequency folded pendulum design is used at the AEI-SAS for horizontal displacement monitoring, as described in chapter 7.1.2. A folded pendulum, shown in figure 7.4 on page 109, consists essentially of a test mass with two hinging supports. The support at one end of the test mass is an ordinary pendulum with a positive restoring force. The other side of the test mass is supported by an inverted pendulum contributing a negative restoring force.

Inverted Pendulum (IP)

An Inverted Pendulums (IP) is a rigid pendulum leg supporting a mass, so that its centre of mass is above its pivot point. Gravity pulls the IP over as it deviates from the vertical axis. The IP is a classical research problem of control engineering, solved by placing the IP on a movable cart and stabilizing it by means of feedback controls. An IP is inherently unstable, if no restoring forces are provided. Such a restoring force can be provided by passive mechanical springs, as shown in figures 2.10a and 2.10b, or an active system, as shown in figure 2.10c.

An IP with a passive mechanical restoring force provided by a flexure at the pivot point, is shown in figure 4.1 on page 62. Such a three leg IP with 0.4 m leg length is used at the AEI-SAS for horizontal seismic pre-isolation of the optical table. In VIRGO, the IP legs have a length of about 6 m and are used to pre-isolate seismic motion of the Superattenuator, a multi stage suspension chain for the interferometer optics. The effective restoring force of the IP flexure is reduced by the force exerted by the gravitational pull. By adding payload mass the natural frequency is tunable towards very low frequencies at the verge of instability. Mathematical calculations and experimental measurements of the IP are presented in chapter 4.

Tilted axis configurations

Using low frequency pendulums for seismic sensors is a convenient way to broaden the sensitivity range of measurement devices towards lower frequencies. In the following examples, the low natural frequency is achieved by operating the pendulum with a very shallow potential well. By tuning the pendulum towards the verge of instability, the natural frequency of the pendulum can be drastically reduced.
An example of such a low frequency device is the Lehman seismometer [Walker1979, Dobeson2005] using a horizontally suspended pendulum, with a tilted vertical rotational axis, resembling a *garden gate*, see figure 2.11a. With a slightly tilted vertical rotational axis, the garden gate pendulum performs horizontal oscillations around its equilibrium position. The gravitational restoring force is reduced by changing the angle, θ, of the rotational axis, thereby pushing the pendulum away from its indifferent equilibrium. With an angle of 0° the pendulum has no restoring force, thus cannot find a stable resting position. The period, T, of the garden gate pendulum was tuned to a maximum of around 20 s according to:

$$T = 2\pi\sqrt{l \,/\, g \sin(\theta)}\,,$$

with a pendulum length of 0.5 m at an angle of $\theta = 0.3°$ [Pillet2007]. The equivalent length, L_{eff} of the oscillator is thereby about 100 m, shown in figure 2.11a.
In a similar design by Zöllner [Zöllner1873] the garden gate pendulum is used twice, combined into a linkage-like configuration, as shown in figure 2.11b. The pendulum was built for the purpose of observing changes in the direction of gravity due to tidal forces. Zöllner converted the pendulum it into a seismometer. The Zöllner pendulum was used as horizontal pendulum in several world-wide operating seismographs, such as devices invented by Galitzin (around 1904-1911) [Galitzin1906], Wood-Anderson (1922), and Sprengnether (1940) [Lenhardt2008].

LaCoste zero length spring

Another example for a tilted pendulum configuration is shown in figure 2.12a. It introduces a zero length spring designed by LaCoste for a long period vertical seismograph [LaCoste1934]. The elongation of a zero length spring is equal to the distance between the points where it is attached. In other words, if the initial length is defined as the actual physical length minus the elongation, then this type of spring has a zero initial length. The force of such a zero length spring is proportional to the total length of the spring. Zero length springs of this type are wound by pre-stressing them during the winding procedure, so that with no force applied, the windings are already in contact. The pendulum mass, suspended from a zero length spring, see figure 2.12a, rests in neutral equilibrium and has therefore, in principle, an infinite free period. An infinite period means the pendulum is unstable.
A finite period is obtained by making the angle of the spring slightly smaller than 90°, or by tilting the frame of the device. When balanced against gravity a very long period oscillation in the vertical direction can be obtained. Due to the delicate equilibrium of forces in the LaCoste linkage design, it is sensitive to thermal fluctuations and is difficult to operate without a stabilizing feedback system.

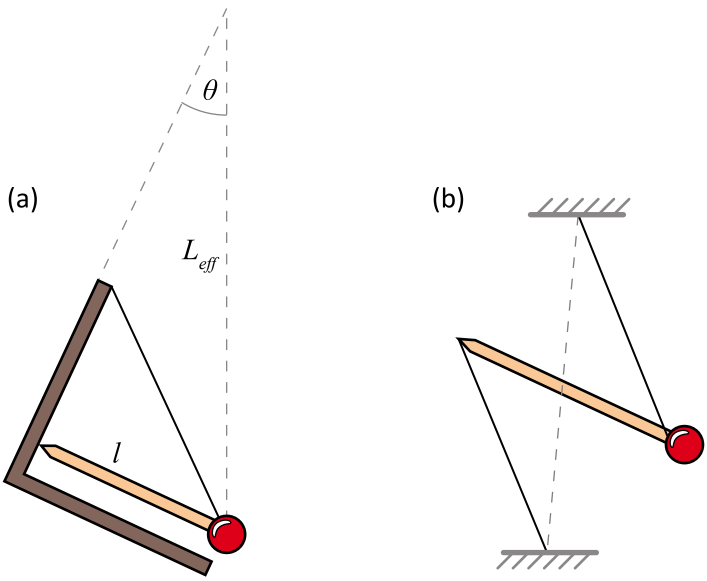

Figure 2.11.: Horizontal low frequency pendulums: (a) tilted garden gate pendulum and (b) Zöllner pendulum, comprising two linked garden gate pendulums.

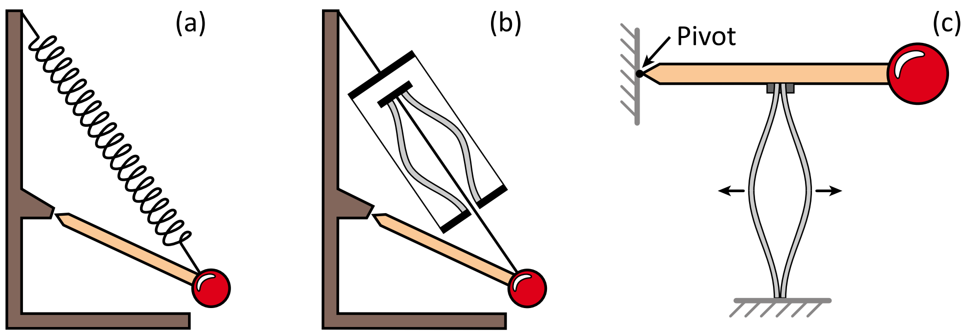

Figure 2.12.: Tilted oscillators. (a) The original LaCoste pendulum introduces a zero length spring, which would exert zero force if it had zero length. Normal springs have usually an offset length at zero force. (b) The LaCoste-Euler pendulum utilizes Euler buckling blades replacing the LaCoste spring. (c) Euler buckling springs consist of a pair of blades that buckle under the applied load. One blade bends towards the pivot, the other one bends away from it, thereby defining the spring-rate of each spring blade. The sum of the two spring-rates can be reduced by choosing different properties for the two blade springs.

Euler buckling springs

According to [Hosain2012], the LaCoste zero length springs, which are pre-stressed during the fabrication process, are operated at 90% of the yield strength of the material. The authors replaced the LaCoste spring by the Euler buckling springs, as sketched in figure 2.12b. The proposed Euler buckling springs are a low frequency spring system which can be dynamically tuned to achieve 0.15 Hz resonance frequency in a unit of 20 cm height.
Euler buckling springs, shown in figure 2.12, consist of a pair of flat leaf springs, that buckle under lateral compression when a critical load is exceeded. A reduced spring-rate can be obtained by choosing an appropriate ratio between the bending stiffness of the blades [Winterflood2002a]. An offset towards the pivot leads to a low or eventually negative spring rate, while with an offset away from the pivot a much higher spring rate can be obtained. Thus, a pair of matched spring blades, with one going in each direction, can be used to reduce the total spring rate composed of a positive and a negative separate spring rate [Winterflood2002b]. Unfortunately, the Euler buckling springs are non-linear and it is hard to reduce the spring-rate over a reasonable operating range with this method. Euler buckling springs are used, together with other linkages and low frequency pendulums, in a prototype vibration isolator system for the Australian International Gravitational Observatory (AIGO), shown in figure 2.23.

Mechanical linkages

Mechanical linkages are generally used to transform a given input force or movement into a desired output force or movement constrained by the mechanics of the linkage. Linkages became popular in the mid-18th century, when steam engines developed into practical tools and the demand arose to translate the rotational motion into a linear oscillation. Additionally, linkages can provide a linear motion of a specific link. One particular linkage, the Watt–linkage, was already introduced in figure 2.9b. The Watt–linkage has two pleasant properties: it constraints the motion of the connecting bar to a linear movement and it has a low the natural frequency when used as pendulum.
The Roberts straight-line linkage, shown in figure 2.13a, invented by R. Roberts around 1841, was used to saw off pilings under water [Ferguson1963]. It comprises two movable legs connected to a triangular link, with the tip of the triangle performing (within tolerable limits) straight-line motion. The principle of the straight-line movement of the Roberts linkage was adopted by a group at the University of Western Australia, to construct a horizontal seismic isolation stage [Winterflood1996]. The Roberts linkage isolator, as shown in figure 2.13b, comprises a stiff frame (shown as triangle) suspended from wires. The upper tip of the triangle moves in a flat plane. With the mass suspended in this point, the pendulum would be in indifferent stability, thus unstable. So the mass is slightly lowered to allow the suspension point to move in a shallow potential well. By changing the depth of the potential well, the natural frequency of the Roberts Linkage can be tuned down to 150 s [Winterflood1999]. To achieve very low frequency, it should be arranged such that the potential well is as shallow as possible. With a positive low restoring force and therefore a low natural frequency the system remains stable.

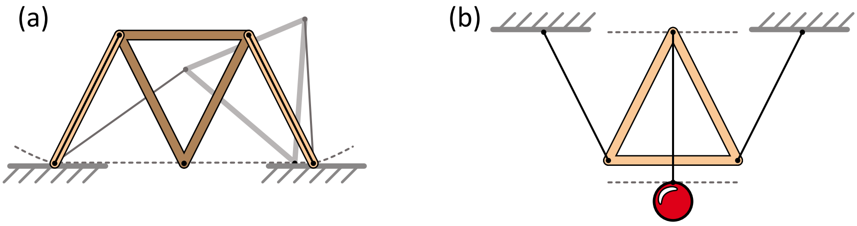

Figure 2.13.: Schematic representations of the Roberts linkage: (a) the original invention, performing straight-line motion (marked by a dashed line) at the tip of the triangle, (b) a Roberts linkage converted into a horizontal isolator for the Australian International Gravitational Observatory (AIGO), with a triangle suspended from wires. The dashed line indicates the movement of the mass, which stays in the same horizontal plane.

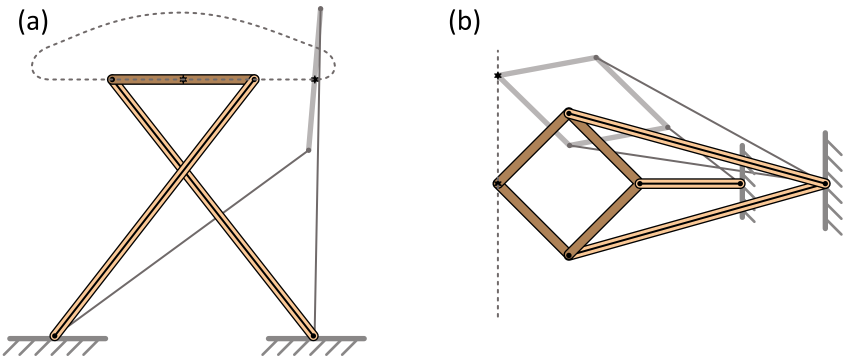

Figure 2.14.: Straight-line linkages: (a) Chebyshev linkage, performing a (nearly) straight-line motion, but making a quick jump, if moved too far. (b) Peaucellier's exact straight-line linkage performs a straight line with its tip.

Many of the previously described isolation techniques using pendulums and linkages are used to construct a compact vibration pre-isolation system for the Australian International Gravitational Observatory (AIGO), shown in figure 2.23. See chapter 2.5, page 40 for details.

X-linkage

A different kind of linkage, the Chebyshev straight-line linkage or X-linkage, was invented around 1867 by the Russian mathematician P. L. Chebyshev. The linkage was used as a guideline for an X-pendulum, designed for a seismic attenuation system for TAMA300. The X-linkage is essentially a crossed pair of pendulum legs, connected at their tips by a solid link, see figure 2.14a. The central point of the link performs thereby a linear motion (within reasonable boundaries). Chebyshev's original intent was to demonstrate that it is impossible to construct a linkage that can generate a perfectly straight line movement. Peaucellier finally proved in 1873 that it is possible to construct an exact straight-line linkage [Ferguson1963], as shown in figure 2.14b. The X-pendulum is an upside-down version of the Chebyshev linkage. The pendulum was proposed for use in the Japanese TAMA300 detector. An X-pendulum is shown in

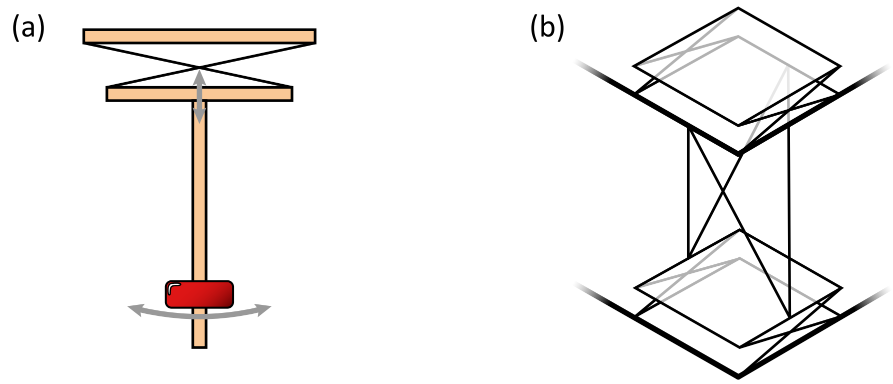

Figure 2.15.: Schematics of an X-pendulum designed for a prototype vibration isolator for TAMA300. (a) single element of a 1-dimensional X-pendulum. The arrows indicate the movement path of the adjacent part of the system. (b) The 2-dimensional version with two stacked X-pendulums, each rigidly connected to a plate. [Tatsumi1999]

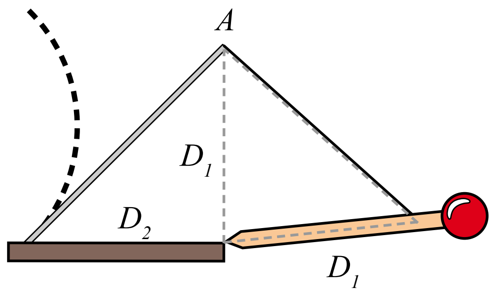

Figure 2.16.: A schematic representation of the mechanics of a Willmore vertical seismometer, introducing a linkage between the pendulum and the spring blade. The rigid pendulum and the pre-bent blade are connected by a steel wire. The blade becomes flat under load, thus the spring blade and the pendulum form an isosceles triangle between the pendulum leg and point A, indicated by dashed triangle. Theoretically, an infinite period is achievable, when distances D_1 and D_2 are equal.

figure 2.15a. It has four wires: two wires form a cross from one corner of the support plate to the opposite corner of the suspended plate, and the other two form a similar mirrored cross on the other side. The object to be suspended is connected rigidly to the suspended plate. The system moves as if constrained by two pins moving inside of two slots in horizontal and vertical direction [Barton1994]. In a later prototype, two X-pendulums were stacked to achieve 2-dimensional motion [Tatsumi1999], as shown in figure 2.15b. Four double pendulums were combined to suspend an optical table [Barton1999]. The TAMA300 detector, using X-pendulums for seismic isolation of an optical table, is described in chapter 2.5.

Leaf springs

The linkages presented so far operate close to a regime, where the pendulum has no definite position of equilibrium. Another interesting implementation of such a linkage

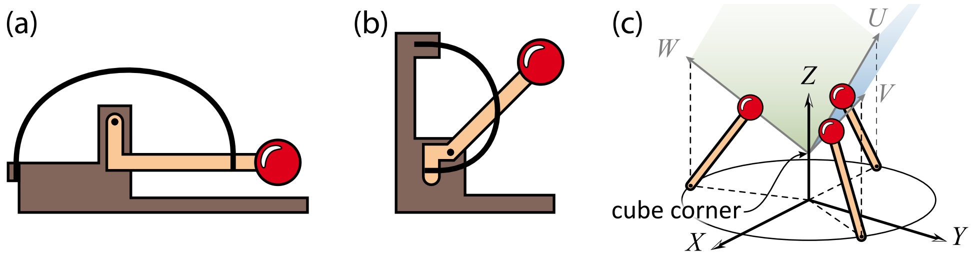

Figure 2.17.: Leaf spring pendulums with inertial masses that are supported by leaf springs: (a) a vertical pendulum, (b) a tilted pendulum inclined against the vertical axis, (c) a triplet of inclined pendulums as it is used in Streckeisen STS-2 broadband seismometers, the seismometer type used in AEI-SAS.

is the Willmore seismometer [Willmore1966], which uses a leaf spring mounted as a cantilever, connected by a wire to a pendulum, as shown in figure 2.16. The spring blade is straight when the pendulum is in its rest position, and forms an arc when unstressed. The spring has such a size and strength, that its length, when the beam is in rest position, is equal to the length of the pendulum. This way the leaf spring and the pendulum work as a linkage, forming an isosceles triangle between the pendulum leg and point A in figure 2.16. The isosceles triangle is marked by a thin dashed line. Theoretically, an infinite period is achieved when the distances D_1 and D_2 are equal. Practically, pendulum periods of 30 s were reported [Willmore1966].
Wielandt introduced a small vertical seismometer [Wielandt1982], whose inertial mass is supported by a leaf spring, see figure 2.17a. In a limited range around its equilibrium position the leaf spring suspension is comparable to a LaCoste suspension, but it applies less stress to the spring material and manufacturing it is more simple. The leaf spring is astatic, which means the suspension is tuned in such a way that the pendulum is at the verge of instability. A small deviation from this regime would make the pendulum unstable.
Modern triaxial broadband seismometers such as the Streckeisen STS-2 and the Nanometrics Trillium are based on such vertical astatic single leaf springs. The seismometers use a triple set of identical tilted astatic pendulums inclined against the vertical axis, as shown in figure 2.17b. The position of the seismic masses of the three pendulums resemble edges of a cube standing on its corner, as shown in figure 2.17c, when the masses are in their rest position. To obtain the conventionally used $East = X$, $North = Y$ and $Vertical = Z$ signals, the internal signals U, V, W of the STS-2 are electrically recombined according to [Wielandt2002]:

$$\begin{pmatrix} X \\ Y \\ Z \end{pmatrix} = \frac{1}{\sqrt{6}} \begin{pmatrix} -2 & 1 & 1 \\ 0 & \sqrt{3} & -\sqrt{3} \\ \sqrt{2} & \sqrt{2} & \sqrt{2} \end{pmatrix} \begin{pmatrix} U \\ V \\ W \end{pmatrix} .$$

Quasi-zero-stiffness isolator

Almost any seismic suspension can be made astatic by inserting an external force acting normal to the line of mass motion and pushing the mass away from its equilibrium. A theoretical model of a quasi-zero-stiffness isolator is presented in [Carella2009]. Such a

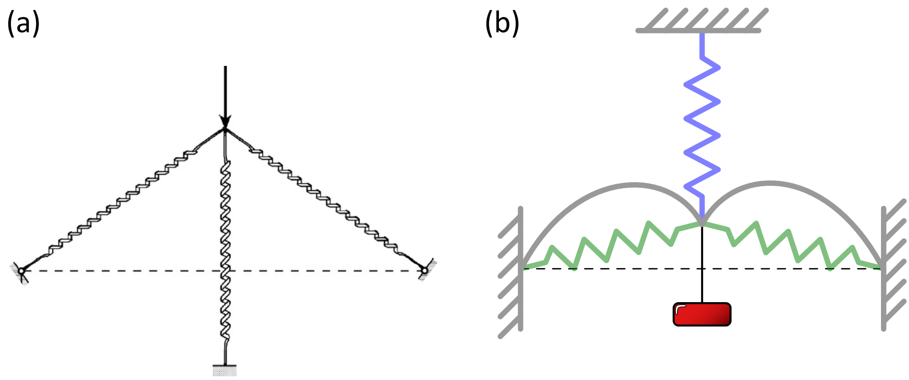

Figure 2.18.: Two similar low frequency isolators with one vertical spring and two ancillary springs, reducing the vertical effective stiffness. (a) A model of a theoretical Quasi-zero-stiffness isolator, from [Carella2009]. The arrow indicates an applied force, displacing the connection point of the springs from equilibrium position. (b) A Geometric Anti-Spring (GAS) filter simplified to a linear spring model. The red block and the vertical spring are balanced in an equilibrium position. The ancillary springs reduce the effectice spring constant of the system. See chapter 5.1.

system has one vertical spring and oblique ancillary springs, as shown in figure 2.18a. The ancillary springs can be linear, pre-stressed or non-linear. The authors derive the maximum transmissibility under the assumption of light damping and give the so called jump-down frequencies, at which the transmissibility of the non-linear system jumps to a lower value. They show that there are advantages in having non-linear and pre-stressed oblique springs. However, the practical realisation of oblique springs with precise non-linear characteristics is considered difficult. Neither the restoring force of the original suspension nor the ancillary spring force can be made perfectly proportional to the displacement. While linear components of the force may cancel out, the non-linear terms will remain and cause the oscillation to become non-harmonic and even unstable at large amplitudes. Viscous and hysteretic behaviour of the springs would also become noticeable [Wielandt2002].

Geometric Anti-Spring (GAS) filters

A similar mechanical system is the Geometric Anti-Spring (GAS) filter [Bertolini1999a], shown in figure 2.18b. These filters are tunable mechanical oscillators formed from flat elastic blades. The blades are bent and radially compressed against each other, forming a crown of curved blades. The constrained radial stress creates an anti-spring effect that allows a very low effective stiffness to be achieved in the vertical direction. GAS filters are used in the AEI-SAS as vertical seismic isolators. The forces acting within a pair of GAS filter blades can be simplified as an expanded vertical spring and two contracted ancillary springs facing each other. The model is similar to the quasi-zero-stiffness isolator. The GAS filters show a non-linear behaviour, however, in the mathematical model the springs are assumed linear. The linear ancillary springs create a negative force component that reduces the effective spring constant of the system. A mathematical description of the GAS filters is given in chapter 5.1.

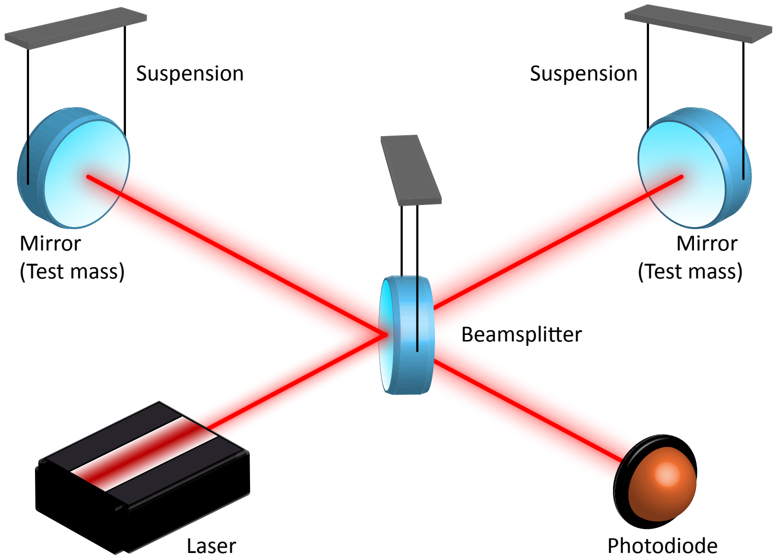

Figure 2.19.: Schematic representation of a Michelson laser interferometer used in ground-based gravitational-wave detectors. Optical components are suspended by wires for vibration isolation.

Concluding remarks

The natural frequencies of pendulums and linkages, presented in the previous sections, are reduced by introducing an additional force that pushes the pendulums towards unstable equilibrium conditions. The previously presented blade spring suspensions are made astatic by inserting an external force, exerted by a mechanical oscillator. The low frequency performance of such suspensions is, in practice, limited by anomalous low-frequency oscillator behaviour, such as fluctuations of the Young's modulus, hysteretic properties, random walk of equilibrium point and spontaneous de-stabilization events, which occasionally lead to collapse [DeSalvo2011]. These phenomena are especially exaggerated in the GAS filter design in which a weak spring constraint is achieved by balancing two comparably enormously stiff springs. That is the reason of the particularly low Q factor of the GAS system. The kinetic energy of the GAS springs is a very small fraction of the elastic energy that is sloshing through the blades during an oscillation. The kinetic energy at low frequencies is comparable to the energy loss per cycle [Bertolini2012].

2.5. Seismic isolation in gravitational wave observatories

Seismic isolation techniques used at gravitational wave observatories GEO600, Virgo, LIGO, TAMA300, and KAGRA, as well as the AIGO test facility and the AEI 10 m Prototype are presented in the following sections. All facilities use different isolation techniques for the optics suspensions. The interferometric ground-based gravitational

wave detectors use a Michelson interferometer configuration with mirrors as test masses suspended from wires. The basic schematic of a Michelson interferometer is shown in figure 2.19. The laser beam is split at a central beam splitter, reflects from end mirrors, is recombined at the central mirror and detected by a photodiode. Changes in the length of the arms, from noise or gravitational waves, cause intensity changes at the photodetector.
In all detectors the interferometer is positioned in a large scale vacuum system to isolate it from environmental influences, such as thermal and atmospheric fluctuations, and acoustic noise. The interferometer's core optical components are suspended from wires. Thus, the mirror mass and the wire form a pendulum which provides horizontal isolation above the pendulum's resonance frequency increasing with a slope of f^{-2}. The isolation performance can be improved by building a chain of several masses suspended from wires. The isolation improves according to f^{-2n}, where n is the number of isolation stages. In reality, the attenuation power of a simple chain of pendulums rapidly saturates, because the vertical seismic noise passes unattenuated through the chain, and a fraction of it projects on the interferometer axis, due to mechanical imperfections. To obtain large attenuation factors it is necessary to alternate vertical and horizontal attenuators, of roughly the same power. This is done by suspending the wires from cantilever blade springs.
GEO600 was the first to use monolithic final suspension stage. Virgo and LIGO are currently being upgraded with this technology to take advantage of Silica's low mechanical losses and reduce the mirror suspension thermal noise. Low-frequency isolating devices, as discussed in chapter 2.4, can be used to pre-isolate the optics suspensions from the ground motion. Seismic pre-isolation of the mirror suspension at Virgo is realized passively by a 6 m tall inverted pendulums and a chain of pendulums on cantilever blades. At initial LIGO, active seismic isolation was achieved by stacks of springs and masses, such as in GEO600.
The figure 2.20 illustrates latest sensitivities of major interferometric ground-based gravitational wave detectors. The lower frequency part of the detectors is related to the quality of their seismic isolation system. Virgo, with its outstanding seismic isolation performance, is sensitive in the lowest frequency band. Therefore, most interferometric gravitational wave detectors are being upgraded to improve their seismic isolation.

GEO600

The gravitational wave detector GEO600 is a 600 m long ground based interferometric detector in Germany, near Hannover. Horizontal seismic isolation of optical components is accomplished by the use of a triple cascaded pendulum suspension, as shown in figure 2.21. The triple pendulum is suspended from two stages of cantilever blade springs providing vertical isolation. The lowest suspension stage is entirely made of fused silica. It is produced by bonding flame-drawn silica fibres to the mirror masses. In GEO600 the first-ever implementation of monolithic suspensions in an interferometric gravitational-wave detector was realized [Goßler-thesis].
The seismic pre-isolation for mirror suspensions is built as stacks with rubber spacers acting as damped springs and filtering masses made of steel plates. The rubber is used to passively isolate the suspensions from high frequency vibrations. Because the rubber is not vacuum compatible, the stacks are sealed within metal bellow baffles. The baffles

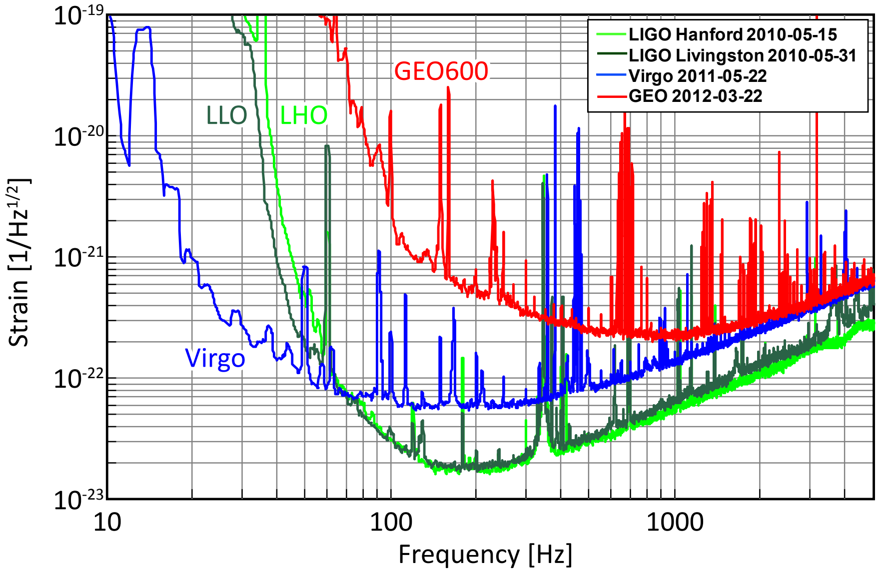

Figure 2.20.: Sensitivities of the major gravitational wave detectors: Virgo, GEO600, and LIGO (LHO in Hanford, Washington and LLO in Livingston, Louisiana). At the LLO, a Hydraulic External seismic Pre-Isolator (HEPI) is used to reduce the seismic noise at low frequency. Both initial LIGO detectors rely on spring-mass stacks for passive vibration isolation. At Virgo, the mirror suspensions are seismically isolated by the Superattenuator (see figure 2.22). At GEO600, stacks of rubber and steel plates are used for high-frequency vibration isolation of the mirror suspension. The lack of pre-isolation at GEO600 explains the increased noise at low frequencies caused by seismic noise. However, due to a multi stage suspension (among other advances) GEO600 achieves sensitivities comparable to the large-scale detectors at higher frequencies. Data taken from [Reitze2012] who combined the data from [Abbott2009a, Grote2009, Accadia2012a].

are connected to a separate pumping system, to prevent pollution of the main vacuum system. Additionally, the stacks are equipped with piezo actuators and geophones for active feedback control. The signal of the ground motion measuring geophones can be filtered and fed back into the piezo actuators to counteract the ground vibration. So far, active feedback was never used, due to problems with electronics. At present, the active feedback is being revised [Wittel2011]. No further seismic isolation is foreseen for the immediate future. Instead, the detector sensitivity is being optimised around 200 Hz and expanded towards higher frequencies.

Virgo

The French-Italian gravitational wave detector Virgo has an interferometer arm length of 3 km. It was the only detector that included a low-frequency seismic pre-isolation system as part of its conceptual design. The Superattenuator is used as passive isolator for the main interferometer optics [Braccini2005]. The Superattenuator is shown on the left-hand side in figure 2.22. It has three inverted pendulum (IP) legs composed of 6 m long aluminium tubes. The IP legs provide passive horizontal seismic pre-isolation for a chain of six vertical isolators, the mechanical filters [Braccini1996]. The IP stage

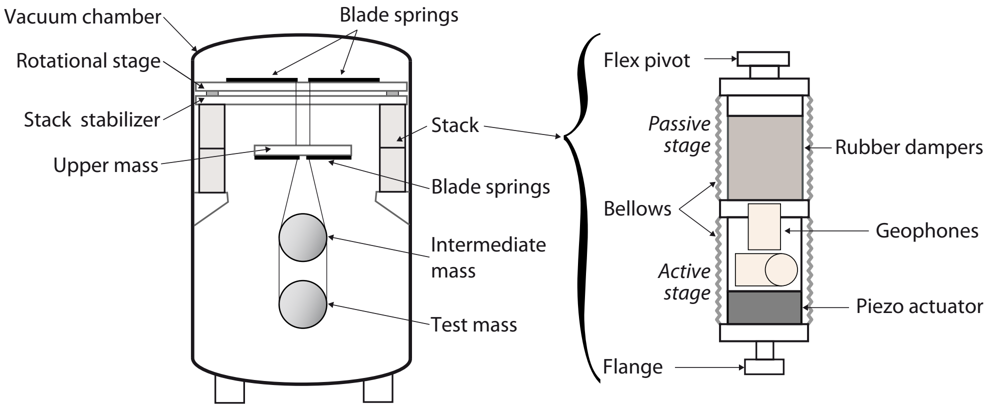

Figure 2.21.: Schematic representation of one of the vacuum chambers of GEO600. The test mass mirror is monolithically suspended from the intermediate mass. The upper mass with vertical blade springs is suspended by steel wires from cantilever blades for passive seismic isolation of the mirror. Additional passive and active pre-isolation components for the mirror suspension are implemented in the stacks. Passive high frequency seismic attenuation is provided by rubber dampers. Piezo actuators and geophones are installed for active isolation. One of stacks is omitted from this sketch for clarity.

was designed to have a horizontal resonance frequency of 30-40 mHz and to achieve isolation factors of 65 dB at 1 Hz [Losurdo1999].
The Superattenuator with its multi-stage pendulum chain composed of a cascade of six mechanical filters is sketched on the left-hand side in figure 2.22. For vertical isolation, each filter unit is equipped with marraging steel blade springs pointing to the centre of the filters. The filters are suspended from each other by steel wires, forming a multi-pendulum for horizontal isolation. Each filter is suspended from the filter above. This way, the system can be considered as a chain of serially coupled oscillators in horizontal and vertical degrees of freedom, providing seismic isolation in 6 degrees of freedom. The upper mechanical filter, filter zero, is used to provide active mode damping and vertical actuation of the filters suspended below. The vertical mechanical resonance of the filters is around 1.5 Hz and is softened by a magnetic anti-spring system to 400 mHz [Beccaria1997]. From the top filter to the centre of the mirror, the whole structure has a length of about 8 meters.
Virgo is currently being upgraded into the Advanced Virgo configuration, as summarized in Virgo's technical design report [Accadia2012b]. Only minor changes of the seismic attenuation were necessary:

- upgrades on the Superattenuator
  - new monolithic IP legs
  - additional piezo actuators and displacement sensors below the IP bottom ring to compensate for tilt instabilities
- Seismic and acoustic noise was found to intrude into the interferometer via the input-output optics. To mitigate this problem seismically attenuated benches will replace old fashioned optical benches, including an External Injection Bench

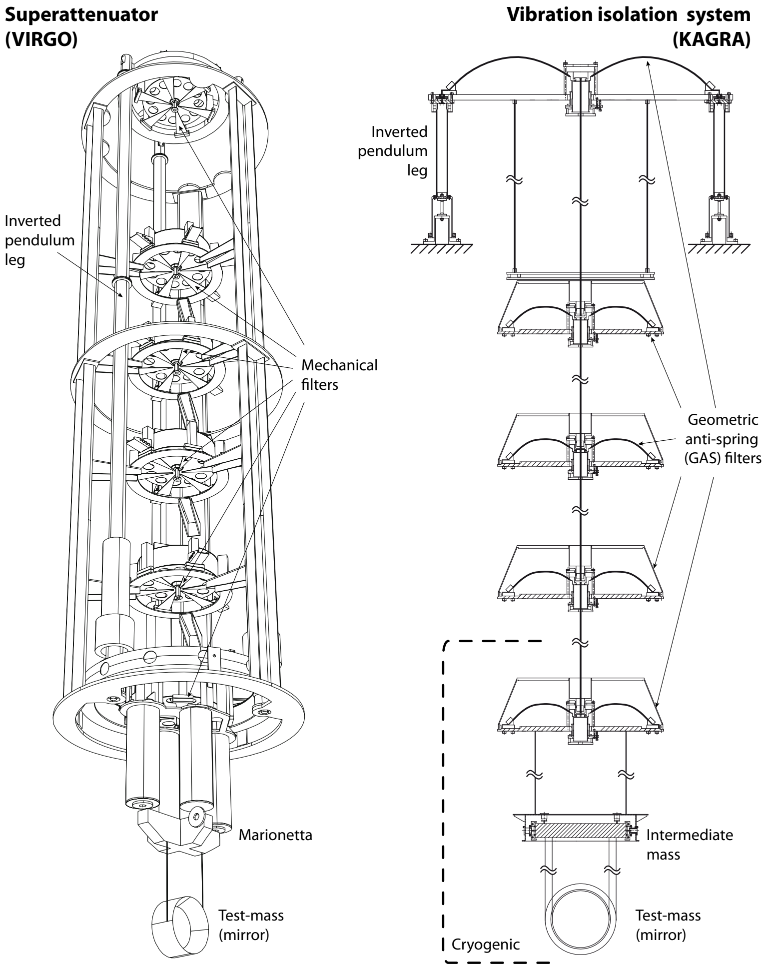

Figure 2.22.: Two different passive seismic attenuation systems: The Virgo Superattenuator (left) and the vibration isolation system type-A designed for KAGRA (right). Both systems make use of the inverted pendulum (IP) legs for horizontal isolation and a chain of mechanical filters for vertical and horizontal isolation. The Superattenuator's vertical mechanical filters achieve low frequency resonances by means of Magnetic Anti-Springs. In KAGRA's vibration isolation system the mechanical filters of the Superattenuator evolved to Geometric Anti-Spring (GAS) filters, which are simpler, are more compact, and provide higher attenuation.
The three 6 m long Inverted Pendulum legs of the Superattenuator are the horizontal pre-isolation stage for six cascaded mechanical filters. The filters are used for horizontal and vertical seismic attenuation of the mirror suspension. The lowest mechanical filter is equipped with a steering device, the Marionetta, which is used to actuate the mirror suspension. Image from [Abernathy2011].
The horizontal isolation stage designed for KAGRA has 50 cm long IP legs supporting a large GAS filter. Four smaller GAS filters are suspended in a chain from the upper GAS filter. The overall length of the vibration isolation system is planned to be about 12 meters from the top GAS filter to the mirror, dictated by mining requirements. At the time of writing the last GAS filter is planed to be placed within the cryogenic enclosure of the vacuum system, and the vibration isolation system for KAGRA is in the production phase of the prototype.

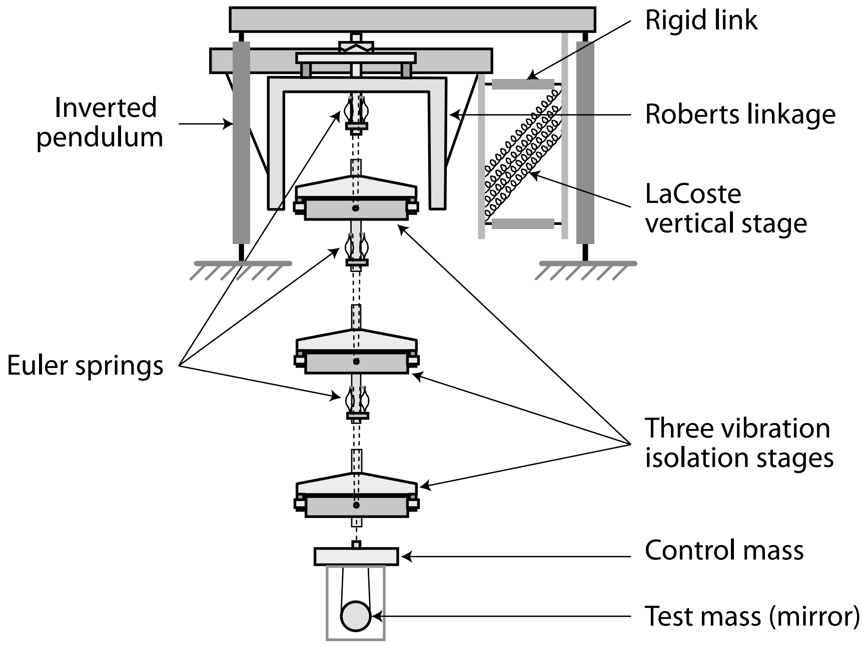

Figure 2.23.: Schematic representation of the vibration isolator system for the Australian International Gravitational Observatory (AIGO). The system has different stages of pre-isolation for the mirror suspension: inverted pendulum legs and Roberts linkage for horizontal pre-isolation, a LaCoste linkage with zero length springs and Euler springs cascaded in a chain for vertical isolation.

(EIB) with a SAS, positioned outside of the vacuum system, isolating alignment optics from seismic motion

- five in-vacuum optical benches, each suspended by a multi-stage vibration isolator named MultiSAS, to host photodiodes for longitudinal and angular control, and isolate them from environmental disturbances

Both EIB-SAS and AEI-SAS are derived from the HAM-SAS developed at Caltech for Advanced LIGO [Stochino2009]. The EIB-SAS was designed and tested at Nikhef, Amsterdam for Advanced Virgo alignment optics. The EIB-SAS design is very similar to the AEI-SAS. The difference is, that EIB-SAS will be operated in air, while AEI-SAS was designed for in-vacuum use. Operating in air relaxes many requirements, especially on cleanliness for vacuum compatibility and performance requirements. As the first major hardware upgrade of Advanced Virgo, the EIB-SAS was installed in November 2011. It is used as a benchmark for MultiSAS, since they both makes use of the similar subsystems and components. One of the five MultiSAS supported tables will be the detection bench at the output of the interferometer.

AIGO

The Australian International Gravitational Observatory (AIGO) is a 80 m arm-length test facility which is capable of extending to an interferometer arm-length of 5 km

[Chin-thesis]. A compact passive vibration isolation system for mirror suspensions, shown in figure 2.23, was designed and built at AIGO. Its overall performance is similar to that of Virgo and KAGRA. The vibration isolator prototype utilizes different seismic isolation techniques, which are presented in chapter 2.4. IP legs, forming a 'Wobbly Table', and a Roberts linkage are used for horizontal isolation. A LaCoste linkage with zero length coil springs and buckled Euler springs, cascaded in a chain, are used for vertical isolation. The isolation elements of the AIGO vibration isolator are nested into a single compact device to reduce the dimensions of the whole system.
The Inverted Pendulums and the LaCoste springs are actuated by coils and magnets for positioning and damping. The coil springs of the LaCoste stage are heated to compensate for slow temperature drifts and to correct for creep in the isolation chain. Position control at the Roberts linkage stage is done by heating of the individual wires. A multi degree of freedom control system is required to achieve the high performance of the system. In the low frequency band up to 10 mHz the control system corrects for drift, and provides positioning and alignment of the pre-isolator. Up to 1 Hz the control system is used to damp normal modes of the system. For higher frequencies the control system suppresses high frequency noise, performing active vibration isolation. Resonant modes and mode interaction between isolation components and different degrees of freedom complicate the operation of the local control system, resulting in a complex filter design [Barriga2009, Dumas2009].

LIGO

The Laser Interferometer Gravitational Wave Observatory (LIGO) is a combination of two nearly identical observatories located in the USA: the LIGO-Livingston Observatory (LLO) in Livingston, Louisiana and the LIGO-Hanford Observatory (LHO) in Hanford, Washington. Each detector has an arm length of 4 km and the two sites are separated by about 3000 km. A third detector, originally with 2 km arm length, using the same facilities alongside the LHO 4 km detector, is planned to be relocated to India, to operate as a third LIGO-India observatory.
The initial LIGO design had only a single stage of mirror suspension for seismic isolation and a three stage-stack of masses on rubber damped springs. In Livingston, this system was insufficient to compensate for local traffic and the microseismic motion. To solve this shortcoming, additional seismic isolators were retrofitted with active Hydraulic External Pre-Isolators (HEPI) in order to extend the Livingston detector's poor duty cycle [Hardham2001]. Figure 2.24 illustrates the HEPI system supporting vacuum chambers. The system provided the necessary actuation range to cope with large (mainly tidal) drifts in the arm lengths.
In Advanced LIGO, the isolation system will be completely replaced. The new system will reduce the seismic noise at the low frequency band. Additionally to the HEPI system, Advanced LIGO will be equipped with an active In-vacuum Seismic Isolation (ISI) platform, as shown in figure 2.24, carrying a passively isolating quadruple pendulum suspension [Giaime2001]. The attenuation of seismic motion is provided by combining the HEPI system with the active ISI system and the quad suspensions. The test masses will be monolithically suspended by fused silica fibres, which provide a lower thermal noise than the steel wire sling suspensions in initial LIGO.
During the early Advanced LIGO research and development (R&D) activities, both

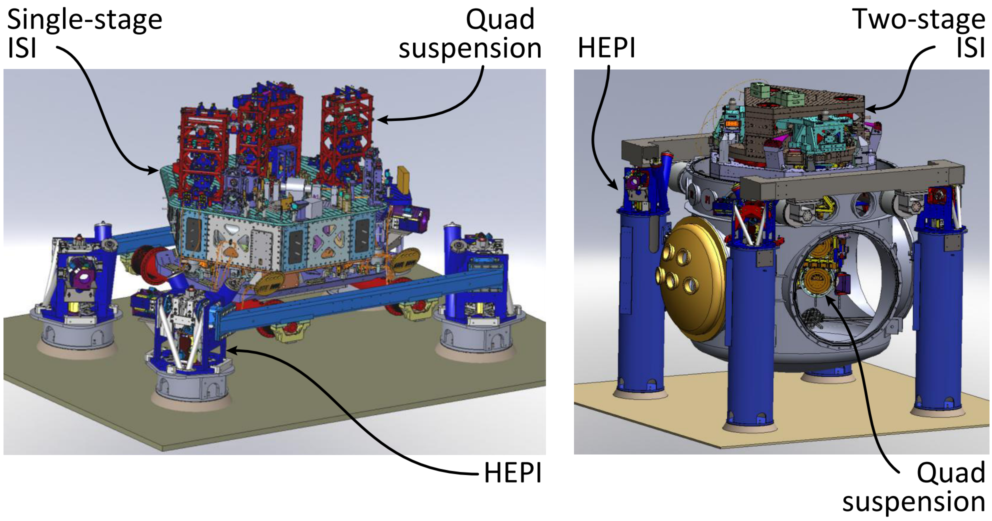

(a) The Horizontal Access Module (HAM). The vacuum chamber around ISI is omitted for clarity.

(b) Basic Symmetric Chamber (BSC). The upper part of the vacuum chamber around ISI is omitted for clarity.

Figure 2.24.: Active seismic isolation for Advanced LIGO. The HAM chamber and the BSC are supported by Hydraulic External Pre-Isolators (HEPI). HEPI is an active hydraulic pre-isolator for the Internal Seismic Isolator (ISI). Interferometer optics are suspended in a quadruple (four isolation stages) suspension system, with a monolithic mirror suspension, which provides the bulk of the seismic attenuation. Pictures from [Calloni2012].

in-vacuum active (ISI) and passive isolation technologies were investigated in parallel. In 2001, the Advanced LIGO committee settled for the fully active system. The R&D results on the passive Seismic Attenuation Sytem (SAS) [Bertolini2000] were successfully implemented in TAMA300 [Marka2002].
In 2005, a newly designed Horizontal Access Module-Seismic Attenuation System (HAM-SAS) was suggested for Advanced LIGO [Bertolini2006d]. The system was developed as a simpler, and cheaper alternative of the active attenuation system, that was growing more and more complex. In the HAM-SAS design, the old initial LIGO optical benches were re-used. The system was built using components of the TAMA-SAS suspension chains. HAM-SAS was designed to deliver the required attenuation as a completely passive mechanical isolator, using four IP legs and four GAS filters as seismic pre-isolators for the optical table, as shown in figure 2.25. HAM-SAS also contained reserved housings for additional active attenuation, in case inertial sensors with sensitivity exceeding its attenuation performance were to become available in the future. Its configuration with the three horizontal degrees of freedom (x, y, yaw) naturally diagonalized from its three vertical ones (z and two tilts) was, by design, particularly favourable for minimizing cross talk between feedback loops. The system was tested under time pressure in a short measurement campaign in 2006. The test results were promising but deemed not satisfactory for LIGO requirements. The project was abandoned once again in spring 2007 [Shoemaker2007] in favour of the three-stage

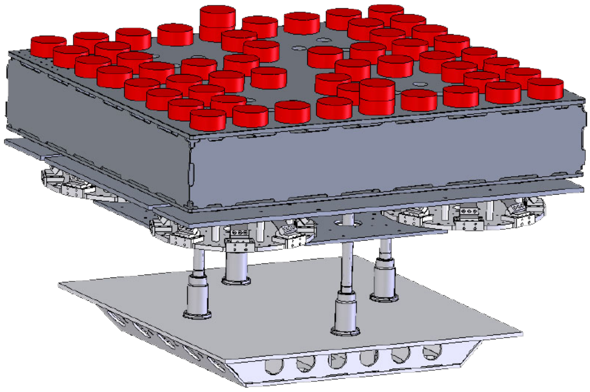

Figure 2.25: The Horizontal Access Module - Seismic Attenuation System (HAM-SAS) designed for the Advanced LIGO detector. Seismic isolation is performed by four IP legs and four GAS filters, supporting the original HAM optical table. The red masses shown on the table surface were used to simulate a uniform mass distribution.

active system, which is still in development.
The HAM-SAS was modified in 2008 to meet the AEI 10 m Prototype requirements [Goßler2010]. Information about the re-design and the AEI-SAS in general are given in chapter 3. The same design was also adopted at Nikhef for Advanced Virgo for its laser bench and for its in-vacuum auxiliary optics benches. Experience and knowledge are mutually exchanged between AEI and Nikhef, so that both groups can benefit from the shared information.

TAMA300 and KAGRA

TAMA300 was a 300 m arm-length interferometric ground-based gravitational wave observatory. More recently focus has shifted to the Large-scale Cryogenic Gravitational-Wave Telescope (LCGT), now known as KAGRA, which is being built underground in the Kamioka mine in Japan [Takahashi2012].
The vibration isolation system initially installed in TAMA300 was a stack of rubber and steel plates [Takahashi2002] as shown in figure 2.26b. Having found that the stacks were providing insufficient attenuation, a commercial active attenuation stage was installed below the vacuum tanks. This effort failed due to injection of extra noise outside the active attenuation band. Having learned about the limitations of active systems, a passive system was favoured.
A prototype of a passive seismic isolation system using an X-pendulum is shown in figure 2.26a. Four double X-pendulums were combined to suspend an optical table [Barton1999]. The tuning of the period was difficult mainly due to the stretching of the wires and the flexibility of the plates. The performance of the table was limited by parasitic low frequency resonances. The resonances consisted mainly of tilt modes and coupling of horizontal and vertical degrees of freedom. The X-pendulum prototype was replaced by the Seismic Attenuation System (TAMA-SAS), which was designed based on R&D for the LIGO detector and implemented in TAMA300.
A TAMA-SAS prototype was manufactured in 2002–2003 as the baseline design for an in-vacuum isolator for the Fabry-Pérot test masses for TAMA300. The prototype tests were performed in two full-scale towers built at LIGO and tested in an interferometer at the University of Tokyo (Hongo-campus), achieving the desired attenuation results [Takamori-thesis, Takamori2002].

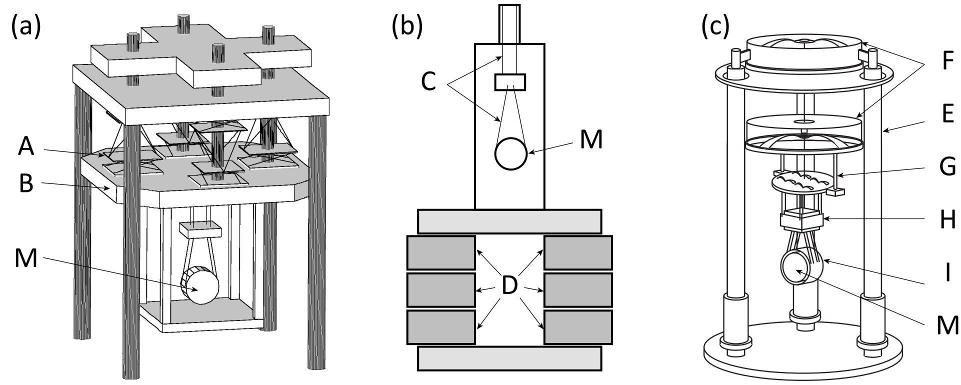

Figure 2.26.: Schematics of different vibration isolation versions in TAMA300. (a) Prototype with four X-pendulum units A, holding an intermediate plate B, from which a double suspension of the mirror M is hanging. Picture from [Barton1999]. (b) The initial vibration isolation installed in TAMA300 uses (like GEO600) rubber and stainless steel stacks D, as vibration isolator for the double suspension C of the mirror M. Picture from [Takahashi2002]. (c) The Seismic Attenuation System (TAMA-SAS), retrofitted around 2005 for better isolation performance, is composed of inverted pendulum legs E, for horizontal pre-isolation. The IP legs are supporting two GAS filters F, for vertical pre-isolation. A third vertical stage with miniature GAS filters G is holding a double pendulum suspension system with an intermediate damping stage H for the recoil-mass I and test mass (mirror) M. Picture from [Arai2008].

In a major upgrade of the detector in 2004, the vibration isolation stacks were replaced by the passive mechanical TAMA-SAS, shown in figure 2.26c, to gain seismic pre-isolation for the mirror suspension [Agatsuma2008]. In TAMA-SAS, three 2.5 m long IP legs are used to support two monolithic GAS filters cascaded in series. This vertical filter chain of filters suspended from each other by steel wires is the vertical isolator for the payload, as shown in figure 2.26c. The payload consists of: a platform with four embedded mini-GAS filters for vertical isolation, an intermediate stage for eddy-current damping, and a test-mass with a recoil-mass [Takahashi2008]. The TAMA-SAS improved the low frequency performance of TAMA300, but did not achieve the same attenuation performance of their prototype twins tested in Hongo, as reported by [Takamori-thesis]. The problem was much later traced to the heavier cabling used in TAMA300, which was short-circuiting the attenuation performance. The configuration of cascaded GAS-filters, derived from Virgo's magnetic anti-spring filters, can also be found in the MultiSAS design for KAGRA [Takahashi2012] and the suspended auxiliary optics benches for Advanced Virgo made at Nikhef [Accadia2012b].
A natural evolution from TAMA-SAS is the KAGRA vibration isolation system shown on the right-hand side of figure 2.22. The isolation system will use three 50 cm IP legs and a chain of four or five cascaded GAS filters [DeSalvo2012]. Experience with IP legs and GAS filters gained at the TAMA300 interferometer [Aso-thesis], as well as developments of the AEI-SAS and the SAS systems developed at Nikhef for Advanced Virgo, are being transferred to the KAGRA design. Such open collaboration between working groups and good will for exchange of experience are exemplary for the base of good science and progress.

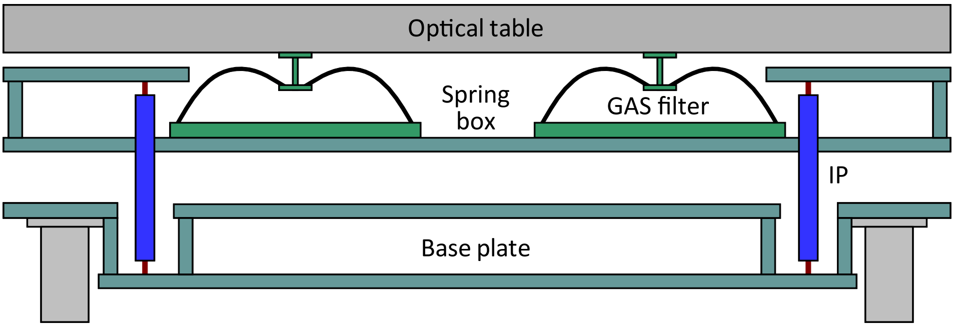

Figure 2.27.: A simplified sketch of a cut-through of AEI-SAS mechanics. The optical table is positioned on three GAS filters. The GAS filters are sandwiched in a rigid spring box, which is positioned on three IP legs. The IP legs are supported by a stiffened baseplate.

AEI 10 m Prototype

Testing of new technology for future gravitational wave detectors is the main purpose of the AEI 10 m Prototype. Its construction started in 2008 and is still ongoing. The facility has three walk-in vacuum tanks, with three seismically isolated optical tables. The optical tables are integrated with their supporting Seismic Attenuation Systems (SAS). Two of these tables were installed in 2011 and 2012 in the framework of this thesis. The third system will be assembled and tested in 2013.
The specific custom design of the Seismic Attenuation System for the AEI 10 m Prototype is called the AEI-SAS. Each AEI-SAS is a six degree-of-freedom vibration isolator that provides seismic pre-isolation for suspended optics which will be located on top of the optical tables. The AEI-SAS design is derived from the HAM-SAS prototype device, originally designed for the Advanced LIGO detector [Stochino2009]. Major differences between HAM-SAS and AEI-SAS are described in chapter 3.2.
The key isolating systems of the AEI-SAS is a three-leg IP, isolating horizontal motion, and three GAS filters for vertical isolation. The horizontal and vertical systems are spatially separated for maximum decoupling of horizontal and vertical degrees of freedom, as shown in figure 2.27. The AEI-SAS is designed to provide attenuation factors around $70 - 80$ dB at a few hertz in vertical and horizontal directions.
The passive system is paired with an active control system using co-located sensors and actuators, which are described in chapter 7. The sensors and actuators can be used to damp the fundamental modes of the isolator and to maintain a set position of the optical table. Additional information about the AEI 10 m Prototype is given in chapter 8.
The AEI-SAS is the core of this work. Description of major mechanical components and measurements of the performance of the AEI-SAS are given in subsequent chapters.

3. The AEI Seismic Attenuation System (SAS)

This chapter gives an overview of the AEI-SAS assembly. Its design is derived from a chain of developments, culminating into the design of the Horizontal Access Module - Seismic Attenuation System (HAM-SAS). The enhancements on the way from the HAM-SAS to the AEI-SAS design are listed in section 3.2. Construction notes of the AEI-SAS are given in section 3.3.

3.1. AEI-SAS assembly

The key isolation elements of the AEI-SAS are shown in figure 3.1. The system consists of IP legs supporting an intermediate plate and vertically isolating GAS filters. Both elements are passive mechanical isolators, effective, like harmonic oscillators, above their corresponding resonance frequencies. The conceptual design of the SAS is based on the decoupling of vertical and horizontal motion. Therefore, the IP legs and the GAS filters are positioned on different levels of the system. However, measurements have confirmed that total avoidance of coupling between isolating elements is impossible. Horizontal motion of IP legs couples into tilt modes of the GAS filters. Furthermore, the vertical compliance of the IP legs is transmitted to the GAS filters. The GAS filters, on their part, have a non-negligible horizontal compliance. All these effects complicate the performance of the system, by producing unwanted resonance peaks in the transfer function in figures 6.5 and 6.6.
A schematic illustration of the AEI-SAS is shown in figure 3.2. The progressive assembly of the system is shown in figures 3.3 - 3.11, illustrating the the functions of all its different systems.

Base plate

The base plate is the foundation of the AEI-SAS, as shown in figure 3.3. This base plate consists of stainless steel, welded to a honeycomb stiffened structure. Three IP legs are bolted to the base plate with 120° separation, as shown in figure 3.4. The base provides a rigid support for the IP legs.
Additionally to the IP legs, the base plate supports the entire internal electrical cabling of the AEI-SAS. The cables are clamped with PolyEther Ether Ketone (PEEK) clips to prevent them from slipping. Goretex® cables, insulated with porous expanded teflon, are used due to their ultra-high vacuum compatibility and maximum mechanical flexibility. They connect the Control and Data acquisition System (CDS) to all in-vacuum devices in the system. The internal electrical cabling scheme is illustrated in the appendix in figure E.2. More information about the internal electrical cabling is

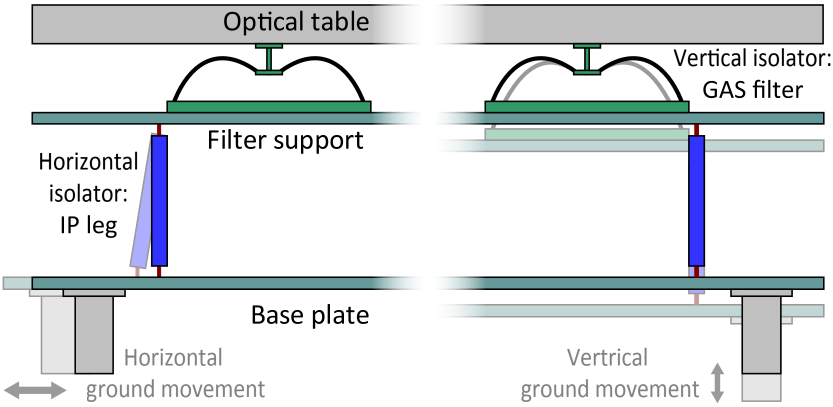

Figure 3.1.: Simplified schematic of the Seismic Attenuation System (AEI-SAS). The AEI-SAS comprises three IP legs for horizontal isolation and three GAS filters for vertical isolation. Only one of three parts of each system is shown, depicting (left) horizontal and (right) vertical movement. Both isolation stages are explained in detail in chapters 4 and 5. In contrast to this simplified illustration, the plates are folded to reduce the height of the system, see figure 3.2.

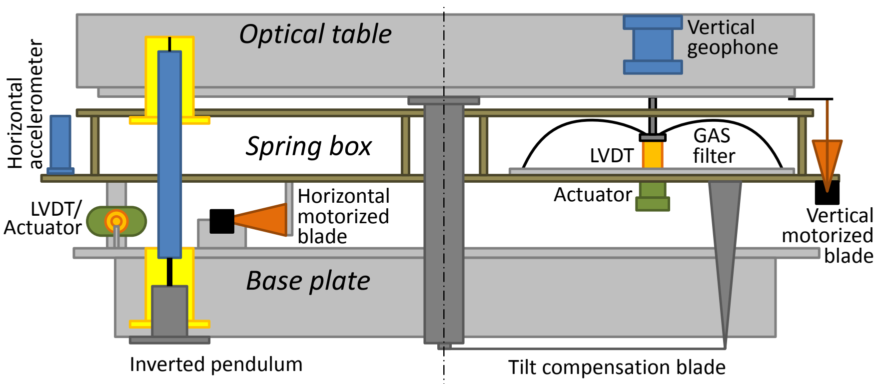

Figure 3.2.: Schematic illustration of a side-on cutaway picture of the Seismic Attenuation System (SAS). The main isolating elements are three Inverted Pendulum (IP) legs and three Geometric Anti-Spring (GAS) filters. Sensors, such as LVDTs, accelerometers, and geophones, as well as coil-magnet actuators and horizontal motorized adjusters are present three times in the system. They are spaced around the table on a centred circle at 120° from each other. For clarity only one example of each of these is shown. The only exception are the four vertical motorized blades that are placed in each corner of the table. Other major components are a base plate, a spring box, and an optical table. The base plate supports the AEI-SAS and is bolted to the ground inside the vacuum system. The IP legs support the stiffened spring box. The spring box consists of two large aluminium plates, between which three GAS filters are sandwiched. The GAS filters support the optical table.

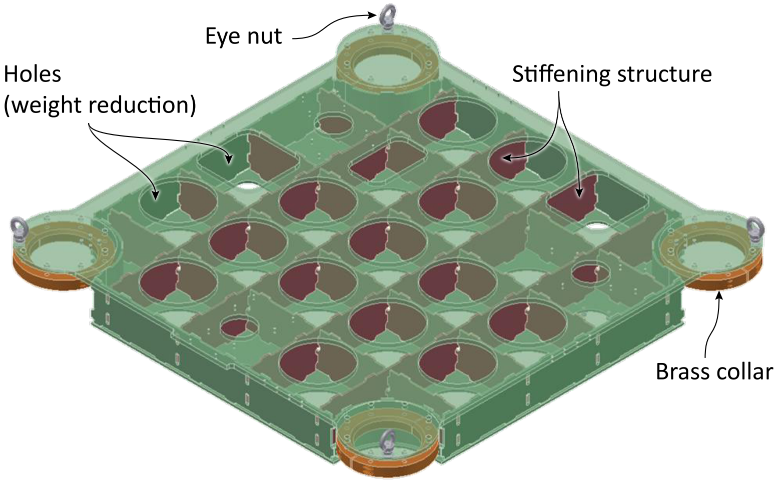

Figure 3.3.: A drawing of the welded baseplate, with the upper plate shown semi-transparent to reveal the internal stiffening structure. The holes in the base plate have been designed with different sizes to reduce the mass of the structure and allow to insert components (IP legs, and Tilt stabilization pole and blades) through them. The eye nuts on each corner of the base plate are used to crane the assembled AEI-SAS into the vacuum system. The brass collars were designed to bolt the base plate to the legs in the vacuum system, but had to be omitted due to imprecise manufacturing tolerances of the vacuum system.

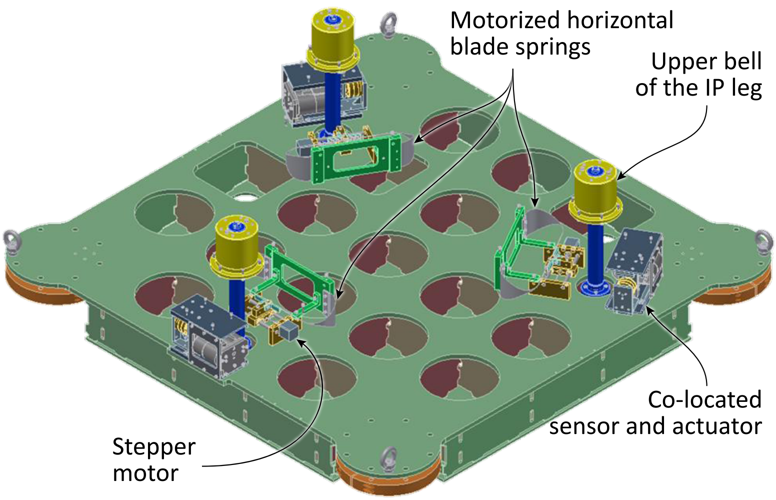

Figure 3.4.: The base plate supports three Inverted Pendulum (IP) legs, three horizontal sensors (LVDT) with their co-located co-axial voice-coil actuators, and motorized blade spring actuators. The IP legs in the drawing are shown with upper bells from which the spring box will be suspended. The three co-located sensor/actuator pairs are distributed on the outer ring, near the IP legs, while the motorized blade spring are on the inner circle, with 120° between each other. Sensors and actuators are described in chapter 7.1.

given in appendix E.
The base plate also supports horizontal sensors and actuators, as shown in figure 3.4. They are spaced around the base plate on a centred circle at 120° from each other. By placing the devices on a circle in the vicinity to the IP legs, the control complexity is minimized by implementing single-input and single-output controls. The signals from the sensors can be fed back directly to their corresponding co-located actuators. The relative displacement sensors, Linear Variable Differential Transducers (LVDT), measure displacements of the spring box with respect to the base plate. The LVDTs are described in chapter 7.1.1. The voice-coil actuators are discussed in chapter 7.1.4. Any rotational or translational modes can by achieved by using suitable vectorial combinations of the devices. Coordinate transformation matrices, which transform the local coordinates of the devices into coordinates parallel to the L-shape of the interferometer, are given in appendix D.
Three horizontal motorized blade springs are acting from the base plate on the spring box adjusting its static position. The parasitic stiffness of the blades is as low as necessary to provide static forces, but without reducing the performance of the system. More information on the motorized blade springs is given in chapter 7.1.5 on page 109.

Spring box

The spring box rests on the upper bells of the three IP legs. It consists of two aluminium plates stiffened with vertical stiffening spacers. The spring box provides a rigid platform for the GAS filters. The lower spring box plate is shown on figure 3.5. Below the lower plate, the blade springs for the tilt stabilization system are attached. Stiffening plates and pre-assembled GAS filters are sandwiched between the lower and upper spring box plate, as shown in figure 3.6. The upper plate, and with it the whole spring box, is suspended from three IP legs, as shown in figure 3.7.
Three horizontal accelerometers are positioned in the spring box, sensing horizontal motion and rotations around the vertical axis. If the accelerometers were placed on the optical table, at low frequency they would have been overwhelmed by angular motion of the bench. Placing the accelerometers on the spring box, which is constrained to horizontal movement, reduces the crosstalk from the angular degrees of freedom. Thus, the ultimate limit to the inertial control is set by the ground tilt, which can increase, for instance, due to bad weather conditions. This allows to substantially lower the unity gain frequency of the inertial control while minimizing re-injection of tilt motion, thus improving the attenuation performance at low frequency where the angular noise dominates.

Intermediate plate

The intermediate plate is the interface between the GAS filters and the optical table, as shown in figure 3.8. The plate was originally designed to simplify the construction effort of the initial HAM-SAS prototype, which was constructed to support the original HAM optical table. The basic idea was inherited for the AEI-SAS: the optical table is installed when the assembly of the system is finished.
The intermediate plate in the AEI-SAS has several functions:

- The optical table is positioned on the intermediate plate.

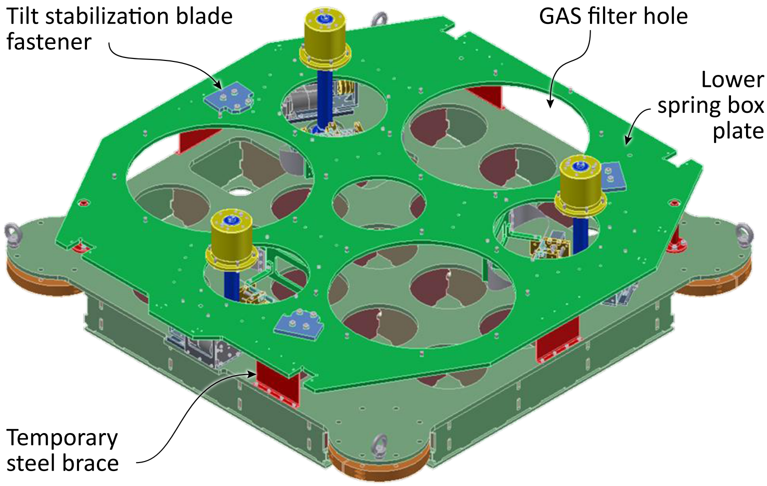

Figure 3.5.: The lower spring box plate rests on temporary steel braces, which are used to lock the movement of the system during transportation and installation procedures. The three large holes in the spring box plate will accommodate the Geometric Anti-Spring (GAS) filters. The tilt stabilization blades are bolted underneath the lower spring box plate, as illustrated in figure 3.9.

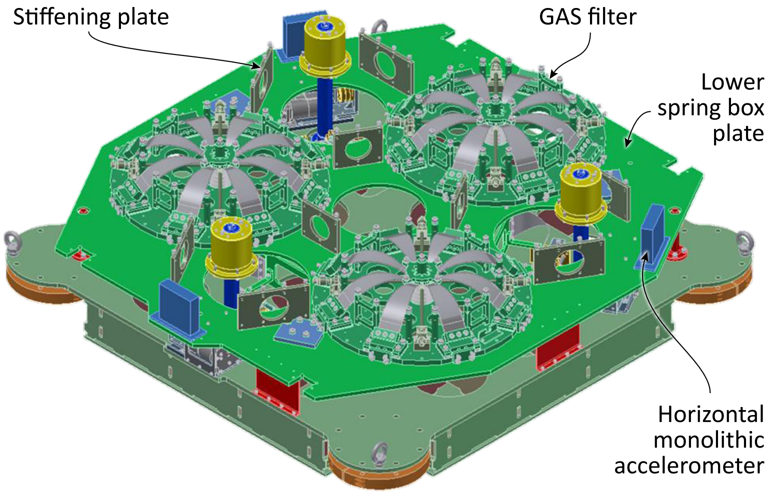

Figure 3.6.: The lower spring box plate is equipped with GAS filters, horizontal monolithic accelerometers, and vertical stiffening plates (with holes for weight reduction). The accelerometers are shown for completeness. To prevent their destruction, they are installed when the assembled system is positioned in the vacuum system.

- Vertical movement limiters for the GAS filters are positioned at each corner of the plate.
- The intermediate plate rigidly limits the keystones of the GAS filters to each other.
- The tilt stabilization arm is fixed in the centre of the plate. The pole is connected with steel wires to tilt compensation blades, which are bolted to the spring box (see figure 3.9).
- Four vertical motorized blade springs are acting between the intermediate plate and the spring box. The motorized blades set the static vertical position and tilt of the intermediate plate.

See additional information on the intermediate plate in chapter 7.4.

Tilt stabilization

The vertical isolation stage of the AEI-SAS is composed of three GAS filters, which operate as parallel connected springs. The common mode of the three springs is the vertical motion of the table. The differential movement of the springs allows a tilting of the table surface about the x and y axes. Without corrections, the virtual pivot point of the tilt would be located a few cm above the keystones and about 25-30 cm (depending on the payload configuration) below the plane of the centre of mass of the bench and payload. Therefore the gravity induces a negative restoring torque that overwhelms the small tilt stiffness contributed by the torsional stiffness of the GAS filters and makes the system unstable. A tilt stabilization system made of an arm and three springs is installed below the intermediate plate [Sannibale2008].
In the AEI-SAS, blade springs attached to the spring box are used to tune the tilt mode, as shown in figure 3.9. The tip of each blade is connected by a tensioned wire to an arm that is rigidly fastened to the intermediate plate below the optical table. The tilt stability torque is provided by the stiffness of the blades and tuned by choosing their thickness. The tension of the wire applies a force to the blades. The force is defined by the frequency of the tensioned wire, acting like a piano-string and a frequency of $f = 170\,\mathrm{Hz}$ corresponds to a force F of about 44 N, according to the following formula [Dubbel]:

$$f = \frac{1}{2L}\sqrt{\frac{F}{\rho A}} \tag{3.1}$$

with

- f, the harmonic eigenfrequency of the wire
- $L = 500\,\mathrm{mm}$, wire length
- $\rho_{\text{stainless steel}} = 7800\,\mathrm{kg/m^3}$, wire material density
- $A = \frac{\pi}{4}d^2$, wire cross-section area
- $d = 0.5\,\mathrm{mm}$, wire diameter.

The tension of the wire is adjusted according to the bench tilt range. The diameter of the wire was selected in order to maximize the frequency of its first violin mode.

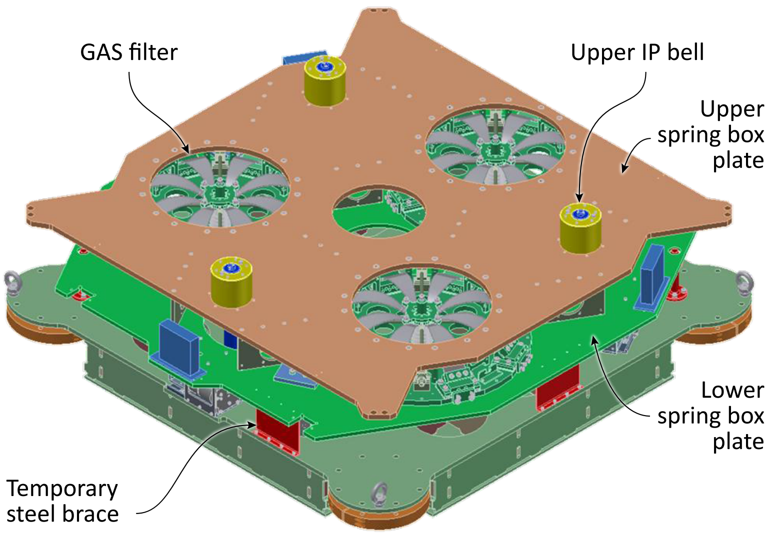

Figure 3.7.: The spring box is suspended from the upper bells of the Inverted Pendulums (IP). The upper spring box plate is bolted to stiffening plates and to spacers on the outer rim of the GAS filter plates. The lower spring box plate is bolted underneath. After the complete spring box is suspended from the IP bells, the temporary braces can be removed and the AEI-SAS can move freely in horizontal degrees of freedom.

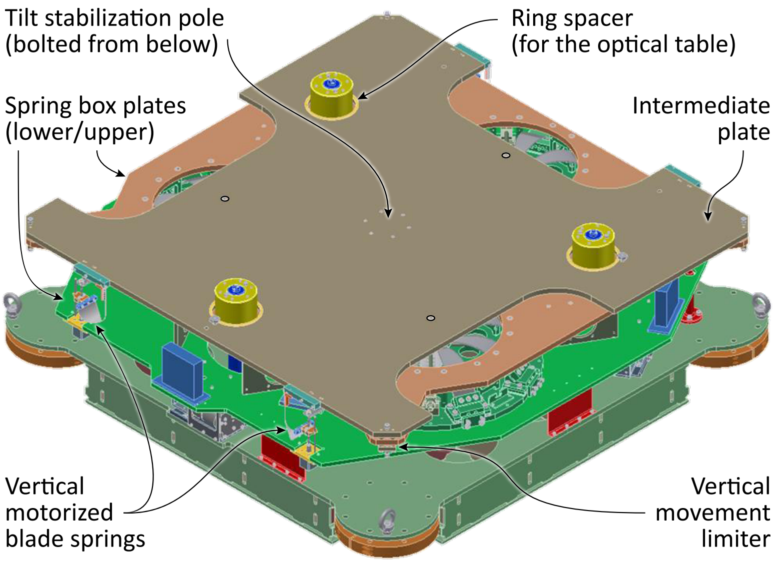

Figure 3.8.: A drawing of the intermediate plate supported by three GAS filters. Vertical movement limiters are installed at each corner of the plate. Vertical motorized blade springs are shown near the corners of the plate, acting against the spring box. The tilt stabilization pole is bolted underneath the intermediate plate. The optical table will be placed on ring spacers around the upper bells of the IP legs.

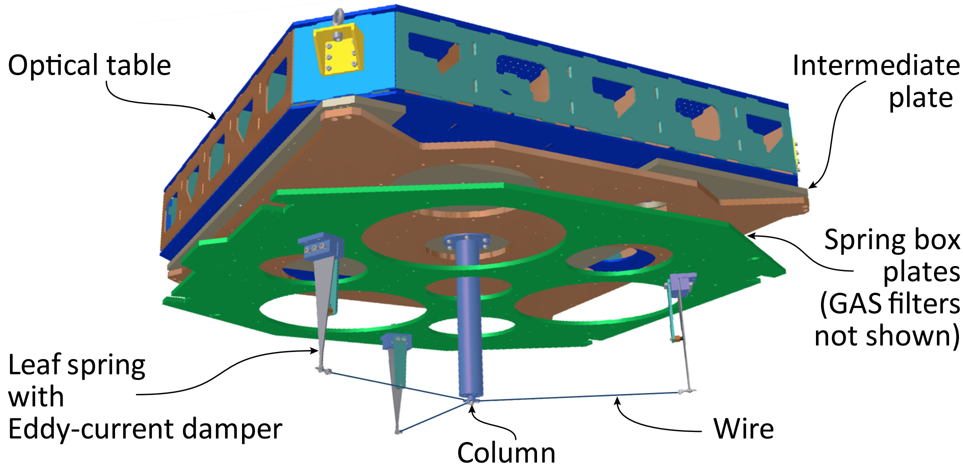

Figure 3.9.: Tilt stabilization system for the optical table consists of a set of vertical springs fastened to the spring box. The tips of the springs are connected with steel wires to a rigid column, which is attached to the intermediate plate.

Optical table

The optical table is positioned on top of the intermediate plate, interfaced by Fluorel™ pads, which will be discussed in more detail in chapter 7.4. The optical table in the AEI 10 m Prototype facility is a square-shaped stainless steel breadboard with side length 1750 mm and 400 mm thick, stiffened by an internal honeycomb web structure, as shown in figure 3.10. The optical table is the final component, to be installed in the system, as shown in figure 3.11.
The V–shaped holes in the side walls of the optical table are foreseen for ballast rods. Three rods are placed in each of the holes, providing a total of 30 rod emplacements inside the optical table. Each rod has a mass of 7 kg. The rods do not rattle, because they sit on a four point kinematic mount in the V–shaped holes.
Vertical geophones are bolted underneath the breadboard inside the optical table. They are sealed in vacuum cans, as shown in figure 3.12 to provide vacuum compatibility. The geophones measure the vertical motion of the optical table and its tilt around the two horizontal degrees of freedom. An overview of the geophones is given in chapter 7.1.3.

Total mass

The total mass of the AEI-SAS is about 1800 kg. Table 3.1 gives an overview of the mass of the sub-systems of the AEI-SAS. The additional mass of the ballast rods is used to maintain the mass load required by each GAS filter. Whenever something is placed on top of the table, the same amount of ballast needs to be removed. The mass positioned on one edge of the table needs to be counteracted with the same amount of mass on the opposite edge. Therefore, a set of smaller tuning ballast discs with increments from 0.1 kg to 2 kg is used. The small tuning weights are distributed on

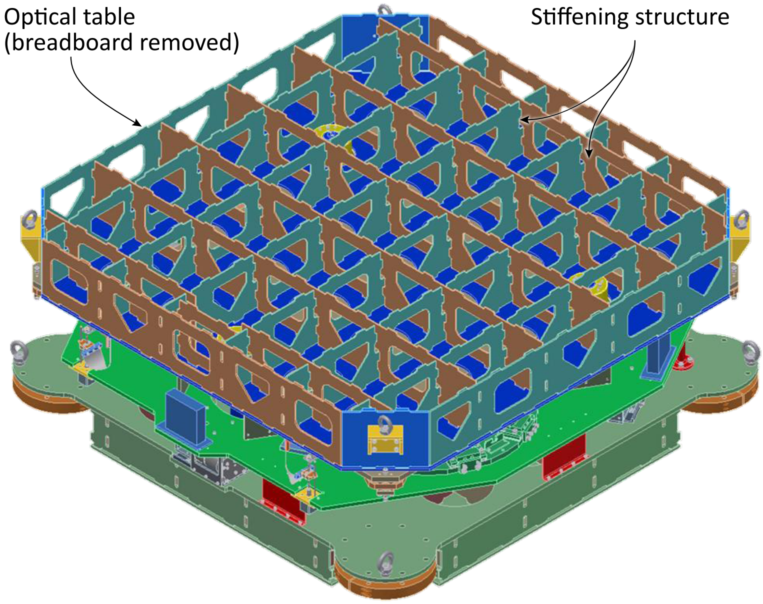

Figure 3.10.: A drawing of the optical table on top of the AEI-SAS. The breadboard is removed to reveal the internal stiffening structure. The holes in the structure walls reduce the mass of the optical table.

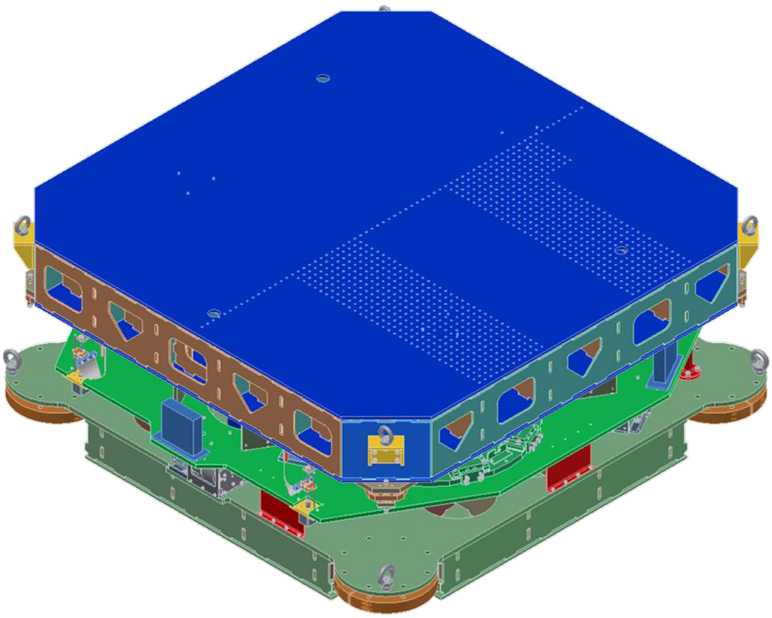

Figure 3.11.: A drawing of the optical table positioned on top of the AEI-SAS. The rectangular holes are made to reduce the mass of the optical table. The V-shaped holes in the sides of the optical table contain ballast rods (not shown) for levelling and to maintain the mass budget of the system.

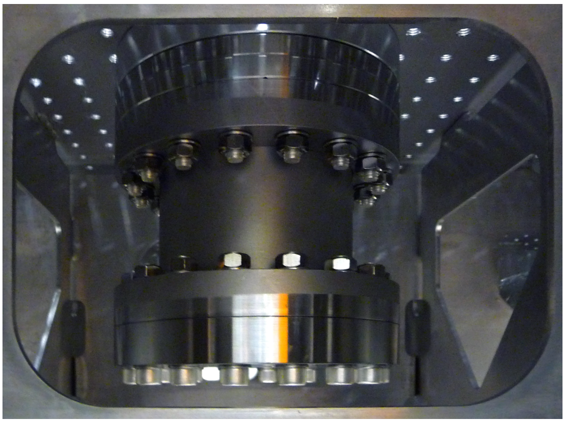

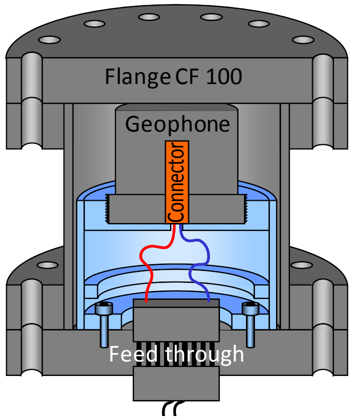

Figure 3.12.: A picture of a vacuum can (left), containing a vertical geophone, bolted inside the optical table underneath the breadboard. The cans are filed with different tracer gases, which can be identified if a can leaks in the vacuum. The sketch of the vacuum can (right), shows how the geophone is placed on an rigid aluminium stand and bolted to the flange. The original connector (shown in orange) is replaced by an in-house built connector, as shown in figure F.1 on page 157.

top of the optical table to finely level the table surface and to set the vertical height of the table. About 100 kg of these additional small tuning ballasts were placed in the spring box to control the natural resonance of the IPs.

Tuning of the natural frequencies of IPs and GAS filters

Due to mechanical separation of the vertical and horizontal isolation stages, the natural frequency of the IPs can be tuned independently of the GAS filters. The tuning process starts with the GAS filters, which are the upper isolation stage, by placing tuning masses on the optical table until their optimal working point is reached. This tuning mass also affects the IP frequency. After finishing the GAS filters, the IP natural frequency can be further lowered by placing tuning masses into the spring box. Upper boundaries for the maximum tuning mass are given in chapter 4.1. Further details regarding the tuning are given in chapter 4 for IP and chapter 5 for GAS filters.

Table alignment for the Suspension Point Interferometer (SPI)

A Suspension Point Interferometer (SPI) [Dahl2010] is used to monitor and stabilize the residual relative motion between the seismically isolated optical tables. The SPI is composed of a set of Mach-Zehnder interferometers which allow relative motion suppression via active feedback. Therefore, the surfaces of the optical tables have to be levelled with respect to each other during the installation process.
Each table is individually levelled by a spirit level with a precision of ± 0.1 mm/m. A hydrostatic level - a transparent flexible hose filled with isopropanol - is used to measure the relative height difference between two tables. Over a distance of 10 meters the measurement accuracy of ± 1 mm was limited by the concave meniscus on the surface of the liquid. Isopropanol was chosen, since its concave meniscus is significantly smaller than the one of water, which is typically used for this technique. The measurement

AEI-SAS components	**Component mass [kg]**	**Total mass [kg]**
Base plate	490	
Stepper motors (horizontal)	15	
LVDT/actuator pairs	15	
	Total base platform	**520**
Geometric anti-spring filters	150	
Spring box lower plate	99	
Spring box upper plate	64	
Stepper motors (vertical)	10	
Stiffeners	5	
Accelerometers	3	
	Total spring box	**331**
Optical table	530	
Ballast rods	220	
Intermediate plate	115	
Vertical geophones (in cans)	30	
Inverted pendulum legs	24	
Tilt stabilization column	5	
	Total optical bench	**924**
	Total AEI-SAS mass	**1 775**

Table 3.1.: Total mass estimation of an AEI-SAS table, derived from the CAD-model. The mass of more than 1 000 bolts and nuts in sizes from M 16 to M 3 is missing, which is an additional mass of estimated 50 kg.

has shown, that the relative height difference between the two tables is about 10 mm, which can be compensated with the GAS filters. The filters are limited to a maximum vertical displacement of ± 10 mm. To avoid consuming the GAS spring dynamic levelling budget, coarse adjustment of the height difference was achieved by stainless steel shims placed between the base plate and the legs inside the vacuum system. Fine levelling of the optical table surfaces with respect to each other will be done with the aid of the SPI.

3.2. Enhancements of the AEI-SAS with respect to HAM-SAS

As described in chapter 2.5 on page 41, the AEI-SAS is based on the HAM-SAS design, which was presented at the Amaldi-6 in 2005 [Bertolini2006d]. Most of the HAM-SAS design aspects were adopted, while other elements were re-designed. Design differences are compared in the following:

- Three instead of four IPs and GAS filters are used in the AEI-SAS. This way, the system is not over-constrained. The manufacturing process is simplified and the complexity of the control is reduced.
- The dimensions of the IP restoring flexures and the GAS filter blades are adapted to the AEI 10 m Prototype requirements.
- The design of the HAM-SAS counter weight bells for the IP legs, as shown in figure 4.1, is tested in the AEI-SAS. In HAM-SAS, the bells were designed but never tested due to lack of time. The IP bells were too heavy and will be re-machined to reduce their weight and tested again in the third AEI-SAS. See chapter 4.3 for more information about the IP.
- Additional stiffeners were applied to the AEI-SAS spring box to shift internal resonances to higher frequencies.
- The GAS filters in the AEI-SAS are sandwiched between two spring box plates. To increase the rigidity, the filters are bolted at the full filter base plate perimeter. In the HAM-SAS, the GAS filters were suspended from the upper spring box plate and only a fraction of the filter base plate was sandwiched between the spring box plates.
- The Centre of Percussion (CoP) compensators (Magic Wands) in the GAS filters of the AEI-SAS are manufactured from silicon carbide. The wands made of this material are more rigid than the original aluminium tubes, thus widening the frequency range of their effectiveness. The CoP and Magic Wands are discussed in chapters 4.2 and 5.2, respectively.
- The motorized coil-springs are replaced by blade springs. The blade springs have internal modes at higher frequencies reducing in this way the contamination of the overall response function. These new blade springs are designed with eddy current dampers to further reduce the high frequency resonances.

- The HAM-SAS intermediate plate between the GAS filters and the optical table was adapted to the AEI-SAS design. The plate is bolted on top of the keystones, to rigidly link them to each other. Further more, vertical movement limiters for the GAS filters are mounted at the corners of the plate, and the plate supports the tilt stabilization arm.
- Fluorel™ pads were introduced in the AEI-SAS, to remove a resonant mode of the intermediate plate. The pads are placed between the intermediate plate and the optical table. This way, they act as an additional oscillator, shifting the rigid body modes of the spring box to higher frequencies and damping oscillations of the plate.
- The initial tilt compensation coil springs were held responsible for high Q resonances above 10 Hz in HAM-SAS test measurements. Therefore, the coil springs are replaced by tunable blade springs with eddy current dampers.
- In HAM-SAS no inertial control was foreseen; just horizontal and vertical geophones for monitoring the isolation performance were mounted on top of the optical bench during the test campaign. In AEI-SAS, three monolithic horizontal low-frequency accelerometers and three vertical geophones sealed in vacuum cans are used to monitor and control the horizontal and vertical motion. The geophones are installed inside the AEI-SAS optical table underneath the breadboard. The monolithic accelerometers are much better positioned in the spring box, where the are insensitive to the optical table tilt.
- The AEI-SAS optical table was newly designed with a stiffening welded honeycomb structure. V-shaped holes in the flanks of the table are foreseen to facilitate ballast rods. To keep the payload budget, the ballasts can be removed to compensate the weight of any equipment installed on the optical table. This handy feature was copied from the HAM-SAS design.

3.3. Construction notes

The assembly of the AEI-SAS started in 2010. The parts for the tables were manufactured by Galli&Morelli in Lucca, Italy. Each single part of the table was cleaned, wrapped in aluminium foil and sent to the AEI in Hannover, Germany to be assembled. Each of the three AEI-SAS tables consist of over 1000 aluminium and stainless steel parts, plus nuts and screws. Most of the parts were unwrapped after arrival and cleaned again in an ultrasonic bath. The construction of the tables was often slowed down by tests and modifications of the subsystems. During the assembly of the first table, the parts were found to be re-poluted between cleaning and delivery. All large parts, including the optical tables, all spring box plates, and base plates were sent back to the manufacturer for re-cleaning.
The two AEI-SAS were assembled in a clean air, laminar flow box ensuring dust free conditions. At any time of the assembly and installation a clean-room suit, latex gloves, a face mask and a hairnet were mandatory. After assembly, the AEI-SAS was craned out of the flow box and immediately installed into its final position, where the base plate is bolted to legs inside the vacuum system.

The construction of an AEI-SAS mainly follows the sequence described in section 3.1 and is illustrated in figures 3.3−3.11. The assembly starts with the baseplate. For the time of the assembly the base plate is positioned on temporary legs, which are removed prior to installing the system into the vacuum system. The internal electrical cabling is arranged on the baseplate before the spring box is installed.
As previously described, the spring box is supported by three IP legs. The spring box consists of two aluminium plates, between which the GAS filters are housed. Stiffening spacers solidly connect the two plates. The lower plate is installed first. During the installation, the plate rests on intermediate steel braces, which restrain the horizontal movement of the system during installation procedures and transportation. The spring box contains, in addition to the GAS filters, the horizontal accelerometers. However, provisions are taken, so that the accelerometers can be installed after the AEI-SAS is placed into the vacuum system. This is done because the accelerometer's flexures are fragile and the device could accidentally be damaged during the assembly procedure, and to allow for the possibility that improved sensors could be implemented later without disassembling the entire table. Before installing the upper plate of the spring box, the upper IP bells are installed, from which the spring box is suspended. The upper bells connect the upper IP flexure to the spring box, as shown in figure 4.1. After that, the spring box can be released from the temporary braces and the AEI-SAS is free to move horizontally.
At the time of writing (end of 2012) two of three AEI-SAS have been completed and installed in the vacuum system, ready to be equipped with the SPI. The third AEI-SAS with the West-table will be assembled during the course of the year 2013. This table will be used as a test-bed for improvements of the first two AEI-SAS tables.
If necessary, the AEI-SAS can be dis-assembled for maintenance and retrofitting, due to the fact, that most of the components are pre-assembled before being installed. Retrofitting of the AEI-SAS is considered for the future, if any modifications of the third AEI-SAS turn out to improve the performance.

4. Horizontal isolator: Inverted Pendulum (IP)

Inverted pendulums are excellent horizontal seismic isolators, as briefly discussed in chapter 2.4. They can be tuned to extremely low natural frequencies at a comparably short leg length. In the AEI-SAS, the natural frequency of a 0.4 m short IP is tuned to 0.1 Hz. A regular pendulum at this frequency would have a length of 25 m. The IPs are used in several gravitational wave observatories as horizontal isolators. For example, at Virgo, IPs are installed in the Superattenuator [Losurdo1999, Braccini2005]. At Tama300, the IPs are used in the TAMA-SAS [Marka2002]. IPs were also suggested for the Advanced LIGO detector [Takamori2007] as low frequency seismic isolators.
At the AEI-SAS, a three-leg inverted pendulum provides seismic isolation for horizontal translational (x, y) modes and for *yaw* (rotation about z). Each IP leg has two flexures, shown in figure 4.1: a short soft flexure on top and a larger stiff flexure on the bottom. The upper flexure, with a negligibly small spring constant, serves as a hinge between the IP leg and the spring box. The flexure allows the spring box to move in the horizontal plane constraining its *roll* and *pitch* movement (tilt about x and y axes). It is loaded in tension, to prevent buckling. The lower stiff flexure provides the necessary restoring force for the system to keep the IP leg in the upright position. The lower flexure needs to be suitably sized, to matching the required payload and compensate for the destabilizing gravitational torque. The upper and lower flexures are shown in figure 4.1. They are machined from Maraging C-250 steel (Marval 18 from [Aubert-Duval]) and heat treated (precipitation hardened) to increase yield strength of the material and reduce creep under stress [Virdone2008, Beccaria1998, DeSalvo1997].

4.1. Theory of the IP

Angular stiffness of the IP

The angular stiffness, κ, of the lower flexure is an important property, which will be used to calculate the natural frequency of the IP. The spring constant was never directly measured in an experiment. Instead, its value is calculated here, using the assuming material properties and using dimensions of the flexure.
The torque, τ, in a flexure with angular stiffness, κ, bent by an angle, θ, is given by:

$$|\vec{\tau}| = \kappa\theta \,, \tag{4.1}$$

analogous to forces in a spring with linear spring constant, k, elongated by x:

$$|\vec{F}| = kx \,. \tag{4.2}$$

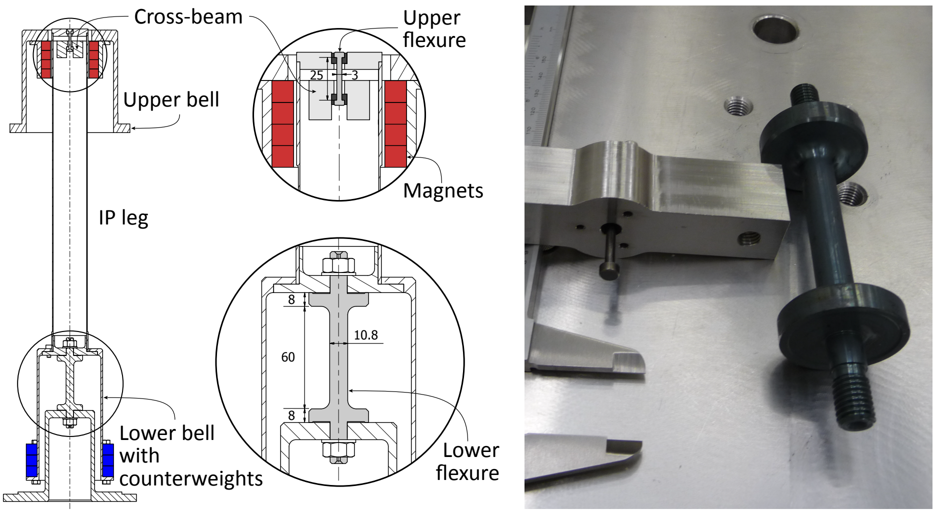

Figure 4.1.: An Inverted Pendulum (IP) leg, with soft upper and stiff lower flexure. Both flexures are machined from Maraging steel. The dimensions of the flexures are shown in units of mm. The upper flexure is used in tension to prevent buckling. The lower flexure provides restoring forces for the IP leg. The magnets (red) for eddy current damping of the leg's higher modes are distributed around the leg inside the upper bell. This upper bell is used to suspend the spring box. The lower bell supports balancing counterweights (blue) for fine tuning of the Centre of Percussion (CoP) effect. The CoP effect is explained in section 4.2. The photograph on the right-hand side shows the two flexures side by side. The calliper tips indicates the length (25 mm) of the short flexure. The short flexure is shown within a cross-beam, from which the upper bell is suspended.

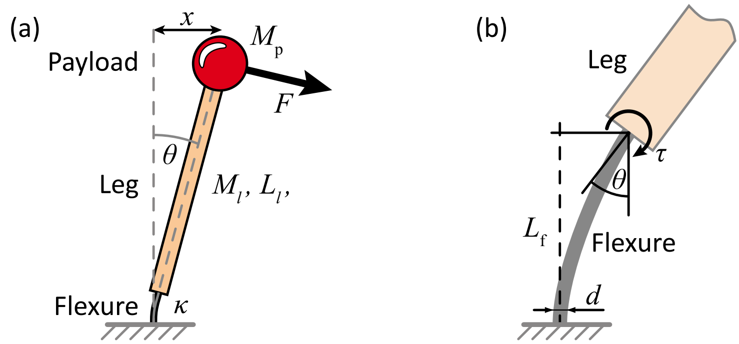

Figure 4.2.: An Inverted Pendulum (IP) in a schematic model (a) with a payload mass, M_p, on a rigid leg with length, L_l. The restoring force for the IP provides a flexure with angular stiffness, κ, in units of Nm. (b) The flexure is a rod with length, L_f, and a round cross section with diameter d. A force, F, deflects the IP by x until the leg is at the angle, θ. This force applies a bending moment, or torque, τ, to the tip of the flexure.

According to [Dubbel] the angle of a flexure, curved by torque at its tip, is given by:

$$\theta = \tau \frac{L_\mathrm{f}}{E I_y}\,, \tag{4.3}$$

with the flexure length, L_f, elasticity (Young's) modulus, E, and area moment of inertia, $I_y = \pi d^4/64$, for a flexure with a round cross-section with diameter d.
With equation (4.1) inserted in equation (4.3), the angular stiffness is given as:

$$\kappa = \frac{\tau}{\theta} = \frac{E I_y}{L_\mathrm{f}} = \frac{E}{L_\mathrm{f}} \frac{\pi d^4}{64} \approx 2070\,\mathrm{Nm}\,, \tag{4.4}$$

with the values $E = 186\,\mathrm{GPa}$ [Braccini2000], $d = 10.8\,\mathrm{mm}$, and $L_\mathrm{f} = 60\,\mathrm{mm}$.

Natural frequency of the IP

The horizontal natural frequency of the AEI-SAS is assessed using a simple model of an IP, as illustrated in figure 4.2a. The three leg IP is regarded as one system. For each IP leg, one third of the total payload mass is assumed. For simplicity, the IP leg is considered a rigid mass-less leg with length, L_l. It is connected to the ground by a flexure with angular stiffness, κ, and supports a point-mass payload, M_p. The payload has a moment of inertia, I. Hence, the equation of motion is given as a sum of all torques in the system:

$$I\ddot{\theta} = -\kappa\theta + M_\mathrm{p} g L_l \sin(\theta)\,, \tag{4.5}$$

with the gravitational acceleration, g, the deviation angle from the perpendicular position, θ, the elastic torque of the flexure, $\tau_\mathrm{el} = -\kappa\theta$, and the gravity torque, $\tau_\mathrm{grav} = M_\mathrm{p} g L_l \sin(\theta)$, acting on the point mass, M_p.
The angular deviation, θ, from the vertical leg position is written as $\sin(\theta) = x/L_l$. The term $\sin(\theta)$ can be expanded in a Taylor series:

$$\sin(\theta) = \theta - \frac{\theta^3}{6} + \frac{\theta^5}{120} - \mathcal{O}(\theta^7)\,. \tag{4.6}$$

Thus, for sufficiently small angles, the series is dominated by the first term: $\sin(\theta) \approx \theta$. With this small angle approximation the equation (4.5) becomes:

$$I\ddot{\theta} = -\theta\,(\kappa - M_{\mathrm{p}} g L_l) \ . \tag{4.7}$$

The effective elastic constant of the IP, $\kappa_{\mathrm{eff}} = \kappa - M_{\mathrm{p}} g L_l$, is defined as the spring constant, κ, of the lower flexure reduced by the anti-spring constant from gravity, $\kappa_{\mathrm{grav}} = M_{\mathrm{p}} g L_l$.
The equation of motion can be rewritten with respect to linear displacement of the payload mass. In the small angle approximation the angle of the displaced payload point mass is given as:

$$\theta \approx x/L_l \, . \tag{4.8}$$

With the moment of inertia, $I = M_{\mathrm{p}} L_l^2$, equation (4.7) yields:

$$M_{\mathrm{p}} L_l^2 \frac{\ddot{x}}{L_l} = -\frac{x}{L_l}\,(\kappa - M_{\mathrm{p}} g L_l) \tag{4.9}$$

$$\ddot{x} = -x\left(\frac{\kappa}{M_{\mathrm{p}} L_l^2} - \frac{g}{L_l}\right) \, . \tag{4.10}$$

The angular stiffness κ could be substituted by a linear spring constant, k, with $k = \kappa/L_l^2$, as defined in equation (B.6). The equation (4.10) would then simplify to:

$$\ddot{x} = -x\left(\frac{k}{M_{\mathrm{p}}} - \frac{g}{L_l}\right) \, . \tag{4.11}$$

The value k is an auxiliary quantity. Thus, the angular stiffness κ is used to define equations in this work, to provide equations with real physical values of the system.
In frequency domain the equation of motion (4.10) is written as:

$$-\,\omega^2 \tilde{x}(\omega) = -\tilde{x}(\omega)\left(\frac{\kappa}{M_{\mathrm{p}} L_l^2} - \frac{g}{L_l}\right) \, , \tag{4.12}$$

with $\tilde{x}(\omega)$ the Fourier transformed of $x(t)$. Then, the natural angular frequency, ω_{n}, of the IP is given as:

$$\omega_{\mathrm{n}} = \sqrt{\frac{\kappa}{M_{\mathrm{p}} L_l^2} - \frac{g}{L_l}} \, . \tag{4.13}$$

Since g is obviously constant, κ is a constant property of the material and geometry of the glexure, and the length of the IP leg is fixed, the natural frequency of the IP can be tuned towards lower frequencies by increasing the payload mass on the spring box. The goal of the tuning is to achieve the lowest possible natural frequency at which the system is still stable. An IP becomes unstable, when with increasing mass its natural frequency crosses zero. In the simplified model, the maximum mass, $M_{\mathrm{p}}^{\mathrm{max}}$, can be found by setting the natural frequency in equation (4.13) to $\omega_{\mathrm{n}} = 0\,\mathrm{Hz}$:

$$0 = \frac{\kappa}{M_{\mathrm{p}} L_l^2} - \frac{g}{L_l} \quad \Rightarrow \quad M_{\mathrm{p}}^{\mathrm{max}} = \frac{\kappa}{g L_l} \approx 502\,\mathrm{kg} \, , \tag{4.14}$$

with the IP leg length, $L_l = 0.42\,\mathrm{m}$ and the spring constant of the flexure, $\kappa \approx 2070\,\mathrm{Nm}$. Thus, according to equation (4.13), a payload of one IP greater than 502 kg leads to instability of the system. In that case, the gravitational torque prevails and the IP becomes unstable, which means the IP tilts over thereby damaging the IP flexures. To prevent such catastrophic events, the IPs are equipped with oscillation range limiting safety structures.

In reality, the payload of one single IP is one third of the mass supported by three IP legs: $M_{\mathrm{p}} = M_{\mathrm{sup}}/3$, assuming a homogeneous mass distribution. A rough estimate of M_{sup} can be found in table 3.1, where the total mass supported by three IPs is given as $\sim 1300\,\mathrm{kg}$. It includes the optical table mass and the spring box mass with components, and $\sim 50\,\mathrm{kg}$ screws and nuts. Additional tuning-mass of $\sim 100\,\mathrm{kg}$ was distributed on the optical table and in the spring box to tune the natural frequencies of the GAS filters and the IPs, respectively. Thus the total payload mass of three IP legs is $M_{\mathrm{sup}} \approx 1400\,\mathrm{kg}$, which leads to $M_{\mathrm{p}} \approx 467\,\mathrm{kg}$ for each IP leg. To get a natural frequency of $0.1\,\mathrm{Hz}$, the mass used for computation of equation (4.13) was adjusted to $M_{\mathrm{p}} \approx 494\,\mathrm{kg}$. A list of values used to simulate the IP behaviour is given in table 4.1 on page 73.

Massive IP leg

If the mass of the IP leg is neglected, the IP attenuation grows indefinitely at higher frequencies. In reality the mass of the leg limits the attenuation above a certain value, of the order of the mass ratio between the leg and its payload.
The simple IP can be made more realistic by including the mass of the leg, M_l. The moment of inertia of the leg with respect to the pivot point at the lower flexure is $I_l = M_l L_l^2/3$. The total torque of the system about the pivot point is the sum of the IP leg torque and the torque of the payload point mass:

$$\ddot{\theta} I_{\mathrm{tot}} = \ddot{\theta} L_l^2 \left(M_{\mathrm{p}} + \frac{M_l}{3} \right) . \tag{4.15}$$

The gravity torque acting on the centre of mass of the leg is $M_l g (L_l/2) \sin(\theta)$. Again, the small angle approximation $\theta \approx x/L_l$ can be used (see equation (4.8)). The equation of motion of a massive pendulum with payload is the sum of all torques:

$$\begin{aligned} \ddot{\theta} L_l^2 \left(M_{\mathrm{p}} + \frac{M_l}{3} \right) &= -\theta\kappa + \left(\theta M_{\mathrm{p}} g L_l + \theta M_l g \frac{L_l}{2} \right) && (4.16) \\ &= -\theta \left(\kappa - g L_l \left(M_{\mathrm{p}} + \frac{M_l}{2} \right) \right) . && (4.17) \end{aligned}$$

The linear equation of motion of the top of the IP leg is obtained by taking the second derivative of equation (4.8), so that $\ddot{\theta} \approx \ddot{x}/L_l$, and inserting it in equation (4.17):

$$\begin{aligned} \frac{\ddot{x}}{L_l} L_l^2 \left(M_{\mathrm{p}} + \frac{M_l}{3} \right) &= -\frac{x}{L_l} \left(\kappa - g L_l \left(M_{\mathrm{p}} + \frac{M_l}{2} \right) \right) && (4.18) \\ \ddot{x} \left(M_{\mathrm{p}} + \frac{M_l}{3} \right) &= -x \left(\frac{\kappa}{L_l^2} - \frac{g}{L_l} \left(M_{\mathrm{p}} + \frac{M_l}{2} \right) \right) . && (4.19) \end{aligned}$$

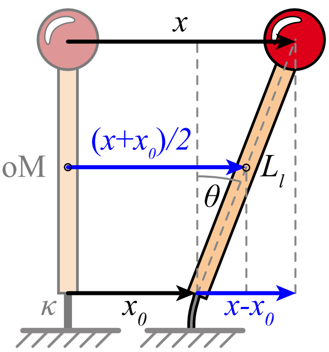

Figure 4.3: Coordinates of the IP system, with ground motion, x_0, payload position, x, and interconnecting distance, $x - x_0$. The coordinate of the Centre of Mass (CoM) of the leg is given as $x_0 + (x - x_0)/2 = (x + x_0)/2$. The deflection angle of leg rotation is given by $\theta \approx \sin(\theta) = (x - x_0)/L_l$.

With $M_l = 0$, the equation (4.19) is equal to the simple model in equation 4.10. In the frequency domain, equation (4.19) is written as:

$$-\omega^2 \tilde{x}\left(M_\mathrm{p} + \frac{M_l}{3}\right) = -\tilde{x}\left(\frac{\kappa}{L_l^2} - \frac{g}{L_l}\left(M_\mathrm{p} + \frac{M_l}{2}\right)\right), \tag{4.20}$$

with $\tilde{x}(\omega)$ the Fourier transform of $x(t)$. The system obviously oscillates with its natural frequency, such that $\omega = \omega_\mathrm{n}$. Thus, the natural frequency of the massive IP is given as:

$$\omega_\mathrm{n} = \sqrt{\frac{\frac{\kappa}{L_l^2} - \frac{g}{L_l}\left(M_\mathrm{p} + \frac{M_l}{2}\right)}{\left(M_\mathrm{p} + \frac{M_l}{3}\right)}}. \tag{4.21}$$

With values from table 4.1 the natural frequency is computed again to $f_\mathrm{n} \approx 0.1\,\mathrm{Hz}$. Equation (4.19) can be summarized as:

$$\ddot{x}B = -xA\,, \tag{4.22}$$

with

$$A = \frac{\kappa}{L_l^2} - \frac{g}{L_l}\left(M_\mathrm{p} + \frac{M_l}{2}\right) \tag{4.23}$$

$$B = M_\mathrm{p} + \frac{M_l}{3}\,. \tag{4.24}$$

The natural frequency ω_n can thus be written as:

$$\omega_\mathrm{n} = \sqrt{\frac{A}{B}}\,. \tag{4.25}$$

Ground motion and IP transmissibility

To calculate the transmissibility, the horizontal movement of the ground needs to be considered. Figure 4.3 shows an IP system affected by ground motion. Let x_0 be the displacement of the ground and x the displacement of the payload. The left-hand side of the equation of motion is given, analogous to equation (4.17), as the sum of the torques caused by acceleration. The tilt of the payload mass about the pivot point is unaffected by ground motion, thus is:

$$\tau_\mathrm{p} = \ddot{x} M_\mathrm{p} L_l \,. \tag{4.26}$$

The torque of the leg's centre of mass at $L_l/2$ about the pivot is:

$$\tau_l^{\mathrm{CoM}} = \ddot{x}^{\mathrm{CoM}} M_l \frac{L_l}{2} = (\ddot{x} + \ddot{x}_0) M_l \frac{L_l}{4} \,, \tag{4.27}$$

with $x^{\mathrm{CoM}} = (x + x_0)/2$, as shown in figure 4.3. The torque of the massive IP leg exerted by ground acceleration is given as:

$$\tau_l = I_l \ddot{\theta} = \frac{\ddot{x} - \ddot{x}_0}{L_l} \frac{M_l L_l^2}{12} \,, \tag{4.28}$$

with the moment of inertia, $I_l = M_l L_l^2/12$, of the leg rotating about its centre of mass, and

$$\theta \approx \frac{x - x_0}{L_l} \qquad \Rightarrow \qquad \ddot{\theta} \approx \frac{\ddot{x} - \ddot{x}_0}{L_l} \,. \tag{4.29}$$

The sum of the reaction torques of the system on the right-hand side of the equation of motion is found in the same way as in (4.17). Hence, the equation of motion is written as:

$$\tau_\mathrm{p} + \tau_l^{\mathrm{CoM}} + \tau_l = -\theta \left(\kappa - g L_l \left(M_\mathrm{p} + \frac{M_l}{2} \right) \right) \,. \tag{4.30}$$

Inserting the torques given in equations (4.26) – (4.28) and with $\theta \approx (x - x_0)/L_l$ from equation (4.29) yields:

$$\ddot{x} L_l \left(M_\mathrm{p} + \frac{M_l}{4} + \frac{M_l}{12} \right) + \ddot{x}_0 L_l \left(\frac{M_l}{4} - \frac{M_l}{12} \right) = -\frac{x - x_0}{L_l} \left(\kappa - g L_l \left(M_\mathrm{p} + \frac{M_l}{2} \right) \right) \,. \tag{4.31}$$

Thus, the equation of motion of a massive IP driven by ground motion is given as:

$$\ddot{x} \left(M_\mathrm{p} + \frac{M_l}{3} \right) + \ddot{x}_0 \frac{M_l}{6} = -(x - x_0) \left(\frac{\kappa}{L_l^2} - \frac{g}{L_l} \left(M_\mathrm{p} + \frac{M_l}{2} \right) \right) \,. \tag{4.32}$$

The equation of motion (4.32) can be summarized again as:

$$\ddot{x} B + \ddot{x}_0 C = -(x - x_0) A \,, \tag{4.33}$$

with

$$A = \frac{\kappa}{L_l^2} - \frac{g}{L_l} \left(M_\mathrm{p} + \frac{M_l}{2} \right) \tag{4.34}$$

$$B = M_\mathrm{p} + \frac{M_l}{3} \tag{4.35}$$

$$C = \frac{M_l}{6} \,. \tag{4.36}$$

Chapter 4

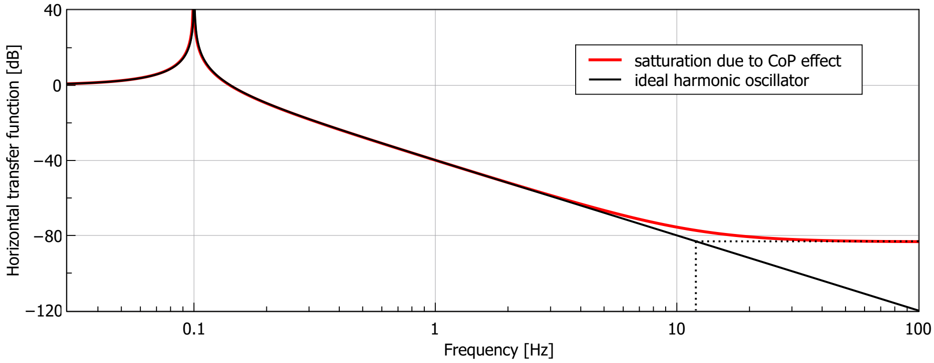

Figure 4.4.: Transfer function of an IP with a massive leg compared to an ideal harmonic oscillator. The transfer function of a massive IP leg with resonance frequency at 0.1 Hz is plotted for realistic values, as given in table 4.1. Above the corner frequency $f_c = 12\,\text{Hz}$ the transmissibility saturates towards −83 dB due to the Centre of Percussion (CoP) effect.

The factors A and B are identical to those in the case without ground motion, as shown in equations (4.23) and (4.24). In the frequency domain, the equation of motion (4.33) is written as:

$$-\omega^2\tilde{x}B - \omega^2\tilde{x}_0C = -(\tilde{x} - \tilde{x}_0)A\,. \tag{4.37}$$

The natural frequency of the payload is found by setting $\tilde{x}_0 = 0$ and is thus identical to equation (4.25):

$$\omega_\text{n} = \sqrt{\frac{A}{B}}\,, \tag{4.25a}$$

and evaluates to $f_\text{n} = \omega_\text{n}/2\pi \approx 0.1\,\text{Hz}$ with values from table 4.1.
Using the abbreviated notation, the transfer function can be written as:

$$\frac{\tilde{x}(\omega)}{\tilde{x}_0(\omega)} = \frac{A + C\omega^2}{A - B\omega^2} \tag{4.38}$$

$$= \frac{\omega_\text{n}^2 + \beta\omega^2}{\omega_\text{n}^2 - \omega^2}\,, \tag{4.39}$$

with

$$\beta = \frac{C}{B}\,. \tag{4.40}$$

Figure 4.4 shows a transfer function of an IP with a massive leg driven by ground motion. It is plotted using realistic values from table 4.1. The transmissibility of an ideal harmonic oscillator, for example an IP with a massless leg, continues decreasing with a slope of $1/f^2$ for increasing frequencies above its resonance frequency. However, the massive IP leg transfer function in equation (4.39) saturates towards a plateau at hight frequencies. The transmissibility remains constant at high frequencies at the value β:

$$\frac{\tilde{x}}{\tilde{x}_0} \approx \beta \qquad \text{for} \qquad \omega^2 \gg \omega_\text{n}^2/\beta\,. \tag{4.41}$$

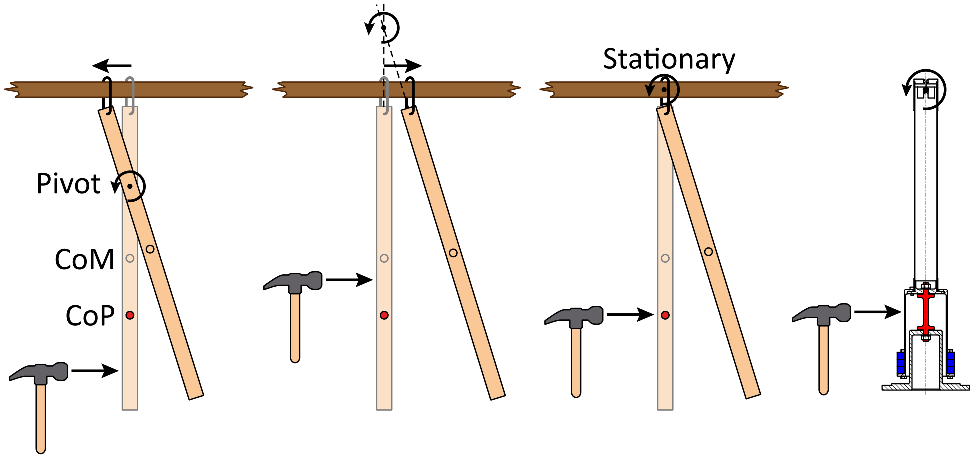

Figure 4.5.: A visualization of the Centre of Percussion (CoP) effect. A massive bar is suspended from a horizontal rail and can slide on it without friction. If the bar is hit exactly at the CoP, the suspension point of the bar remains stationary. In other cases the suspension point slides along the rail. In this context, the displacement of the suspension point the called the CoP effect. This principle can be transferred to the IP, where the force from ground motion acts on the lower flexure. With the CoP shifted into the lower flexure, the upper flexure ideally remains stationary.

The plateau begins above a corner frequency ω_c:

$$\omega_c = \frac{\omega_n}{\sqrt{\beta}}\,, \tag{4.42}$$

in which the addends of the nominator of equation (4.39) are equal.
With values from table 4.1 the corner frequency of the isolation plateau is found as:

$$f_c = \frac{\omega_c}{2\pi} \approx 12\,\mathrm{Hz}\,,$$

and the level of the isolation plateau is given as:

$$\beta = \frac{C}{B} \approx 20 \cdot \log_{10}(6.8 \cdot 10^{-5}) \approx -83\,\mathrm{dB}\,. \tag{4.43}$$

Since β gives the level of the isolation plateau, the goal is to reduce its value as far as possible, ideally to $-\infty$ dB. The plateau is associated with the Centre of Percussion effect, which is briefly discussed below.

4.2. Centre of Percussion (CoP) effect

The term Centre of Percussion (CoP) is usually associated with sporting implements, such as baseball bats, rackets, or swords. The CoP is a point along the implement, at which a perpendicular impact force produces no reaction force at the pivot point. A simple gedankenexperiment illustrating the CoP effect is shown in figure 4.5. If an external force acts on the bar below the CoP, the bar rotates counter-clockwise about

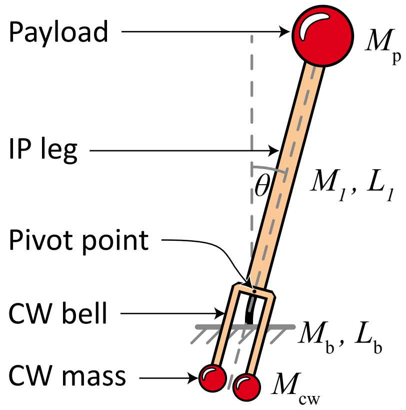

Figure 4.6: The saturation of the transmissibility of a simple massive IP leg is attributed to the Centre of Percussion (CoP) effect. This effect can be reduced by using a bell-shaped compensator with Counter Weights (CWs). These CW ballasts move the CoP of the massive IP leg right onto the pivot point at the lower flexure. Realistic values and explanations for IP parameters are given in table 4.1.

a virtual pivot point below the suspension point. The suspension shifts then to the left. If the force is applied below the CoP, the suspension point translates along the rail to the right. Only if hit exactly in the CoP, the suspension point remains stationary since it coincides with the pivot point. Therefore, if external forces are not localized at the CoP of the IP, translational forces occur at the suspension point.

The CoP principle can be applied to the IP leg. Ideally, the CoP should be at the lower flexure, where the movement of the ground displaces the IP leg. This way, no motion is measurable at the upper flexure. Then the spring box (and with it the optical table) remain stationary. In reality, the ground motion acts on the lower flexure of the IP and creates a rotation of the leg. The pivot point, about which the leg should ideally be rotating, is at the centre of mass of the payload. Instead, due to the moment of inertia of the leg, the pivot point is displaced vertically from the payload. The ground oscillations are transmitted to the payload, so that the horizontal transfer function, measured at the payload, saturates. This saturation due to the movement of the upper IP flexure is called the CoP effect.

Since, the ground motion is transmitted to the payload, the isolation performance of the IP is limited. The CoP effect causes an isolation plateau in the transfer function of the IP, starting above a corner frequency. The isolation plateau and the corner frequency are shown in the transfer function in figure 4.4.

The level, β, of the saturation plateau in equation (4.40) depends only on the masses of the IP leg and the payload mass. The plateau disappears when $\beta \to 0$ or $20\log_{10}(\beta) \to -\infty\,\text{dB}$. However, this is only possible if the relation of the payload mass and the leg mass was infinite. This solution is impractical. A better solution would be to shift the CoP.

The shifting of the CoP is done with a bell-shaped CoP compensator [Losurdo-thesis] with modifiable Counter Weight (CW) ballasts. The bell holding the CW masses is rigidly attached to the IP legs, as shown in figure 4.6. The CoP is then shifted right onto the lower flexure. The fine tuning of the CoP position can be done by adjusting the CW ballast mass.

Compensation of the CoP effect with bell and counter weights

A simplified model of a massive IP leg with a CoP compensator is shown in figure 4.6. The equation of motion for a massive IP with a CW bell that compensates for the CoP effect is obtained by summing all torques of the system: gravity torque, elastic torque of the flexure, and torque produced by acceleration. The equation of motion is derived in full length in equation (5.29) in [Takamori-thesis]. Analogous to equation (4.37) the equation of motion of a ground-driven massive IP with counterweights is given as:

$$-\omega^2\tilde{x}B - \omega^2\tilde{x}_0 C = -(\tilde{x}-\tilde{x}_0)A\,, \tag{4.37a}$$

so that the transfer function is given as:

$$\frac{\tilde{x}(\omega)}{\tilde{x}_0(\omega)} = \frac{A + C\omega^2}{A - B\omega^2} \tag{4.38a}$$

$$= \frac{\omega_{\mathrm{n}}^2 + \beta\omega^2}{\omega_{\mathrm{n}}^2 - \omega^2}\,, \tag{4.39a}$$

with

$$\omega_{\mathrm{n}} = \sqrt{\frac{A}{B}} \qquad \text{and} \tag{4.25a}$$

$$\beta = \frac{C}{B}\,. \tag{4.40a}$$

Here the factors A, B, and C are given as:

$$A = \frac{\kappa}{L_l^2} - \frac{g}{L_l}\left(M_{\mathrm{p}} + \frac{M_l}{2} - \frac{M_{\mathrm{b}}L_{\mathrm{b}}}{2L_l} - \frac{M_{\mathrm{cw}}L_{\mathrm{b}}}{L_l}\right) \tag{4.44}$$

$$B = M_p + \frac{M_l}{4} + \frac{L_{\mathrm{b}}^2 M_{\mathrm{b}}}{4L_l^2} + \frac{L_{\mathrm{b}}^2 M_{\mathrm{cw}}}{L_l^2} + \frac{I_l + I_{\mathrm{b}}}{L_l^2} \tag{4.45}$$

$$C = \frac{M_l}{4} - \frac{L_{\mathrm{b}}(2L_l + L_{\mathrm{b}})M_{\mathrm{b}}}{4L_l^2} - \frac{L_{\mathrm{b}}(L_l + L_{\mathrm{b}})M_{\mathrm{cw}}}{L_l^2} - \frac{I_l + I_{\mathrm{b}}}{L_l^2}\,. \tag{4.46}$$

The parameters, of which the factors A, B, and C are composed, are shown in figure 4.6 and explained in table 4.1.
With $I_l = M_l L_l^2/12$, the moment of inertia about the centre of mass of the IP leg and $I_{\mathrm{b}} = M_{\mathrm{b}} L_{\mathrm{b}}^2/12$, the moment of inertia about the centre of mass of the bell, the factors B and C become:

$$B = M_{\mathrm{p}} + \frac{M_l}{3} + \frac{L_{\mathrm{b}}^2 M_{\mathrm{b}}}{3L_l^2} + \frac{L_{\mathrm{b}}^2 M_{\mathrm{cw}}}{L_l^2} \tag{4.45a}$$

$$C = \frac{M_l}{6} - \frac{L_{\mathrm{b}}(3L_l + 2L_{\mathrm{b}})M_{\mathrm{b}}}{6L_l^2} - \frac{L_{\mathrm{b}}(L_l + L_{\mathrm{b}})M_{\mathrm{cw}}}{L_l^2}\,. \tag{4.46a}$$

The factors A, B, and C given here can be reduced to the more simple ones stated in the previous section (see equations (4.34)-(4.36)) by setting either the counter weight mass and bell mass, or alternatively the bell length to zero.

Chapter 4

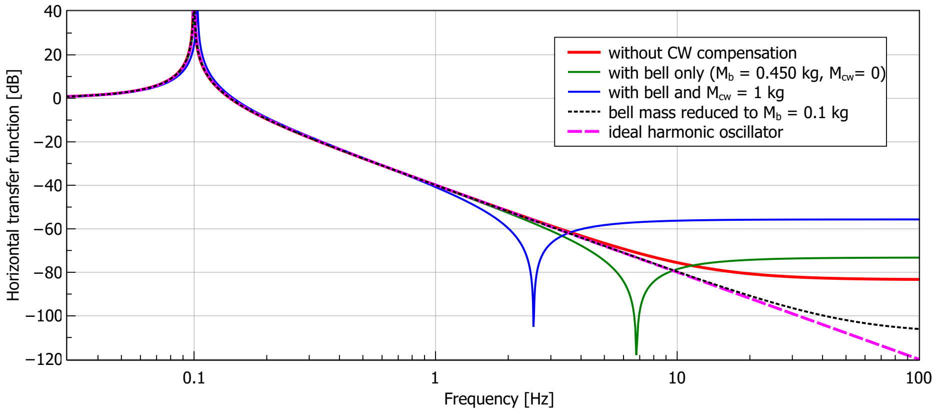

Figure 4.7.: The transfer functions of inverted pendulums for different parameter settings. (red) Without CoP compensation (CW mass set to zero) the transmissibility saturates around −83 dB. (green) The mass of the bell alone overcompensates the system. An overcompensation notch appears around 7 Hz and the isolation plateau saturates around −72 dB. (blue) With additional CW mass of 1 kg the notch shifts, towards 2.5 Hz and the plateau rises towards −55 dB. (black dotted) A new bell, with a mass reduced from 450 g to 100 g, can be used to remove the notch and improve the performance to −110 dB. (pink dashed) The ideal harmonic oscillator includes only the payload mass.

The transfer function of a massive IP, with masses of the bell and of the counter weights, is plotted in figure 4.7. The plots are produced using equation (4.38a) with A, B, and C values from equations (4.44), (4.45a), and (4.46a), respectively, with realistic parameters from table 4.1. At low frequencies, the transmissibilities are nearly identical. Without CoP compensation (CW and bell masses are set to zero) the transfer function saturates to −83 dB above 11 Hz. In the real system, the bell is over dimensioned. The computation shows, that the mass of the bell alone overcompensates the system, producing an overcompensation notch around 7 Hz and increasing the isolation plateau to around −72 dB. With an additional CW mass of 1 kg the notch shifts, towards 2.5 Hz and the plateau rises to −55 dB. The 1 kg CW mass is intentionally chosen extremely high, to demonstrate the overcompensation effect. The ideal harmonic oscillator plot is produced by setting all masses to zero, except for the payload mass. Its transfer function shows no isolation plateau, hence the $1/f^2$ slope does not change for higher frequencies. To increase the isolation performance of the IP to about −110 dB, a lighter bell mass can be used. With a mass reduced from 450 g to 100 g the notch disappears and the plateau level lowers.

4.3. Experimental measurements of the CoP effect on the IP

Measurements of the horizontal transfer functions of the AEI-SAS were performed in a horizontal shaker stand. The shaker is a welded construction made of I-profiles with four poles. The whole AEI-SAS is suspended by steel wires from the tips of the four poles, as shown in figure 4.8. The suspended system is displaced by a voice-coil actuator.

Parameter	Value	Description
M_p	494 kg	Payload mass
M_l	0.2 kg	IP leg mass
M_b	0.45 kg	Bell mass
M_cw	variable	Counter weight mass
L_l	0.42 m	IP leg length
L_b	0.2 m	Bell length
κ	2070 Nm	Angular stiffness of the flexure
E	186 GPa	Elasticity (Young's) modulus of Maraging C-250 steel

Table 4.1.: A table of realistic values, which were used to plot the transfer functions of a massive IP in figure 4.7 using equation (4.38a). Most of the values are estimations, chosen to fit the model to measurements, shown in figure 4.9. In the real system the values are either not measurable or the real assembly is more complex than the simplified model.

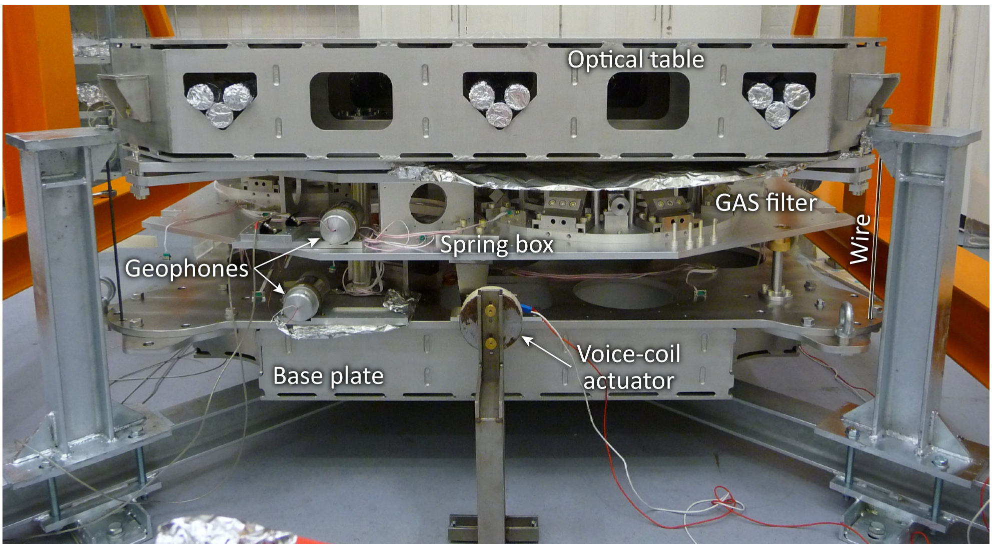

Figure 4.8.: The horizontal shaker is used to measure horizontal transfer functions of the AEI-SAS. The shaker has four poles, manufactured from steel I-profiles, from which the whole AEI-SAS is suspended by four steel wires. A voice-coil actuator provides the force to shake the baseplate horizontally. A transfer function is measured by comparing the baseplate motion to table motion measured by identical horizontal geophones.

During the shaking process, the displacement of the baseplate and displacement of the table top are measured with identical horizontal L-4C geophones. In agreement with equation (4.13), the three-leg IP was tuned to a resonance frequency of 0.1 Hz by adding mass to the spring box. Several excerpts of measured transfer functions are shown in figure 4.9. The full horizontal transfer function is shown and discussed in figure 6.5.
The actual IP transfer function in figure 4.9 is masked by the horizontal spring box modes and by the resonances of the suspension frame. Therefore, the measurement is limited up to 10 Hz. However, an overcompensation notch is always present during the measurements if the bell is attached. The fits in figure 4.9 show computed transfer functions of the AEI-SAS for different CW settings. The curves are produced by plotting equation (4.38a) with values from table 4.1. The natural frequencies measured at 0.1 Hz are considered identical for all CW values. The CW masses in the measurement shift the overcompensation notch position in frequency. The counterweight mass values had to be reduced by a factor of ~ 2 with respect to the real masses, to fit the simplified model to the measurements of the real system.
A theoretical isolation plateau was assessed using equation (4.42). At high frequencies, the plateau level is a constant, β, proportional to the ratio of the corner frequency, f_c, of the overcompensation notch and IP natural frequency, f_n:

$$\beta \approx 20 \log_{10} \left(\frac{f_\mathrm{n}}{f_\mathrm{c}} \right)^2 \qquad \text{for high frequencies.} \tag{4.47}$$

The term $20 \log_{10}$ converts the dimensionless ratio β into units of dB. The measured notch frequencies and their corresponding calculated plateau levels are summarized in table 4.2. The computed isolation plateaus are around $\beta = -60$ dB.

Conclusions

The IP transfer function measurements show that the CW bell was designed too heavy. The bell mass alone (without any CW masses) causes a notch in the transfer function. That means, the bell itself overcompensates the CoP effect. Therefore, the bell mass will be reduced and tested in the third AEI-SAS. With a lighter bell, the overcompensation will disappear. An improvement of the performance to -110 dB is possible. In the first two systems, the bells were installed, but left without CW masses. In principle, they can be detached from the IP leg to avoid overcompensation.
A new shaker stand is designed for the third AEI-SAS. The shaker will be used to measure the vertical and horizontal transfer function of the whole AEI-SAS. As preparation for the assembly of the third table, the IP legs will be tested separately on the new shaker. Lighter CW bells will be manufactured and tested. If the improvement is significant, the CW bells can be retrofitted into the first and second table. For that, the spring box and the optical table can be lifted to insert the new lighter CW bells.

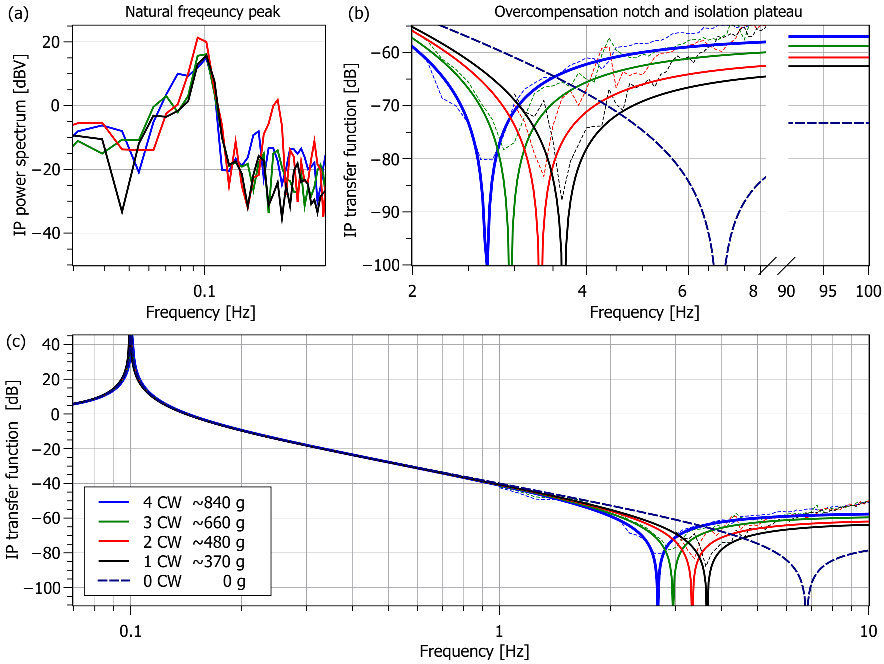

Figure 4.9.: Measurements of the IP performance in the horizontal shaker. All plots show measurements with four different Counter Weight (CW) masses, varying from $370 - 840\,\mathrm{g}$. (a) The power spectra of the IP with different CW configurations show natural frequencies around 0.1 Hz. (b) The transfer functions around the overcompensation notches are a magnification of the lower plot focused on the notches. The dotted lines depict measured values. The solid lines are fitted transfer function. The high frequency fragment shows the constant isolation plateau caused by the CoP effect. (c) The full fitted transfer functions depict the positions of the overcompensation notch with respect to the natural frequency peak at 0.1 Hz. The notch frequency is determined by the length of the bell and its mass, and has no effect on the natural frequency. The fits are computed with equation (4.38a) using realistic values from table 4.1. The counterweight masses shown in plot (c), are the values used to fit the plots. The real CW masses are by a factor of ~ 2 larger than the shown values. The transfer function of a bell without counterweights is indicated as a blue dashed line. Its overcompensation notch is around 7 Hz and the plateau level is around $-70\,\mathrm{dB}$. The notch frequencies and isolation plateau values are summarized in table 4.2.

CW masses	CW mass [kg]	Notch frequency [Hz]	Isolation plateau level [dB]
4	840	2.7	-57
3	660	2.9	-59
2	480	3.4	-61
1	370	3.6	-62.5
0	0	6.7	-73

Table 4.2.: The isolation plateau of the IP is calculated using notch frequency measurements. The values for 0 CW masses are not measured, but calculated. The ratio of the notch frequency, f_c the the natural frequency $f_n = 0.1\,\mathrm{Hz}$ gives the isolation plateau, $\beta \approx f_n^2/f_c^2$, as defined in equation (4.47). The plateau values are sown in figure 4.9b.

5. Vertical isolator: Geometric Anti-Spring (GAS) filter

In the AEI-SAS, three Geometric Anti-Spring (GAS) filters are used as vertical isolators. These filters are composed of eight radially compressed buckled blades, as shown in figure 5.1. The tips of the blades are attached to a keystone, as shown in figure 5.2. The blades are machined from maraging steel sheets, and nickel plated for corrosion protection. They provide the mechanical compliance in vertical and tilt degrees of freedom, as introduced in chapter 2.4 on page 34.

Comparable GAS filters are described in a number of publications. First tests and feasibility studies were presented in [Bertolini1999a, Cella2002, Cella2005] and improvements in [Stochino2007]. After being implemented in Tama300 [Takamori-thesis, Takahashi2008] and tested in HAM-SAS [Sannibale2008, Stochino2009, Boschi-thesis] the GAS filters are now being introduced in the AEI-SAS [Goßler2010, Dahl2012b, Wanner2012], in Advanced Virgo [Accadia2012b] and in KAGRA [Takahashi2012].

The basic theory of the working principle of the GAS filters is given in section 5.1. Just like the inverted pendulums, the GAS filters suffer from the CoP effect. The CoP and its compensators, magic wands, are discussed in section 5.2. Measurements on individual, pre-assembled GAS filters are collected in section 5.3. The section includes measurements of the transfer function, natural frequency, and temperature dependence of the GAS filter's working point. The chapter concludes with a description of the assembly and tuning procedure of the GAS filters in section 5.4.

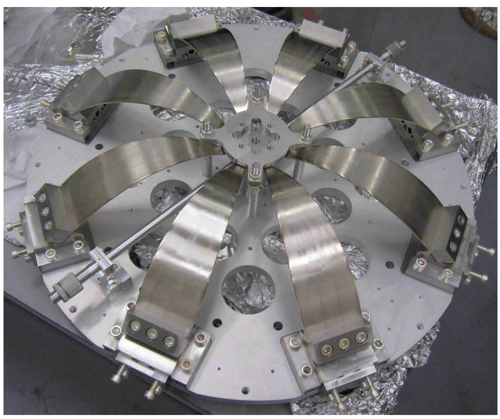

Figure 5.1: A GAS filter is a set of radially compressed blades. An assembled GAS filter with two aluminium Magic Wands is shown. Aluminium was replaced by silicon carbide, as shown in figure 5.6.

Chapter 5

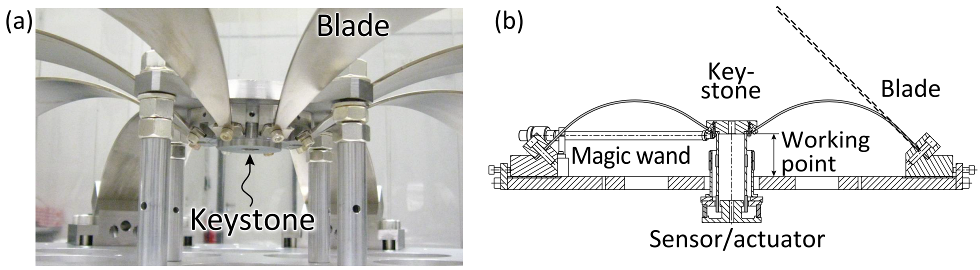

Figure 5.2.: (a) A view inside the GAS filter, between two blades, showing the keystone held in position by a safety plate on four aluminium poles. (b) A sketch of the GAS filter, showing the blades connected to the keystone. The dashed line represents a relaxed blade before being compressed. A sensor/actuator pair, also shown in figure 7.3, is attached to the keystone. The electrical zero-crossing point of the sensor is designed to be at the mechanical working point of the filter. One of two Magic Wands is shown. The Wands are used to compensate the centre of percussion effect, as described in section 5.2.

5.1. Theory of the GAS filters

A GAS filter is a complicated mechanical system of elastic blade springs. To understand the principle behaviour of a GAS filter, the system can be modelled as a simple set of linear auxiliary springs, as shown in figure 5.3. The total force of two opposing blade springs can be split into a vertical and horizontal components. The vertical force is represented by an expanded spring counteracting the weight of the payload. The horizontal component is represented by a pair of contracted lateral springs facing each other. These lateral springs create an additional negative force, if they are deflected from an equilibrium position. However, in the equilibrium position they nullify each other's lateral force and have no effect in vertical direction.

Forces in equilibrium position

In the static equilibrium position the lateral springs cancel their forces, $F_x = 0$, as shown in figure 5.3a. The force of the vertical spring, F_z, counteracts the weight of the suspended mass, F_g. Without an external force, the sum of all forces is zero:

$$F_g + F_z = 0 \quad \Rightarrow \quad Mg + \left(-k_z(l_z^{\mathrm{eq}} - l_z^0)\right) = 0 \tag{5.1}$$

with

M, the payload mass for which the equilibrium position is achieved

g, the gravitational acceleration

k_z, the spring constant of the vertical substitute spring

l_z^{eq}, the length of the deflected spring in equilibrium position

l_z^0, the length of the unloaded spring.

Forces out of equilibrium

If the mass is deflected from the equilibrium position upwards by the distance z, the force of the ancillary spring, F_x, becomes non-zero in Z–direction, as shown in

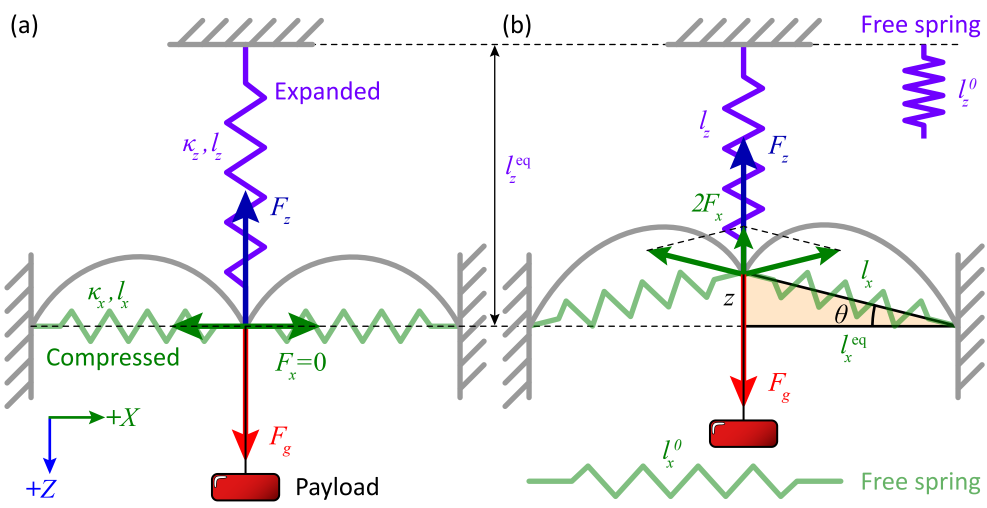

Figure 5.3.: The GAS filter mechanics represented by a simplified model with an expanded vertical and a pair of contracted ancillary springs, (a) in a static equilibrium position, and (b) with the blade contact point displaced by length, z, which creates an additional vertical force, F_x, thereby reducing the effective stiffness of the system around equilibrium.

figure 5.3b. The forces of the vertical spring and the lateral springs add up and point in the direction of the displacement. The lateral springs are working pairwise, thus the vertical force, $2F_x$, shown in figure 5.3b, is the sum of a pair of forces from two opposing springs.
The total force deflecting the vertical spring ($k_z\Delta z$) is caused by three forces: the external acceleration force of the mass ($M\ddot{z}$), the force produced by the lateral springs ($k_x\Delta x \sin\theta$), and the gravitational force acting on the payload (Mg). Thus, the equation of motion becomes:

$$M\ddot{z} + k_x\left(l_x - l_x^0\right)\sin(\theta) + Mg = k_z(l_z - l_z^0)\,, \tag{5.2}$$

with

- l_x^0, the length of the free ancillary spring
- l_x, the length of the compressed ancillary spring
- l_z^0, the length of the free vertical spring
- l_z, the length of the deflected vertical spring
- θ, the angle to which the suspension point of the mass is displaced.

According to figure 5.3, the length l_z of the deflected vertical spring can be expressed by the equilibrium length l_x^{eq} of the spring and the deflection z from the equilibrium position:

$$l_z = l_z^{\mathrm{eq}} - z\,. \tag{5.3}$$

Furthermore, the sine term can be written as:

$$\sin(\theta) = \frac{z}{l_x}\,. \tag{5.4}$$

Thus, with equations (5.3) and (5.4) the equation of motion (5.2) becomes:

$$M\ddot{z} + k_x \left(l_x - l_x^0\right) \frac{z}{l_x} + Mg = k_z(l_z^{\mathrm{eq}} - z - l_z^0)\,. \tag{5.5}$$

Equation 5.1 inserted in 5.5, eliminates static equilibrium forces, yielding only the external forces:

$$M\ddot{z} + k_x \left(1 - \frac{l_x^0}{l_x}\right) z = -k_z z\,. \tag{5.6}$$

Thus, the equation of motion of the GAS filter around its equilibrium point resembles an harmonic oscillator:

$$M\ddot{z} + \underbrace{\left[k_z + k_x - k_x \frac{l_x^0}{l_x}\right]}_{k_{\mathrm{eff}}} z = 0 \tag{5.7}$$

with the effective spring constant,

$$k_{\mathrm{eff}} = k_z + k_x \left(\frac{l_x - l_x^0}{l_x}\right)\,. \tag{5.8}$$

The effective spring constant is smaller than the vertical substitution spring constant, k_z, reduced by the compression factor

$$\frac{l_x - l_x^0}{l_x} \quad \text{when} \quad l_x^0 > l_x\,,$$

which depends on the compression ratio of the lateral springs. The reduction of the spring constant due to the geometric configuration of the ancillary springs is referred to as the Geometric Anti-Spring (GAS) effect. Due to the spring constant reduction, the GAS filter can be tuned so soft, that the $\sim 320\,\mathrm{kg}$ payload can easily be lifted with one finger.

Without the lateral springs, the vertical spring alone would still be able to hold the payload in equilibrium position. However, the force required to deflect the payload vertically from the equilibrium position would be enormous. The lateral springs reduce this force. Thus, the compression rate of the lateral substitution spring can be used to tune the system towards the verge of instability. The system becomes unstable at $\kappa_{\mathrm{eff}} = 0$.

Working point computation

The working point of the GAS filter depends on the compression rate of the blades and the payload mass, here called equilibrium mass, M^{eq}. To see how the system behaves when an additional mass is added, a new mass is defined as $m = M^{\mathrm{eq}} + \delta m$ as a sum of the equilibrium mass, M^{eq}, and a small additional mass, δm. In the equilibrium position, as shown in the simplified model in figure 5.3a, the forces between the vertical spring and the mass are balanced. The equilibrium position of the blades, l_z^{eq}, is given in equation (5.1) as:

$$l_z^{\mathrm{eq}} = \frac{M^{\mathrm{eq}} g}{k_z} + l_z^0\,. \tag{5.9}$$

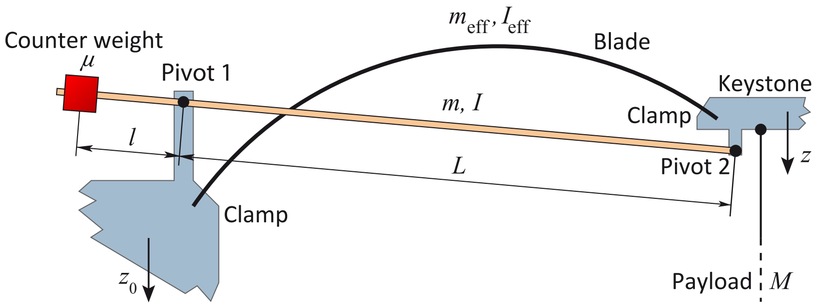

Figure 5.4.: Schematic representation of one GAS filter blade spring with a CoP compensator (*magic wand*). The blade spring is clamped to the GAS filter base plate, the tips of all GAS filter blades are clamped to the keystone. The moment of inertia of the blades produces a transmissibility saturation, attributed to the Centre of Percussion (CoP) effect. Therefore, a compensator is used, to move the CoP of the blade towards its clamping point. The isolation performance of the GAS filter can be improved by tuning the position of the Counter weight mass, μ along the short side of the wand, l. Picture based on [Stochino2007].

Chapter 5

With this equilibrium spring length, l_z^{eq}, inserted in equation 5.5, the equation for a static system (with $m\ddot{z} = 0$) becomes:

$$0 = -mg - k_x \left(1 - \frac{l_x^0}{l_x}\right) z + k_z \left(\frac{M^{\mathrm{eq}} g}{k_z} + l_z^0 - z - l_z^0\right) , \tag{5.10}$$

With the Pythagorean theorem, l_x can be written as $l_x = \sqrt{z^2 + l_x^{\mathrm{eq}\,2}}$, and equation 5.10 becomes:

$$0 = g(-m + M^{\mathrm{eq}}) - k_x \left(1 - \frac{l_x^0}{\sqrt{z^2 + l_x^{\mathrm{eq}\,2}}}\right) z - k_z z \, . \tag{5.11}$$

Hence, the equation can be solved for $\delta m = m - M^{\mathrm{eq}}$:

$$\delta m = \frac{z}{g} \left(\frac{l_x^0}{\sqrt{z^2 + l_x^{\mathrm{eq}\,2}}} - (k_x + k_z)\right) . \tag{5.12}$$

This additional mass, δm, tells, how the equilibrium position, z, changes with respect to small payload mass variations.

5.1.1. Transfer function computation

The isolation performance of the GAS filter is evaluated by comparing the ground motion, z_0, transmitted through the blades to the payload, which is moved by z. Such a transfer function is easily computed, as presented by [Stochino2007], by writing down the Lagrangian of a simplified mechanical model, as shown in figure 5.4. The Lagrangian of the system is defined as the sum of the kinetic energies minus the

Parameter	Value	Description
M	320 kg	Payload mass
m	0.042 kg	Mass of one compensator tube
m_{eff}	0.34 kg	Effective point mass of one blade spring
μ	0.286 kg	Counter weight point mass
L	0.235 m	Distance between pivot 1 and pivot 2, and length of the compensator tube
l_{eff}	0.095 m	Distance from pivot 1 to the effective CoM of the blade
l	variable	Distance from pivot 1 to the CW mass
k_z	505.3 $\frac{N}{m}$	Spring constant of the vertical substitute spring

Table 5.1.: The values of the simple GAS filter model with a CoP compensator, as shown in figure 5.4, are used in equation (5.21) to plot the transfer function in figure 5.9. The effective values are rough estimations chosen to fit the model to the measurements. These auxiliary values are not simple to obtain from the real system.

potential energy:

$$\mathscr{L} = T_M + T_\mu + T_{m_{\text{eff}}} + T^{\text{rot}}_{m_{\text{eff}}} + T_m + T^{\text{rot}}_m - V \tag{5.13}$$

$$\begin{aligned} &= \frac{1}{2}M\dot{z}^2 + \frac{1}{2}\mu\left(\frac{l}{L}\dot{z} - \frac{L+l}{L}\dot{z}_0\right)^2 \\ &+ \frac{1}{2}m_{\text{eff}}\left(\frac{l_{\text{eff}}}{L}\dot{z} + \frac{L-l_{\text{eff}}}{L}\dot{z}_0\right)^2 + \frac{I_{\text{eff}}}{2L^2}(\dot{z}-\dot{z}_0)^2 \\ &+ \frac{1}{2}m\left(\frac{2L-d}{2L}\dot{z} + \frac{d}{2L}\dot{z}_0\right)^2 + \frac{I}{2L^2}(\dot{z}-\dot{z}_0)^2 \\ &- \frac{1}{2}k_z(z-z_0)^2\,, \end{aligned} \tag{5.14}$$

The terms T_M, T_μ, $T_{m_{\text{eff}}}$, T_m are the kinetic energies of the payload mass, M, counter weight mass, μ, effective mass of the blade spring, m_{eff}, and the mass of the magic wand, m. The potential energy, V, is given by the vertical substitute spring with spring constant, k_z. The elastic curved blade is substituted by a linear vertical spring with a spring constant, k_z, as shown in figure 5.3. In this model, the distributed mass of the blade is simplified to an effective rigid body with a mass, m_{eff}. The blade's moment of inertia, $I_{\text{eff}} = m_{\text{eff}} l_{\text{eff}}^2$, is a function of m_{eff} with the centre of mass at distance, l_{eff}, from pivot 1. The CoP compensator, or magic wand, is modelled as a thin tube with length $d = L + l$ divided by pivot 1 into a long tube with the length, L, and a short adjustable distance, l, to the counter weight. Thus, the moment of inertia of the long compensator tube fixed at pivot 1 is given as $I = mL^2/12$. The values of the model are summarized in table 5.1.
The equation of motion is obtained by solving the Euler-Lagrange equation defined as:

$$\frac{\mathrm{d}}{\mathrm{d}t}\left(\frac{\partial\mathscr{L}}{\partial\dot{z}}\right) - \frac{\partial\mathscr{L}}{\partial z} = 0\,. \tag{5.15}$$

Thus the equation of motion of the payload mass driven by ground motion is given analogously to the equation of motion of the IP in equation (4.33) as:

$$\ddot{z}B + \ddot{z}_0 C = -(z - z_0)A\,, \tag{5.16}$$

with

$$A = k_z \tag{5.17}$$

$$B = M + \mu\frac{l^2}{L^2} + m_{\text{eff}}\frac{l_{\text{eff}}^2}{L^2} + \frac{I_{\text{eff}}}{L^2} + m\left(\frac{2L-d}{2L}\right)^2 + \frac{I}{L^2} \tag{5.18}$$

$$C = -\mu\frac{(L+l)l}{L^2} + m_{\text{eff}}\frac{(L-l_{\text{eff}})l_{\text{eff}}}{L^2} - \frac{I_{\text{eff}}}{L^2} + \frac{md(2L-d)}{4L^2} - \frac{I}{L^2}\,. \tag{5.19}$$

Analogue to the equation of motion (4.37) of the IP, the equation of motion (5.16) of the GAS filter with CoP compensator is written in the frequency domain as:

$$\omega^2\tilde{z}B + \omega^2\tilde{z}_0 C = (\tilde{z} - \tilde{z}_0)A\,, \tag{5.20}$$

with $\tilde{z}$ and $\tilde{z}_0$ the Fourier transform of z and z_0, respectively. The transfer function of the GAS filter with a CoP compensator is then given as:

$$\frac{\tilde{z}}{\tilde{z}_0} = \frac{A + C\omega^2}{A - B\omega^2} \tag{5.21}$$

The natural frequency of the payload is found by setting $\tilde{z}_0 = 0$. Thus, without ground motion the natural frequency of the payload oscillation, including all additional masses of the system is given by:

$$\omega_{\text{n}} = \sqrt{\frac{A}{B}}\,, \tag{5.22}$$

identical to the natural frequency of the IP in equation (4.25). With this natural frequency, the transfer function can be written as:

$$\frac{\tilde{z}}{\tilde{z}_0} = \frac{\omega_{\text{n}}^2 + \beta\omega^2}{\omega_{\text{n}}^2 - \omega^2}\,, \tag{5.23}$$

with

$$\beta = \frac{C}{B}\,, \tag{5.24}$$

identical to the IP in equation 4.39. Again, β is the value responsible for the plateau in the transfer function. The CoP compensator can be used to tune β towards zero, by varying the position, l, of the counter weight mass, μ. For $\beta < 0$ the CoP effect is overcompensated, thus a notch appears in the transfer function at a corner frequency, above which the isolation plateau starts. For $\beta > 0$, the system is undercompensated, thus an isolation plateau is visible. For $\beta \to 0$ the transfer function of the GAS filter is similar to the transfer function of the harmonic oscillator. The goal of the mechanical GAS filter tuning is to reduce β towards zero.

A computed transfer function of a GAS filter with CoP compensator is shown in figure 5.5 with varying counter weight positions. The blade mass is multiplied by

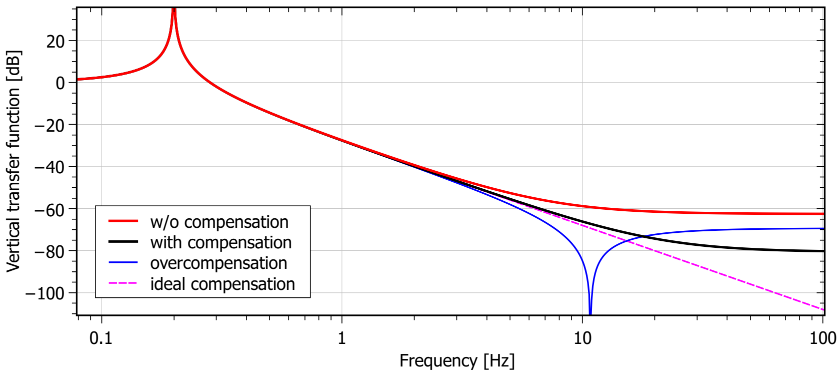

Figure 5.5.: A computed vertical transfer functions of a single GAS filter, plotted using equation (5.23) and values from table 5.1 for different compensation factors. The GAS filter's transfer function is identical to the transfer function of an IP, as shown in figure 4.7. Both transfer functions feature an isolation plateau caused by the CoP effect. The CoP is compensated by counter weights. Inaccurate tuning can over-compensate or under-compensate the CoP effect. Overcompensation causes a notch in the transfer function, above which the isolation plateau starts. Undercompensation (not shown) causes a plateau without a notch; however, the plateau level is higher than the plateau without compensation.

the number of the blade springs (eight). The two compensators are accounted for, by taking two times the compensator tube mass and the counter weight mass. The transfer functions show a single GAS filter in different configurations:

red without compensation. This was plotted, by setting all compensator masses to zero. The computed isolation plateau level (around -65 dB) is comparable to the measurement in figure 5.7, showing the performance of a single GAS filter without compensators.

black with compensation – with the distance from the pivot 1 to the CW set to $l = 6.5\,\mathrm{cm}$. See the measurement in figure 5.7.

blue overcompensated – at $l = 10\,\mathrm{cm}$. An overcompensation notch is located around 10 Hz.

magenta ideal compensation – resembling an ideal harmonic oscillator. Produced, by setting $\beta = C/B = 0$ to simulate ideal compensation.

The equation describing the GAS filter's transfer function contains auxiliary values (m_{eff} and l_{eff}), which are not directly measurable in the real system. These values make the computed transfer function hard to directly compare to measurements of the real mechanical system. However, one can clearly see from the equations and in the plots, that the GAS filter transfer function is identical to the transfer function of an IP (see figure 4.7). Both feature an isolation plateau which can be lowered by varying the position or the mass of the counter weights.

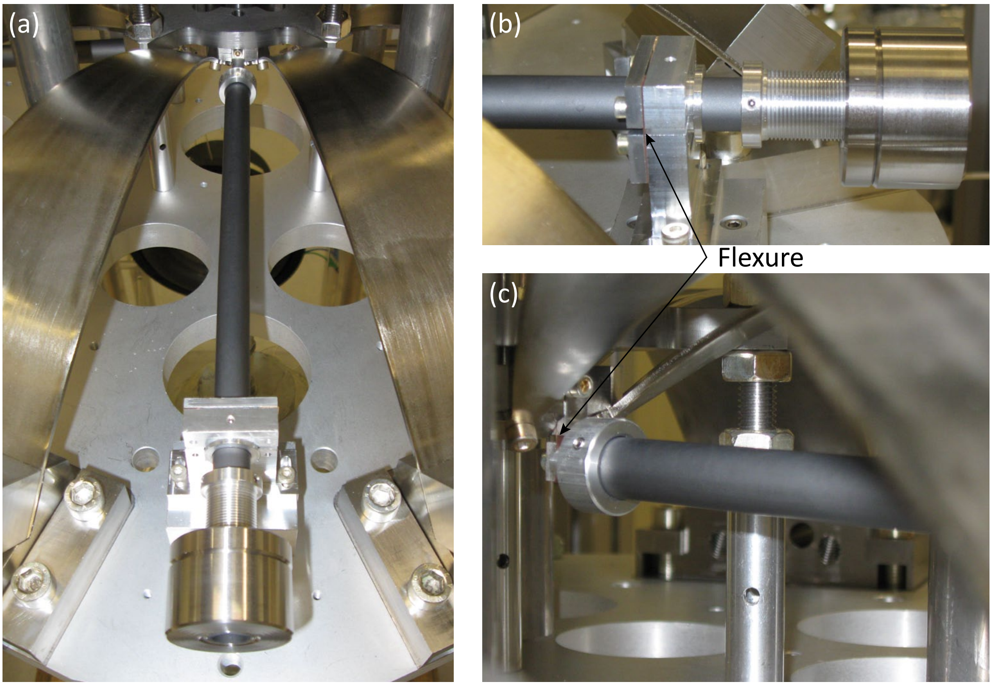

Figure 5.6.: (a) The compensator of the Centre of Percussion (CoP) effect, the Magic Wand, is a silicon carbide tube. (b) The counter weight mass is movable along the thread, thereby tuning the CoP effect. The compensator flexes about the pivot point defined by two beryllium cobalt flexures. (c) A flexure connects the tip of the compensator to the keystone.

5.2. Centre of Percussion (CoP) compensator: magic wand

According to equation 5.21, and confirmed by measurements, the inertia of the GAS filter's blade springs limits the vibration isolation power to around −60 dB. An isolation plateau appears in the transfer function of a GAS filter, as shown in figure 5.13. This limiting effect is again the Centre of Percussion (CoP) effect. The same effect limits the performance of the IP legs, as described in chapter 4.2. The isolation performance of the GAS filter can be improved up to −80 dB by using add-on compensators, the so-called *magic wands* [Stochino2007]. The compensators used at the AEI-SAS are made of Silicon Carbide (SiC), illustrated in figure 5.6. As illustrated in figure 5.4, a counter weight at the end of the compensator is used to shift the CoP right on top of the effective pivot of the blades. To achieve maximum rigidity and minimum weight, SiC proved to be a better material than aluminium, pushing the natural frequency of the wand assembly above 300 Hz.
The compensating effect of the magic wands was tested on filters with higher natural frequencies than the final GAS filters, that were installed into the AEI-SAS. At higher frequency, the filters were less prone to hysteresis effects and had a larger Q, which simplified the measurements of oscillation frequencies. After the tests, the filters were

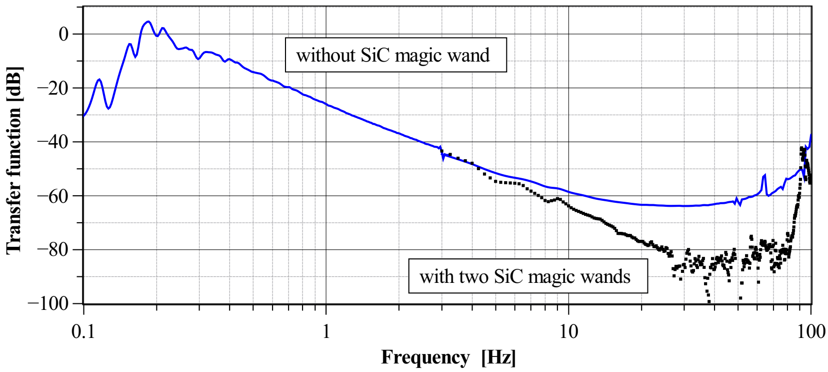

Figure 5.7.: The performance of one single GAS filter tuned to 200 mHz. The plot compares the performance with and without SiC magic wands measured in a vertical shaker test-stand. Above 30 Hz the displacement transmitted through the GAS filter is below the resolution of the sensor, masking the true transfer function. The increase in the transfer function at high frequencies is attributed to the flank of a group of resonances above 300 Hz produced by GAS filter blades. These resonances can be damped with eddy current dampers.

tuned to natural frequencies below 200 mHz and installed into the AEI-SAS.
The tuning of the CoP compensators is shown in figure 5.7. The figure illustrates measurements of the transfer function of one single GAS filter, which was tuned to a resonance frequency around 200 mHz. The two different measurements are depicting the isolation performance of a filter without and with built in CoP compensators. The measurement with the compensator shows an improvement of the isolation performance of almost 20 dB, a factor of 10. The maximum displacement transmissibility below −80 dB corresponds to a vertical ground noise reduction of a factor of 10000 above 23 Hz. The measurement is limited by sensor noise above 23 Hz. The sensor noise also reduces the coherence of the measurement signals, as shown in figure 5.8.
The coherence in figure 5.8 is not existent above 20 Hz, which indicates, that the signals are noise dominated and the shown transfer function in this frequency range is not real. Additionally, the figure illustrates in a swept sine measurement, that the CoP compensators of this particular GAS filter are slightly overcompensated. In the swept sine measurement, every measurement point is sinusoidally excited at the corresponding frequency.
The compensators are tuned by comparing the transmissibilities in the frequency region of maximum isolation and changing the position of the counter weight. The equation (5.21), describing the compensation of the performance by the counter weights, predicts a notch, at the corner frequency, at which the CoP is overcompensated. The same equation gives an estimation of the isolation plateau, formed by the CoP effect. Since the measurements were masked by noise at the frequency of interest, the filters were tuned by looking for the overcompensation notch. Figures 5.9 and 5.10 illustrate the procedure, of finding the optimal setting for the CoP tuning of the GAS filters.
Figure 5.9 shows transfer functions for different settings of the counterweight position measured with random noise excitations. The region of interest above 40 Hz, where the theoretical isolation plateau should be lowered by CoP compensation, is masked by sensor noise. However, the overcompensation notch is clearly visible. Thus the value

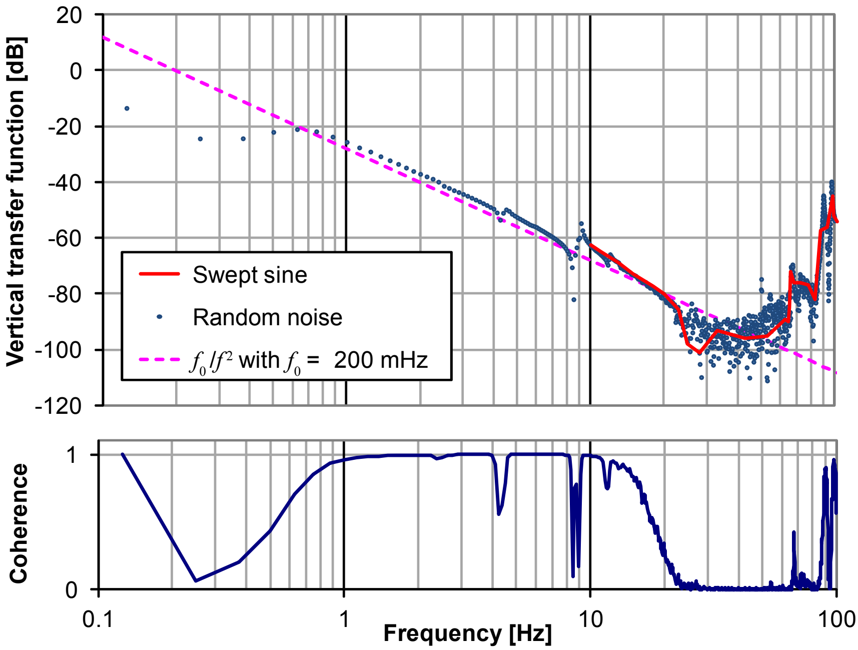

Figure 5.8.: Transfer function and coherence a CoP compensated GAS filter tuned to a natural frequency of 200 mHz. The transmissibility above 20 Hz is limited to below −80 dB due to sensor noise. The transfer function was measured by applying a random noise signal to the actuator. The coherence around 20 Hz drops to zero, which also indicates that the signal is noise dominated. An additional swept sine measurement was used to resolve the plateau in the transfer function. The swept sine measurement shows a small notch between 20 − 30 Hz, which might indicate, that this filter was slightly overcompensated by the magic wands. The peaks above 60 Hz are attributed to resonances in the shaker structure as they are visible in all GAS filter measurements. The pink dashed line illustrates the f^{-2} slope starting from 200 mHz.

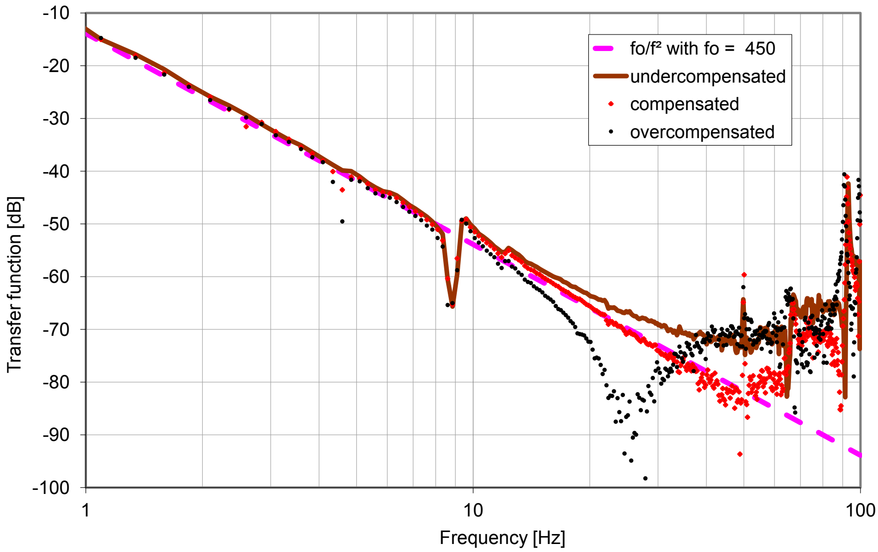

Figure 5.9.: GAS filter transfer function, measured with random noise excitation. Overcompensation is visible best if compared to the f^{-2} slope (pink dashed line).

with the least overcompensation (red line) was chosen to set the counterweights of the CoP compensators.
Figure 5.10 shows an additional illustration of the transfer function, measured with the swept sine method. The measurements were done by shifting the counter weights of the compensators in 1 mm steps. Only few curves are plotted for clarity. The overcompensation (blue shades) and undercompensation (red/brown) are clearly visible, if compared to the f^{-2} slope indicated by the pink dashed line. Counterweight position at 0 mm (black line) appears to be optimal for this particular filter.

5.3. Measurements regarding GAS filters

5.3.1. Resonance frequency and working point

The GAS filters are pre-assembled and tuned on a vertical shaker test stand, shown in figure 5.11. One filter at once can be suspended in the shaker from commercial garage springs. The shaker is a cage made of aluminium profiles. A set of ballasts of around 320 kg is suspended from the keystone, simulating the weight of the optical bench. From the weight of the payload, the garage springs elongate and allow a free oscillation of the GAS filter base plate at a natural frequency of around 6 Hz. The base plate is driven vertically by a commercial 2500 W sub-woofer; its membrane was partly removed and the coil was rigidly connected to the GAS filter base plate.
The working point of GAS filters, measured between the lower surface of the keystone and the upper surface of the GAS filter plate, is designed to be around 8.5 mm. This working point position is measured with a ruler and set in each pre-assembled GAS filter by tuning the blade compression. The natural frequency is measured by letting

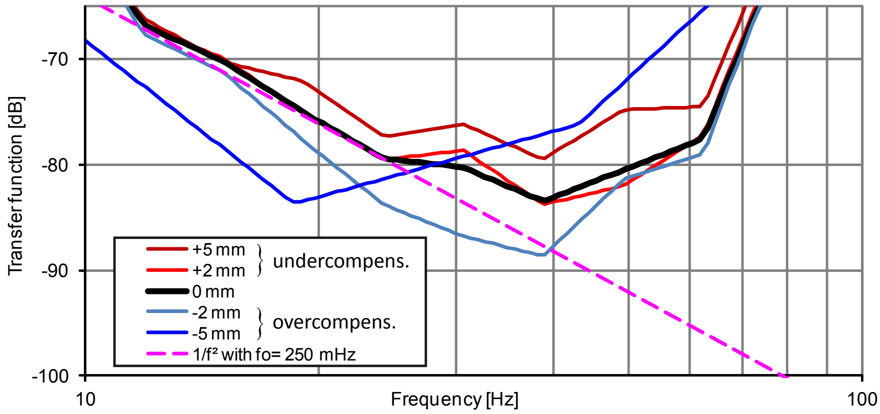

Figure 5.10.: Swept sine measurement of GAS filter transfer functions in a narrow frequency range. Different counter weight positions along the CoP compensator change the height of the isolation performance above 20 Hz. The counter weight position 0 mm (black) is chosen for this filter, because no sign of overcompensation is visible.

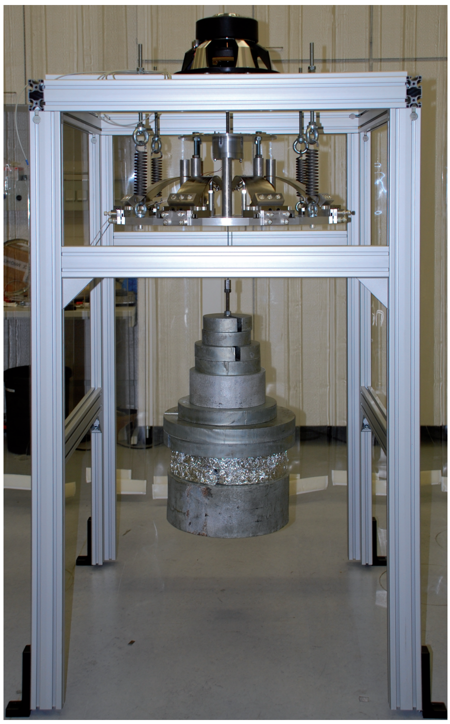

Figure 5.11: Vertical shaker, used for tuning and performance testing of the GAS filters. The GAS filter is suspended from four commercial garage springs. A sub-woofer is bolted to the aluminium frame; its membrane is connected to the GAS filter base plate. The loudspeaker drives the base plate of the GAS filter at different frequencies. The amplitude is measured by a geophone on the plate. Ballast weights of about 320 kg are connected via a wire to the keystone, simulate the weight of the table, which rests on the three filters in the AEI-SAS. The residual motion transferred through the filter to the ballast is measured by an identical geophone, placed underneath the ballast. The comparison of the two geophone signals represents the transfer function of the GAS filter.

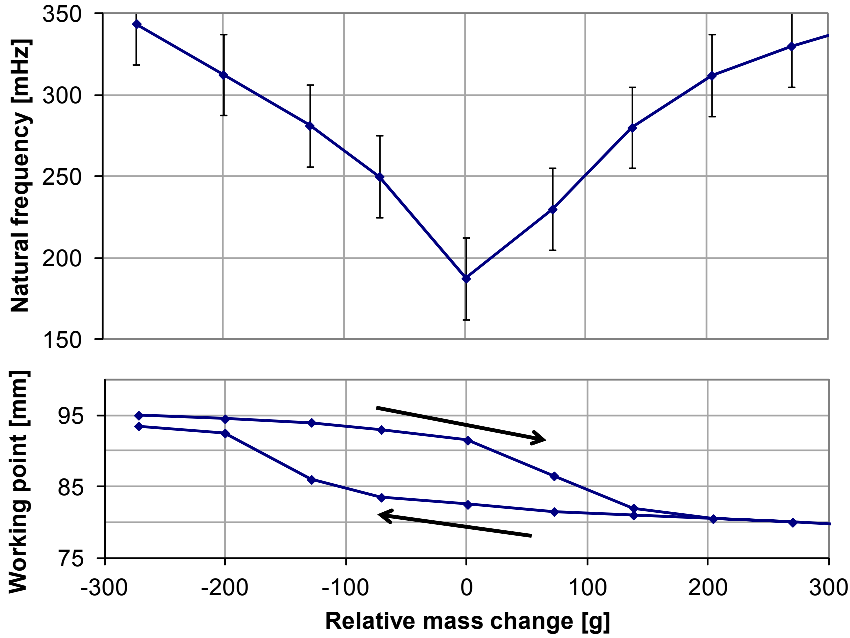

Figure 5.12.: Sensitivity of GAS filter to payload variations. A GAS filter was tuned to its lowest natural frequency (around 200 mHz) by compressing the blade springs. Due to low Q of the oscillation at low frequency, the natural frequency was only measurable with an accuracy of 25 mHz. At the minimum natural frequency, a mass deviation of ± 200 g results in an increase of the natural frequency by about 100 mHz. This payload variation corresponds also to a working point height change of $5 - 10$ mm. The working point height measurement shows a clearly visible hysteresis of the GAS filters. At the minimum natural frequency, the key stone displacement hysteresis is at maximum ± 5 mm, at a read-out accuracy of 0.5 mm. All filters were tuned to the lower hysteresis curve, where the working point is closer to the calculated optimum of 8.5 mm. Further away from the working point, the displacement hysteresis disappears.

the payload oscillate and measuring the average period over several oscillations. A vertical geophone measures the movement of the payload. The geophone signal is picked up with an oscilloscope, and the oscillation maxima are read out from the screen.
Figure 5.12 illustrates how the working point changes, when the mass of the payload is changed. A mass change of 200 g results in a change of the natural frequency of around 100 mHz. The same mass change corresponds to a position change of about $5 - 10$ mm. All GAS filters were tuned to ≈ 200 mHz, which was easily achievable. Below that, the hysteresis dramatically increased and faded into filter bi-stability. The key stone displacement hysteresis of ± 3 mm is maximal at minimum natural frequency. Above and below the minimum natural frequency, the working point hysteresis disappears. Furthermore, the quality factor of the oscillation drops dramatically at very low natural frequencies. The low Q makes is hard to measure the period of the system.

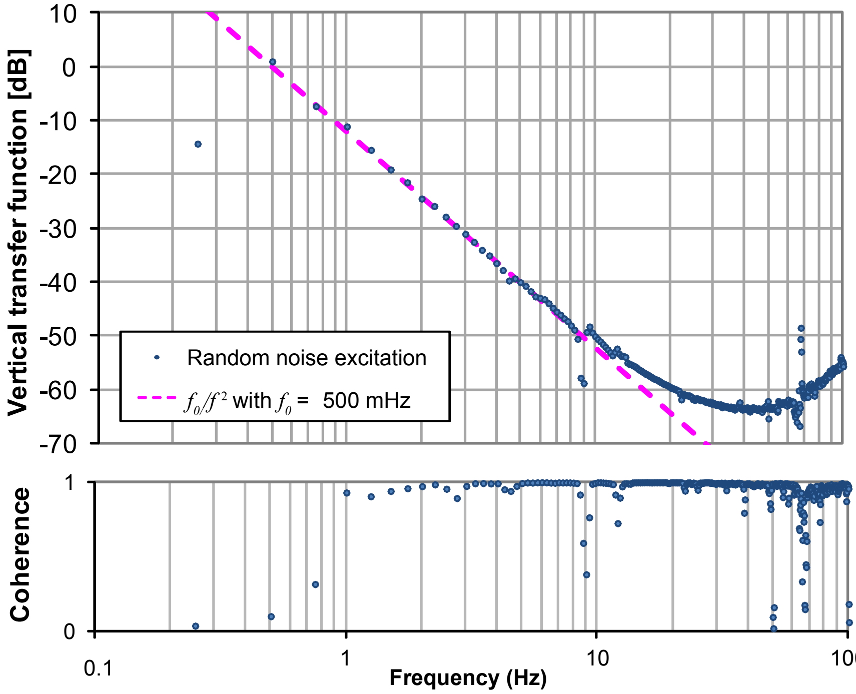

Figure 5.13.: Transfer function and coherence of one single GAS filter tuned to a natural frequency of 500 mHz without CoP effect compensation. The coherence decreases below one hertz due to poor measurement resolution at low frequency. Elsewhere, the coherence is good. The pink dashed line indicates the f^{-2} slope of the transfer function. Due to inertia of the blades, causing the Centre of Percussion (CoF) effect, the isolation performance saturates above 10 Hz. For testing purposes, this measurement was done at 500 mHz natural frequency. In the final configuration, the natural frequency of the GAS filters was tuned further below 200 mHz.

5.3.2. Transfer function

A measurement of the vertical transfer function of a single GAS filter, as shown in figure 5.13, indicates, that the transmissibility of the filter features a saturation plateau, analogously to inverted pendulums. Above a certain corner frequency, the transfer function becomes constant for high frequencies. The isolation plateau is formed due to the Centre of Percussion (CoP) effect, which is caused by the moment of inertia of the blade spring body.

5.4. GAS filter assembly

The GAS filters are pre-assembled individually. Their blade springs are bent into working position and installed pairwise facing each other. The tips of the blades are bolted to a keystone. This way, the blade pairs remain bent and keep each other from snapping back. Each blade is bent by means of a bending tool, as shown in figure 5.14. The tool forces the blade to stay at a curvature with a radius of 199.6 mm. This way, a

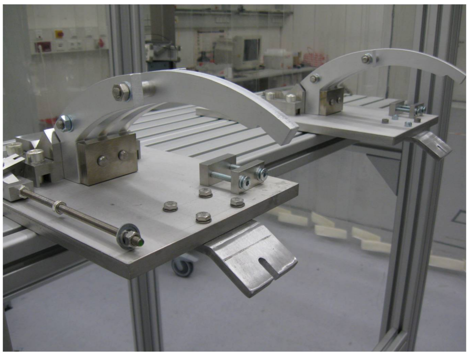

(a) Two equal bending tools are used in parallel, to bend two blades, which are installed in the GAs filter opposing each other.

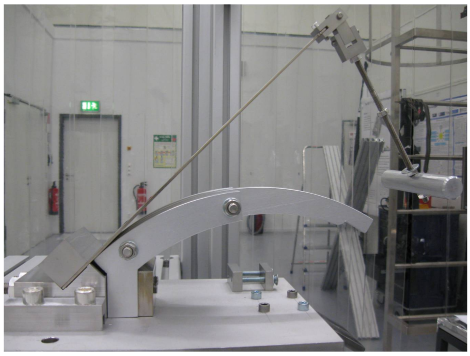

(b) A bending tool, with a flat flexure bolted to the tool. At the tip of the flexure, a pivoting device is bolted, to which again a threaded rod and a handle are bolted.

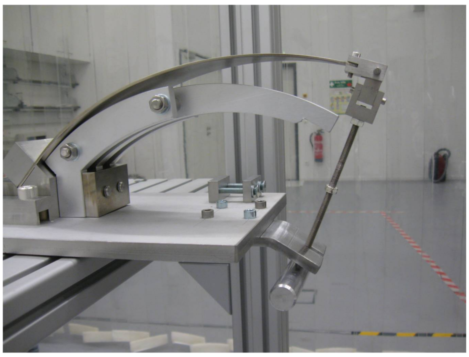

(c) The blade spring is bent by manually pushing down the handle, until the hanle can be secured by a hook.

(d) At the end, the blade tip is clamped to the bending tool, this way both can be transported together. After the blade is bolted to the GAS filter plate and its tip is attached to the keystone, the tool can be removed.

Figure 5.14.: The assembling procedure of the geometric anti-spring (GAS) filter. During the assembly the keystone is held in place by a threaded rod, otherwise the blades would escape upwards. The rod is replaced by a safety structure, after all blades are installed, see figure 5.1a.

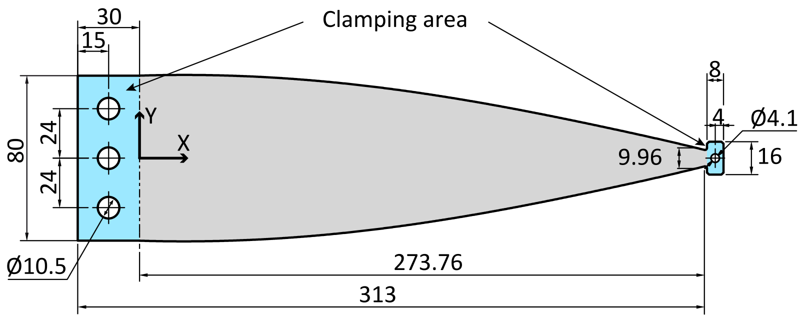

Blade length X [mm]	Blade width Y [mm]
0.00	40
27.26	40.31
54.52	39.58
81.78	37.84
109.04	35.13
136.30	31.53
163.56	27.15
190.82	22.12
218.08	16.57
245.34	10.67

Figure 5.15.: The shape of a GAS filter blade spring is computed in a finite element calculation to provide a uniform stress distribution when the blade is buckled. The blue areas are clamped, the rest of the blade is free to bend. The profile of the free (grey) part of the blade is machined the coordinates given in the table. The blade thickness is 2.30 mm.

bent blade has almost its final shape, so that only little additional lateral compression is required to tune the GAS filter.

The outline of a blade spring is shown in figure 5.15. The blades are profiled to provide a uniform stress distribution along the buckled blade body [Cella2005, Cella2002, Takamori-thesis]. The blades are cut out from a sheet of commercial maraging steel, the same material as used for the IP flexures. The surface of the blades is nickel-plated for corrosion protection. The material is precipitation hardened (baked at 425°C for 100 hours in argon atmosphere) to increase the yield strength of the material.

When a GAS filter is assembled, a payload is suspended from the keystone to tune the filter's natural frequency, as described in the subsequent section. Three pre-assembled and tuned GAS filters are then installed into the AEI-SAS to support the optical table. In the AEI-SAS, the scientific payload is complemented by a set of ballast weights. These ballast rods are installed inside the optical table to achieve the required weight. Every piece of equipment placed on top of the table has to be weighed and the same amount of ballast removed to retain the same load in the system. The overall payload budget of each AEI-SAS is about 220 kg.

GAS filter tuning

Each pre-assembled GAS filter is tuned individually to minimise its natural frequency. The tuning process is a series of repeating steps of measuring the natural frequency and changing the compression of the blade springs. The compression of two opposing buckled blades is performed stepwise, by turning the tuning bolts at the clamp of each blade pair. The bolts are turned with a hex key (with 6 edges) by 1/6 of a full rotation. Then the natural frequency is measured and the tuning process starts over until the desired natural frequency is achieved.
The natural frequency, and with it the corresponding effective spring constant of the GAS filter, is only tuned by mechanical adjustment of the blade compression. The payload of about 320 kg remains constant. Natural frequencies of a few tenths of a hertz can easily be obtained this way. Lower frequencies can be achieved by applying positive feedback [Mantovani2005], but was not tested at the AEI-SAS yet.
Each GAS filter is tuned separately to achieve a natural frequency around 200 mHz at a nominal load of about 320 kg: the nominal load is one third of the total payload on the three GAS filters. The payload, as shown in table 3.1, consists of the optical table with payload ballast rods, vertical geophones in cans, and additional tuning mass of about 50 kg. Thus the nominal mass for each GAS filter is about 970/3 kg $\approx$ 320 kg.
The natural frequency, f_n, of GAS filters can be approximated just like for harmonic oscillators as shown in chapter 2.3:

$$f_\mathrm{n} = \frac{1}{2\pi}\sqrt{\frac{\kappa}{m}} \tag{2.1a}$$

with the vertical spring constant, κ, and the payload mass, m. By adjusting the compression rate of the blades, a GAS filter reaches its nominal spring constant of about $\kappa \approx 400\,\mathrm{N/m}$ at a natural frequency of $f_\mathrm{n} \approx 180\,\mathrm{mHz}$. At this tuning, for small displacements, the GAS filter behaves like a harmonic oscillator. Hence, according to:

$$\kappa = \frac{mg}{x}\,, \tag{2.4a}$$

the height changes by $x \approx 2\,\mathrm{mm}$ for a payload change of $m \approx 110\,\mathrm{g}$. The maximum vertical displacement range is limited by end-stops at $\pm 5\,\mathrm{mm}$. Because the GAS filter is a non-linear device, its stiffness increases substantially when the keystone deviates from the working point. The designed working point of 85 mm between the keystone's lower surface and the GAS filter plate's upper surface is used as a zero point setting for the vertical displacement sensor (LVDT). Each GAS filter incorporates one LVDT co-located with a voice-coil actuator below the keystone for position monitoring and feedback in vertical degree of freedom.

6. AEI-SAS performance

The previous chapters discussed measurements of single components of the AEI-SAS. In this chapter, the performance of the fully assembled system is reviewed.

- The temperature dependence of the position of the AEI-SAS (in particular of the GAS filters and the IP flexures) is shown in section 6.1.
- To identify the modes of the system, the vertical degree of freedom of the AEI-SAS was excited by internal actuators. The response of the system to the actuator force was measured on top of the optical table. This vertical force-to-motion transfer function is described in section 6.2.
- Inertial transfer function measurements reproduce the true mechanical isolation performance of the system.
  - The horizontal transfer function was measured in the shaker stand using identical geophones on the optical table and on the base plate. The base plate was shaken horizontally by a voice-coil actuator.
  - The vertical inertial transfer function of the AEI-SAS was measured in the vacuum system (in air) with identical geophones on the optical table and on the ground. In this measurement, the actuation came directly from the ground.

  Both measurements are presented in section 6.3.

The performance evaluation process is still ongoing. The measurements presented in this chapter, show solely mechanical responses of the system. First successful tests of active modal damping are shown in chapter 7.

Chapter 6

6.1. Temperature dependence

The temperature dependence of the AEI-SAS was tested in a long-term measurement of the central table. The figure 6.1 illustrates how temperature variations affect the position of the optical table. Over the duration of 4.5 days, the vertical and horizontal degrees of freedom of the AEI-SAS were monitored in vacuum, together with the air temperature measured outside of the vacuum system. The temperature is transferred to the in-vacuum mechanics through the legs of the vacuum tank, to which the AEI-SAS base plate is bolted. The displacement caused by temperature variations was measured with horizontal and vertical LVDTs. Three of these displacement sensors are connected to the GAS filter keystone, measuring its vertical displacement relative to the spring box. Three horizontal sensors measure the motion of the spring box relative to the baseplate. The sensor signals were transformed by means of a simple geometric coordinate transformation into coordinates parallel to the L-shape of the

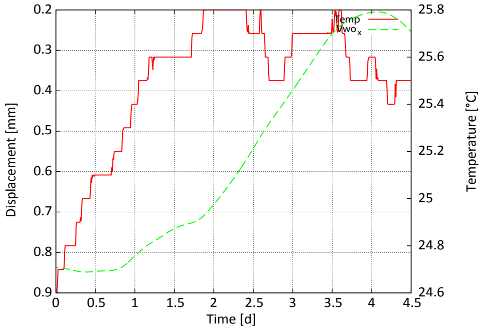

(a) Vertical displacement: 0.65 mm

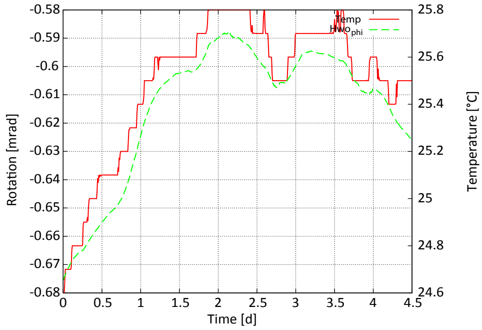

(b) Yaw around z-axis: 0.09 mrad

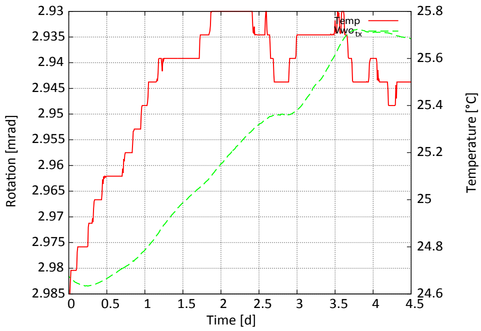

(c) Roll around x-axis: 0.05 mrad

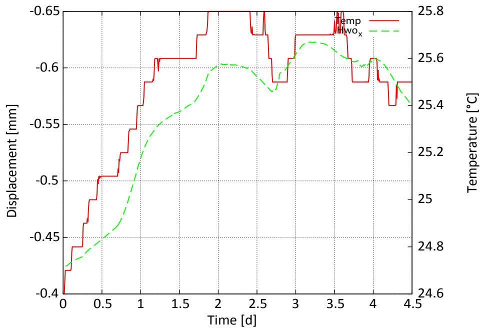

(d) Horizontal displacement in x-axis: 0.2 mm

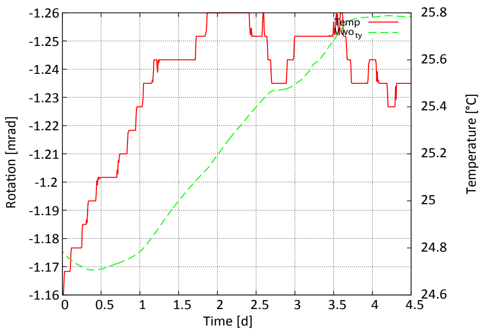

(e) Pitch around y-axis: 0.09 mrad

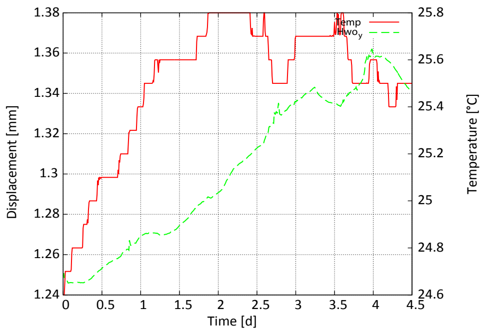

(f) Horizontal displacement in y-axis: 0.12 mm

Figure 6.1.: Correlation between the in-vacuum displacement of the optical table and the temperature (no cables were attached to the optical table). Over the 4.5 days the temperature changed by a maximum of 1.2 K. The left column shows the vertical degrees of freedom, and the right column shows the horizontal degrees of freedom. Please note, that some vertical axes of the plots are flipped, to match the the direction of the temperature trend. The GAS filters show a vertical temperature induced displacement of about -0.5 mm/K. The maximum thermal tilt of the optical table is about 0.04–0.08 mrad/K. With 0.5 m from table centre to the sensor, the tilt corresponds to a differential vertical filter motion of 20–40 µm. The IP flexures show a horizontal temperature induced displacement of about $100 - 170$ µmm/K in x and y directions. Rotation (Yaw) about the vertical axis is roughly 0.08 mrad/K. The rotation corresponds to a horizontal IP-top motion of about 40 µm.

vacuum system. The transformation matrices are shown in chapter D.
The measurements show, that an increase of the temperature by 1.2 K was measured during the 4.5 days of the test period. This caused the combined vertical position of all three GAS filters to lower by 0.5 mm/K. Tilting about x and y axes was in the order of 0.04 mrad/K and 0.08 mrad/K, respectively. The tilting looks dramatic in the plot. However, the relative displacement between the filters corresponds to vertical deviations of only 20–40 µm/K.
The IP flexures are sensitive to thermal drift as well. The optical table moves horizontally by 100 µm/K. The rotation about the vertical z-axis is about 80 µrad/K, which corresponds to a horizontal motion of the table's outer edge of about 80 µm/K.

Temperature dependence with cables

The same test was repeated with 60 stiff ribbon cables suspended in vacuum from cantilevers and clamped to the optical table, as shown in figure 6.3. The number of cables in this test is the same number as will be used for the SPI (see chapter 3.1) on the central table. The test was done to clarify, if the cables introduce additional torque to the optical table due to thermal expansion of the cables. However, due to little temperature difference (maximum 1.6 K), the test was inconclusive. The results are shown in figure 6.2.

Conclusions

The results are summarized in table 6.1. The conclusion of the tests is, that thermal drift in the central AEI-SAS does not significantly increase with the cables. Furthermore, after the installation of the cables, that introduce static forces and torques, no attention was paid to the vertical reposition the optical table to the nominal working point. The thermal sensitivity, in particular of the pitch and roll modes, is dictated by the relative mistuning of the natural frequencies of the three GAS filters. Thus, due to the small temperature differences (1.2 K and 1.6 K), the results provide only lower limits for the thermal sensitivity.

The thermal drift of the GAS filters is driven by the thermo-elasticity of the maraging steel blade springs. According to literature [Cella2005, Braccini2000], the vertical displacement from the equilibrium position depends on the mechanical and thermodynamical parameters of the blade spring material. That means, that the Young's modulus and the thermal expansion coefficient change with the temperature. The effective thermal expansion coefficient for the working point position is given as

$$\alpha_G = 2\alpha_L + \alpha_E \,, \tag{6.1}$$

with

$\alpha_L = 10\,\mathrm{ppm/K}$, the linear thermal expansion factor of the blade, and

$\alpha_E = -254\,\mathrm{ppm/K}$ the thermoelastic coefficient of maraging steel.

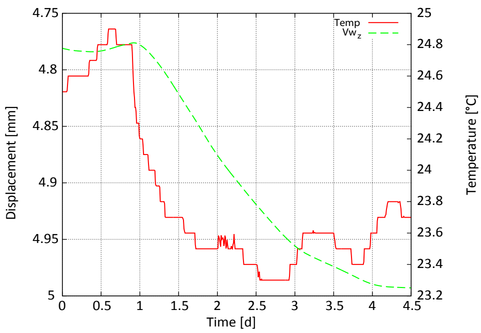

(a) Vertical displacement: 0.2 mm

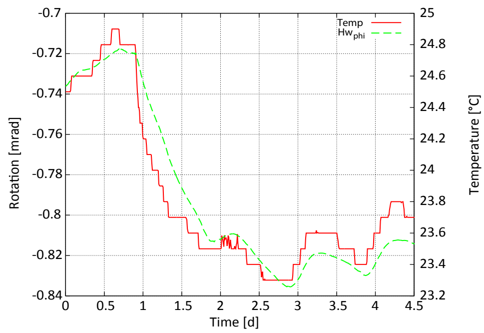

(b) Yaw about z-axis: 0.12 mrad

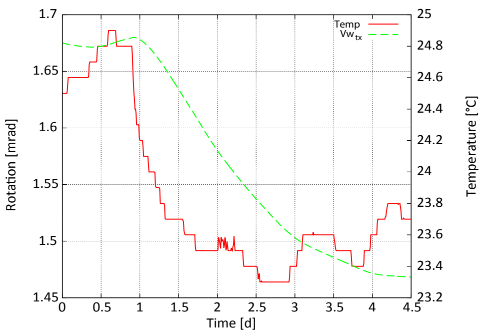

(c) Roll qbout x-axis: 0.2 mrad

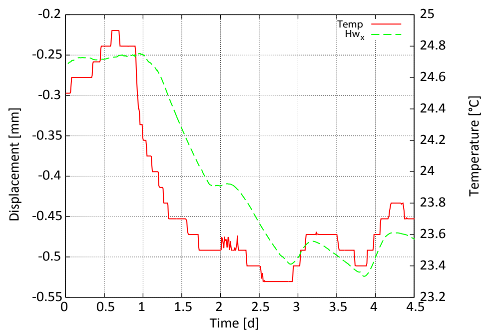

(d) Horizontal displacement in x-axis: 0.25 mm

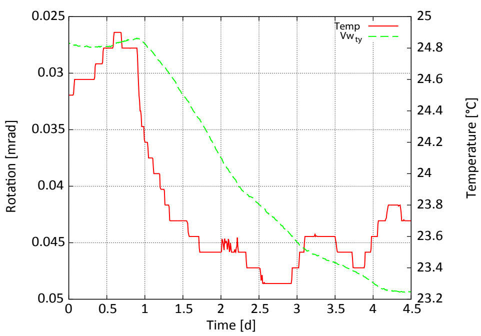

(e) Pitch about y-axis: 0.025 mrad

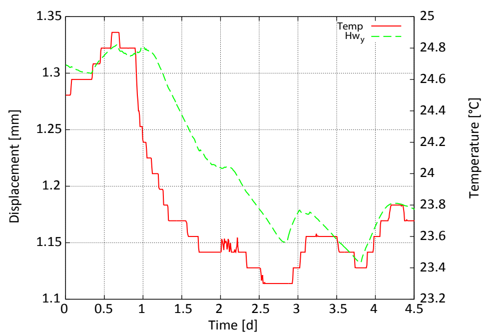

(f) Horizontal displacement in y-axis: 0.2 mm

Figure 6.2.: Correlation between the in-vacuum displacement of the optical table and the temperature. Here, 60 rigid in-vacuum cables representing the SPI wiring were clamped to the surface of the optical table. Over the 4.5 days the temperature changed by a maximum of 1.6 K. The left column shows the vertical degrees of freedom, caused by displacement of the GAS filters. The right column shows the horizontal degrees of freedom caused by IP flexures. Please note, that some vertical axes of the plots are flipped, to match the the direction of the temperature trend. The GAS filters show a vertical temperature induced displacement of about 0.1 mm/K. The maximum vertical thermal tilt of the optical table is about 0.1 mrad/K. The tilting corresponds to a vertical filter motion of 70 µm. The IP flexures cause a horizontal temperature induced displacement of about $0.16 - 0.13$ mm/K in x and y directions. Rotation (Yaw about the vertical axis) is about 0.08 mrad/K corresponding to horizontal IP-top motion of about 40 µm.

Thus, the working point position changes by the factor $\alpha_G = -234\,\mathrm{ppm/K}$. Then the displacement of the keystone dependent on temperature (using $\Delta \equiv \mathrm{d}/\mathrm{d}T$) is given as:

$$\Delta z \approx \alpha_G \cdot \frac{g}{\omega_\mathrm{n}^2} \approx -0.646\,\frac{\mathrm{mm}}{\mathrm{K}}\,, \tag{6.2}$$

for a filter tuned to $\omega_n = 2\pi \cdot 300\,\mathrm{mHz}$. This result is consistent with the measured vertical GAS filter displacement of $-0.54\,\mathrm{\mu m/K}$. Note, that the individual GAS filters were tuned to 200 mHz, but due to the tight bolting of the GAS filter plates to the spring box, the natural frequency shifted towards 300 mHz.

The temperature drift has also a clearly recognizable influence on the IP flexures. The movement of the IP versus temperature is caused by the change in the overall stiffness of the IP. According to [Losurdo-thesis], the stiffness-change can be approximated as:

$$\frac{\Delta k_x}{k_x} \approx (\alpha_E + \alpha_L)\,\frac{g}{L\,w_\mathrm{n}^2}\,, \tag{6.3}$$

with values for α_E and α_L shown in equation 6.1. In the case of a short IP ($L = 0.5\,\mathrm{m}$) tuned to 100 mHz the stiffness-change is given as:

$$\frac{\Delta k_x}{k_x} \approx -0.0134\,\frac{1}{\mathrm{K}}\,, \tag{6.4}$$

more than 1% per kelvin. In the AEI-SAS k_x (and k_y) are in the order of 500 N/m at 100 mHz tuning. The drift in the position is driven by the static forces, F^static, that are applied to centre the IP (via the correction springs), and that forces are of the order of a few newtons. When k_x changes, the position-change follows as:

$$\Delta x \approx \frac{F^\mathrm{static}}{k_x}\,\frac{\Delta k_x}{k_x} \approx 27\,\frac{\mathrm{\mu m}}{\mathrm{K}}\,\frac{F^\mathrm{static}}{\mathrm{N}}\,, \tag{6.5}$$

which is consistent with the observed 100 µm/K. In a perfect IP, which is always centred and levelled with no static force applied, the temperature will change the stiffness but that will not result in any movement.

The flexures are bolted to the base plate of the AEI-SAS, and the base plate is bolted to the legs of the vacuum system. Thus, the temperature transfer time to the flexures is faster than to the GAS filters, since they are better separated from the walls of the vacuum system. The in-vacuum thermal sensitivity strongly depends on the transportation process of the thermal energy through the whole system to the blades. The heat transport mechanism and path define the time over which temperature variations are transferred to the system. Fast changes are rejected while very slow changes sooner or later will go through. Therefore, the effect of changing air temperature seems to be visible only about a day later in the vertical position of the GAS filters.
The thermal effect on the GAS filters is slightly increased with cables. When the temperature increases, the optical table tilts about the x-axis, as if the cables would pull up its south edge. However, the total vertical movement decreases. This might indicate that the tilting axis is horizontally shifted away from the centre of the optical table.

Figure 6.3: The SPI cables are suspended from cantilever bridges to reduce their strain on the central optical table. These 60 cables are clamped to the table surface to reduce their vibrations and prevent slipping. The test was performed, to verify how the cables affect the AEI-SAS when temperature outside of the vacuum varies. The results show that the cables do not significantly increase the thermal drift of the system, as summarized in table 6.1.

GAS filters	w/o cables	with cables
z [mm/K]	0.54	0.13
T_x [mrad/K]	0.04	0.13
T_y [mrad/K]	0.08	0.02
IP flexures	w/o cables	with cables
R_z [mrad/K]	0.08	0.08
x [mm/K]	0.17	0.16
y [mm/K]	0.10	0.13

Table 6.1.: Results of the measurements of correlations between the in-vacuum displacement of the optical table and the temperature. The measurement results without cables are shown in figure 6.1, while the measurement with the SPI cables is shown in figure 6.2. The vertical z motion and tilt about x and y axes are caused by the GAS filters. The horizontal degrees of freedom and rotation about the z axis are caused by IP flexures.

6.2. Vertical force response

The response of the AEI-SAS mechanics to force input was measured on the system installed in the vacuum system, but not pumped down. The measurement was done, by applying a sinusoidal signal to the vertical actuators moving the GAS filters. The actuator force was compared to the optical table displacement measured by LVDTs and geophones. Such a measurement does not show the seismic isolation performance of the system, but gives valuable information about the natural frequencies of the system modes.
The figure 6.4 shows two measured force-to-displacement transfer functions. The LVDTs are measuring relative displacements between the spring box and the optical table. The geophones sense the inertial motion of the optical table. The LVDT/actuator measurement (grey dots) agrees with the geophones (blue line) up to 10 Hz. The built-in actuators generate a force between the optical table (in fact the intermediate plate) and the spring box. Therefore, at the resonance of the spring box bouncing mode at 35 Hz, the spring-box moves with a large amplitude while the table remains still. When the spring box is shaken by the ground, the peak at 35 Hz is also visible on the table, even though attenuated. The cause of the resonances above 200 Hz is not confirmed yet.

6.3. Horizontal and vertical transfer functions

The transfer functions of the horizontal and vertical mechanical isolators of the AEI-SAS are shown in figures 6.5 and 6.6, respectively. At low frequencies, around the natural frequencies of the isolators, both transmissibilities are larger than 0 dB (factor of 1). Thus, the displacement amplitude of the optical table is larger than base plate/ground displacement. These natural modes will be actively damped by feed-back controls, using sensors and actuators of the AEI-SAS. At the time of writing, first modal damping tests have shown promising results, as shown in figure 7.9.

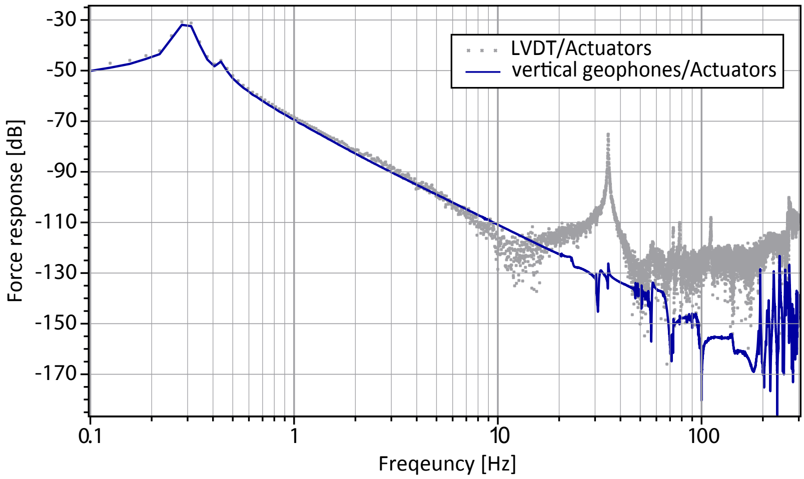

Figure 6.4.: The vertical force response function (blue solid) of the optical table measured by applying forces with vertical actuators and measuring the transfer function to the vertical geophones. The peaks above 200 Hz are caused by blade springs of the GAS filters. The second plot (grey dots) is a force response measured between the actuators and the LVDTs. It shows a large peak around 35 Hz belonging to a tilt mode of the spring box caused by vertical compliance of the upper IP flexures.

Horizontal isolation performance

The horizontal transfer function measurement was done in the horizontal shaker stand. The AEI-SAS system was suspended in the shaker. A voice-coil actuator, bolted to the ground, was used to shake the base plate, simulating ground motion. The signals of two geophones (one on the optical table and one on the base plate) were computed into a transfer function.
The transfer function was measured in two steps, to avoid excitation of the pendulum mode of the shaker around 1.5 Hz. The horizontal performance is described in figure 6.5. The maximum horizontal isolation of -80 dB was achieved above 4 Hz. At higher frequencies the isolation performance of the system is masked by the horizontal spring box modes and by the resonances of the suspension frame.

Vertical isolation performance

Since the vertical shaker stand is still being constructed, the vertical transfer function was measured by comparing the motion of the optical table to ground motion. No additional external forces were applied for this measurement.
The vertical transfer function of the central table, shown in figure 6.6, was measured with the built-in vertical geophones versus the ground motion measured by the STS-2 seismometer (blue). The plot shows, that the vertical natural frequency of the system is at 0.3 Hz, although the individual GAS filters were tuned to below 200 mHz. Colleagues at Nikhef discovered that stress in the GAS filter plate induced by tightly bolting it to the spring box plate might have increased the natural frequency [Bertolini2012]. In future, the filters should be bolted hand-tight to keep the natural frequency low.
The vertical isolation performance of the AEI-SAS is at least around -50 dB. At

frequencies between 0.5–3 Hz, the coherence is relatively high. Above 3 Hz the sensors pick-up some background noise due to in-air operation. Therefore, the coherence is low.

The general idea of the SAS design is the decoupling of vertical and horizontal modes, which are in the order of 0.1 Hz. However, the SAS is a complicated mechanical system. Its natural modes are mixed and are hard to distinguish in measurements. Above these natural frequencies, the isolation performance increases until a maximum is achieved around 4 Hz in both degrees of freedom.
At higher frequencies, the isolation performance is disguised by resonant peaks in all degrees of freedom. Some of the peaks have been identified and counter-measures foreseen. Other peaks are under investigation and will certainly be identified during the test of the third AEI-SAS in 2013. Nevertheless, the AEI-SAS nicely performs its task: providing seismic pre-isolation for the optics suspensions, the natural modes of which will be around 0.9 Hz–3 Hz.

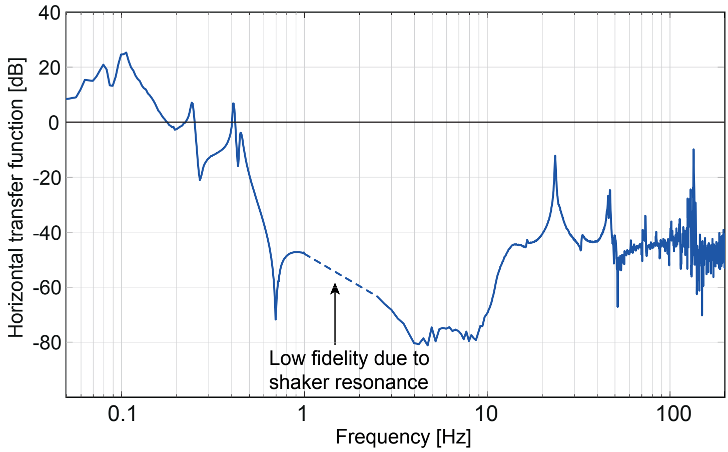

Figure 6.5.: A horizontal transfer function of the AEI-SAS was measured in the horizontal shaker stand. The plot consists of three measurements stitched together. The low frequency part shows horizontal natural frequencies of the IP around 100 mHz, other natural modes of the system are excited by the shaker and coupled into the horizontal measurement. The middle (dashed) part is not a truly measured table performance, due to the resonance of the shaker suspension at 1.5 Hz. The measurement shows about -80 dB isolation around $4-9$ Hz. The shoulder at 10 Hz is attributed to a resonant mode of the intermediate plate damped by Fluorel™ pads. The 24 Hz peak is attributed to the shaker stand rocking mode and is not a real resonance of the system.

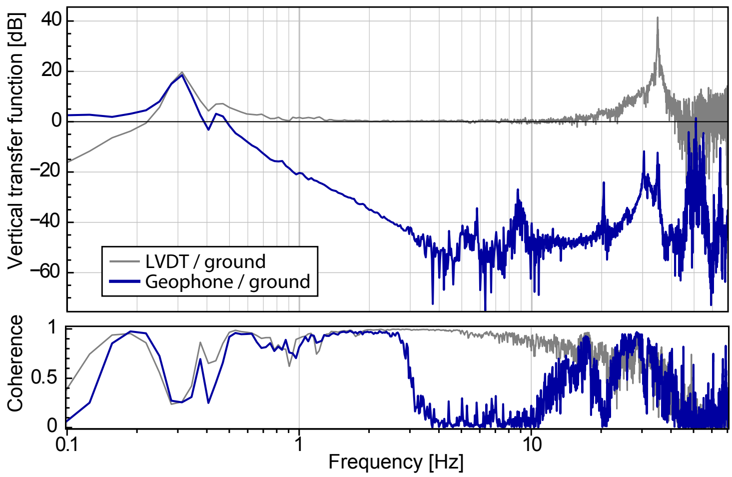

Figure 6.6.: The vertical transfer function and the coherence of the AEI-SAS. The first two plots are vertical transfer functions measured by geophones and LVDTs versus ground motion measured by the STS-2 seismometer. Between $1-10$ Hz the spring box movement has the same amplitude as the ground. Above 10 Hz, the LVDTs sense a rigid body mode corresponding to the vertical bouncing of the spring box at 35 Hz. Thereby, the spring box bounces on the upper IP flexures, which act as extensional springs. The lower plots show the coherence of the transfer functions. Up to 1 Hz the coherence is high, except at the resonances. Above 3 Hz the coherence drops to zero. Thus, the true transmissibility is mostly superimposed by sensor noise.

7. Control strategy

The AEI-SAS is a mostly passive mechanical attenuator of ground excitations above the natural frequencies of IP legs and the GAS filters. Their natural frequencies are in the order of 0.1 and 0.2 Hz, respectively. As discussed in figure 2.1 in chapter 2, the ground motion around 0.2 Hz shows a large micro-seismic peak, which is close to the fundamental modes of the AEI-SAS. This microseismic motion will excite the system's fundamental modes into large scale motion. To damp resonances at these fundamental modes, the system is equipped with a variety of sensors and actuators.
The controls of the AEI-SAS can be used for different tasks, such as:

- damping of fundamental modes of the system,
- maintaining the static position of the table,
- damping of rigid body modes (for example, bouncing modes of the spring box),
- and reducing the effective stiffness of eigenmodes.

Servo control loops and data recording are carried out with the digital real-time Control and Data acquisition System (CDS) [Bork2009], which has been tested for use in next generation gravitational wave detectors. Control algorithms are implemented via Matlab/Simulink models, from which a real-time capable module is subsequently generated.
The sensors and actuators, required for active controls are described in section 7.1. The successful implementation of mode damping and static positioning into the control envelope is shown in section 7.2. Damping of spring box resonances was tested with passive mechanical resonant dampers and with active controls, as shown in section 7.3. Both methods were shown to be effective. Eventually, however, these resonances were de-coupled from the table top by introducing Fluorel™ pads and damped, as discussed in section 7.4. Active reduction of the effective stiffness of eigenmodes will be tested soon. Conclusion and outlook on the future control strategy is given in section 7.5.

7.1. Sensors and actuators for local control

The AEI-SAS isolates passively all six degrees of freedom: three horizontal and three vertical, see figure 7.1. The horizontal degrees of freedom x and y, and the rotation about the vertical axis, (yaw), are isolated by a three-leg IP. The vertical degree of freedom, along the z axis, and the rotations about x and y ($roll$ and $pitch$), are isolated by three GAS filters. The vertical and horizontal stages can be handled separately. To fully determine the position of the optical table, each stage is augmented with three displacement sensors (LVDTs). Analogously, three actuators per isolation stage are required for positioning in three degrees of freedom. Therefore, triplets of sensors and

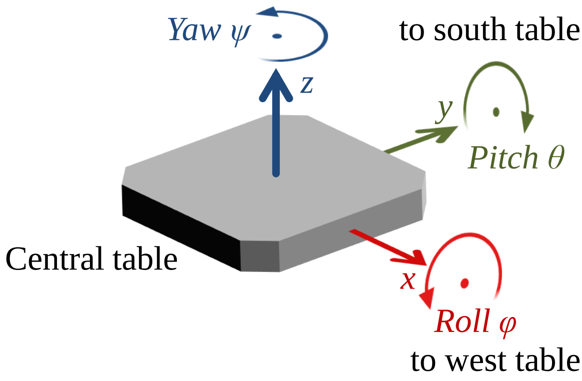

Figure 7.1: The coordinate system of the central AEI-SAS. The SAS was omitted for clarity, only the optical table is shown. The x and y axes are aligned parallel to the L-shape of the vacuum system and are valid for all three tables.

actuators are positioned on a circle with a spacing of 120°, as shown in figure 7.2. Their distances from the centre of the optical table are given in the same figure.
LVDTs are non-contact displacement sensors measuring relative positions. Three horizontal LVDTs measure the spring box position relative to the ground. The three vertical LVDT sensors measure the vertical displacement of the optical table with respect to the spring box. The LVDTs are sensitive within a frequency band ranging from DC to above 100 Hz.
Accelerometers and geophones are inertial motion sensors. The horizontal accelerometers sense the horizontal spring box motion and rotation about the vertical axis. They are sensitive within a frequency range from 0.1 Hz up to their internal resonances at 300 Hz. Vertical geophones are installed inside the optical table to monitor its vertical movement and tilt motion in the frequency range from 0.1 Hz to about 400 Hz.
The AEI-SAS is a mostly passive device, requiring only weak actuators to damp the fundamental modes. Voice-coil actuators are used to perform modal damping and low frequency positioning. Three vertical and three horizontal actuators drive the optical table relative to the ground. Additionally, the control system is used to adjust and maintain the static position of the system. For that, motorized blade springs are used to manually set the working point of the optical table, thereby removing the static load from the voice-coil actuators.

7.1.1. Relative motion sensor: LVDT

The position of the table is monitored by Linear Variable Differential Transformers (LVDTs). The LVDTs in the AEI-SAS are non-contact measurement devices with nanometre resolution and 20 mm range. They consist of two coaxial coils: a small primary excitation coil and a larger secondary sensing coil [Tariq2002]. The excitation coil is driven by a sinusoidal signal at 15 kHz generating an alternating magnetic field. The sensing coil consists of two sets of windings, mounted and connected in series, but with opposed orientation. The excitation coil induces a signal proportional to displacement when it slides between the two windings of the sensing coils. Thereby, the induced 15 kHz signal increases in one sensing winding, and decreases in the other. The output is demodulated synchronously with the excitation source. The resulting rectified voltage is proportional to the displacement of the coil and its polarity indicates

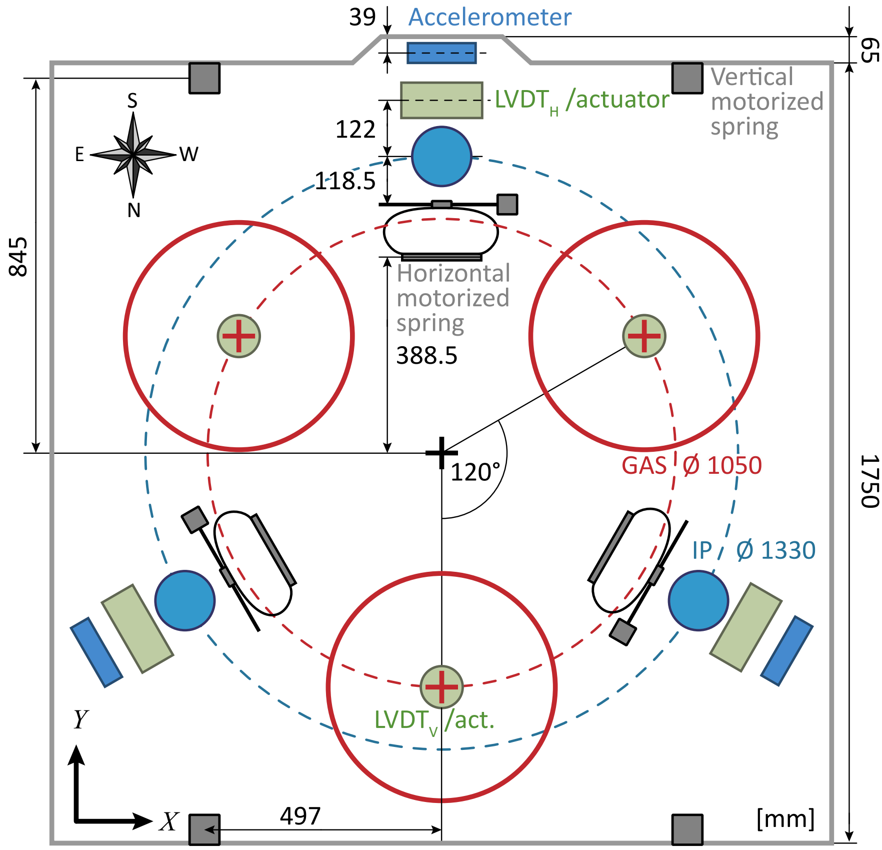

Device	Distance [mm]
Accelerometer (hor.)	901
Horizontal LVDT	787
Geophone (vert.)	600
Vertical LVDT	525
Horizontal motorized spring	388.5

Figure 7.2.: The positions of sensors and actuators in the central AEI-SAS. Triplets of devices (horizontal accelerometers, vertical geophones, horizontal and vertical LVDTs with co-located actuators, and horizontal motorized blades springs) are positioned on a circle, spaced by 120°. Four vertical motorized blade springs are placed near each corner of the optical table. The vertical LVDTs/actuators are positioned in the centre of each GAS filter. The vertical geophones (not shown) are positioned inside the optical table above the GAS filters at a slightly larger radius. The table summarizes the distances of the devices from the centre of the optical table.

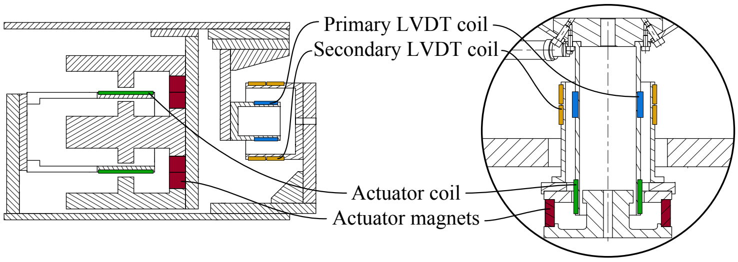

Figure 7.3.: Drawing of a horizontal (left) and a vertical (right) LVDT with their co-located actuators. The coils with the same function are indicated by the same colour. The circle on the right-hand side is an enlarged image of the GAS filter illustration (figure 5.1).

the direction of the displacement [NI]. Over a total range of 6 mm the output of the horizontal and vertical LVDTs is linear within ±0.2 % and ±0.5 %, respectively. To measure the resolution of the sensors, the LVDT output was measured with a signal analyser. The readout noise was measured to be 15 μV/$\sqrt{\text{Hz}}$ and was quite flat from 0.1 Hz to 100 Hz. After dividing by the calibration factor of 1.85 V/mm, the displacement noise is 8 nm/$\sqrt{\text{Hz}}$.

7.1.2. Horizontal inertial sensors: accelerometers

Accelerometers are used in the AEI-SAS to measure the horizontal inertial motion of the spring box, which is the same as the optical table motion at low frequencies below few Hz. The accelerometers monitor the vibration isolation performance outside the control loop frequency band. The AEI-accelerometers are custom-made uni-axial devices machined with electric discharge machining from a single block of aluminium, and therefore called monolithic. The AEI-accelerometer mechanical design is similar to monolithic accelerometers used in TAMA-300 [Bertolini2006a]. Newly-designed corner-filleted flexures have been implemented to reduce the elastic restoring force and to increase strength for transport.
The test mass is suspended from a folded pendulum, as shown in figure 7.4. The folded pendulum reduces the natural frequency of the accelerometer. Additionally the folded pendulum rigidly constraints the motion of the seismic mass in a single direction to make it largely insensitive to all five orthogonal degrees of freedom.
The AEI-accelerometers are tuned to a natural frequency of 0.3 Hz. A miniaturized LVDT with reduced dynamic range and strongly enhanced sensitivity is used to sense the test mass position. The sensor signal is fed back to a coil-magnet actuator to re-centre the test mass. The feedback for the AEI-accelerometers is processed using the real-time CDS.
The sensitivity of AEI-accelerometers is about 2.8×10^{-10} ms^{-2}/$\sqrt{\text{Hz}}$ at 1 Hz, which is close to the noise level of a Streckeisen STS-2 seismometer at 1.5×10^{-10} ms^{-2}/$\sqrt{\text{Hz}}$ at 1 Hz [Nakayama2004].

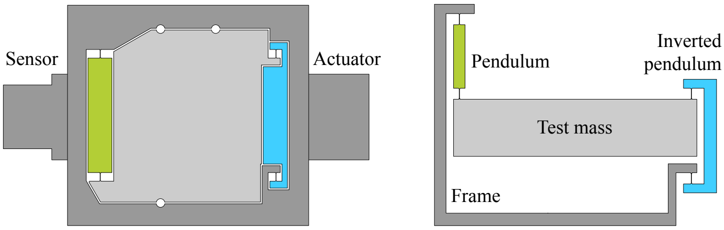

Figure 7.4.: A drawing (left) and a schematic view (right) of the actual mechanics of the AEI-accelerometer. The position of the accelerometer's test mass (light grey) is measured by a miniaturized LVDT-sensor and is fed back to a voice-coil actuator which maintains centring of the mass. The right picture sketches the mechanical scheme of a folded pendulum (Watt-linkage). The left arm (green) is a normal pendulum and the the right one (blue) is an inverted pendulum. All flexures are in tension to prevent buckling.

7.1.3. Vertical inertial sensors: geophones

Three vertical geophones are installed within the honeycomb structure of the optical table to monitor its residual vertical motion. These commercial geophones are model L-22D from Mark Products (now Sercel [Sercel]). They have a natural frequency of 2 Hz and a sensitivity of $88\,\mathrm{V(m/s)^{-1}}$. The geophones are not vacuum compatible, therefore they are sealed in air-tight tubes with ConFlat flanges. The tubes are filled with different marker gases to trace potential leaks.
Like most of the components in the AEI-SAS, three vertical geophones per table are distributed on a circle at 120° intervals, as shown in figure 7.2. A simple geometry-inferred matrix transforms the signals of the three vertical geophones into the vertical and two rotational degrees of freedom within the control and data system.

7.1.4. Voice-coil actuators

Three vertical and three horizontal voice-coil actuators [Wang2002] are used in the AEI-SAS, for example, for active damping of natural modes. Figure 7.3 shows an illustration of the actuators co-located with corresponding LVDT sensors. The horizontal voice-coil actuators are placed close to the IP legs, as shown in figure 7.2, actuating between the base plate and the spring box. They are positioned tangentially to a circle with 120° spacing. A coordinate transformation matrix is used to apply forces to the table in a coordinate system aligned to the interferometer arms. The vertical actuators are coaxial to each GAS filter, actuating between the keystone and the spring box. The horizontal actuators provide a force per unit current of 5 N/A. Vertical actuators, with about 7 N/A, are slightly stronger.

7.1.5. Motorized blade springs

Motorized springs driven by stepper motors are installed for static fine tuning of AEI-SAS position and for thermal drift compensation. Different sets of blades, shown in figure 7.5, are used to correct the static position of the table in vertical and horizontal degrees of freedom. Thus, after mass re-distribution, the tables can be re-positioned at the original relative orientation to each other, by using a reference measurement.

Chapter 7

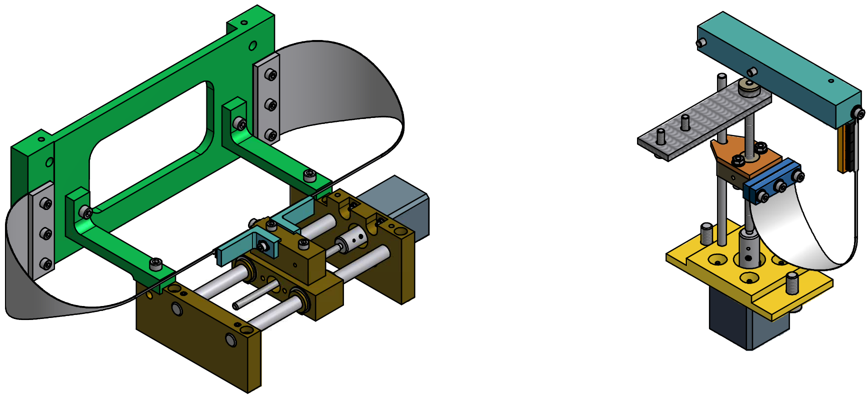

Figure 7.5.: Motorized blade springs used in the AEI-SAS for fine corrections of optical table position. Three horizontal (left) and four vertical (right) springs are controlled by vacuum compatible stepper motors.

The tips of the spring blades are connected to a sliding carriage moved by a threaded rod attached to a stepper motor.
The thickness of the CuBe blade springs is 0.25 mm. The horizontal blades have been enlarged in order to cope with ± 1 mrad mislevelling of the IP base. The outline of the blade is designed to orient the resulting force along the movement direction. Three horizontal pairs of blades are positioned near each inverted pendulum leg, actuating between the base plate and the spring box. Four vertical single blades, one at each corner of the optical table, act on the optical table from the spring box.
The IP stage of AEI-SAS is tilt sensitive. When the system is installed on legs inside the vacuum system, there is no possibility of fine-tuning of the angle of the base plate. One has to rely on the levelness of the support structure in the vacuum system. After installation into the vacuum system, the horizontal stage of the AEI-SAS had to be centred with the motorized springs. Thereby, the springs were almost at their limit when the IP stage was centred. The situation improved slightly when the baseplate was tightened to the support structure. Therefore, the base plate seems to deform under the weight of the system, and flattens when bolted to the support legs. In future, the blades of the motorized springs will be replaced by thicker blades to add extra force. Then the springs will not be at their limit any more and can be used to adjust the horizontal position of the system to adjust the orientation or to counteract temperature drift.
All motorized blades are driven by stepper motors of the type C17.2 from Arun Microelectronics Limited controlled by driver units IDX 7505 from Trinamic Motion Control. The stepper motors are vacuum compatible up to 10^{-10} mbar and bakeable to 200°C. The motors are two phase hybrid stepper motors, with side length of $31 \times 31 \times 41$ mm and a torque rate of 0.2 Nm. Each motor has a step angle of 1.8° providing 200 steps per revolution [Arun].

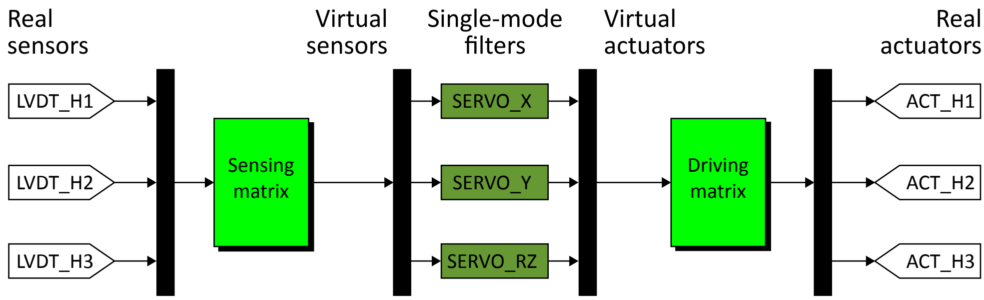

Figure 7.6.: A simplified illustration of the AEI-SAS horizontal control model. The horizontal and vertical models are identical. The signals from real sensors are transformed by a sensing matrix into a set of virtual sensors. These virtual sensor signals show the displacement of the optical table in x and y directions, and rotations about the vertical z-axis. The servo filters convert each individual virtual sensor signal into virtual actuator signals, which then are transformed back into real actuator signals and fed into the actuators.

7.2. Damping of fundamental modes

The low-frequency eigenmodes of the AEI-SAS are damped by observing the motion of the table with the sensors, filtering these signals, and feeding them back to the actuators. Figure 7.6 shows a simplified illustration of the horizontal control model. The separate horizontal and vertical controls are identical. A simple coordinate transformation matrix transforms the individual input signals of the three horizontal sensors into a set of three virtual sensors. The matrix is initially generated from the geometrical positions of sensors and actuators, as discussed in chapter D. Since the pure geometrical reconstruction is not sufficient to have a decent decoupling of the modes, the output matrix will be diagonalised. The virtual sensors provide signals of the horizontal motion in x and y directions, and the rotation signal about the vertical z-axis.
Figure 7.7 shows a modelled open loop transfer function, including the damping filter and integrator for the fundamental mode of the system in the x-direction. Other degrees of freedom are damped with similar filters. The virtual sensor signals are filtered individually. The damping filter is composed of a number of zeros and poles, which are listed in a table in figure 7.7. The open loop transfer function model is produced by multiplying the damping filter with the modelled transfer function of the IP. The model shows that the filter is only effective around the resonance frequency at 0.1 Hz with unity gain (at 0 dB) crossing around 0.2 Hz. Below 0.05 Hz and above 0.2 Hz the open loop gain is below unity, thus the damping is ineffective there. The slope at low frequency is generated by the integrator.
The integrator is required to maintain a set-point position of the system. The static position of the system is measured by LVDTs. Small deviations from the set-point are corrected by voice-coil actuators. An integrator adds the deviations from the set-point over time and gives the accumulated offset, multiplied by the integral gain, to the controller output. For large displacements, the motorized blade springs can be used to remove the static load from the voice-coil actuators. An automatic correction with the motorized blade springs can, in principle, be implemented but is not foreseen yet.

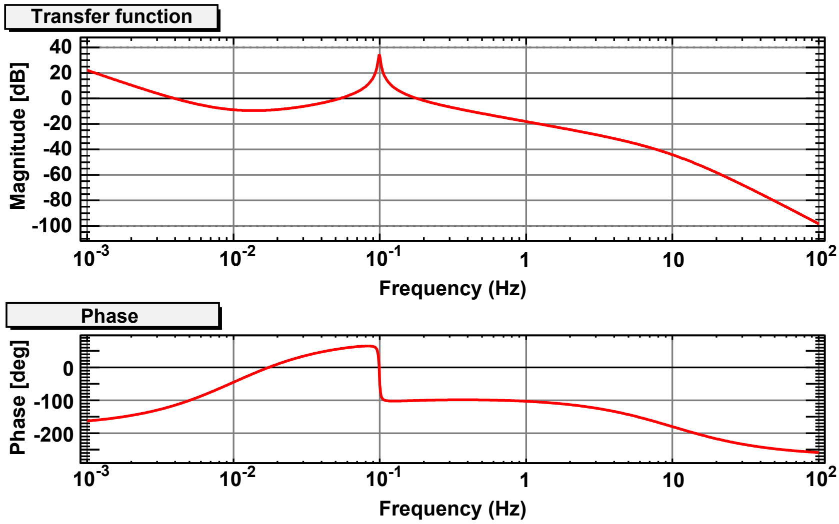

Filter	Zeros [Hz]	Poles [Hz]	Gain [dB]
Damping	0	10; 10	+22
Integrator	0.01; 0.01; 0.01	0; 0; 0	-120

Figure 7.7.: A bode plot showing a model of an open-loop transfer function including the feedback filter, damping the optical table motion in x-direction. The filter is effective around the mechanical resonance frequency at 0.1 Hz between 0.05 and 0.2 Hz. The low-frequency slope is caused by an integrator, used to maintain static set-point. The integrator was turned off during the damping performance evaluation in figure 7.9. The table shows zeroes and poles defining the integrator and the damping filter for the x-direction with their corresponding gain values. Similar values are used for other degrees of freedom.

The damping performance is evaluated by measuring the force response (i.e. displacement vs. applied force) measured with an open loop. Such a measurement shows how the mechanical system reacts to an artificial input signal, filtered by the damping factor and applied to the actuators. The force of the actuators driving the spring box in x-direction is compared to the signal of the LVDTs, which sense the horizontal spring box displacement with respect to the baseplate. As shown in figure 7.8, the excitation swept-sine signal is fed into the damping loop at input point (EXC). The response of the system to the signal is measured at (IN1). Between these input and output points the loop remains open. Such an force response transfer function is shown in figure 7.9a.
The damping effect on the IP, measured in air, is shown in figure 7.9. Figure 7.9a illustrates an open-loop transfer function measured with and without damping, and the coherence of the signals. The coherence is an indicator of the quality of the measurement. Above 3 Hz, where the coherence is small, the signal is mostly noise dominated. The two large bumps in the transfer function around 10 Hz and 80 Hz belong to rigid body modes of the AEI-SAS. For example, the 10 Hz resonance belongs

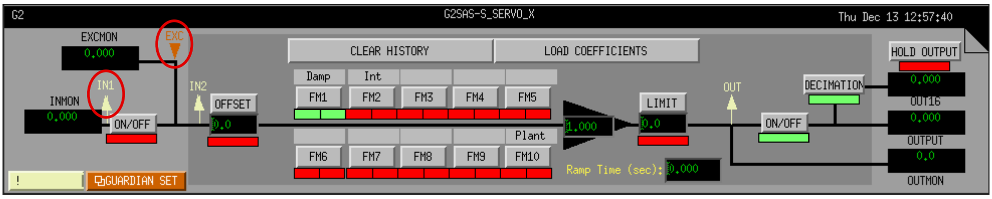

Figure 7.8.: An example of a filter module window showing 10 filter banks (FM1-FM10). The active filters (Damp) are shown in green, while inactive filters (Int) are red. The integrator was turned off during the step response measurements in figure 7.9b. The filter (Plant) is a modelled transfer function of the system. It is used to model the total open-loop gain in figure 7.7. The excitation input signal for the swept-sine measurement of the open-loop transfer function is inserted at EXC (red circle). The loop output is measured at IN1.

to a complicated mode which involves the spring box, the intermediate plate, and the optical table. The resonance at the horizontal eigenmode of the IP legs (0.08 Hz) was resolved in an additional measurement (black) with reduced excitation level. Two peaks close together are visible, attributed to a coupled x- and y-motion of the optical table. The modes of the table are in the basis of the legs, i.e. triangular. The cross-coupling is very strong near all the fundamental resonances, even from horizontal to vertical. In future, the signals will not be decomposed into the table modes, but instead into the best lab-aligned modes. However, the measurement shown in figure 7.9a shows that damping of the peaks is also possible with just geometrical feedback, as long as the feedback force is just a viscous damping. This kind of damping is usable even with strong couplings between the different modes around the resonances.
The step response measurements in figure 7.9b are time series with and without damping. The two measurements illustrate the response of the AEI-SAS to two horizontal kicks (at 10 s and 110 s) with an amplitude of 1 mm and 2 mm respectively. The measurement was done without an integrator, which would push the table to its set-point (for example zero). The undamped oscillation (measured in air) shows a quality factor of about $Q \approx 7$. In vacuum, the quality factor will increase. The damped measurement indicates that the damping is close to critical damping. This is intended, because with a lower damping factor the decay time would become too long at this period of around 10 s.

7.3. Damping of internal resonances

Internal resonances in the AEI-SAS reduce the isolation performance above 10 Hz. The resonances described here are attributed to oscillations of the spring box. The resonances are caused by horizontal compliance of the GAS filters and vertical oscillations of the spring box due to longitudinal compliance of upper IP flexures. Two alternative damping methods were tested to damp these resonances: passive resonant damping and active viscous damping. In the end, a third solution was chosen: Fluorel™ pads were inserted between the spring box and the intermediate plate, see section 7.4.

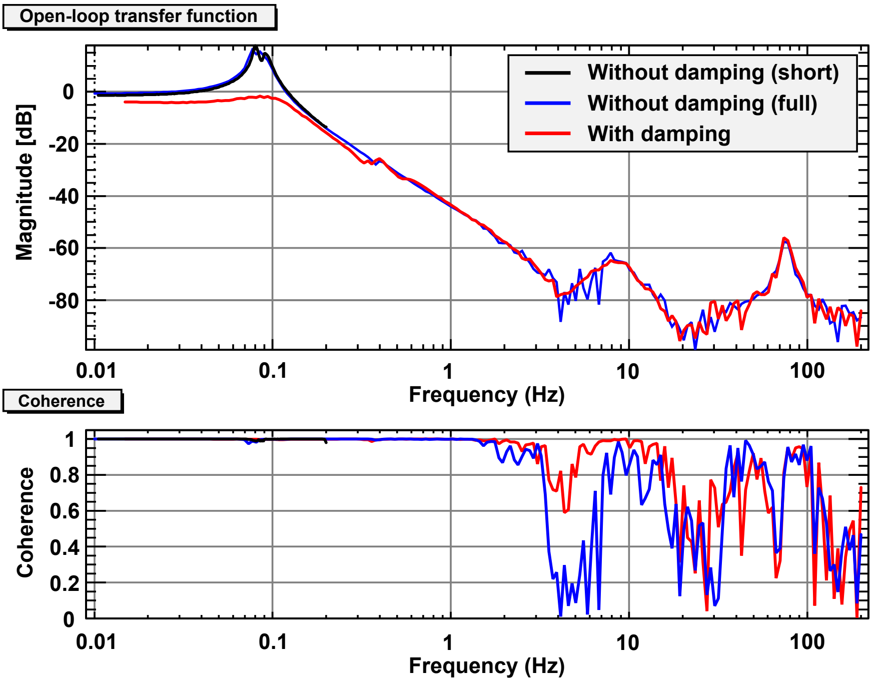

(a) The force response transfer function and signal coherence measured with and without damping. The short measurement (black) resolving the peak around the resonance frequency is done with reduced excitation to prevent saturation of the sensors at the resonance.

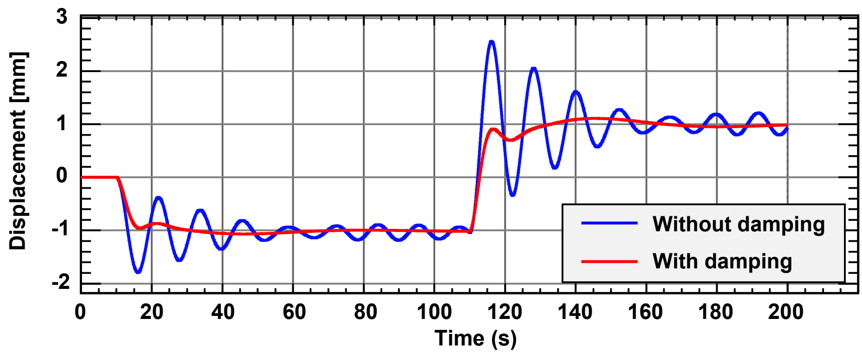

(b) The step response measurements with and without damping were performed without an integrator, which is designed to push the system to a set-point (for example zero).

Figure 7.9.: Two illustrations of the active damping performance of the horizontal eigenmode of the AEI-SAS in x-direction measured in air.

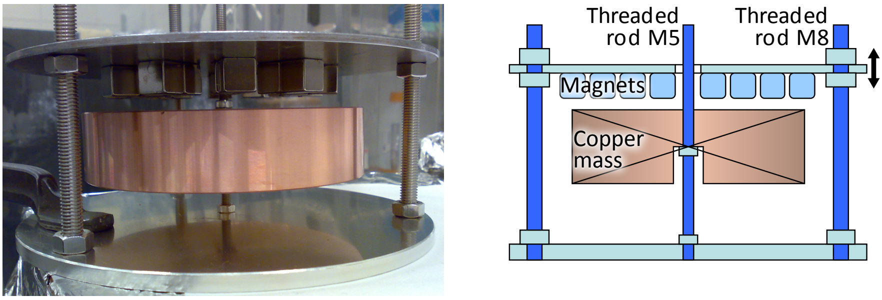

Figure 7.10.: A picture of the horizontal resonant damper (left) and the drawing of its cross section (right). The resonant damper consists of a copper mass on a flexure (threaded rod). The frequency of the oscillator is tuned by rotating the copper mass up and down the thread of the rod. The resonance of the mass oscillation is measured by a guitar tone pick-up. The vibration of the copper mass is eddy current damped by magnets above the mass. For clarity the magnets are shown at a bigger distance than during operation.

Resonant damping

Resonant damping was tested with tunable mechanical dampers, which consisted of a mass on a flexible vertical rod, as shown in figure 7.10. The resonance frequency of the dampers was tuned to the same frequency as the resonance that needed to be damped. The oscillations of the damper mass were eddy-current damped by magnets. The damping factor was adjusted by varying the vertical distance between the magnets and the damper body. Three resonant dampers were manufactured and placed in the spring box. Two of them were nearly identical horizontal dampers tuned to resonance frequencies of 13 Hz and 17 Hz. The third device was a bi-directional damper, with the mass bolted to a horizontal flexure. The cross section of this flexure was machined to have different thicknesses in vertical and horizontal directions. By adjusting the thickness of the flexure, the damper was tuned independently in vertical and horizontal degrees of freedom. This damper was tuned to 17 Hz in horizontal and to 34 Hz in vertical direction.

As shown in figure 7.11, the horizontal resonant damping reduced the quality factor of the spring box resonances by about 10 dB (factor of 3). The bi-directional damper was overdamped by the magnets and did not work properly. The project was abandoned due to lack of time. The performance of the bi-directional damper could be improved by iterative testing of eddy-current damping of the isolator. Additionally, the orientation of the damper and its position in the spring box would need to be varied to achieve optimal damping.

Active viscous damping

Alternatively to the resonant damping, active damping of the modes was tested in a brief measurement campaign. Viscous damping was applied by sending the horizontal accelerometer signals directly to the actuators. A second order bandpass filter at $1 - 40$ Hz was used. The results are shown in figure 7.12. The resonance peaks were reduced by a factor of 10.

In the end, both AEI-SAS were installed without any resonant dampers. Instead,

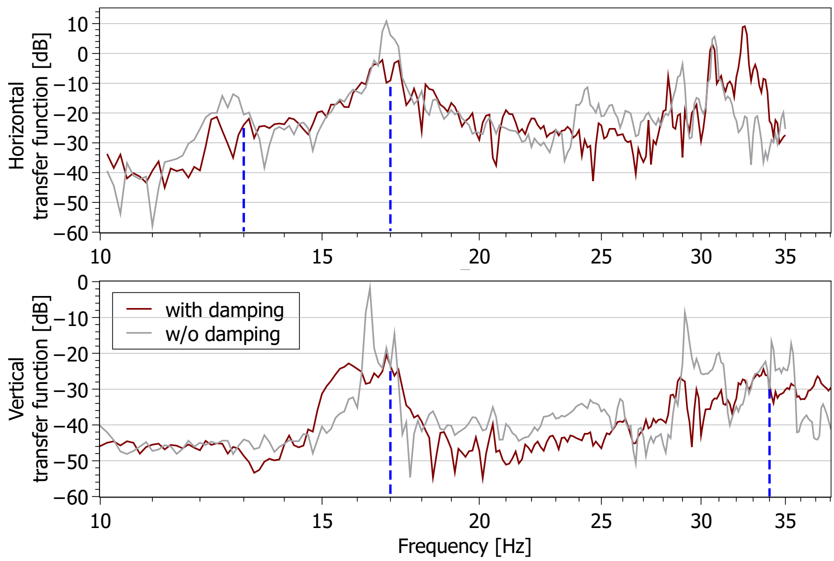

Figure 7.11.: The horizontal and vertical transfer function measurements show the effect of the resonant dampers on rigid body modes of the spring box. The transfer functions were measured with two identical geophones positioned on the ground and on the optical table. The system was installed in the vacuum system but measured in air. The dampers were tuned to the spring box resonance frequencies at 13 Hz and 17 Hz in horizontal, 34 Hz in vertical direction. The quality factors of the resonances measured on the optical table is reduced by about 10 dB (factor 3) in horizontal and almost 20 dB (factor of 10) in vertical direction around 16-17 Hz. The effect of the vertical damper is inconclusive.

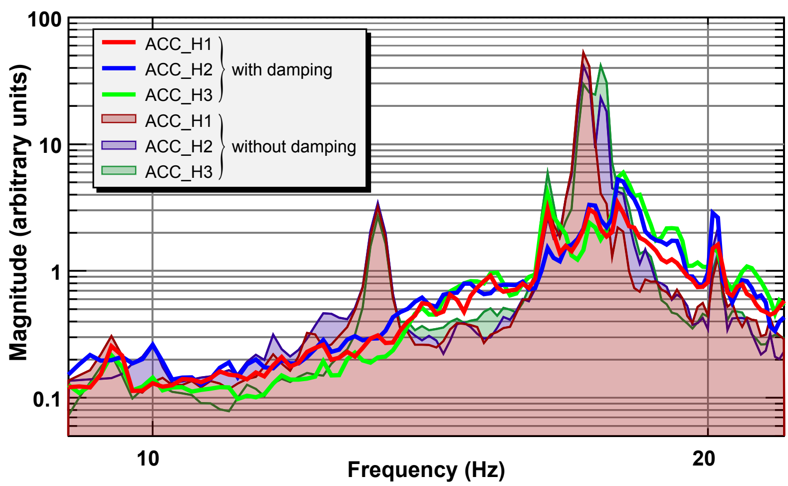

Figure 7.12.: The active viscous damping of the rigid body modes of the spring box using horizontal LVDTs and actuators. The quality factors of the resonances were reduced by a factor of 10 at 13 Hz and 17 Hz.

Fluorel™ pads were inserted between the intermediate plate and the optical table, as shown in section 7.4. The pads act as springs for the intermediate plate, which acts as an additional oscillator layer. The pads change the rigid body bodes of the spring box and decouple the optical table from high-frequency oscillations of the intermediate plate.

7.4. Fluorel pads on the intermediate plate

In the original design of the AEI-SAS, the optical table and the intermediate plate were separated by aluminium ring spacers, shown as yellow rings around the IP bells in figure 3.8. Even though, the table was bolted to the GAS filter keystones (through the intermediate plate), the distance between the connection point of the GAS filter and the ring spacers was discovered to be too large. In this configuration, as shown in figure 7.13a, the GAS filters were pushing up while the weight of the optical table and the payload were pushing down, as indicated by red arrows. This distance caused the intermediate plate to flex like a cantilever blade.

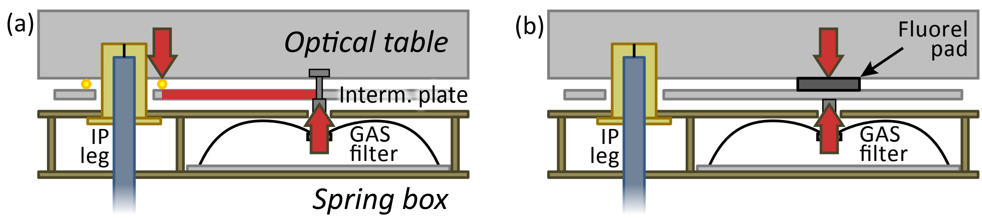

Figure 7.13.: A schematic drawing of the intermediate plate in the AEI-SAS. (a) In the original design, the optical table was bolted to the GAS filter keystones. The horizontal distance between the GAS filter and the ring spacers around the IP legs caused a cantilever-like flexing of the intermediate plate (represented as red bar). (b) In the final design, all stiff connections between the optical table and the intermediate plate were removed and replaced by Fluorel™ pads. The pads were positioned above the GAS filters to reduce the flexing area of the intermediate plate. These pads decouple the optical table from high-frequency oscillations of the intermediate plate and the spring box.

To solve the problem, every stiff connection between the intermediate plate and the optical bench was removed. Fluorel™ pads (roughly 1.5 cm × 6 cm with a hight of about 1 cm) were placed directly above the GAS filters, acting as spacers between the intermediate plate and the optical table. Thereby, the flexing part of the intermediate plate was shortened.
Fluorel™ is a vacuum compatible Viton®-like fluorelastomer (a fluorocarbon-based synthetic rubber). The Fluorel™ acts like an additional spring for the intermediate plate, introducing another six degree of freedom oscillator into the system. This additional oscillator changes the modes of the spring box, since the 100 kg mass of the intermediate plate is now an independently oscillating mass. The model in figure 7.14 illustrates how the masses of the AEI-SAS are coupled by vertical springs. Assuming simple coupled harmonic oscillators, the intermediate plate produces a broad (low Q) resonance around 11 Hz, as seen in figure 7.15. Furthermore, the pads decouple the optical table from (some) high-frequency oscillations coming from the intermediate plate and the spring box.

Chapter 7

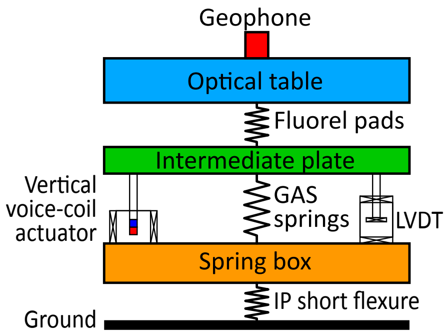

Figure 7.14: A simple model illustrating the vertical spring constants of the AEI-SAS. The model consists of three rigid bodies: the spring box, the intermediate plate, and the optical table connected by springs. Without the Fluorel™, the optical table and the intermediate plate are connected forming a single solid body

The intermediate plate remains bolted to the GAS filters, but the optical table rests on the Fluorel™ pads, without being bolted. Both AEI-SAS tables were retrofitted with the pads. The resulting transfer functions, comparing measurements with and without Fluorel™ are shown in figure 7.15. The 17 Hz peak, a vibrational mode of the spring box, is reduced by at least 40 dB. A finite element analysis of the intermediate plate might show the modes of the plate's motion. Then, an oscillation node can be chosen as an optimal position for the Fluorel™ pads.

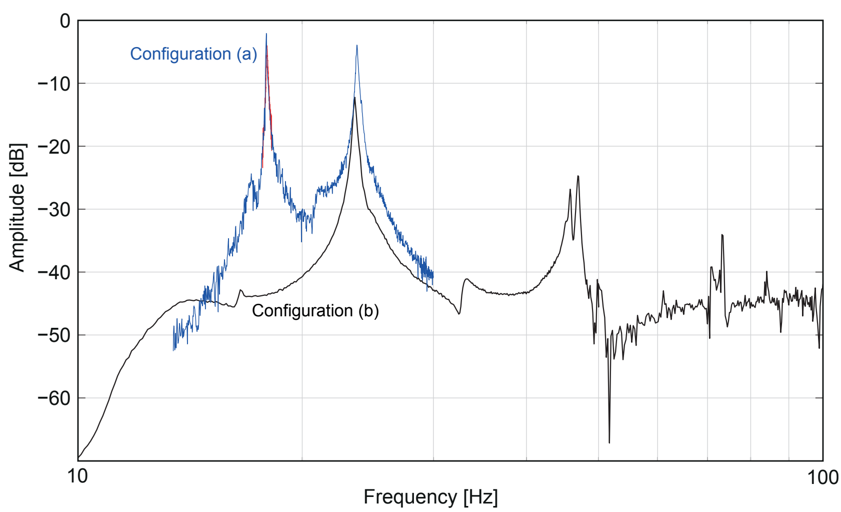

Figure 7.15.: Horizontal transfer functions of the AEI-SAS in two configuration: (a) the optical table bolted to the keystones of the GAS filters through the intermediate plate, and (b) with Fluorel™ pads placed above the GAS filters acting as a spring between the intermediate plate and the optical table. The table motion at the 17 Hz resonance peak produced by the spring box is reduced by about 40 dB (a factor of 100). With the Fluorel™ pads, the intermediate plate acts like an additional oscillator producing a broad resonance around 11 Hz. The original spring box resonance are changed, due to the additional oscillator.

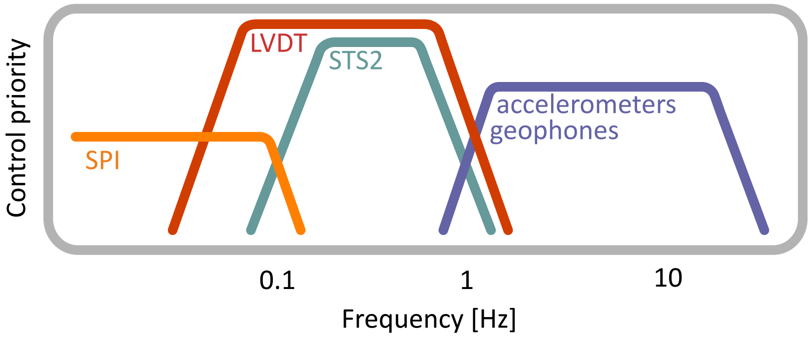

Figure 7.16.: The sensors in the AEI-SAS will be blended at certain frequencies to ensure that they are used within their most sensitive frequency range. Sensors and actuators will be used to stabilize and control the position of the optical table.

7.5. Future control strategy

In future, the control system of the AEI-SAS will be refined. Advanced controls will further improve the isolation performance of the system. Improvement of cross-coupling between the 6 degrees of freedom and better controllability of the system are anticipated from:

- diagonalisation of the output matrices, which transform the virtual sensor outputs into actuator signals
- blending of different sensors
- including the STS-2 seismometer into the control topology.

So far, the matrices transforming the sensor and actuator signals are defined purely by geometry. However, the modes are cross-coupled around the resonances. In future, the signals will not be decomposed into the table's geometrical modes, but instead into the best table-aligned modes.
The signals from the sensors (SPI, LVDT, geophones, accelerometers, seismometers, see section 7.1) will be blended to operate at their most sensitive frequency range, as shown in figure 7.16. By blending the sensors, the table motion can be further reduced by active feedback. Low-frequency table motion can be reduced by summing the calibrated STS-2 signals with the LVDT signals below the natural modes, because the seismometer is more sensitive in this frequency range. Blending the signals of LVDTs and inertial sensors (accelerometers/geophone) can be used to increase the servo bandwidth and reduce the table motion at frequencies up to 10 Hz. The blending filters will be 5th order complementary filters. The SPI will monitor and correct the relative inter-table position from DC to around 0.1 Hz. Thereby, the central table will be used as reference and the west and south tables will follow its motion.

Chapter 7

8. The AEI-SAS in the 10 m Prototype

The previous chapters focused on the Seismic Attenuation System and its major components. The subsequent chapter reviews the scope of the AEI-SAS within the AEI 10 m Prototype project, as one of its major components. Those elements essential for the operation of the facility are discussed in section 8.1 and future experiments are presented in section 8.2.

8.1. Main features of the Prototype facility

The major elements of the 10 m Prototype facility are the ultra-high vacuum system, seismically isolated optical tables, and the Suspension Platform Interferometer (SPI). The vacuum system isolates the experiments from environmental influence. The seismically isolated optical tables are a versatile platform for optical experiments. The SPI interconnects the tables in order to couple their residual motion.

Vacuum system

A large scale ultra-high vacuum system, shown in figure 1.7, has been built to isolate all experiments in the AEI 10 m Prototype from environmental noise sources, such as acoustic and thermal fluctuations. The 100 m^3 vacuum system consists of three walk-in tanks connected by vacuum tubes. A screw pump with a pump rate of 170 ls^{-1} is attached to one of the tubes, pumping from atmospheric pressure. Within 12 h, the system can be evacuated to 10^{-6} hPa, using two magnetically levitated turbo-molecular pumps with a pumping speed of 2000 ls^{-1} each, backed by a scroll pump. After about one week of pumping, a pressure of 10^{-7} hPa is reached.
Large flanges at the doors of the tanks, at the tube sections, and at the lids of the tanks are sealed by pairs of Viton® O-rings. The space between these two O-rings is pumped by a second scroll pump, allowing to reach a low residual gas pressure in a differential pumping scheme. The two scroll pumps, for backing and differential pumping, are installed in a separate pump room. The scroll pumps are mounted on two granite plates separated by Sorbothane hemispheres for vibration isolation.

Suspension Platform Interferometer (SPI)

The fundamental modes of the interferometer's optics suspension are around $0.8 - 3$ Hz. At these frequencies, the optical tables isolate ground motion from the suspensions. Below these frequencies, where the AEI-SAS is not effective, another sensor is required. Therefore, the relative motion of these tables will be stabilized by the Suspension

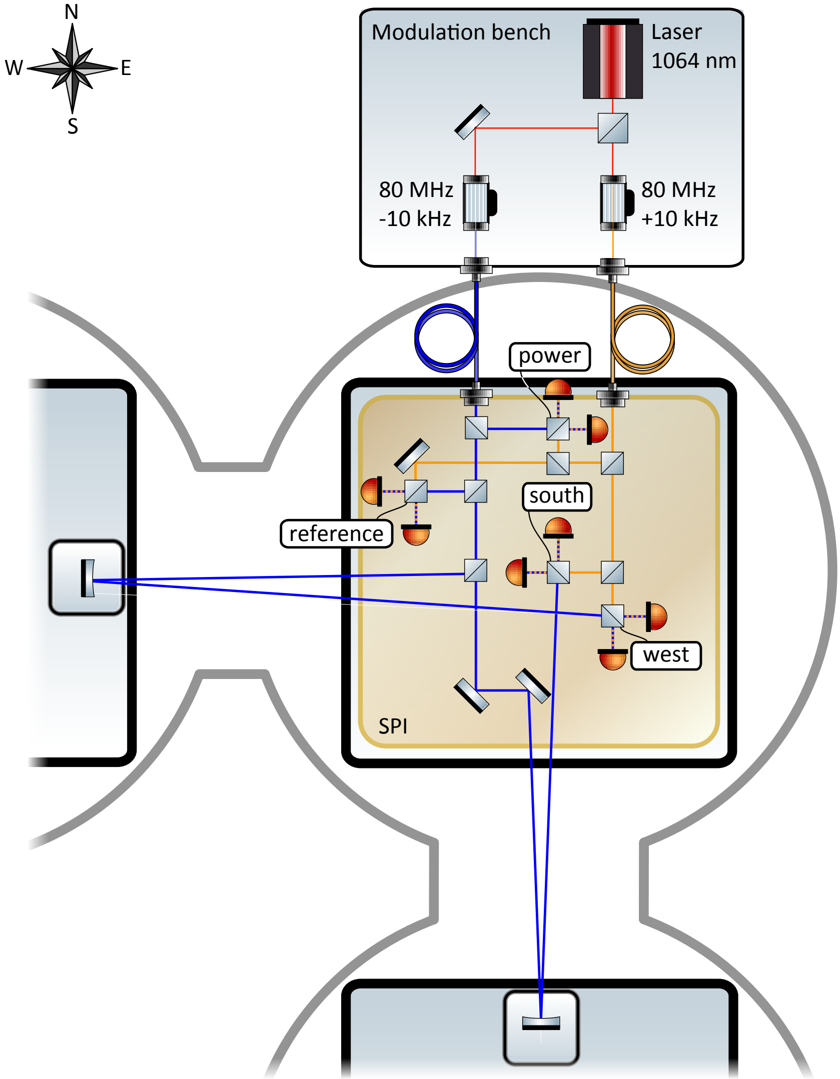

Figure 8.1.: Simplified sketch of the major components of the SPI. The size of the SPI is strongly exaggerated: the base plate has a side length of 0.250 m, while the table side length is 1.75 m. A laser beam is split at the modulation bench and frequency-shifted by acousto-optic modulators operating near 80 MHz, with the two channels set to a heterodyne frequency difference of ±10 kHz. The beams are fed into the vacuum system via polarization maintaining single-mode optical fibres and split into four different interferometers. The interferometer marked as (power) is used for power stabilization and diagnostic purposes. The (reference) marked interferometer is used to cancel common mode fluctuations by subtracting them from all other interferometer outputs. The other two interferometers measure the differential motion between the central table, and the south and west table, respectively. Due to spatial restrictions, the beams on the central SPI baseplate are re-directed through additional mirrors, omitted here for simplicity.

Platform Interferometer (SPI). This residual motion is still present, although the tables are bolted to the same concrete foundation and the centres of the optical tables are separated by only 11.65 m.

The SPI is a set of four heterodyne Mach-Zehnder interferometers, as shown in figure 8.1. The power and reference interferometers are used for power monitoring and common noise subtraction. The two measurement interferometers (south and west) sense the differential motion of the optical tables in five degrees of freedom. The roll motion about the beam axis is not measured. The major component of the SPI, a low thermal expansion Zerodur plate with 250 mm side length, is located on the central table. The SPI optics are bonded to this plate to reduce thermal drift of the optical components. The far tables are solely equipped with a small plate carrying the end mirrors of the measurement interferometers. The signals of both measurement interferometers are used in feedback loops to actively reduce the differential table motion. Thereby, the far tables follow the motion of the central table.

The requirements of the SPI are specified as lowering of the differential motion between the tables below $100\,\mathrm{pm}/\sqrt{\mathrm{Hz}}$ and angular motion below $10\,\mathrm{nrad}/\sqrt{\mathrm{Hz}}$ at 10 mHz. See [Dahl2010, Dahl2012a] for specific details.

Initially, the SPI will be installed and tested on the two assembled (central and south) tables. The third (west) table, once assembled, will be equipped with the west interferometer end mirror and included into the control loop.

8.2. Experiments in the AEI 10 m Prototype

The seismically isolated optical tables allow for a variety of experiments to be set-up in the vacuum system. The main purpose of the AEI 10 m Prototype is the development and testing of new techniques for ground-based interferometric gravitational wave detectors, such as GEO600, and proposed third generation detectors, for instance the Einstein Telescope [Abernathy2011]. The AEI 10 m Prototype is designed to facilitate a Michelson interferometer, capable of reaching a sensitivity effectively limited by quantum noise in the measurement band. Experiments, such as exploring quantum mechanical effects in macroscopic objects [Müller-Ebhardt2008] and operating an interferometer below the Standard Quantum Limit (SQL) [Gräf2012] are being developed.

Laser system

The interferometer sensitivity is highly dependent on the quality of the laser. Thus, the AEI 10 m Prototype interferometer is equipped with an in-house developed 35 W solid-state laser [Frede2007] built by neoLASE. The laser light is coupled into the vacuum system via a photonic crystal fibre. A Pre-Mode Cleaner (PMC) is rigidly mounted to the in-vacuum table. It provides further spatial mode filtering and beam jitter suppression. The PMC serves as a fixed spatial reference for experiments; power fluctuations after this point are sensed and fed back to stabilize the laser output to a relative intensity noise of 5×10^{-9} [Westphal2012], following the amplitude stabilisation principle, as demonstrated in [Kwee2009]. At the time of writing the laser is being assembled and tested. About 8 W of highly stabilized light will be used for the

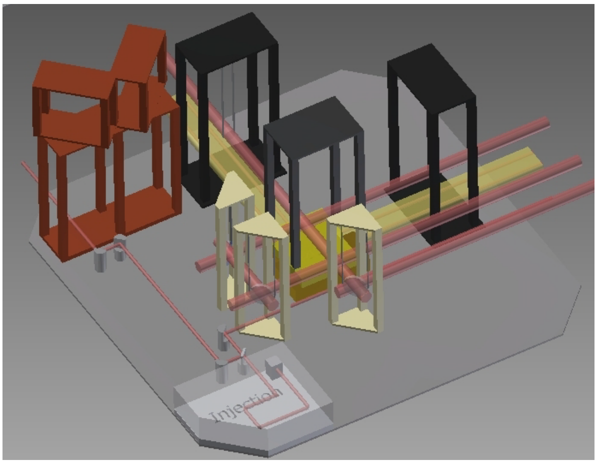

Figure 8.2: Virtual mock-up of the central table, showing different kinds of suspensions, visualizing the population on the table surface and tracing the paths of the laser beams. With just the SQL-interferometer (black), the reference cavity (red), and their necessary steering optics (bright yellow) the table will be quite crowded. The SPI (shown in gold) is positioned under the beam splitter suspension. The sizes of components somewhat accurately represent their envelope, and more accurately their footprint. The steering mirror holders have not been designed, but are shown as small as they can be. Three large laser beams, shown in red, go to the West table: one in the arm, and one each for the input and output mode-matching telescopes. The SPI beams are shown in yellow.

interferometer and further experiments.

Frequency reference cavity

The distance of about 10 m between the optical tables is used as length reference to improve the frequency stability of the laser. A triangular ring cavity, the *reference cavity*, is formed between three suspended mirrors, stretching between two tables, as shown in figure 8.3. The cavity round trip length is 21.2 m, with a finesse of about 5000, and an input power of 130 mW. The stability requirement of about $10\,\mathrm{Hz}/\sqrt{\mathrm{Hz}}$ at 20 Hz falling with f^{-1} [Kawazoe2010] is achieved by individually suspending all cavity mirrors from triple cascaded pendulums. The frequency reference cavity will be installed on the first two tables, after the SPI has been tested.
The mirrors of the reference cavity have a mass of 850 g to minimize the radiation pressure effects. Triple cascaded pendulums will be used to isolate horizontal seismic motion; two blade spring stages will provide vertical isolation above their corresponding natural frequencies of about 1 Hz. BOSEM style shadow sensors [Aston-thesis] with co-located voice-coil actuators and eddy current dampers will be used to locally measure the suspension resonances and apply control feedback to the upper suspension stage. Suspension test models, as shown in figure 8.2, will soon be assembled to measure the internal resonances of the suspension cages and to verify that the overall mass of about 13.5 kg per suspension fits into the payload budget of the tables.

SQL-interferometer

The SQL-interferometer, as shown in figure 8.3, is the first major experiment designed for the AEI 10 m Prototype facility with three fully operational tables. The SQL-interferometer is a Michelson-style interferometer with an arm length of about 10 m. The interferometer is optimized to be dominated by quantum noise in the measurement

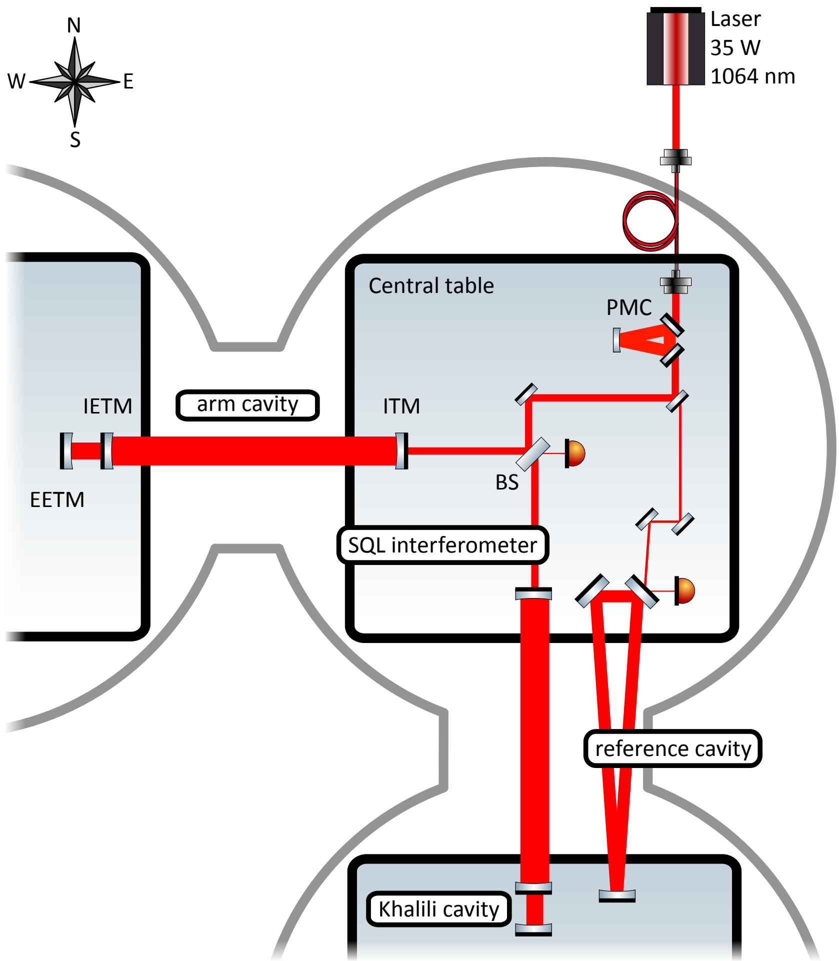

Figure 8.3.: Optical layout of the sub-SQL interferometer and. The 8 W laser light is sent through a photonic-crystal fibre into the vacuum system, additionally spatially filtered by a pre-mode cleaner (PMC). 130 mW of the laser power are split off to stabilize the laser frequency by sensing the length of the triangular reference cavity with a finesse of 7300. The larger part of the light enters the Michelson interferometer, enhanced by arm-cavities with a finesse of 670, and sensed at the antisymmetric dark tuned port, where the light is quantum noise limited. In the initial configuration, the interferometer will be operated without the anti-resonant cavities (Khalili cavities), which will be retrofitted to reduce the coating thermal noise.

band around 200 Hz. This allows interferometric experiments at the standard quantum limit and research of macroscopic quantum mechanical effects [Westphal2012]. The interferometer infrastructure will allow to reach or even surpass the SQL by using macroscopic (100 g) test masses. Once the SQL is reached, squeezed-light input is foreseen to achieve sub-SQL sensitivity [Goßler2010].
The readout of large scale interferometers, such as gravitational wave detectors, is limited in the high frequency band by photon counting noise, called *shot noise*, as shown in figure 1.6. The shot noise causes a back-action force, measurable as small uncertainties during continuous measurements of mirror positions; the effect is called *radiation pressure noise* [Purdy2012]. The opto-mechanical coupling is inversely proportional to the mirror mass, thus the mass for the mirrors of the SQL-interferometer was chosen to be 100 g, as a trade-off between suspension thermal noise and coating thermal noise.
Cavities with a finesse of 670 are included into the arms of the Michelson interferometer to increase the shot noise to signal ratio. The initial design involves additional end mirror cavities, called Khalili cavities [Khalili2005], which will be retrofitted later to reduce the coating thermal noise. The Khalili cavities are tuned on anti-resonance for the carrier light. The number of coating layers contributes to the coating thermal noise. In the Khalili cavities, as shown in figure 8.3, a mirror with few coating layers is used as Input End Test Mass (IETM) while the End End Test Mass (EETM) is highly reflective, it therefore has many coating layers. The light from the arm cavity interferes destructively inside the Khalili cavity. Hence, the light is reflected by the anti-resonant Khalili cavity, not at the coating of the IETM. The number of coating layers involved is thereby smaller and the coating thermal noise will be reduced.

9. Thesis conclusion and outlook

This thesis gives a description of the assembly, performance evaluation, and improvement of the AEI-SAS. In the course of the thesis, two of three AEI-SAS were fully assembled and tested. The third AEI-SAS will be used to test improvement techniques for the system. The upgrades can be implemented later into the two existing devices. To verify the performance of the AEI-SAS, a horizontal shaker stand was developed, from which the system was suspended and shaken by a voice-coil actuator. The transfer function measured in the shaker provided a real displacement transmissibility of the system. The AEI-SAS achieved a maximum seismic isolation of $-80\,\mathrm{dB}$ in horizontal and $-50\,\mathrm{dB}$ in vertical degrees of freedom. Many resonances, which reduced the performance of the system above 10 Hz, were identified and counter-measures successfully tested. Newly introduced Fluorel™ pads damped the resonances of the intermediate plate and removed resonant modes of the spring box. The challenge of identifying and removing these resonances was a major cause for delay of the assembly of the tables.

During the assembly of the system, six Geometric Anti-Spring (GAS) filters were individually assembled and tuned to natural frequencies as low as 200 mHz. The GAS filter tuning and performance evaluation measurements were performed on a specially constructed vertical shaker stand. The tuning process involved subsequently increasing the radial compression of the blade springs of each GAS filter. In future, eddy-current damping for the GAS filter blades will reduce the blade resonances around 300 Hz. Therefore, a small magnet will be attached to each maraging steel blade. A copper cup on a pole will be bolted underneath, allowing the magnet to be inserted into the cup. The individual GAS filters achieved a maximum vertical vibration isolation of $-80\,\mathrm{dB}$. Achieving this low isolation level was made possible by Centre of Percussion (CoP) effect compensators, called magic wands. Their material was changed from aluminium to silicon carbide to increase their stiffness.

The horizontal isolation of each AEI-SAS is provided by a three-leg Inverted Pendulum (IP). The natural frequency of each IP was tuned towards 100 mHz. Each IP was equipped with CoP effect compensators, called bells, originally designed for HAM-SAS. These bells were shown to overcompensate the isolation performance of the AEI-SAS, due to their high mass. Therefore, the two AEI-SAS were installed without the compensators. In future, redesigned slim compensators can be used to improve the horizontal isolation performance.

The IP flexures and the IP legs have a non-negligible vertical compliance. It was discovered to be the cause for a tilt/bounce mode of the spring box at 17 Hz. Ideally, the upper and lower IP flexures should be identical. In future, thicker upper flexures and stiffer legs, made of steel instead of aluminium, will be used to increase the frequency of this mode.

The AEI-SAS, although a mostly passive mechanical system, is augmented with sensors and actuators. They are used for active feedback control of the table motion and damping of the natural modes of the system. The first successful tests of viscous modal damping were presented in this thesis. Advanced feedback controls will provide better results, especially once the SPI will be integrated into the control scheme. The total low-frequency table motion will be reduced by pushing the SPI control authority up to 1 Hz.

The content of this thesis is focussed on the work on the AEI-SAS. Further work did not find its way into the thesis, such as multiple long-term seismic measurements in the Prototype hall before vacuum system installation, or the participation in fabrication and testing of fused silica fibres in Glasgow for the Advanced LIGO suspensions.
Further, more radical changes are imaginable for future SAS designs:

- In the AEI-SAS, most components were built from aluminium for historical reasons: the aluminium HAM optical table was reused for HAM-SAS, therefore everything was made of aluminium. When the HAM-SAS design was converted to the AEI-SAS, the optical table and the base plate materials were changed to stainless steel, but not the intermediate plate and spring box. For more rigidity, stainless steel should be used for all large plates.

- The blades of the GAS filters have a sharp resonant mode around 300 Hz, depending on the tuning of the individual blades. Instead of using eddy-current damping, a resonant damping approach is conceivable. For that a small mass on a flexible rod (for example made of Viton®) can be clamped to the blade without machining it. By changing the length of the rod, the resonance frequency of the damper can be tuned to the exact resonance of each blade.

- The GAS filters are subject to thermal fluctuations and hysteresis. Especially when heated, the blades become softer. Thus, the GAS filters could be actively actuated by locally heating the blades to compensate for thermal drift and hysteresis effects.

- The intermediate plate was found to be rather soft at its fundamental bending modes. The plate exists in the AEI-SAS mainly due to historical reasons. In future designs the plate could be omitted. The optical table would then be placed directly on the GAS filters.

- The aluminium spring box is supposed to be a rigid structure supporting the GAS filters. Instead of bolting the spring box plates together, they should be welded to provide more rigidity.

- Alternatively, the spring box could be omitted completely, by connecting the GAS filters directly to the IP legs. Thereby the GAS filters could be placed upside-down and bolted directly to the optical table. The key stones would be placed directly on top of the IP legs. This would save vertical space and reduce horizontal GAS filter compliance coupling to the optical bench. However, in this configuration the tilt restoring force would be very low and a tilt stabilizer would become essential.

Appendix

A. Mathematical derivation of the harmonic oscillator

Mathematics is the tool specially suited for dealing with abstract concepts of any kind and there is no limit to its power in this field. All the same the mathematics is only a tool and one should learn to hold the physical ideas in one's mind without reference to the mathematical form.

Paul Dirac

Harmonic oscillators play an important role in physical and mechanical applications. Mathematical solutions of complicated mechanical systems can usually be simplified to describe them as solutions of harmonic oscillators. Examples of harmonic oscillators can be a mass on a spring or a pendulum with a mass, as shown in figure A.1. An oscillator performs periodic oscillations around its resting position.
An ideal (mathematical) pendulum is described as a massless leg with a payload on top performing small oscillations around the resting position. The restoring force of a pendulum is exerted by the gravity. A physical pendulum includes the mass of the leg, so that the moment of inertia of the massive leg must be taken into account.
A simple harmonic oscillator is a mass-spring system. The influence of gravity can be neglected for simplicity. Thus, the orientation of the spring can be in vertical or horizontal direction. In the simplest case, frictionless movement and massless linear spring can be assumed.
For a complete mathematical description of harmonic oscillators, please refer to relevant literature about vibration isolation, e.g. [Inman2001], from which the following section is derived. The following sections are brief summaries of the mathematics of the undamped free and the damped driven harmonic oscillator. Most books only focus on the driven harmonic oscillator, with the driving force acting on the mass. This section

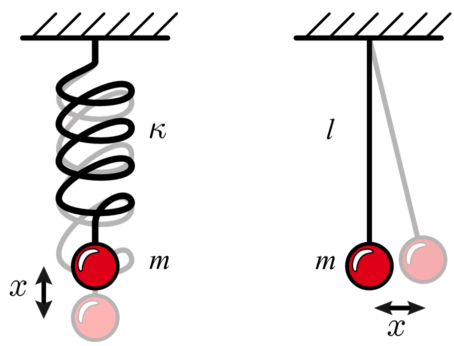

Figure A.1: Two examples of harmonic oscillators: a spring-mass oscillator and a mathematical pendulum. The masses are deflected by the distance, x, and perform oscillations at resonance frequency. The restoring force is provided by the spring or gravity, respectively.

describes the case, where the driving force originates from the oscillating ground, thus, the suspended mass is seismically isolated.

A.1. Undamped harmonic oscillator

The equation of motion of an undamped harmonic oscillator without external driving force is given as:

$$m\ddot{x} + \kappa x = 0 \tag{A.1}$$

where, m is the oscillator mass and κ the spring constant. Its solution can be written in three equivalent ways:

$$x(t) = a\mathrm{e}^{i\omega_n t} + a^*\mathrm{e}^{-i\omega_n t}\,, \tag{A.2}$$

with complex constants a and a^* and natural frequency $\omega_n = 2\pi f_n = \sqrt{\frac{\kappa}{m}}$.
An equivalent representation of the solution is:

$$x(t) = A\sin(\omega_n t + \phi)\,, \tag{A.3}$$

with real-valued constants A and ϕ, A being the amplitude and ϕ the phase of the oscillation.
The third possible representation of the solution is:

$$x(t) = A_1\cos(\omega_n t) + A_2\sin(\omega_n t)\,, \tag{A.4}$$

with real-valued constants A_1 and A_2. Initial conditions determine each pair of constants, which are related by:

$$A = \sqrt{A_1^2 + A_2^2} \qquad \phi = \tan^{-1}\left(\frac{A_1}{A_2}\right) \tag{A.5}$$

$$A_1 = a + a^* = 2\,\mathrm{Re}(a) \qquad A_2 = i(a - a^*) = -2\,\mathrm{Im}(a) \tag{A.6}$$

$$a = \frac{A_1 - iA_2}{2} \qquad a^* = \frac{A_1 + iA_2}{2} \tag{A.7}$$

with complex conjugate pairs, a and a^*, and real numbers, A_1 and A_2.

A.2. Damped driven harmonic oscillator

Figure A.2 shows a damped harmonic oscillator with a driving force originating from the ground. The mass, m, is connected to the ground by a spring with spring constant, κ, and a damping mechanism, with viscous (velocity dependant) damping coefficient, c. When the ground oscillates with $y(t)$, the displacement is transmitted through the spring-damper system to the mass, which oscillates with $x(t)$. As a reaction to the driving force of the ground oscillation, the system produces counter-forces in the spring and the damper. The sum of all counter-forces in the system is equal to the acceleration of the mass:

$$m\ddot{x} = -\kappa(x - y) - c(\dot{x} - \dot{y}) \tag{A.8}$$

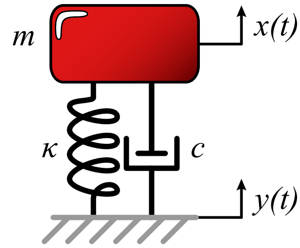

Figure A.2: System sketch of a damped harmonic oscillator. Shown are a mass, m, which is connected to the ground by a spring with spring constant, κ. The system is viscously damped with damping coefficient, c. The driving force originates from the ground, expressed as ground displacement $y(t)$.

or

$$m\ddot{x} + c\dot{x} + \kappa x = c\dot{y} + ky\,. \tag{A.9}$$

After dividing by m and using the substitutions:

$$\frac{\kappa}{m} = \omega_n^2 \qquad \text{and} \qquad \frac{c}{m} = 2\zeta\sqrt{\frac{\kappa}{m}} = 2\zeta\omega_n = \frac{\omega_n}{Q}\,,$$

equation (A.9) can be rewritten to:

$$\ddot{x} + 2\zeta\omega_n\dot{x} + \omega_n^2 x = 2\zeta\omega_n\dot{y} + \omega_n^2 y\,, \tag{A.10}$$

where $\omega_n = 2\pi f_n$ is the natural frequency of the undamped spring, and the damping ratio, ζ, is defined as:

$$\zeta = \frac{c}{c_c} = \frac{c}{2\sqrt{m\kappa}} = \frac{c}{2m\omega_n} = \frac{1}{2Q}\,, \tag{2.7}$$

including Q, the quality factor of the oscillation, with $Q = \frac{\sqrt{m\kappa}}{c} = \omega_n\frac{m}{c}$, and c_c, the critical damping at $\zeta = 1$. Thus, with Q being a known physical quantity, the equation of motion (A.9) can be written without using the damping ratio, ζ:

$$\ddot{x} + \frac{\omega_n}{Q}\dot{x} + \omega_n^2 x = \frac{\omega_n}{Q}\dot{y} + \omega_n^2 y\,. \tag{A.11}$$

The total solution of the differential equation for $x(t)$ is a sum of the homogeneous solution and the particular solution, which are derived below.

Homogeneous solution

The homogeneous solution, which describes the transient behaviour of the system depending on the initial conditions, depends on initial conditions and the driving excitation function. The homogeneous differential equation:

$$m\ddot{x} + c\dot{x} + \kappa x = 0 \tag{A.12}$$

has for initial conditions $x(0) = x_0$ and $\dot{x}(0) = v_0$ the solution:

$$x_h(t) = A\mathrm{e}^{-\zeta\omega_\mathrm{n}t}\sin(\omega_n^{damp}t + \phi) \tag{A.13}$$

with

$\omega_n = \sqrt{\frac{\kappa}{m}}$, the undamped natural frequency

$\omega_n^{damp} = \omega_n\sqrt{1-\zeta^2}$, the damped natural frequency

$\zeta = \frac{c}{2m\omega_n}$, the damping ratio

and the constants A and ϕ determined by initial conditions:

$$A = \sqrt{x_0^2 + \left(\frac{v_0 + \zeta\omega_\mathrm{n} x_0}{\omega_n^{damp}}\right)^2}\,, \qquad \phi = \tan^{-1}\left(\frac{x_0\omega_n^{damp}}{v_0 + \zeta\omega_\mathrm{n} x_0}\right)\,.$$

Alternatively, the homogeneous solution is rewritten as:

$$x_\mathrm{h}(t) = \mathrm{e}^{-\zeta\omega_\mathrm{n} t}\left(\frac{v_0 + \zeta\omega_\mathrm{n} x_0}{\omega_n^{damp}}\sin(\omega_n^{damp} t) + x_0\cos(\omega_n^{damp} t)\right)\,. \tag{A.14}$$

Equations (A.13) and (A.14) show, that the homogeneous solution is transient: the amplitude of the oscillation is negligible for large times, t.

Particular solution

The particular solution is the steady state solution, after the homogeneous transient term died out. Assuming a sinusoidal driving force $y(t)$:

$$y(t) = Y\sin(\omega_\mathrm{d} t) \quad \Rightarrow \quad \dot{y}(t) = \omega_\mathrm{d} Y\cos(\omega_\mathrm{d} t)\,, \tag{A.15}$$

with driving amplitude, Y, and driving frequency, $\omega_d = 2\pi f_d$, the equation of motion (A.10) yields:

$$\ddot{x} + 2\zeta\omega_\mathrm{n}\dot{x} + \omega_\mathrm{n}^2 x = \underbrace{2\zeta\omega_\mathrm{n}\,\omega_\mathrm{d} Y}_{F_{0\mathrm{c}}}\cos(\omega_\mathrm{d} t) + \underbrace{\omega_\mathrm{n}^2\,Y}_{F_{0\mathrm{s}}}\sin(\omega_\mathrm{d} t)\,. \tag{A.16}$$

The particular solution, x_p can be seen as a superposition of two types of harmonic inputs: a sinusoidal part, x_ps, with amplitude, $F_{0\mathrm{s}} = \omega_\mathrm{n}^2\,Y$, and a cosine part, x_pc, with amplitude $F_{0\mathrm{c}} = 2\zeta\omega_\mathrm{n}\,\omega_\mathrm{d} Y$. Therefore, in a linear system like this, the steady-state solution is just the superposition of the two individual particular solutions:

$$x_\mathrm{p} = x_\mathrm{ps} + x_\mathrm{pc} \tag{A.17}$$

Particular solution: Sine-term The equation of motion with the sinusoidal part of the excitation force is written as:

$$\ddot{x} + 2\zeta\omega_n\dot{x} + \omega_n^2 x = F_{0\mathrm{s}}\sin(\omega_d t)\,, \tag{A.18}$$

with $F_{0\mathrm{s}} = \omega_n^2\,Y$. The particular solution of the sine part, x_ps, is solved with the Ansatz:

$$x_\mathrm{ps} = A_\mathrm{s}\cos(\omega_d t) + B_\mathrm{s}\sin(\omega_d t)\,, \tag{A.19}$$

The coefficients of the sine-term A_{s} and B_{s} are obtained by inserting the Ansatz for x_{ps}, from equation (A.19) and its derivatives, into the equation on motion (A.18), and solving the equation system for A_{s} and B_{s}:

$$A_{\mathrm{s}} = \frac{-2\zeta\omega_n\omega_d F_{0\mathrm{s}}}{(\omega_n^2-\omega_d^2)^2+(2\zeta\omega_n\omega_d)^2}\,, \qquad B_{\mathrm{s}} = \frac{(\omega_n^2-\omega_d^2)F_{0\mathrm{s}}}{(\omega_n^2-\omega_d^2)^2+(2\zeta\omega_n\omega_d)^2}\,. \tag{A.20}$$

According to equivalence of equations (A.4) and (A.3), the sine-part of the particular solution $x_{\mathrm{ps}}(t)$ from equation (A.19) can be expressed as:

$$x_{\mathrm{ps}}(t) = X_{\mathrm{s}}\sin(\omega_d t+\theta_{\mathrm{s}})\,, \tag{A.21}$$

where X_{s} is the amplitude and θ_{s} is the phase of sine-part of the solution, which are defined according to equation (A.5) as:

$$X_{\mathrm{s}} = \sqrt{A_{\mathrm{s}}^2+B_{\mathrm{s}}^2}\,, \qquad \theta_1 = \tan^{-1}\left(\frac{A_{\mathrm{s}}}{B_{\mathrm{s}}}\right)\,. \tag{A.22}$$

So that, the particular sine-part solution of equation (A.18) yields:

$$x_{\mathrm{ps}}(t) = \frac{\omega_n^2 Y}{\sqrt{(\omega_n^2-\omega_d^2)^2+(2\zeta\omega_n\omega_d)^2}}\sin(\omega_d t-\theta_{\mathrm{s}}) \tag{A.23}$$

with the sine-part phase of the driving force,

$$\theta_{\mathrm{s}} = \tan^{-1}\left(\frac{2\zeta\omega_n\omega_d}{\omega_n^2-\omega_d^2}\right)\,.$$

Particular solution: Cosine-term The cosine-term x_{pc} is obtained by the same method, using the cosine-part of the equation of motion (A.16):

$$\ddot{x}+2\zeta\omega_n\dot{x}+\omega_n^2 x = F_{0\mathrm{c}}\cos(\omega_d t)\,, \tag{A.24}$$

with $F_{0\mathrm{c}} = 2\zeta\omega_n\,\omega_d Y$. The cosine-part is solved with the same Ansatz, rewritten from equation (A.19):

$$x_{\mathrm{pc}} = A_{\mathrm{c}}\cos(\omega_d t)+B_{\mathrm{c}}\sin(\omega_d t)\,. \tag{A.25}$$

The coefficients A_{c} and B_{c} are then:

$$A_{\mathrm{c}} = \frac{(\omega_n^2-\omega_d^2)F_{0\mathrm{c}}}{(\omega_n^2-\omega_d^2)^2+(2\zeta\omega_n\omega_d)^2}\,, \qquad B_{\mathrm{c}} = \frac{2\zeta\omega_n\omega_d F_{0\mathrm{c}}}{(\omega_n^2-\omega_d^2)^2+(2\zeta\omega_n\omega_d)^2}\,, \tag{A.26}$$

and the cosine-part of the particular solution is defined according to the equivalence of equations (A.4) and (A.3) as:

$$x_{\mathrm{pc}}(t) = X_{\mathrm{c}}\cos(\omega_d t-\theta_{\mathrm{c}}) \tag{A.27}$$

with amplitude, X_{c}, and phase angle, θ_{c} defined analogue to equation (A.22) as:

$$X_{\mathrm{c}} = \sqrt{A_{\mathrm{c}}^2+B_{\mathrm{c}}^2}\,, \qquad \theta_{\mathrm{c}} = \tan^{-1}\left(\frac{B_{\mathrm{c}}}{A_{\mathrm{c}}}\right)\,. \tag{A.28}$$

Thus, the cosine-part of the particular solution is given as:

$$x_{\mathrm{pc}}(t) = \frac{2\zeta\omega_n\omega_d Y}{\sqrt{(\omega_n^2-\omega_d^2)^2+(2\zeta\omega_n\omega_d)^2}}\cos(\omega_d t-\theta_c)\,, \tag{A.29}$$

with the cosine-part phase of the driving force,

$$\theta_{\mathrm{c}} = \tan^{-1}\left(\frac{2\zeta\omega_n\omega_d}{\omega_n^2-\omega_d^2}\right) = \theta_{\mathrm{s}}\,.$$

Note, that the angle θ_{c} is equal to θ_{s} because the phase angle is independent of the excitation amplitude. The phase difference between the two particular solutions is accounted for by using the sine and cosine solution.

The total particular solution is given as the sum of the sine- and cosine-parts, from equations (A.23) and (A.29), respectively, written as:

$$\begin{aligned} x_{\mathrm{p}} &= x_{\mathrm{ps}} + x_{\mathrm{pc}} && \text{(A.30)}\\ &= \frac{\omega_n^2 Y\sin(\omega_d t-\theta_{\mathrm{s}}) + 2\zeta\omega_n\omega_d Y\cos(\omega_d t-\theta_{\mathrm{s}})}{\sqrt{(\omega_n^2-\omega_d^2)^2+(2\zeta\omega_n\omega_d)^2}}\,. && \text{(A.31)}\end{aligned}$$

After some rewriting of the equation and introducing an additional phase θ, equation (A.31) yields:

$$\underbrace{Y\omega_n\left(\frac{\omega_n^2+(2\zeta\omega_d)^2}{(\omega_n^2-\omega_d^2)^2+(2\zeta\omega_n\omega_d)^2}\right)^{\frac{1}{2}}}_{X}\cos\left(\omega_d t-(\theta_{\mathrm{s}}+\theta)\right)\,. \tag{A.32}$$

The two phase terms are defined as

$$\theta_{\mathrm{s}} = \tan^{-1}\left(\frac{2\zeta\omega_n\omega_d}{\omega_n^2-\omega_d^2}\right) \qquad \text{and} \qquad \theta = \tan^{-1}\left(\frac{\omega_n}{2\zeta\omega_d}\right) \tag{A.33}$$

With frequency ratio $r = \frac{\omega_{\mathrm{d}}}{\omega_{\mathrm{n}}}$, the magnitude, X, of the particular solution in equation (A.31) is denoted as:

$$X = Y\sqrt{\frac{1+(2\zeta r)^2}{(1-r^2)^2+(2\zeta r)^2}}\,. \tag{A.34}$$

The transfer function is given as the ratio X/Y. The harmonic oscillator isolates the ground motion, when $X/Y < 1$. To compute, at which corner frequency the vibration isolation starts, the transfer function is analysed at $X/Y = 1$. Solving for r, (and assuming only real values) the corner frequency ratio is calculated as:

$$\sqrt{\frac{1+(2\zeta r)^2}{(1-r^2)^2+(2\zeta r)^2}} = 1 \quad \Rightarrow \quad r = \sqrt{2}\,. \tag{A.35}$$

Thus, the isolator starts working above a frequency ratio $r > \sqrt{2}$; in other words, when the driving frequency is $\sqrt{2}$ larger than the natural frequency:

$$\omega_{\mathrm{d}} > \omega_{\mathrm{n}}\sqrt{2}\,.$$

The magnitude of a transfer function and the phase are plotted in a Bode diagram in figure 2.7 and discussed in chapter 2.3 on page 23.

The calculation would have been much shorter in the frequency domain. However, by descending into the frequency domain one deprives oneself of the pleasure of doing classical calculus in the good old time domain.

B. Linear stiffness of the IP

The flexing spring of the inverted pendulum (IP) can be substituted by a linear spring, as shown in figures B.1. The physical properties of the two systems remain identical. A flexure with torsion spring constant, κ, bent by an angle, θ, exerts a reaction torque, τ, given by:

$$\tau = -\kappa\theta\,. \tag{B.1}$$

The formula is analogous to the force in a spring with linear spring constant, k, elongated by x:

$$F = -kx\,. \tag{B.2}$$

Generally, the torque is defined as a force rotating a lever (IP leg) about its pivot (flexure). Thus, using the simplified model of the IP, as shown in figure 4.2a, the force, F, applied perpendicular to the IP leg with length L_l, bends the flexure. The tip of the leg is displaced by x. Since the force acts normal to the leg at radial distance, L_l, from the pivot, the torque on the flexure is given as:

$$\tau = FL_l = -kxL_l\,. \tag{B.3}$$

In the small angle approximation, as shown in equation (4.8), x is given as:

$$x \approx L_l\theta\,. \tag{B.4}$$

Inserting equation (B.4) in equation (B.3), and using the definition (4.1) of τ, gives:

$$\tau = \underbrace{-kL_l^2}_{-\kappa}\theta. \tag{B.5}$$

Thus the relation of k and κ, is given as:

$$\kappa = kL_l^2\,. \tag{B.6}$$

The torsion spring constant κ can be substituted by a linear spring constant k. This substitution is used in several publications [Losurdo-thesis, Takamori-thesis, Stochino-thesis]. However, in this thesis, κ – an existing property of the flexure – is preferred to the auxiliary value, k.

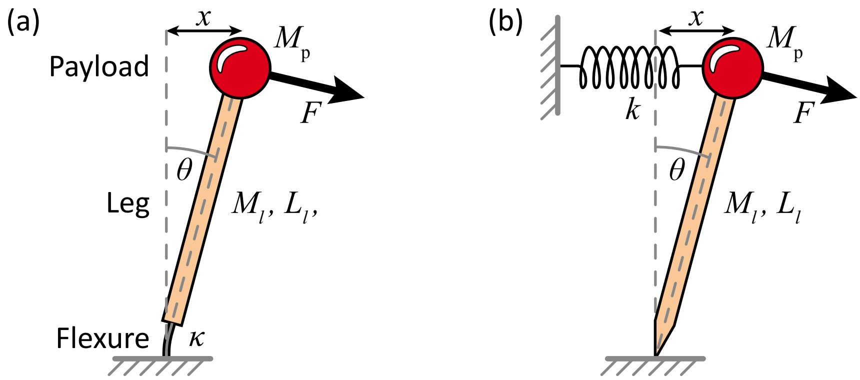

Figure B.1.: The torsion spring constant, κ, can be substituted by a linear spring constant, $k = \kappa/L_l^2$. The physical properties of the two systems are identical.

C. Fourier transform for deterministic functions

A periodic deterministic function of time, $s(t)$, is a representation of a signal with perfect time resolution, but it contains no explicit frequency information. Such a function can be converted into a function of frequency, $\tilde{s}(f)$, by means of the Fourier integral transform, which exists in several definitions. A general form for the transformation and the inverse transformation can be written as:

$$\mathcal{F}\big(s(t)\big) = \tilde{s}(\omega) \quad = \quad \sqrt{\frac{|b|}{(2\pi)^{1-a}}} \int_{-\infty}^{\infty} \mathrm{d}t\, s(t)\, \mathrm{e}^{ib\omega t} \tag{C.1}$$

$$\mathcal{F}^{-1}\big(\tilde{s}(\omega)\big) = s(t) \quad = \quad \sqrt{\frac{|b|}{(2\pi)^{1+a}}} \int_{-\infty}^{\infty} \mathrm{d}\omega\, \tilde{s}(\omega)\, \mathrm{e}^{-ib\omega t} \tag{C.2}$$

with the angular frequency $\omega = 2\pi f$, and the coefficients (a, b). The convention (0, -2π) is often used for signal processing, the convention (-1, 1) is usual in classical physics, (1, -1) in pure mathematics and system engineering, and (0, 1) in modern physics and software packages like Mathematica [Mathematica]. The latter convention is a symmetric transformation with equal pre-factors in front of the integral. Table C.1 shows Fourier transforms for different parameters (a, b).
Here shown is one convenient definition of the symmetric Fourier transform pair

Common convention	Settings	Fourier transform	inverse Fourier transf.
Mathematica default Modern physics	(0, 1)	$\frac{1}{\sqrt{2\pi}} \int_{-\infty}^{\infty} \mathrm{d}t\, s(t)\mathrm{e}^{i\omega t}$	$\frac{1}{\sqrt{2\pi}} \int_{-\infty}^{\infty} \mathrm{d}\omega\, \tilde{s}(\omega)\mathrm{e}^{-i\omega t}$
Pure mathematics Systems engineering	$(1, -1)$	$\int_{-\infty}^{\infty} \mathrm{d}t\, s(t)\mathrm{e}^{-i\omega t}$	$\frac{1}{2\pi} \int_{-\infty}^{\infty} \mathrm{d}\omega\, \tilde{s}(\omega)\mathrm{e}^{i\omega t}$
Classical physics	$(-1, 1)$	$\frac{1}{2\pi} \int_{-\infty}^{\infty} \mathrm{d}t\, s(t)\mathrm{e}^{i\omega t}$	$\int_{-\infty}^{\infty} \mathrm{d}\omega\, \tilde{s}(\omega)\mathrm{e}^{-i\omega t}$
Signal processing	$(0, -2\pi)$	$\int_{-\infty}^{\infty} \mathrm{d}t\, s(t)\mathrm{e}^{-i2\pi\omega t}$	$\int_{-\infty}^{\infty} \mathrm{d}\omega\, \tilde{s}(\omega)\mathrm{e}^{i2\pi\omega t}$

Table C.1.: Fourier transforms for different parameters (a, b)

[Rahman2011]:

$$\mathcal{F}\big(s(t)\big) = \tilde{s}(f) \quad = \int\limits_{-\infty}^{\infty} \mathrm{d}t\, s(t)\, \mathrm{e}^{-i2\pi f t} \tag{C.3}$$

$$\mathcal{F}^{-1}\big(\tilde{s}(f)\big) = s(t) \quad = \int\limits_{-\infty}^{\infty} \mathrm{d}f\, \tilde{s}(f)\, \mathrm{e}^{+i2\pi f t}\,. \tag{C.4}$$

Equation (C.3) can be rewritten as

$$\tilde{s}(f) = |\tilde{s}(f)|\, \mathrm{e}^{i\phi(f)}. \tag{C.5}$$

Thereby, $\phi(f)$ is the phase-delay spectrum with units of radian. A phase is an angle, defining the retardation of one wave or vibration with respect to another. One wavelength retardation is equivalent to a phase difference of 2π. As an example, the equation (C.3) transforms a function $s(t)$ with units of V into $\tilde{s}(f)$ with units of Vs or V/Hz. In practice, after calculating the Fourier transform, the power spectral density (PSD) is computed by taking the square of the Fourier transformed function and normalizing it by the bandwidth. Hence, the units of the PSD are V^2/Hz. See definition of the PSD units in table C.2 on page 147.

The Fourier transforms in equations (C.3) and (C.4) are defined for good behaved *physicist friendly* functions. A more detailed definition of a good function can be found in [Champeney1989]. Summarized, a function $s(t)$ is good when it is continuous and integrable [Smith2011], thus:

$$\int\limits_{-\infty}^{\infty} \mathrm{d}t |s(t)| < \infty \qquad \text{or} \qquad s(t) \to 0 \;\text{ for }\; t \to \pm\infty\,. \tag{C.6}$$

A function $s(t)$ that continues endlessly from $-\infty < t < +\infty$ has, in general, an infinite total power. In such a case, where the Fourier integral does not exit (diverges towards infinity), instead of using the full function $s(t)$ one can take a long, but finite, stretch of it, constructing a new function that equals $s(t)$ within the finite stretch but is zero everywhere else. The result is then divided by the length of the bandwidth $2T$:

$$\int\limits_{-\infty}^{\infty} \mathrm{d}t \Rightarrow \lim_{T\to\infty} \frac{1}{2T} \int\limits_{-T}^{+T} \mathrm{d}t\,. \tag{C.7}$$

The existence of Fourier transforms of real-world signals is seldom questioned in practice. Idealized signals, like sine waves continuing infinitely in time, can be resolved by using Dirac's delta function [Lighthill1958].

C.1. Power spectral density (PSD)

The computation of the PSD is a powerful tool to depict the amplitude and thereby the power of the seismic noise as a function of frequency. PSD is the power of a signal

normalized by the bandwidth, thus independent of the sampling frequency and is also not dependent on the duration of the measurement. That makes PSD comparable to different measurements, independent of sampling rates or measurement durations.
A PSD, or spectral noise density describes how the power, $P(t)$, of a time dependent signal, $s(t)$, is distributed in the frequency domain. The power is here the square of the amplitude of the signal:

$$P(t) = |s(t)|^2 \,. \tag{C.8}$$

According to Parseval's theorem, the total power of a signal in the time domain is the same as in the frequency domain. Thus the total power P_t is defined as:

$$P_t \equiv \int_{-\infty}^{\infty} \mathrm{d}t\, |s(t)|^2 = \int_{-\infty}^{\infty} \mathrm{d}f\, |\tilde{s}(f)|^2. \tag{C.9}$$

Experimentalists often use the one-sided PSD, when they want to know how much power is contained in a frequency interval between 0 and f_i. Then, there is no need to distinguish between positive and negative frequencies f, but rather integrate over f as varying from 0 to f_i. In such cases, the one-sided PSD, $\tilde{P}_s(f)$, of the function $s(t)$ is defined as:

$$\begin{aligned} \mathrm{PSD}_s \equiv \tilde{P}_s(f) &= |\tilde{s}(f)|^2 + |\tilde{s}(-f)|^2 && \text{for}\, 0 \leq f < \infty && \text{(C.10)} \\ &= 2|\tilde{s}(f)|^2 && \text{for real function}\, s(t)\,. && \text{(C.11)} \end{aligned}$$

Without the factor 2, definition (C.11) is simply the two-sided PSD. The total power P_t is then just the integral of the one-sided PSD, $\tilde{P}_s(f)$, from $f = 0$ to $f \to \infty$, [Press1992] which is consistent with Parseval's theorem:

$$P_t \equiv |s(t)|^2 = \int_0^{\infty} \mathrm{d}f\, |\tilde{s}(f)|^2 \,. \tag{C.12}$$

C.1.1. Wiener-Khinchin theorem

It is practical to compute the power spectral density (PSD) of a time-domain signal (e.g. with units of V) by using the Fourier transform, then taking the square of the absolute value of the Fourier transformed function and normalizing it by the bandwidth. This way the units of the PSD become V^2/Hz. See definition of the PSD units in table C.2 on page 147.
In a case where the signal, $s(t)$, is a stochastic function of time – which means the average power of the signal is not zero, thus the signal is not square integrable – the Fourier transform does not exist. Instead, according to the Wiener-Khinchin theorem [Cohen1992, Cohen1998], the PSD can be expressed as follows:

The power spectral density (PSD) is the
Fourier transform of the autocorrelation function.

An autocorrelation function can be understood as the search of similarity between a waveform and its time shifted copy, as a function of a time-shift, τ. The autocorrelation tells, how fast does $s(t)$ loose the memory of itself. Thus the autocorrelation function, $R(\tau)$, gives the degree of self-similarity of the signal $s(t)$, with a time interval τ, by which the signal $s(t+\tau)$ is shifted against itself:

$$R(\tau) = \Big(s(t) \times s(t)\Big)(\tau) = \int_{-\infty}^{\infty} \mathrm{d}t\, s(t)s(t+\tau)\,. \tag{C.13}$$

If the function $s(t)$ is defined for all times ($-\infty$ to $+\infty$), so the integral diverges towards infinity, then the normalized autocorrelation $P(\tau)$, computed using equation (C.7), is defined as:

$$P(\tau) = \lim_{T\to\infty} \frac{1}{2T} \int_{-T}^{+T} \mathrm{d}t\, s(t)s(t+\tau)\,. \tag{C.14}$$

Now, the PSD $\equiv \tilde{P}(f)$, is defined as the Fourier transform of the (normalized) autocorrelation function $P(\tau)$:

$$\tilde{P}(f) = \int_{-\infty}^{+\infty} \mathrm{d}\tau\, P(\tau)\mathrm{e}^{-i2\pi f\tau}\,. \tag{C.15}$$

The PSD of $s(t)$ in (C.15) is given in units V^2/Hz, if $s(t)$ was measured in V.

The total power, or variance, in the frequency band from f_1 to f_2 is the integral over the PSD of $s(t)$

$$P_t(f_1, f_2) = 2\int_{f_1}^{f_2} \mathrm{d}f\, \tilde{P}(f)\,. \tag{C.16}$$

Finally, the root mean square (rms) amplitude $s_{\mathrm{rms}}(f_1, f_2)$ of the band-pass filtered time series is then the square root of the total power $P_t(f_1, f_2)$ within the frequency band from f_1 to f_2:

$$s_{\mathrm{rms}}(f_1, f_2) = \sqrt{P_t(f_1, f_2)}\,. \tag{C.17}$$

C.2. Discrete signal analysis

The analytical formalisms stated so far, are presented to give an insight to mathematical working techniques. However, in an experimentalist's everyday life, it is unlikely to have a continuous function, $s(t)$, to be given to work with. Measured data is rather available as a sequence of sampled measurements $s(t_k)$. Therefore, a definition of the discrete Fourier transformation (DFT) is needed.
The samples have a discrete set of time intervals, t_k. The samples are separated by the time Δt, thus the total duration of a measurement with N samples is $T = N\Delta t$. The separation between two data samples in the frequency domain is called a *bin*. Each frequency bin collects the energy within the range of the bin width. The width of a frequency bin, also called frequency resolution, f_{res}. It is the smallest resolvable distance between two samples in the frequency domain. This minimal resolvable frequency

width, f_{res}, corresponds to the reciprocal of the longest possible time interval, which is the total measurement time, $N\Delta t$. Thus, the frequency resolution, f_{res}, is given by the reciprocal length of the DFT or by the sample frequency, f_{s}, divided by the number of sampled data points, N:

$$f_{\mathrm{res}} = \frac{1}{N\Delta t} = \frac{f_s}{N}\,. \tag{C.18}$$

According to Nyquist theorem [Nyquist1928], a band limited analogue signal can be perfectly reconstructed from a sequence of samples, provided the sampling frequency, f_{s}, is larger than two times the highest resolvable frequency, f_{max}, also called Nyquist frequency, f_{Ny}:

$$f_{\mathrm{Ny}} \equiv f_{\mathrm{max}} > \frac{f_{\mathrm{s}}}{2}\,. \tag{C.19}$$

C.2.1. Discrete Fourier transform (DFT)

The *continuous* Fourier transform, as it was defined in equation (C.3) on page 142, is written as:

$$\tilde{s}(f) = \int\limits_{-\infty}^{\infty} \mathrm{d}t\, s(t)\, \mathrm{e}^{-i2\pi f t}\,. \tag{C.3}$$

To define the *discrete* Fourier transform, the continuous function $s(t)$ can be discretized to $s(t_k)$, where t_k is a set of N time intervals, with $k = 0, \ldots, N-1$. Then the discrete Fourier transform can be written as:

$$\tilde{s}_k = \sum_{k=0}^{N-1} s_k\, \mathrm{e}^{-i2\pi n \frac{k}{N}}\,. \tag{C.20}$$

The inverse discrete Fourier transform is applied analogously:

$$s_k = \frac{1}{N} \sum_{n=0}^{N-1} \tilde{s}_n\, \mathrm{e}^{i2\pi n \frac{k}{N}}\,, \tag{C.21}$$

with the discrete Fourier transformed $\tilde{s}_k$ being a complex number that encodes both amplitude and phase of a sinusoidal components of function s_k. The frequency is hereby $\frac{k}{N}$ cycles per sample. The amplitude and phase of the inverse DFT are

$$\frac{|\tilde{s}_k|}{N} = \frac{\sqrt{\mathrm{Re}(\tilde{s}_k)^2 + \mathrm{Re}(\tilde{s}_k)}}{N} \qquad \text{and} \qquad \arg(\tilde{s}_k) = \mathrm{atan2}\big(\mathrm{Im}(\tilde{s}_k), \mathrm{Re}(\tilde{s}_k)\big)\,, \tag{C.22}$$

respectively, where $\mathrm{atan2}(y, x)$ is the two-argument form of the arctan function; for more information look, e.g in [Bronstein], for cyclometric (inverse trigonometric) functions. Similar to continuous one-sided PSD defined in equation (C.11), the discrete one-sided PSD at frequency $f_k = k/T$, is defined as:

$$\tilde{P}_s(f_k) = 2\frac{|\tilde{s}_k|^2}{T}\,. \tag{C.23}$$

The discrete Fourier transform of a waveform like $\cos(2\pi ft)$ develops non-zero values, called spectral leakage, at frequencies other than f. The maximal leakage occurs near the frequency f and decreases further away from it. Therefore, a smooth and properly normalized time domain taper, called window function, is applied to the data to reduce spectral leakage. An extensive overview of common window functions is given in [Heinzel2002]. The discrete Fourier transform is a special case of the Z-transform, see, for example, [Graf2004] for mode details.

C.2.2. Power spectrum (PS) and linear spectrum (LS)

The PSD can be converted into a power spectrum (PS), by

$$\mathrm{PS} = \mathrm{PSD} \times \mathrm{ENBW}\,, \tag{C.24}$$

with the equivalent noise bandwidth (ENBW) of the measurement, PSD in units of V^2/Hz, and PS in units of V^2. The ENBW depends on the window function that was applied to the computed signal. When the input signal consists of random noise, the ENBW is proportional to the average power accumulated in each DFT bin. The power spectrum typically reveals a flat noise floor, caused by this effect. The height of the noise floor is proportional to the ENBW, thus different window functions produce different noise floor levels.

C.2.3. Linear spectral density (LSD)

Once the PSD is obtained, one can easily convert it into a linear spectral density (LSD) with the identity

$$\sqrt{\mathrm{PSD}} = \mathrm{LSD}\,. \tag{C.25}$$

The units of the PSD and the LSD should not be confused. The PSD of $s(t)$ in (C.15) is given in units V^2/Hz, if $s(t)$ was measured in V, and the LSD has the units of $\mathrm{V}/\sqrt{\mathrm{Hz}}$. PSD is the power of a signal normalized by the bandwidth, thus independent of the sampling frequency and is also not dependent on the duration of the measurement. That makes PSD comparable to different measurements, independent of sampling rates.

To calculate the linear spectrum (LS) or the power spectrum (PS) the equation (C.26) is helpful:

$$\mathrm{LS} = \sqrt{\mathrm{PS}} = \mathrm{LSD} \times \sqrt{\mathrm{ENBW}}, \tag{C.26}$$

with the equivalent noise bandwidth (ENBW), defined in equation (C.27) on page 147, as the width of the window function divided by the duration of the measurement. The LSD has the units of $V/\sqrt{\mathrm{Hz}}$ and LS in units of V. Table C.2 summarizes the relationship between the power spectrum, linear spectrum and their spectral densities.

C.2.4. Window functions

The ENBW of the applied window function can be interpreted as the width of a rectangular filter that passes the same amount of white noise as the window function

Abbrev.	Name	Relation	Unit
PSD	power spectral density		$\mathrm{V}^2/\sqrt{\mathrm{Hz}}$
PS	power spectrum	$\mathrm{PS} = \mathrm{PSD} \times \mathrm{ENBW}$	V^2
LSD	linear spectral density	$\mathrm{LSD} = \sqrt{\mathrm{PSD}}$	$\mathrm{V}/\sqrt{\mathrm{Hz}}$
LS	linear spectrum	$\mathrm{LS} = \sqrt{\mathrm{PS}} = \mathrm{LSD} \times \sqrt{\mathrm{ENBW}}$	V

Table C.2.: Relation between the linear spectrum (LS), the power spectrum (PS), and their spectral densities (LSD and PSD). The ENBW is the equivalent noise bandwidth, defined in equation (C.27) [Heinzel2002].

[Agilent]. The ENBW is calculated by:

$$\mathrm{ENBW} = \mathrm{NENBW} \cdot f_{\mathrm{res}} = \mathrm{NENBW} \cdot \frac{f_{\mathrm{s}}}{N} = \frac{\mathrm{NENBW}}{N\Delta t}\,, \tag{C.27}$$

with the frequency resolution, f_{res}, (width of one frequency bin), the sampling frequency, f_{s} and the *normalized* effective noise bandwidth, $\mathrm{NENBW} = \mathrm{ENBW} \cdot N\Delta t$, with $N\Delta t$ the duration of the record. The NENBW is specific for each window function. An overview of few prominent window functions with the associated NENBW value is given in table C.3, according to [Heinzel2002]. For example, a Hanning window with an input of 0.5 seconds will result in an ENBW of (1.5 bins / 0.5 s) = 3 Hz. Thus it is important to know how the PSD was recorded, to re-construct the PS of the signal. Selecting the right window function is tricky, because each window function has its own characteristics and suitability for different applications. To choose a window function, one has to estimate the frequency content of the signal. The Hanning window is in generally suitable for most applications. It has good frequency resolution and low spectral leakage. The Hamming window offers a narrow bandwidth and might be useful in situations where the amplitude accuracy is unimportant. Nuttall and Kaiser are families of window functions with variable parameters. Only examples of one of each window function are given here. Both window function families are similar, they have very low spectral leakage combined with reasonable bandwidth and amplitude error. They are suitable to detect small sinusoidal signals being very close in frequency to large signals, or can be used as a general-purpose window in applications with high dynamic range if amplitude accuracy for sinusoidal signals is not very important. More examples of window functions are given in [Heinzel2002].

Averaging and overlap

Computing one estimate of a spectrum by multiplying one segment of the time series with a suitable window function, to perform a DFT, will produce rather noisy results, due to stochastic nature of the signal. Increasing the length N of the DFT will not improve the signal to noise ratio, but rather reduce the width of one frequency bin without improving the variance. Instead, the average of M estimates is taken, thereby reducing the standard deviation of the averaged result by a factor of $1/\sqrt{M}$. Two aspects must be kept in mind: the signal has to remain stationary during the averaging and the averaging must be done with the power spectrum (PS) or the power spectral

Filter name	NENBW [bins]	Overlap [%]
Hanning	1.5000	50.0
Hamming	1.3628	50.0
Nuttall	1.944	64.7
Kaiser	1.7952	61.9

Table C.3.: An overview of window functions with their normalized effective noise bandwidth (NENBW) values and the corresponding recommended overlap.

density (PSD), the square roots can be computed after the averaging to get the square roots LS or LSD.
A fraction of data gets lost, when a long continuous data stream is split into several non-overlapping segments and each segment is processed by a DFT with a window function, which is zero at its boundaries. Therefore the segments have to overlap, to get the maximal information out of the data stream. The optimal amount of overlap depends on the window function. Relatively wide windows, such as Hanning, are commonly used with 50 % overlap, while narower window functions require a higher overlap. Table C.3 provides the recommended overlap for the listed window functions.

D. Coordinate Transformation Matrix

All sensors and actuators in the AEI-SAS are available in triplets placed at a certain distance from the centre of the table at an angle of 120° between each other. The only exception are the four vertical stepper-motors at each corner of the optical table, as shown in figure 7.2. To convert the signals from local coordinates of sensors (for example the horizontal sensors H_1, H_2, H_3) into interferometer coordinates (x, y, ϑ_z), as shown in figure D.1, a transformation matrix $\mathbf{M}$ is needed in the following form:

$$\vec{H} = \mathbf{M}\,\vec{x} \tag{D.1}$$

The following examples demonstrate how to obtain the geometrical transformation matrix of the coordinate systems for the horizontal and vertical LVDTs. All other matrices (for the actuators, accelerometers, geophones, and stepper motors) are obtained in a similar way.

Horizontal signal transformation

The example shown here, refers to three horizontal LVDTs placed on a circle with a radius, R, around the table centre in an angle of 120° between each other. The table motion produces signals H_1, H_2, H_3 in the three sensors. The sensors are capable only of measuring along their own axis of motion and are insensitive for displacement lateral to their direction of propagation. Hence, a unit vector $\hat{H}$ can be assigned to each sensor pointing into the direction of sensor motion. Those three unit vectors $\hat{H}_1$, $\hat{H}_2$, and $\hat{H}_3$ are basis vectors for the local coordinate system of the sensors.
To intuitively understand the motion of the table, the sensor signals need to be transformed into interferometer coordinates with basis vectors $\hat{e}_x$ and $\hat{e}_y$ pointing

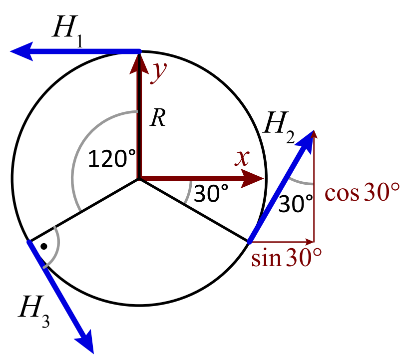

Figure D.1: The sensor orientation and naming convention of horizontal LVDT signals in the central AEI-SAS. A pure rotation about the vertical z-axis is shown.

along the interferometer arms, see figure 7.1.
In the most simple case of a pure translation of the table, the coordinate transformation is a simple vector projection. One can write in general:

$$\vec{H}_i = H_i \cdot \hat{H}_i \stackrel{!}{=} x\hat{e}_x + y\hat{e}_y = \begin{pmatrix} x \\ y \end{pmatrix} . \tag{D.2}$$

The sensor H_1 measures directly the translation in x direction ($\vec{x} = x \cdot (-\hat{e}_x)$) and no component in y direction. The coordinate transformation for vector $\vec{H}_1$ is thereby:

$$\begin{pmatrix} x \\ y \end{pmatrix} \stackrel{!}{=} H_1 \begin{pmatrix} -1 \\ 0 \end{pmatrix} . \tag{D.3}$$

As shown in figure D.1, the translation vector $\vec{H}_2$ for H_2 signals is projected onto the x- and y-axes. Then the components of the signal are given as

$$x = H_2 \cdot \sin(30^\circ) = H_2 \cdot \frac{1}{2} \quad \text{and} \quad y = H_2 \cdot \cos(30^\circ) = H_2 \cdot \frac{\sqrt{3}}{2} .$$

With equation D.2 one receives:

$$\begin{pmatrix} x \\ y \end{pmatrix} \stackrel{!}{=} \begin{pmatrix} H_2 \cdot \sin(30^\circ) \\ H_2 \cdot \cos(30^\circ) \end{pmatrix} = \frac{H_2}{2} \begin{pmatrix} 1 \\ \sqrt{3} \end{pmatrix} . \tag{D.4}$$

Similar to $\vec{H}_2$, the $\vec{H}_3$ projection to the interferometer coordinate system is deduced as:

$$\begin{pmatrix} x \\ y \end{pmatrix} \stackrel{!}{=} \frac{H_3}{2} \begin{pmatrix} 1 \\ -\sqrt{3} \end{pmatrix} . \tag{D.5}$$

The only difference between $\vec{H}_2$ and $\vec{H}_3$ is the sign of the y-component, because the vector $\vec{H}_2$ is pointing into the positive y-direction. Equations (D.3-D.5) can be solved for H1, H2, and H3:

$$H_1 = \begin{pmatrix} -1 & 0 \end{pmatrix} \begin{pmatrix} x \\ y \end{pmatrix} = -x \tag{D.6}$$

$$H_2 = \begin{pmatrix} 1/2 & \sqrt{3}/2 \end{pmatrix} \begin{pmatrix} x \\ y \end{pmatrix} = \frac{1}{2}x + \frac{\sqrt{3}}{2}y \tag{D.7}$$

$$H_3 = \begin{pmatrix} 1/2 & -\sqrt{3}/2 \end{pmatrix} \begin{pmatrix} x \\ y \end{pmatrix} = \frac{1}{2}x - \frac{\sqrt{3}}{2}y \quad , \tag{D.8}$$

so that the coordinate transformation matrix looks as follows:

$$\begin{pmatrix} H_1 \\ H_2 \\ H_3 \end{pmatrix} = \begin{pmatrix} -1 & 0 \\ 1/2 & \sqrt{3}/2 \\ 1/2 & -\sqrt{3}/2 \end{pmatrix} \begin{pmatrix} x \\ y \end{pmatrix} . \tag{D.9}$$

A table rotation by the angle ϑ_z about the vertical axis would be measured by all three horizontal signals. Therefore, the distance, which each sensor covers if the table rotates by ϑ_z, is given as $H_i = R\vartheta_z$. This value is added to each of the previously obtained transformed coordinates:

$$H_1 = -x + R\vartheta_z \tag{D.10}$$

$$H_2 = \frac{1}{2}x + \frac{\sqrt{3}}{2}y + R\vartheta_z \tag{D.11}$$

$$H_3 = \frac{1}{2}x - \frac{\sqrt{3}}{2}y + R\vartheta_z \quad . \tag{D.12}$$

Finally the transformation matrix M is found to be:

$$\begin{pmatrix} H_1 \\ H_2 \\ H_3 \end{pmatrix} = \begin{pmatrix} -1 & 0 & R \\ 1/2 & \sqrt{3}/2 & R \\ 1/2 & -\sqrt{3}/2 & R \end{pmatrix} \begin{pmatrix} x \\ y \\ \vartheta_z \end{pmatrix} \quad , \tag{D.13}$$

with the back-transformation:

$$\begin{pmatrix} x \\ y \\ \vartheta_z \end{pmatrix} = \frac{1}{3} \begin{pmatrix} -2 & 1 & 1 \\ 0 & \sqrt{3} & -\sqrt{3} \\ 1/R & 1/R & 1/R \end{pmatrix} \begin{pmatrix} H_1 \\ H_2 \\ H_3 \end{pmatrix} \quad , \tag{D.14}$$

with R, the distance of the device from the centre of the optical table, as shown in figure 7.2.

All channel outputs shown in this chapter are presumed to be positive, if no sign is assigned to them. Positive displacement should point in the same direction as the x, y, and z positive coordinates. Positive rotations are counter-clockwise, following the right-hand rule: the thumb points towards the rotational axis, the fingers point in the direction of the positive rotation. It is important to mention, that some devices have a different orientation than depicted in figure D.1. Therefore one needs to multiply the according channel with -1 to get the correct output. The actual orientation of sensors and actuators in the central AEI-SAS is sketched in figure D.2.

Vertical signal transformation

The derivation of the transformation matrix for vertical signals is performed identically to the horizontal. The positions of the vertical LVDTs are shown in figure D.3. Figure D.3a illustrates the three vertical devices, with 120° spacing between them. Again, the sensors are handled separately, by deducing which rotational mode they can sense, as illustrated in figure D.3b. In the end, the total vertical displacement, as shown in figure D.3c, is accounted for by adding the z component to each signal.

Figure D.3b shows that signal V_2 from LVDT V_2 can only provides information about the tilting of the optical table by the angle ϑ_x about the x-axis. The sensor signal is zero at tilting about the y-axis. Thus, the V_2 signal is given as:

$$V_2 = \vartheta_x R \, , \tag{D.15}$$

with R, the distance of the device from the centre of the optical table, as given in a table in figure 7.2.

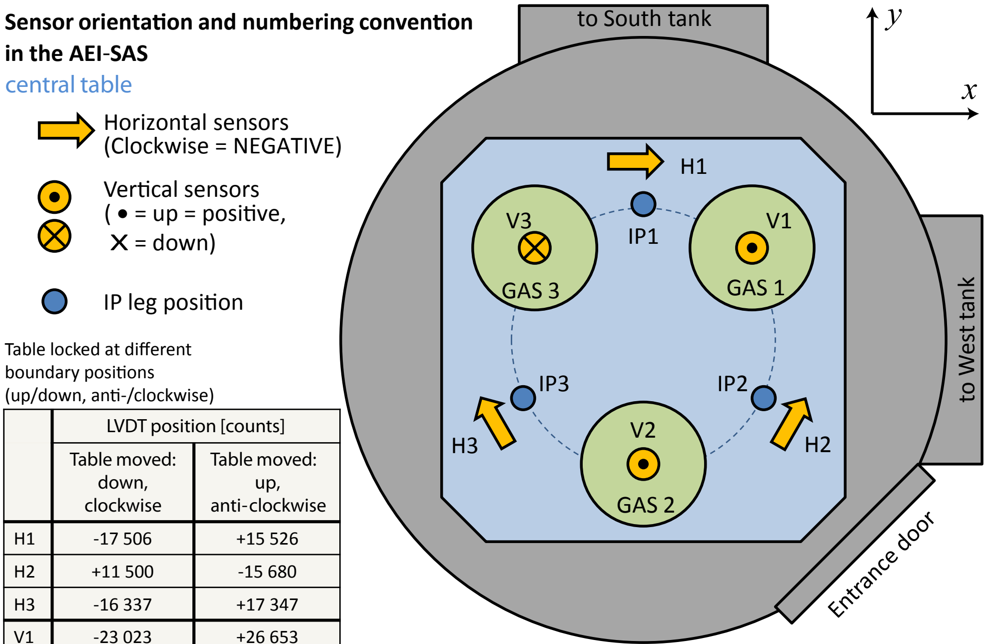

	LVDT position [counts]	
	Table moved: down, clockwise	Table moved: up, anti-clockwise
H1	-17 506	+15 526
H2	+11 500	-15 680
H3	-16 337	+17 347
V1	-23 023	+26 653
V2	-25 238	+26 320
V3	+22 715	-26 786

Figure D.2.: The numbering convention and orientation of sensors in the central table (as it was in February 2010). The orientation of the devices might change later due to repairs or coil replacement. The table shows maximal and minimal achievable values of the sensors. The numbers are given in units of counts, with the maximal/minimal value limited by the analogue-to-digital converter at $\pm(2^{16})/2 = \pm 32\,768$ counts. The orientation of the sensors can be adjusted in the control loop by assigning a minus sign at the corresponding input signals.

The signals V_1 and V_3 provide information about the rotation by ϑ_x and ϑ_y. They are nearly identical, except for the sign of the cosine component:

$$V_1 = \vartheta_x R \sin(30°) - \vartheta_y R \cos(30°) \tag{D.16}$$
$$V_3 = \vartheta_x R \sin(30°) + \vartheta_y R \cos(30°)\,. \tag{D.17}$$

The cosine and sine terms denote the fraction of the full circle radius, on which the sensors are positioned, see figure D.3. For example, the sensor V_2 is positioned at the full distance from the centre of the table. Therefore, its distance ratio is 1. The other two sensors, are half way to the edge of the circle in y-direction (deduced from $\sin(30°) = \frac{1}{2}$) and $\sqrt{3}/2$ in x-direction (as in $\cos(30°) = \sqrt{3}/2$). Thus, the three signals

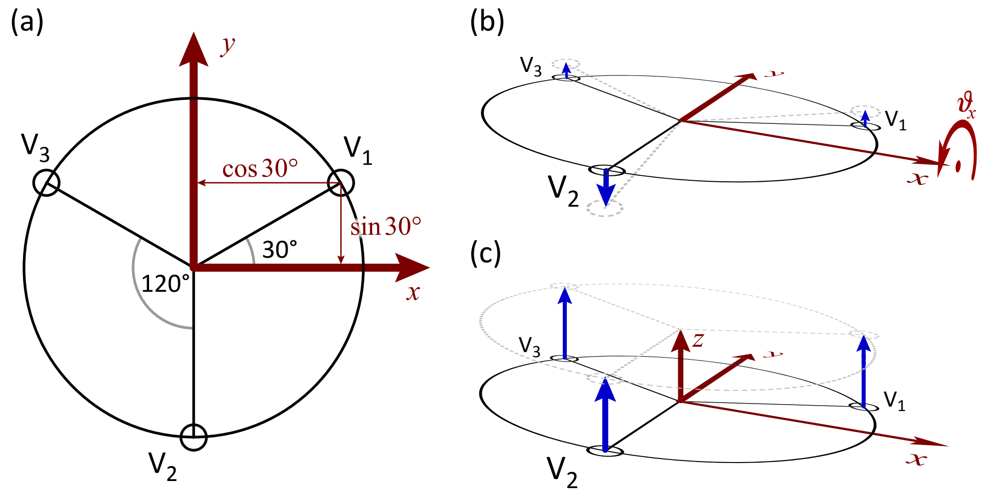

Figure D.3.: (a) The sensor orientation with respect to the interferometer coordinates and the naming convention of vertical LVDT signals in the central AEI-SAS. (b) A pure rotation by a positive angle ϑ_x about the horizontal x-axis produces negative V_2 signals and positive V_1 and V_3. (c) A pure vertical displacement of the optical table is sensed by all three devices.

provide the pure rotational information given as:

$$V_1 = \vartheta_x R \frac{1}{2} - \vartheta_y R \frac{\sqrt{3}}{2} \tag{D.18}$$

$$V_2 = \vartheta_x R \tag{D.19}$$

$$V_3 = \vartheta_x R \frac{1}{2} + \vartheta_y R \frac{\sqrt{3}}{2} \,. \tag{D.20}$$

As illustrated in figure D.3c, all three sensors detect the vertical table motion as a common signal in each device. Therefore, the vertical displacement by z is added to each signal:

$$V_1 = \vartheta_x R \frac{1}{2} - \vartheta_y R \frac{\sqrt{3}}{2} + z \tag{D.21}$$

$$V_2 = \vartheta_x R + z \tag{D.22}$$

$$V_3 = \vartheta_x R \frac{1}{2} + \vartheta_y R \frac{\sqrt{3}}{2} + z \,. \tag{D.23}$$

Finally, the vertical transformation matrix is given as:

$$\begin{pmatrix} V_1 \\ V_2 \\ V_3 \end{pmatrix} = \begin{pmatrix} R/2 & -R\sqrt{3}/2 & 1 \\ R & 0 & 1 \\ R/2 & R\sqrt{3}/2 & 1 \end{pmatrix} \begin{pmatrix} \vartheta_x \\ \vartheta_y \\ z \end{pmatrix} , \tag{D.24}$$

and the back transformation from x,y,z coordinates to the sensor-aligned coordinates:

$$\begin{pmatrix} \vartheta_x \\ \vartheta_y \\ z \end{pmatrix} = \begin{pmatrix} -1/R & 2/R & -1/R \\ 1/\sqrt{2}R & 0 & -1/\sqrt{3}R \\ 1 & -1 & 1 \end{pmatrix} \begin{pmatrix} V_1 \\ V_2 \\ V_3 \end{pmatrix} . \tag{D.25}$$

Again, the radial sensor positions, R, from the centre of the optical table are given in figure 7.2. All other matrices are obtained equivalently, just the distance of the devices needs to be inserted.
The orientation of the the AEI-SASs with respect to the tank is needed to calculate the correct transformation matrix. The AEI-SAS orientation is determined by the optical table. The surface of the breadboards is marked with grooves indicating the position for the SPI. Since the two far tables are designed identically, the south table is rotated counter-clockwise by 90° with respect to the west table. Due to this reason the orientation of the table appears to be arbitrarily chosen and so seems the numeration of the components.

E. Cabling diagram

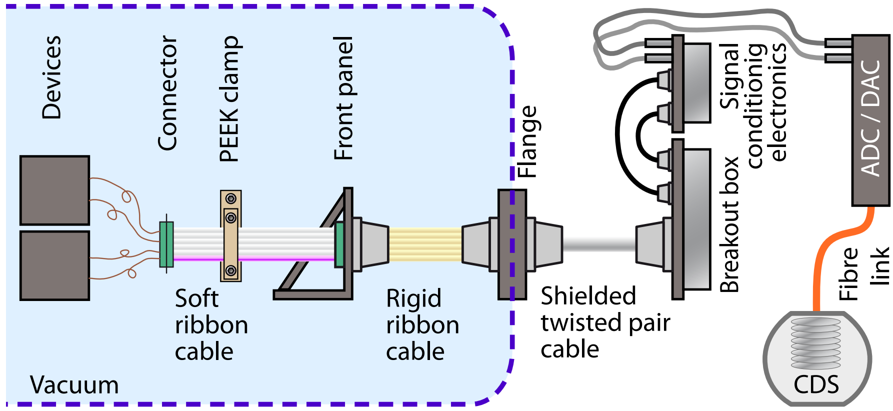

Figure E.1.: A schematic overview of the internal electrical cabling of the AEI-SAS. The chain of cables is shown from randomly chosen devices to the control and data acquisition system CDS.

The internal electrical cabling diagram shown in figure E.2 is an example of, how the cables are distributed on the baseplate of the AEI-SAS. The cables are clamped to the baseplate with clamps made of polyether ether ketone (PEEK). PEEK is an easily machinable and vacuum compatible organic polymer. In the AEI-SAS, the material is used for all spools for coils, to reduce eddy-current damping, which would occur in spools machined from aluminium.

Several kinds of cables are used in the AEI-SAS, as shown in figure E.1. Kapton®-insulated copper wires from all electronic devices are crimped and plugged into vacuum compatible D-sub connectors from [Allectra]. Soft ribbon cables by *Gore* [Gore] inside the system, lead from D-sub connectors to an in-vacuum front panel. Rigid *Gore* ribbon cables are connecting the front panel to the in-vacuum side of the feed-through flanges. The two mentioned kinds of vacuum compatible *Gore* cables were purchased several decades ago for the GEO600 detector; the remains are utilized in many systems of the in the AEI 10 m Prototype dacility. Outside of the vacuum, the feed-through in the flange is connected via a shielded twisted pair cable by *RS components* [RS] to a breakout box, which distributes the signals to the corresponding signal conditioning electronic boxes. The electronic boxes are differentially connected to an analogue-to-digital converter (ADC), which is connected by an optical fibre to the Control and Data acquisition System (CDS) for signal processing.

Appendix E

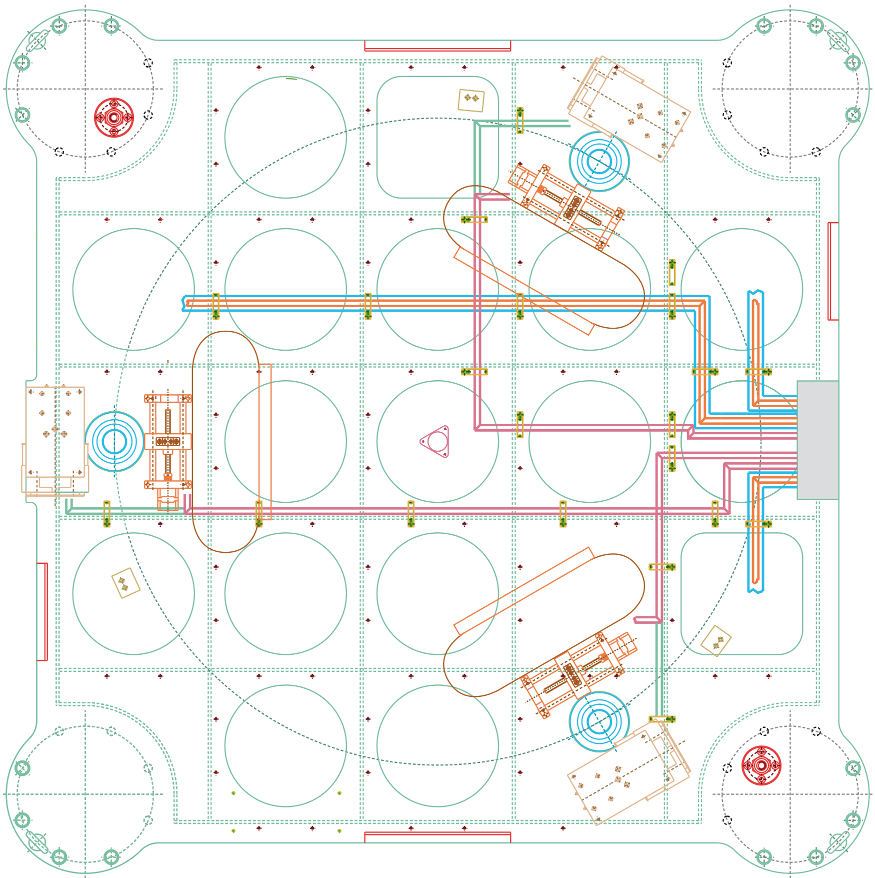

Figure E.2.: The internal electrical cabling plan for the AEI-SAS shows the baseplate with triplets of IP legs, LVDT/actuator pairs, and motorized blade springs. Simple PEEK clips are used to clamp the cables to the baseplate, to prevent them from moving. The cables are sagging as loops, when pulled up to the upper levels, in order to soften them and to prevent from interfering with the performance of the AEI-SAS.

F. Geophones

Connectors

The original connectors were purchased together with the L-22 geophones, several decades ago for the GEO600 detector. The sensors are rather well preserved but the connectors are prone to degradation. Thus, to reduce the likelihood of loosing contact or having noisy signals from the geophones, the decrepit original connectors were replaced by in-house built connectors, as shown in figure F.1.

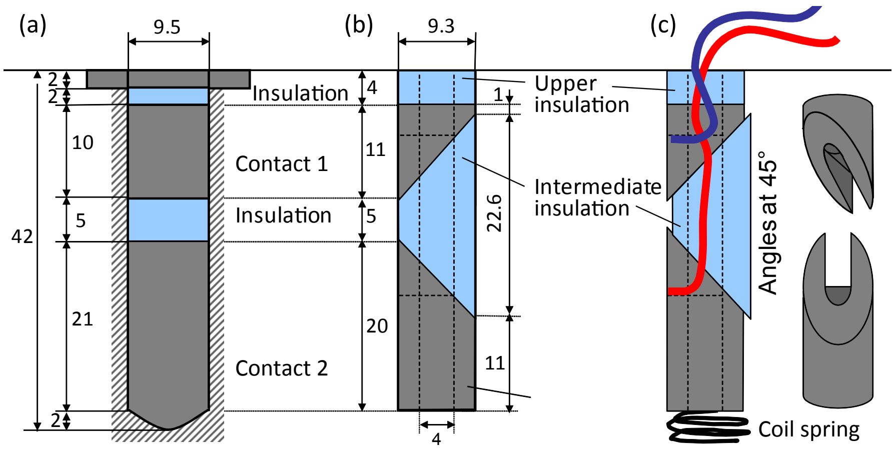

Figure F.1.: (a) The internal structure of the socket of the L-22 geophone. The connector, shown in (b) and (c), is in-house built, replacing the decrepit original plugs. By screwing the geophone into the aluminium holder, shown in figure 3.12, the connector is pressed into the socket. Thereby the contacts of the connector slide along the intermediate insulator and establish a strong connection to the contacts inside the socket.

Containers

The containers of the geophones, made of stainless steel tubes sealed with CF-100 flanges, turned out rather large and heavy, with about 10 kg each. The original plan included using pre-amplifiers for the geophones placed inside the cans. The plots in figure F.2 show a rough comparison of the vertical geophone performances in three different configurations, connecting the pre-amplifiers directly to the geophone (local) or using shielded twisted pair cables, 12 m and 2×24 m (remote). In both remote pre-amplifier configurations the cable shield was only connected to the GND lead at the pre-amplifier input; the sensing coil as well as the geophone case were left floating. The comparison was done by setting up two nominally identical geophones and measuring the coherence spectrum between them. In conclusion, no significant or traceable difference has been observed between the different set-ups.

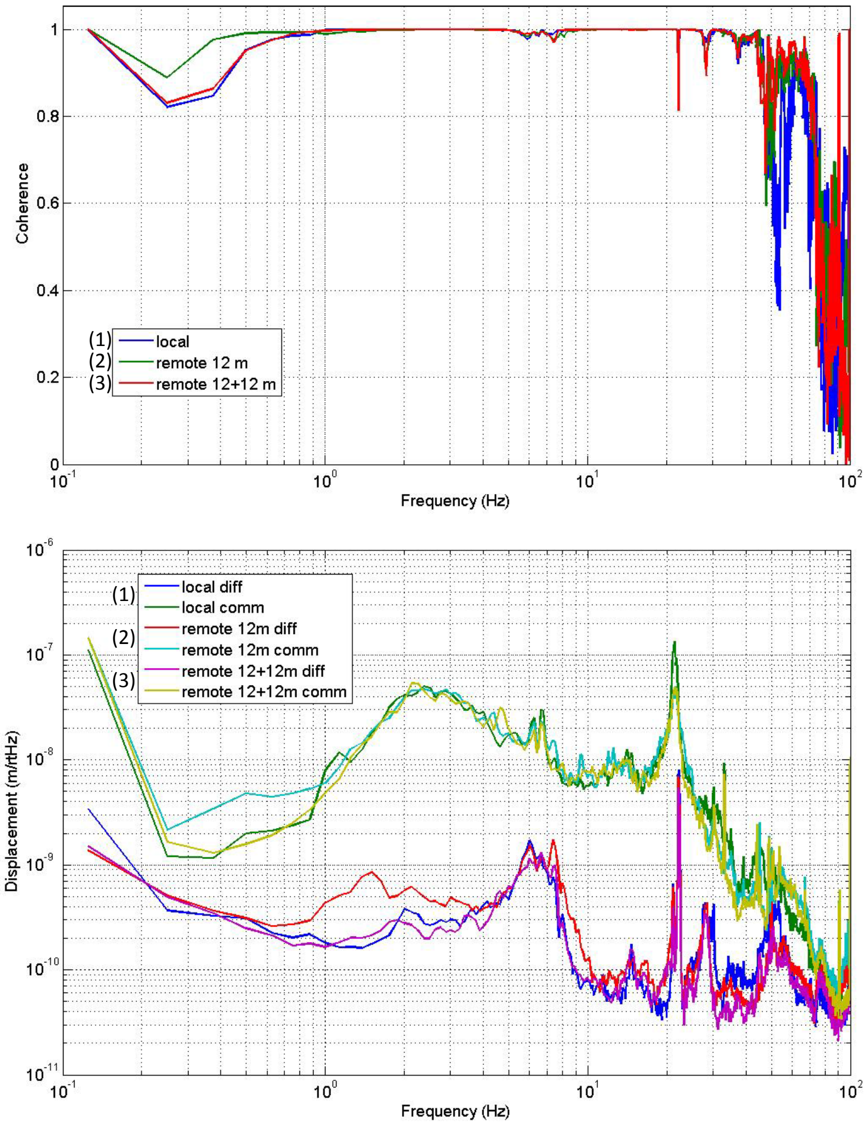

Figure F.2.: Three different configurations of a geophone and its pre-amplifier: (1) local pre-amplifier, directly connected to the geophone, (2) pre-amplifier connected via 12 m shielded twisted pair (STP) cable, (3) pre-amplifier connected via 24 m STP cable. This plots are reproductions of the Prototype logbook page 131 by Alessandro Bertolini.
The first plot shows the coherence between two identical geophones. The bad coherence above 20-30 Hz is due to the supports of the sensors; they were placed on the electronics workshop table, which is responsible for the ∼20 Hz mechanical resonance. The second plot shows the displacement spectrum and the calculated differential signal of the geophone, which is, theoretically, $\sqrt{2} \times self - noise$. Since no significant or traceable difference has been observed, the pre-amplifiers were removed from the cans; the geophone signals are amplified in an electronic box outside of the vacuum system.

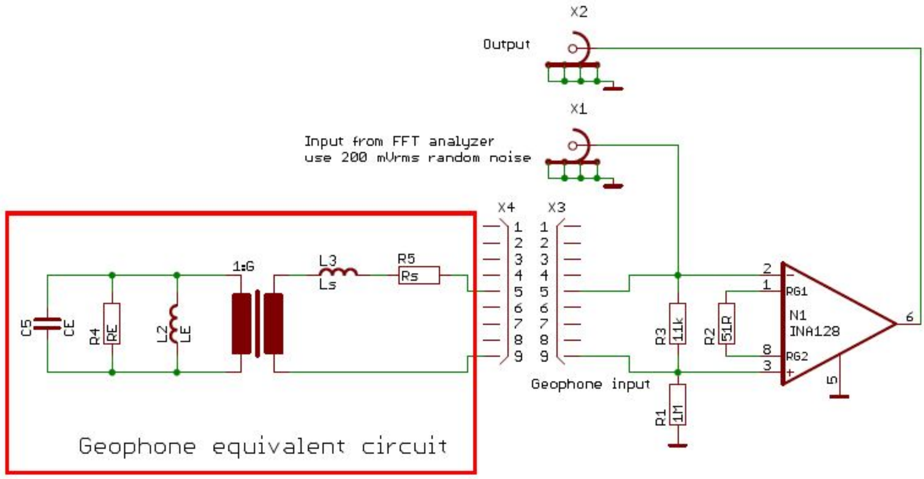

Figure F.3.: Circuit of the *geophone tester* board, used for calibration of the vertical geophones Mark Products L-22D.

Geophone calibration

Three vertical geophones Mark Products L-22D are installed inside of each optical table. This section is a reproduction of a Prototype-logbook entry 480 by Alessandro Bertolini, giving an overview how the geophones are calibrated and showing calibration results.

Nominally, according to the manufacturer, the L-22D consist of a 72.8 g suspended mass for a natural frequency of 2 Hz; the Q of the suspension is about 1.09 and the unloaded sensitivity is 75.7 V/m/sec. In reality the parameters, natural frequency and quality factor in particular, may differ significantly between one and another. Therefore calibration is needed. A reliable estimation of the geophone parameters comes from the measurement of its electromechanical impedance. Every geophone is a reciprocal transducer, i.e. shake its frame produces a current through its coil and vice versa, a current through the coil can move the coil suspension. The input impedance, Z, of a geophone as seen from a voltage source is:

$$Z = R_\mathrm{s} + i\omega L_\mathrm{s} + \frac{i\omega G^2/m}{\omega_0^2 - \omega^2 + 2h\omega_0\omega} \tag{F.1}$$

where R_s and L_s are the coil series resistance and impedance, G is the sensitivity and h ($=1/2Q$) is the suspension damping factor. In the case of L22-D the impedance, Z, is in the range of a few kΩ with a maximum at the mechanical resonance. A simple circuit, named *geophone tester*, as shown in figure F.3, has been built at the AEI to measure Z and extract the parameters of each sensor.

The circuit reproduces the same input configuration used in the real data acquisition amplifier where the geophone is loaded with an 11k resistor to smooth its frequency response at the resonance. In the measurement the loaded geophone impedance is compared with a reference resistor $R1$; since $R1 \gg Z$, with very good approximation,

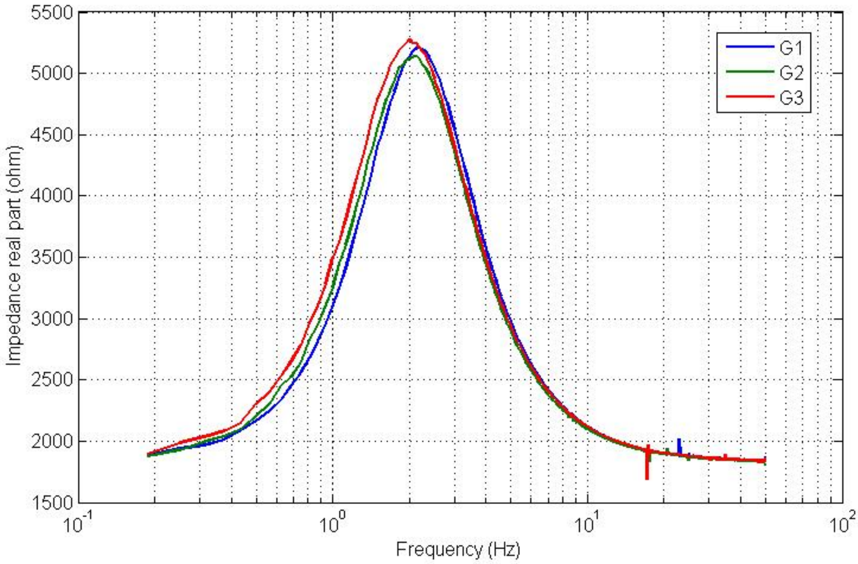

Figure F.4.: Impedance real part of the measured *geophone tester* output. The data were fitted (non-linear least squares) to the model according to equation F.3, using the Matlab curve fitting tool.

the output voltage of the INA is simply:

$$V_{\text{out}} \cong \frac{Z_{\text{loaded}}}{R1} \cdot g \cdot V_{\text{in}} \tag{F.2}$$

where g is the amplifier gain ($\times 1000$). Therefore Z_{loaded} can be measured quite precisely (applying the scaling factor 1000) at the transfer function between V_{out} and V_{in}. The procedure for extracting the geophone parameters is shown below in an example.

Calibration example

A 200 mV_{rms} random noise voltage was applied to the input of the *geophone tester* and the real part of Z_{loaded} was measured. In the calibration, all the geophones are reasonably assumed to have the same nominal mass of 72.8 grams, and the effect of the series inductance is neglected, with typical measured value of 0.37 H. The model used to fit the real part of the impedance Z_n for each n-th device is given as:

$$\text{Re}(Z_n) = R_n + \frac{2h_n\omega_0 G_n^2}{m} \cdot \frac{\omega^2}{(\omega_0^2 + \omega^2)^2 + 4h_n^2\omega_0^2\omega^2} \, . \tag{F.3}$$

The details of the fit are listed below and resumed in table F.1. A general model was used to calculate the results:

$$f(x) = r + \frac{4.372 \cdot g^2 \cdot h \cdot f \cdot x^2}{(f^2 - x^2)^2 + 4 \cdot (h \cdot f)^2 \cdot x^2} \, , \tag{F.4}$$

with coefficients (and their 95% confidence bounds):

Coeff.	Geophone G1	Geophone G2	Geophone G3
f:	2.174 (2.173, 2.176)	2.062 (2.06, 2.063)	2.007 (2.005, 2.009)
g:	66.95 (66.92, 66.99)	65.8 (65.76, 65.83)	67.31 (67.25, 67.36)
h:	0.6696 (0.6686, 0.6707)	0.6941 (0.6932, 0.695)	0.72 (0.7182, 0.7217)
r:	1830 (1830, 1831)	1825 (1825, 1826)	1831 (1830, 1831)
R^2:	0.9999	0.9999	0.9998

with R^2 – the goodness of the fit.
The response of a geophone to velocity, as seen from the data acquisition amplifier is simply:

$$V_n = \frac{-\omega G_n}{\omega_0^2 - \omega^2 + i2h_n\omega_0\omega} \cdot \dot{x} \tag{F.5}$$

The parameters resumed in table F.1 are therefore sufficient to get properly calibrated read outs and allows digital frequency response compensation. The gain at the ADC input, including the amplifier $gain = 2600$, is also shown.

Appendix F

Sensor	Natural freq. [Hz]	Loaded damping	Gain [V/m/s]	ADC gain [V/mm/s]
G1	2.174	0.67	67	174
G2	2.062	0.695	65.8	171
G3	2.007	0.72	67.3	175

Table F.1.: Results of the geophone calibration.

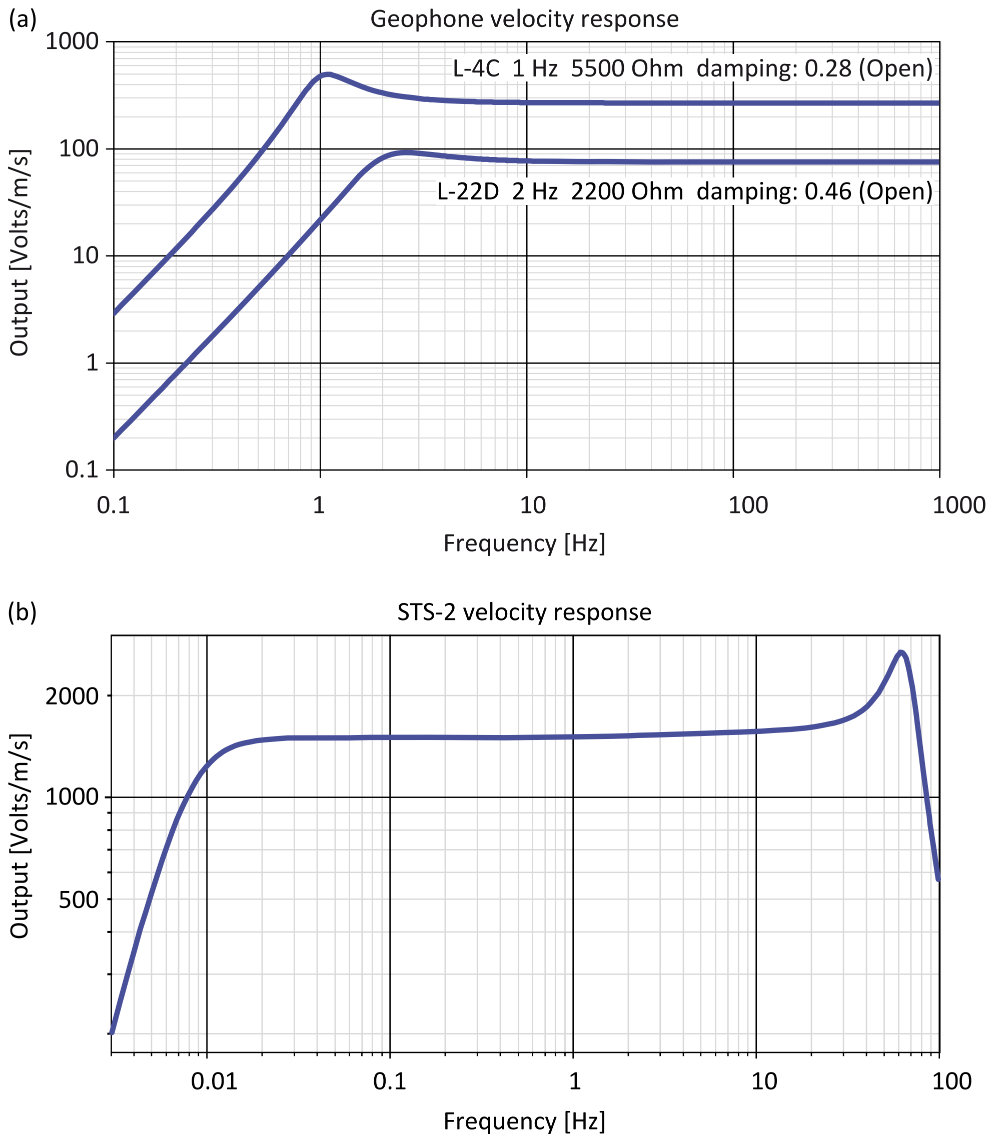

Figure F.5.: Velocity responses of (a) the geophones Mark Products L4C and L-22D, and (b) the broadband seismometer Streckeisen STS-2, reproduced from the corresponding manufacturer's manuals. For most measurements the response of the devices was approximated by a constant value: 276.8 V/(m/s) for the horizontal L4C, 72.8 V/(m/s) for the vertical L-22D, and 1500 V/(m/s) for the STS-2. The geophone values were measured using the procedure described in this chapter.

Bibliography

[Abadie2010a] Abadie J *et al* 2010 All-sky search for gravitational-wave bursts in the first joint LIGO-GEO-Virgo run *Phys. Rev. D* **81** 102001
http://prd.aps.org/abstract/PRD/v81/i10/e102001

[Abadie2010b] Abadie J *et al* 2010 Search for gravitational waves from compact binary coalescence in LIGO and Virgo data from S5 and VSR1 *Phys. Rev. D* **82** 102001
http://prd.aps.org/abstract/PRD/v82/i10/e102001

[Abbott2009a] Abbott B P *et al* 2009 LIGO: the Laser Interferometer Gravitational-wave Observatory. *Rep. Prog. Phys.* **72** 076901
http://iopscience.iop.org/0034-4885/72/7/076901

[Abbott2009b] Abbott B P *et al* 2009 An upper limit on the stochastic gravitational-wave background of cosmological origin *Nature* **460** 990-994
http://www.nature.com/nature/journal/v460/n7258/full/nature08278.html

[Abbott2010] Abbott B P *et al* 2010 Searches for gravitational waves from known pulsars with science run 5 LIGO data *Astrophys. J.* **713** 671
http://iopscience.iop.org/0004-637X/713/1/671/

[Abernathy2011] Abernathy M *et al* 2011 Einstein gravitational wave telescope conceptual design study (St. Stefano a Macerata - Cascina (PI), Italy,) *European Gravitational Observatory via E. Amaldi* **56021** ET-0106C-10, (4)
http://dl.dropbox.com/u/18549909/et-design-study.pdf

[Accadia2011] Accadia T *et al* (Virgo Collaboration) 2011 Status of the Virgo project *Class. Quantum Grav.* **28** 114002
http://dx.doi.org/10.1088/0264-9381/28/11/114002

[Accadia2012a] Accadia T *et al* (Virgo Collaboration) 2012 Virgo: a laser interferometer to detect gravitational waves *J. Instrumentation* **7** P03012
http://dx.doi.org/10.1088/1748-0221/7/03/P03012

[Accadia2012b] Accadia T *et al* (Virgo Collaboration) 2012 Advanced Virgo technical design report *Virgo Technical Documentation System* VIR-0128A-12
https://tds.ego-gw.it/itf/tds/file.php?callFile=VIR-0128A-12.pdf

[Acernese2008] Acernese F *et al* 2008 Mechanical monolithic horizontal sensor for low frequency seismic noise measurement *Rev. Sci. Instrum.* **79** 074501
http://link.aip.org/link/doi/10.1063/1.2943415

[AdLIGO2011] Advanced LIGO team 2011 Advanced LIGO reference design *LIGO public Document Control Center* LIGO-M060056-v2
https://dcc.ligo.org/cgi-bin/DocDB/ShowDocument?docid=m060056

[Agatsuma2008] Agatsuma K *et al* 2008 Control system for the Seismic Attenuation System (SAS) in TAMA300 *Journal of Physics: Conference Series* **122** 012013
http://dx.doi.org/10.1088/1742-6596/122/1/012013

[Agilent] Agilent Technologies, Measurement expressions (handbook) *Agilent Technologies Documentation, Palo Alto, CA, USA*
http://newport.eecs.uci.edu/eceware/ads_docs/pdf/expmeas.pdf

[Aguiar2008] Aguiar O D *et al* 2008 The Schenberg spherical gravitational wave detector: the first commissioning runs *Class. Quantum Grav.* **25** (11) 114042
http://iopscience.iop.org/0264-9381/25/11/114042/

[Akmal1998] Akmal A 1998 Equation of state of nucleon matter and neutron star structure *Phys. Rev. C* **58** (3) 1804–1828
http://arxiv.org/abs/nucl-th/9804027

[Allectra] Allectra *supplier for vacuum components, Berlin*
http://www.allectra.com/index.php/de/2012-02-19-11-22-21/sub-d/82-content/177-connectors

[Amaro-Seoane2012] Amaro-Seoane P *et al* 2012 Doing science with eLISA: astrophysics and cosmology in the millihertz regime *arXiv:* 1201.3621 astro-ph.CO
http://arxiv.org/abs/1201.3621

[Andersson2011] Andersson N 2011 Review: The road to gravitational-wave astronomy *Progress in Particle and Nuclear Physics* **66** 239–248
http://dx.doi.org/10.1016/j.ppnp.2011.01.013

[Arai2008] Arai A *et al* 2008 Recent progress of TAMA300 *Journal of Physics: Conference Series* **120** (3) 032010
http://iopscience.iop.org/1742-6596/120/3/032010

[Arun] Arun Microelectronics Ltd.
http://www.arunmicro.com/techdocs/datasheets/Stepper_motors.pdf

[Aso-thesis] Aso Y 2006 Active vibration isolation for a laser interferometric gravitational wave detector using a suspension point interferometer (PhD. thesis, University of Tokyo)
https://gwic.ligo.org/thesisprize/2006/Aso_Thesis.pdf

[Aston-thesis] Aston S M 2011 Optical read-out techniques for the control of test-masses in gravitational wave observatories (PhD thesis, University of Birmingham)
http://etheses.bham.ac.uk/1665/1/Aston11PhD.pdf

[Aubert-Duval] Aubert & Duval *supplier for steel and alloys*
http://www.aubertduval.com

[Backer1984] Backer D 1984 The 1.5 millisecond pulsar *Annals of the New York Academy of Sciences, 11th Texas Symposium on Relativistic Astrophysics* **422** 180–181
http://dx.doi.org/10.1111/j.1749-6632.1984.tb23351.x

[Barriga2009] Barriga P *et al* 2009 Compact vibration isolation and suspension for Australian International Gravitational Observatory: performance in a 72 m Fabry Perot cavity *Rev. Sci. Instrum.* **80** 114501
http://dx.doi.org/10.1063/1.3250841

[Barriga2010] Barriga P *et al* 2010 AIGO: a southern hemisphere detector for the worldwide array of ground-based interferometric gravitational wave detectors *Class. Quantum Grav.* **27** 084005
http://iopscience.iop.org/0264-9381/27/8/084005

[Barton1994] Barton M A *et al* 1994 Ultralow frequency oscillator using a pendulum with crossed suspension wires *Rev. Sci. Instrum.* **65** 3775
http://dx.doi.org/10.1063/1.1144506

[Barton1999] Barton M A *et al* 1999 Two-dimensional X pendulum vibration isolation table *Rev. Sci. Instrum.* **70** 2150
http://dx.doi.org/10.1063/1.1149728

[Beauduin1996] Beauduin R *et al* 1996 The effects of the atmospheric pressure changes on seismic signals or how to improve the quality of a station *Bull. Seism. Soc. Am.* **86** (6) 1760–1769
http://bnordgren.org/seismo/BSSAv86n6p1760.pdf

[Beccaria1997] Beccaria M *et al* 1997 Extending the VIRGO gravitational wave detection band down to a few Hz: metal blade springs and magnetic anti-springs *Nucl. Instrum. Methods A* **394** (3) 397–408 http://dx.doi.org/10.1016/S0168-9002(97)00661-x

[Beccaria1998] Beccaria M *et al* 1998 The creep problem in the VIRGO suspensions: a possible solution using Maraging steel *Nucl. Instrum. Methods A* **404** 455-469
http://dx.doi.org/10.1016/S0168-9002(97)01123-6

[Benford1991] Benford R *et al* 1991 Progress on the MIT 5-Meter interferometer *Experimental Gravitational Physics* ed. Michelson *et al* (World Scientific, Singapore) 312–315.

[Bertolini1999a] Bertolini A *et al* 1999 Seismic noise filters, vertical resonance frequency reduction with geometric anti-springs: a feasibility study *Nucl. Instrum. Meth. A* **435** 475–483
http://dx.doi.org/10.1016/S0168-9002(99)00554-9

[Bertolini1999b] Bertolini A *et al* 1999 High sensitivity accelerometers for high performance seismic attenuators *AIP Conf. Proc.* **523** 409–410 presented at the Third Edoardo Amaldi Conference, 12–16 Jul 1999, in Pasadena, California (USA)
http://dx.doi.org/10.1063/1.1291892

[Bertolini2000] Bertolini A *et al* 2000 New Seismic Attenuation System (SAS) for the advanced LIGO configurations (LIGO2) *AIP Conf. Proc.* **523** 320–324 presented at the Third Edoardo Amaldi Conference, 12–16 Jul 1999, in Pasadena, California (USA)
http://dx.doi.org/10.1063/1.1291874

[Bertolini2004] Bertolini A *et al* 2004 Monolithic folded pendulum accelerometers for seismic monitoring and active isolation systems *Nuclear Science Symposium Conference Record, IEEE* **7** 4644–4648
http://ieeexplore.ieee.org/xpls/abs_all.jsp?arnumber=1466915&tag=1

[Bertolini2006a] Bertolini A *et al* 2006 Readout system and predicted performance of a low-noise low-frequency horizontal accelerometer *Nucl. Instrum. Meth. A* **564** 579–586 http://dx.doi.org/10.1016/j.nima.2006.04.041

[Bertolini2006b] Bertolini A *et al* 2006 Mechanical design of a single-axis monolithic accelerometer for advanced seismic attenuation systems *Nucl. Instrum. Meth. A* **556** 616–623
http://www.sciencedirect.com/science/article/pii/S0168900205020930

[Bertolini2006c] Bertolini A *et al* 2006 Monolithic folded pendulum accelerometers for seismic monitoring and active isolation systems *Transactions on Geoscience and Remote Sensing, IEEE* **44** (2) 273–276
http://authors.library.caltech.edu/5606/1/BERieeetgrs06.pdf

[Bertolini2006d] Bertolini A *et al* 2006 Design and prototype tests of a seismic attenuation system for the advanced-LIGO output mode cleaner *Class. Quantum Grav.* **23** 111–118
presented at 6th Edoardo Amaldi Conference on Gravitational Waves, Kise Nago, Okinawa, Japan, 20-24 Jun 2005
http://dx.doi.org/10.1088/0264-9381/23/8/S15

[Bertolini2012] Bertolini A 2012 *private communication*

[Billah1991] Billah K Y *et al* 1991 Resonance, Tacoma Narrows bridge failure, and undergraduate physics textbooks *Am. J.Physics* **59** (2) 118–124 http://dx.doi.org/10.1119/1.16590

[Billing1983] Billing H *et al* 1983 Quantum optics, experimental gravity, and measurement theory *Plenum, New York* p.525

[BIPM] Bureau international des poids et mesures (BIPM) international system (SI) of units (on-line brochure) section 5.2
http://www.bipm.org/en/si/si_brochure/chapter5/5-2.html

[Blair1994] Blair D G *et al* 1994 Performance of an ultra low-frequency folded pendulum *Phys. Lett. A* **193** 223–226 http://dx.doi.org/10.1016/0375-9601(94)90587-8

[Bonaldi2009] Bonaldi M *et al* 2009 Nonequilibrium steady-state fluctuations in actively cooled resonators *Phys. Rev. Lett.* **103** 010601
http://link.aps.org/doi/10.1103/PhysRevLett.103.010601

[Bork2009] Bork R 2009 AdvLigo CDS Realtime Code Generator (RCG) Application Developer's Guide *LIGO public Document Control Center* T080135 https://dcc.ligo.org/public/0001/T080135/003/T080135-v3.pdf

[Bormann1998] Bormann P 1998 Conversion and comparability of data presentations on seismic background noise *Journal of Seismology* **2** 37–45 http://dx.doi.org/10.1023/A:1009780205669

[Boschi-thesis] Boschi V 2010 Modeling and simulation of seismic attenuation systems for gravitational wave interferometers (PhD thesis, Univesità di Pisa)
http://www.infn.it/thesis/PDF/getfile.php?filename=4861-Boschi-dottorato.pdf

[Braccini1996] Braccini S *et al* 1996 Seismic vibrations mechanical filters for the gravitational waves detector VIRGO *Rev. Sci. Instrum.* **67** 2899

[Braccini2000] Braccini S *et al* 2000 The maraging-steel blades of the Virgo super attenuator *Meas. Sci. Technol.* **11** 467–476
http://iopscience.iop.org/0957-0233/11/5/304

[Braccini2005] Braccini S 2005 Measurement of the seismic attenuation performance of the VIRGO Superattenuator *Astroparticle Physics* **23** 557–565

[Bronstein] Bronstein I N *et al* 2000 Taschenbuch der Mathematik (Verlag Harri Deutsch, Thun und Frankfurt am Main) 5. Auflage

[BSH] Bundesamt für Seeschiffahrt und Hydrographie (BSH)
http://www.bsh.de/aktdat/marnet_export/Fino1/Fino1WGWReinJahr.png

[Calloni2012] Calloni E for the LIGO Scientific Collaboration and the Virgo Collaboration 2012 Status and developments of Advanced LIGO and Advanced Virgo gravitational wave detectors *Talk at the International Conference on New Frontiers in Physics* June 28 - July 4 2012, Kolymbari, Crete, Greece, internal LIGO document number G1200545-v1, publicly available at
http://indico.cern.ch/getFile.py/access?contribId=219&sessionId=56&resId=0&materialId=slides&confId=176361

[Carella2009] Carrella A *et al* 2009 On the force transmissibility of a vibration isolator with quasi-zero-stiffness *Journal of Sound and Vibration* **322** 707–717
http://dx.doi.org/10.1016/j.jsv.2008.11.034

[Cella2002] Cella G *et al* 2002 Seismic attenuation performance of the first prototype of a geometric anti-spring filter *Nucl. Instrum. Meth. A* **487** 652–660
http://dx.doi.org/10.1016/S0168-9002(01)02193-3

[Cella2005] Cella G *et al* 2005 Monolithic geometric anti-spring blades *Nuclear Instr. and Methods in Phys. A* **540** 502–519
http://arxiv.org/pdf/gr-qc/0406091v2.pdf

[Champeney1989] Champeney D C 1989 A handbook of Fourier theorems (Cambridge University Press) chapter 7

[Chin-thesis] Chin E-J 2007 High performance vibration isolation techniques for the AIGO gravitational wave detector (PhD thesis, University of Western Australia) http://www.gravity.uwa.edu.au/docs/PhDThesis/Euj_Thesis.pdf

[Cohadon1999] Cohadon P F *et al* 1999 Cooling of a mirror by radiation pressure *Phys. Rev. Lett.* **83** 3174–3177 http://arxiv.org/abs/quant-ph/9903094

[Cohen1992] Cohen L 1992 Convolution, filtering, linear systems, the Wiener-Khinchin theorem: generalizations *International Society for Optics and Photonics, SPIE* **1770** 378–393 http://dx.doi.org/10.1117/12.130944

[Cohen1998] Cohen L 1998 The generalization of the Wiener-Khinchin theorem *Int. Conf. on Acoustics, Speech and Signal Processing, IEEE* **3** 1577–1580 http://dx.doi.org/10.1109/ICASSP.1998.681753

[Cutler2006] Cutler C *et al* 2006 Big bang observer and the neutron-star- binary subtraction problem *Phys. Rev. D* **73** 042001 http://link.aps.org/doi/10.1103/PhysRevD.73.042001

[Dahl2010] Dahl K, *et al* 2010 Towards a suspension platform interferometer for the AEI 10m prototype interferometer *Journal of Physics: Conference Series* **228** 012027 http://iopscience.iop.org/1742-6596/228/1/012027

[Dahl2012a] Dahl K *et al* 2012 Suspension platform interferometer for the AEI 10 m prototype: concept, design and optical layout Class. Quantum Grav. **29** 095024 http://arxiv.org/abs/1201.4718

[Dahl2012b] Dahl K *et al* 2012 Status of the AEI 10 m prototype *Class. Quantum Grav.* **29** 145005 http://dx.doi.org/10.1088/0264-9381/29/14/145005

[Damour1987] Damour T 1987 An introduction to the theory of gravitational radiation *Gravitational in Astrophysics* Carter B and Hartle J B (Plenum Press, New York) 3–62

[DeSalvo1997] DeSalvo R 1997 Non stochastic noise in gravitational wave detectors *Proc. of the 2nd Edoardo Amaldi Conf. on Gravitational Waves 1–4 Jul 1997 Geneva, Switzerland* Coccia E, Veneziano G, Pizzella G (World Scientific Publishing, Singapore)

[DeSalvo2009] DeSalvo R 2009 Review: accelerometer development for use in gravitational wave-detection interferometers *Bulletin of the Seismological Society of America* **99** 2B 990–997

[DeSalvo2011] DeSalvo R *et al* 2011 The role of self-organized criticality in elasticity of metallic springs: observations of a new dissipation regime *Eur. Phys. J. Plus* **126** 75
DOI: 10.1140/epjp/i2011-11075-y

[DeSalvo2012] DeSalvo R *for the seismic group* 2011 Seismic attenuation chains concept, design and advancement status (presentation for the external review panel) *Public JGW Document Server* JGW-G1200958
http://gwdoc.icrr.u-tokyo.ac.jp/DocDB/0009/G1200958/001/G1200958-seismic-design-review-4-2012.pdf

[Dobeson2005] Dobeson D 2005 Bulid your seismograph *Silicon Chip Magazine* **204** September 2005
http://www.siliconchip.com.au/cms/A_105119/article.html

[Drever1983] Drever R W P *et al* 1983 Gravitational radiation (North-Holland, Amsterdam) 321–338

[Drever1987] Drever R W P 1987 Outline of a proposed design for a first receiver for installation in the long-baseline facilities, of Fabry-Perot type *Public LIGO Document Control Center* T870001-00-R
https://dcc.ligo.org/public/0028/T870001/000/T870001-00.pdf

[Drever1991] Drever R W P 1991 Fabry-Perot cavity gravity-wave detectors *The Detection of Gravitational Waves* editor Blair D G (Cambridge University Press, Cambridge England) 306–328

[Dubbel] Dubbel H *et al* 2007 *Dubbel-Taschenbuch für den Maschinenbau* (Berlin: Springer)

[Dumas2009] Dumas J-C *et al* 2009 Compact vibration isolation and suspension for Australian International Gravitational Observatory: local control system *Rev. Sci. Instrum.* **80** 114502
http://dx.doi.org/10.1063/1.3250861

[Edgar2009] Edgar M P 2009 Experimental demonstration of a suspended diffractively coupled optical cavity *Optics Letters* **34** (20) 3184–3186
http://dx.doi.org/10.1364/OL.34.003184

[Effa2009] Effa D *et al* 2009 Design and modelling of a MEMS accelerometer for a novel Virtual Button user interface *Science and Technology for Humanity (TIC-STH), IEEE Toronto International Conference* 597 – 602

[Einstein1916] Einstein A 1916 Die Grundlage der allgemeinen Relativitätstheorie *Annalen der Physik* **49** 769–822 (in German)

[Einstein1918] Einstein A 1918 Über Gravitationswellen *Akademie-Vorträge: Sitzungsberichte der Königlich PreuSSischen Akademie der Wissenschaften 1914-1932* 135–167 (in German)

Bibliography

[Einstein1937] Einstein A, Rosen N 1937 On gravitational waves *Journal of the Franklin Institute* **223** 43–54
http://sitemason.vanderbilt.edu/files/doMQo0/sdarticle.pdf

[Estabrook1975] Estabrook F B *et al* 1975 Response of Doppler spacecraft tracking to gravitational radiation *Gen. Relativ. Gravit.* **6** 439–447
http://dx.doi.org/10.1007/BF00762449

[Ferguson1963] Ferguson E S 1963 Kinematics of mechanisms from the time of Watt *Contributions from the Museum of History and Technology* bull.**228** (Smithsonian Institution, Washington D.C.)
http://www.gutenberg.org/files/27106/27106-h/27106-h.htm

[Forward1969] Forward R L 1969 Multidirectional, multipolarization antennas for scalar and tensor gravitational radiation *Gravity research foundation, Honourable mentioned essay*
http://www.gravityresearchfoundation.org/pdf/awarded/1969/forward.pdf

[Forward1978] Forward R L 1978 Wideband laser-interferometer graviational-radiation experiment *Phys. Rev. D* **17** 379–390

[Frede2007] Frede M *et al* 2007 Fundamental mode, single-frequency laser amplifier for gravitational wave detectors *Optics Express* **15** (2) 459–465
http://dx.doi.org/10.1364/OE.15.000459

[Galitzin1906] Galitzin B 1906 Über eine Abänderung des Zöllner'schen Horizontalpendels (Keiserliche Akademie der Wissenschaften, St.Petersburg)

[GEO600] Gravitational wave detector GEO600
http://www.geo600.uni-hannover.de/geocurves/

[Giaime2001] Giaime J *et al* 2001 Advanced LIGO seismic isolation system conceptual design (internal report) *Public LIGO Document Control Center* E010016
https://dcc-llo.ligo.org/public/0023/E010016/000/E010016-00.pdf

[Gore] Gore
http://www.gore.com

[Goßler-thesis] Goßler 2004 The suspension systems of the interferometric gravitational-wave detector GEO600 (PhD thesis, Univesität Hannover)
http://www.amps.uni-hannover.de/dissertationen/gossler_diss.pdf

[Goßler2010] Goßler S *et al* 2010 The AEI 10 m prototype interferometer *Class. Quantum Grav.* **27** 084023
doi:10.1088/0264-9381/27/8/084023

[Gottardi2007] Gottardi L *et al* 2007 Complete model of a spherical gravitational wave detector with capacitive transducers: calibration and sensitivity optimization *Physical Review D* **75** 022002

[Graf2004] Graf U 2004 Applied Laplace transforms and Z-transforms for scientists and engineers: a computational approach using a Mathematica package (Birkhäuser, Basel)

[Gräf2012] Gräf C *et al* 2012 Optical layout for a 10 m Fabry-Pérot Michelson interferometer with tunable stability *Class. Quantum Grav.* **29** 075003
http://arxiv.org/abs/1112.1804

[Grote2009] Grote H *et al* 2009 The GEO600 status *Class. Quantum Grav.* **27** 084003
http://dx.doi.org/10.1088/0264-9381/27/8/084003

[Hardham2001] Hardham C *et al* 2001 Quiet hydraulic actuators for the laser interferometer interferometric gravitational-wave observatory (LIGO) *Control of Precision Systems, ASPE*

[Harms2008] Harms J *et al* 2008 Subtraction-noise projection in gravitational-wave detector networks *Phys. Rev. D* **77** 123010
http://arxiv.org/abs/0803.0226v2

[Havas1979] Havas P 1979 Equations of motion and radiation reaction in the special and general theory of relativity *Isolated Gravitating Systems in General Relativity* ed. Ehlers J (North Holland, Amsterdam) 74–155

[Heinzel2002] Heinzel G *et al* 2002 Spectrum and spectral density estimation by the discrete Fourier transform (DFT), including a comprehensive list of window functions and some new flat-top windows *Max Planck Society eDoc server* 395068
http://pubman.mpdl.mpg.de/pubman/item/escidoc:152164:1

[Hillers2011] Hillers G *et al* 2011 Seasonal variations of observed noise amplitudes at 2–18 Hz in southern California *Geophys. J. Int.* **184** 860–868
doi: 10.1111/j.1365-246X.2010.04886.x

[Hobbs2010] Hobbs G *et al* 2010 The international pulsar timing array project: using pulsars as a gravitational wave detector *Class. Quantum Grav.* **27** 084013

[Honeywell] Honeywell
http://inertialsensor.com/acceleration-measurement-accelerometers.php

[Hosain2012] Hosain M A *et al* 2012 Novel Euler-LaCoste linkage as a very low frequency vertical vibration isolator *Rev. Sci. Instrum.* **83** 085108
http://dx.doi.org/10.1063/1.4745505

[Hough1995] Hough J *et al* 1995 LISA – Laser Interferometer Space Antenna for gravitational wave measurements *Gravitational Wave Experiments* (World Scientific, Singapore) 50–63

[Hulse1974] Hulse R A *et al* 1974 Discovery of a pulsar in a binary system *Astrophysical Journal* **195** L51–L52

[Inman2001] Inman D J 2001 Engineering vibration, 2nd edition (Prentice Hall International, New Jersey)

[Janssen2008] Janssen G H *et al* 2008 European pulsar timing array *AIP Conference Proceedings* **983** 633–635

[KAGRA2012] LCGT got new nickname: KAGRA
http://gwcenter.icrr.u-tokyo.ac.jp/en/archives/828

[Kaspi1994] Kaspi V M *et al* 1994 High-precision timing of millisecond pulsars. 3. Long-term monitoring of PSRs B1855+09 and B1937+21 *Astrophysical Journal* **428** 713–728

[Kawazoe2010] Kawazoe F *et al* 2010 Designs of the frequency reference cavity for the AEI 10m Prototype interferometer *J. Phys. Conf.Ser.* **228** 012028
http://iopscience.iop.org/1742-6596/228/1/012028

[Kennefick1997] Kennefick D J 1997 Controversies in the history of the radiation reaction problem in general relativity *eprint arXiv.org* gr-qc 9704002 v1
http://arXiv.org/abs/gr-qc/9704002v1

[Khalili2005] Khalili F Ya 2005 Reducing the mirrors coating noise in laser gravitational-wave antennae by means of double mirrors *Phys. Lett. A* **334** (1) 67–72

[Kim1995] Kim K H *et al* 1995 A skew-symmetric cantilever accelerometer for automotive airbag applications, *Sensors and Actuators A: Physical* **50** 121–126

[Krylov1996] Krylov I P 1996 A low-frequency pendulum for studying vortex lattice melting *Supercond. Sci. Technl.* **9** 583–588

[Kuroda2010] Kuroda K *et al* 2010 Status of LCGT *Class. Quantum Grav.* **27** 084004
http://iopscience.iop.org/0264-9381/27/8/084004

[Kurrle2008] Kurrle D *et al* 2008 The horizontal hum of the Earth: a global background of spheroidal and toroidal modes *Geophys. Res. Lett.* **35** L06304
doi:10.1029/2007GL033125

[Kwee2009] Kwee P *et al* 2009 Shot-noise-limited laser power stabilization with a high-power photodiode array *Optics Letters* **34** (19) 2912–2914
http://dx.doi.org/10.1364/OL.34.002912

[LaCoste1934] LaCoste L J B *et al* 1934 A new type long period seismograph *Journal of applied physics* **5** 178–180
http://jap.aip.org/resource/1/japiau/v5/i7/p178_s1

[Lenhardt2008] Lenhardt W 2008 Seismology (lecture script, downloadable PDF) *Austrian association for earthquake engineering and structural dynamics*
http://www.oge.or.at/oge_links_e.htm

[Lighthill1958] Lighthill M J 1958 Introduction to Fourier analysis (Cambridge University Press)

[Liu1997] Liu J *et al* 1997 Vibration isolation performance of an ultra-low frequency folded pendulum resonator *Phys. Lett. A* **228** 243–249

[Lockerbie2011] Lockerbie N A *et al* 2011 First results from the 'violin-mode' tests on an advanced LIGO suspension at MIT *Class. Quantum Grav.* **28** 245001

[Losurdo-thesis] Losurdo G 1998 Ultra-low frequency inverted pendulum for the VIRGO test mass suspension (PhD thesis, Univesità di Pisa) *public CERN document server*
http://cdsweb.cern.ch/record/980049

[Losurdo1999] Losurdo G *et al* 1999 An inverted pendulum preisolator stage for the VIRGO suspension system *Rev. Sci. Instrum.* **70** (5) 2507–2515

[Lück2010] Lück H *et al* 2010 The upgrade of GEO 600 *J. Phys. Conf. Ser.* **228** 012012

[Mailly2003] Mailly F 2003 Micromachined thermal accelerometer *Sensors and Actuators A: Physical* **103** 3 359–363

[Mantovani2005] Mantovani M *et al* 2005 One hertz seismic attenuation for low frequency gravitational waves interferometers *Nucl. Instrum. Meth. A* **554** 546–554

[Marka2002] Márka S *et al* 2002 Anatomy of the TAMA SAS seismic attenuation system *Class. Quantum Grav.* **19** 1605–1614 http://iopscience.iop.org/0264-9381/19/7/351/pdf/q20751.pdf

[Mathematica] Wolfram research, Tutorial: Fourier transform *Mathematica documentation center*
http://reference.wolfram.com/mathematica/ref/FourierTransform.html

[Michelson1881] Michelson A A 1881 The relative motion of the Earth and the luminiferous ether *American Journal of Science* **22** 120–129
http://en.wikisource.org/wiki/The_Relative_Motion_of_the_Earth_and_the_Luminiferous_Ether

[Michelson1887] Michelson A A *et al* 1887 On the relative motion of the Earth and the luminiferous ether *American Journal of Science* **34** (203) 333–345
http://en.wikisource.org/wiki/On_the_Relative_Motion_of_the_Earth_and_the_Luminiferous_Ether

[Minigrail] Website of the MiniGRAIL project
www.minigrail.nl

[Musser2007] Musser G 2007 An ear for spacetime *Scientific American* **297** (1) 25 doi:10.1038/scientificamerican0707-25

[Moss1971] Moss G E *et al* 1971 Photon-noise-limited laser transducer for gravitational antenna *Appl. Opt.* **10** (11) 2495–2498
http://dx.doi.org/10.1364/AO.10.002495

[Mours2006] Mours B *et al* 2006 Thermal noise reduction in interferometric gravitational wave antennas: using high order TEM modes *Class. Quantum Grav.* **23** 5777–5784

[Müller-Ebhardt2008] Müller-Ebhardt H *et al* 2008 Entanglement of macroscopic test masses and the standard quantum limit in laser interferometry *Physical Review Letters* **100** 013601

[Nakayama2004] Nakayama Y *et al* 2004 Performance test of STS-2 seismometers with various data loggers *Proc. 8th international workshop on accelerator alignment* (CERN, Geneva) eConf C04-10-04.11 041

[NI] National Instruments tutorial 2006 Measuring position and displacement with LVDTs
http://zone.ni.com/devzone/cda/tut/p/id/3638

[Nyquist1928] Nyquist H 1928 Certain topics in telegraph transmission theory *Transactions of the American Institute of Electrical Engineers* 47 617–644
Reprinted 2002 in *Proceedings of the IEEE* **90** (2) 617–644

[Oreshko2000] Oreshko V V 2000 Pulsar timing instrumental errors. AC-600/1600 facility. *Proc. of the Lebedev Physical Institute, Moscow* **229** 110 (in Russian)

[Paik2009] Paik H J 2009 Gravitational wave detection on the Moon and the moons of Mars *Advances in Space Research* **43** (1) 167–170
http://dx.doi.org/10.1016/j.asr.2008.04.010

[Peters1990] Peters R D 1990 Metastable states of a low-frequency mesodynamic pendulum *Appl. Phys. Lett.* **57** 1825–1827

[Peterson1993] Peterson J 1993 Observations and modeling of seismic background noise *U.S. Dep. of Interiour Geol. Survey* Open-File Report 93–322
http://earthquake.usgs.gov/regional/asl/pubs/files/ofr93-322.pdf

[Pillet2007] Pillet R *et al* 2007 The effects of seismic rotations on inertial sensors *Geophysical Journal International* **171** (3) 1314–1323
http://onlinelibrary.wiley.com/doi/10.1111/j.1365-246X.2007.03617.x/full]

[Pitkin2011] Pitkin M *et al* 2011 Gravitational wave detection by interferometry (ground and space) *Living Rev. Relativity* **14** 5
http://www.livingreviews.org/lrr-2011-5

[Press1992] Press W H *et all* 1992 Numerical recipes: the art of scientific computing (Cambridge University Press) 2nd edition

[Purdy2012] Purdy T P *et al* Observation of radiation pressure shot noise *arXiv*:1209.6334v1 [quant-ph] 27 Sep 2012
http://arxiv.org/pdf/1209.6334v1.pdf

[Rahman2011] Rahman M 2011 Applications of Fourier transforms to generalized functions (WIT Press, Southampton UK) 10
http://books.google.de/books?id=k_rdcKaUdr4C&pg=PA10&redir_esc=y#v=onepage&q&f=false

[Reitze2012] Reitze D 2012 Ground-based Gravitational-wave Astronomy Using Interferometers: Past and Future *LIGO Document Control Center* LIGO-G1200710-v3
https://dcc.ligo.org/DocDB/0093/G1200710/003/plenary_reitze_MG13.ppt
Plenary talk at 13th Marcel Grossmann Meeting, Stockholm, 1-7 July 2012

[Rhie2004] Rhie J *et al* 2004 Excitation of Earth's continuous free oscillations by atmosphere-ocean-seafloor coupling *Nature* **431** 552–556

[RS] RS components
http://www.rs-online.com

[Sannibale2008] Sannibale V *et al* 2008 Recent results of a seismically isolated optical table prototype designed for Advanced LIGO *J. Phys.: Conf. Ser.* **122** 012010

[Sathyaprakash2009] Sathyaprakash B S *et al* 2009 Physics, astrophysics and cosmology with gravitational waves *Living Rev. Relativity* **12** (2)
http://www.livingreviews.org/lrr-2009-2

[Sato2009] Sato S *et al* 2009 DECIGO: The Japanese space gravitational wave antenna *J. Phys.: Conf. Ser.* **154** 012040

[Sercel] Sercel
http://www.sercel.com/Company/history.php

[Schnier1997] Schnier D *et al* 1997 Power recycling in the Garching 30 m prototype interferometer for gravitational-wave detection *Phys. Lett. A* **225** 210–216

[Schulte-Pelkum2004] Schulte-Pelkum V *et al* 2004 Strong directivity of ocean-generated seismic noise *Geochem. Geophys. Geosyst.* **5** Q03004
http://www.agu.org/journals/gc/gc0403/2003GC000520/

[Schutz1999] Schutz B F 1999 Gravitational wave astronomy *Class. Quant. Grav.* **16** A131–A156

[Shoemaker2007] Shoemaker D 2007 Consideration of HAM SAS for Advanced LIGO (talk at LIGO Excomm, 30 April 2007) *internal LIGO Document Control Center* G070284

[Smith2011] Smith J O *III* 2011 Spectral Audio Signal Processing *W3K Publishing* on-line book accessed June 2012
http://ccrma.stanford.edu/~jos/sasp/

[Stochino-thesis] Stochino A 2007 The HAM-SAS seismic isolation system for the Advanced LIGO gravitational wave interferometer (master-thesis, Univesità di Pisa) *Public JGW Document Server* JGW-P0900269-v1
http://gwdoc.icrr.u-tokyo.ac.jp/DocDB/0002/P0900269/001/

[Stochino2007] Stochino A *et al* 2007 Improvement of the seismic noise attenuation performance of the Monolithic Geometric Anti-Spring filters for gravitational wave interferometric detectors *Nucl. Instrum. Meth. A* **580** 1559–1564
http://dx.doi.org/10.1016/j.nima.2007.06.029

[Stochino2009] Stochino A *et al* 2009 The Seismic Attenuation System (SAS) for the Advanced LIGO gravitational wave interferometric detectors *Nucl. Instrum. Meth. A* **598** (3) 737–753

[Suits2006] Suits B H 2006 Long Pendulums in gravitational gradients *European Journal of Physics* **27** L7–L11 (Citing unpublished results of measurements made by F W McNair and co-workers using half-second pendulums are contained in the report of John F Hayford, Inspector of Geodetic Work, to Otto H Tittmann, Superintendent, US Coast and Geodetic Survey, 8 February 1904. A copy of this report is held by the Michigan Technological University Archives and Copper Country Historical Collection.)
http://dx.doi.org/10.1088/0143-0807/27/2/L01

[Suits2012] Suits B H 2012 Long Period Pendulums *homepage, Suits B H, Physics Dept, MTU*
http://www.phy.mtu.edu/~suits/PH3110/pendulums.html

[Taffarello2005] Taffarello L 2005 Status of the commissioning of the AURIGA detector Talk at ILIAS GW Meeting Mallorca October 23–24, 2005
www.ego-gw.it/ILIAS-GW/documents/Palma_Talks/Taffarello.ppt

[Takahashi2002] Takahashi R *et al* 2002 Vacuum-compatible vibration isolation stack for an interferometric gravitational wave detector TAMA300 *Rev. Sci. Instrum.* **73** 2428
http://dx.doi.org/10.1063/1.1473225

[Takahashi2008] Takahashi R *et al* 2008 Operational status of TAMA300 with the seismic attenuation system (SAS) *Class. Quantum Grav.* **25** 114036 http://dx.doi.org/10.1088/0264-9381/25/11/114036

[Takahashi2012] Takahashi R *et al* 2012 Seismic Attenuation System (SAS) in the Kamioka mine (talk GW4.5) *Thirteenth Marcel Grossmann Meeting , 1–7 July 2012, Stockholm, Sweden*
http://www.icra.it/MG/mg13/talks/gw4_takahashi.pdf

[Takamori-thesis] Takamori A 2002 Low frequency seismic isolation for gravitational wave detectors (PhD thesis, University of Tokyo) *LIGO Document Control Center* P030049
http://t-munu.phys.s.u-tokyo.ac.jp/theses/takamori_d.pdf

[Takamori2002] Takamori A *et al* 2002 Mirror suspension system for the TAMA SAS *Class. Quantum Grav.* **19** 1615–1621
http://iopscience.iop.org/0264-9381/19/7/352

[Takamori2007] Takamori A *et al* 2007 Inverted pendulum as low frequency pre-isolation for advanced gravitational wave detectors *Nucl. Instrum. Meth. A* **582** (2) 683–692
http://dx.doi.org/10.1016/j.nima.2007.08.161

[Tanimoto2005] Tanimoto T 2005 The oceanic excitation hypothesis for the continuous oscillations of the earth *Geophys. J. Int.* **160** 276–288
http://dx.doi.org/10.1111/j.1365-246X.2004.02484.x

[Tariq2002] Tariq H *et al* 2002 The linear variable differential transformer (LVDT) position sensor for gravitational wave interferometer low-frequency controls *Nucl. Instrum. Meth. A* **489** 570–576
http://dx.doi.org/10.1016/S0168-9002(02)00802-1

[Tatsumi1999] Tatsumi D *et al* 1999 Two-dimensional low-frequency vibration attenuator using X pendulums *Rev. Sci. Instrum.* **70** (2) 1561–1564

[Tinto1999] Tinto M *et al* 1999 Cancellation of laser noise in an unequal-arm interferometer detector of gravitational radiation *Phys. Rev. D* **59** 102003

[Tokmakov2012] Tokmakov K V *et al* 2012 A study of the fracture mechanisms in pristine silica fibres utilising high speed imaging techniques *Journal of Non-Crystalline Solids* **358** 1699 1709
http://dx.doi.org/10.1016/j.jnoncrysol.2012.05.005

[Vahlbruch2008] Vahlbruch H *et al* 2008 Observation of squeezed light with 10-dB quantum-noise reduction *Phys. Rev. Lett.* **100** 033602

[Virdone2008] Virdone N *et al* 2008 Extended-time-scale creep measurement on Maraging cantilever blade springs *Nucl. Instrum. Meth. A* **593** (3) 597-607
http://dx.doi.org/10.1016/j.nima.2008.05.032

[Volcanodiscovery] Global earthquake monitor archive
http://www.volcanodiscovery.com/earthquakes/archive/

[Walker1979] Walker J 1979 How to build a simple seismograph to record earthquake waves at home *The Amateur Scientist, Scientific American Magazine* July 1997
http://psn.quake.net/lehmntxt.html

[Wang2002] Wang C *et al* 2002 Constant force actuator for gravitational wave detectorŠs seismic attenuation systems (SAS) *Nucl. Instrum. Meth. A* **489** 563–569

[Wang2007] Wang C *et al* 2007 A novel CMOS out-of-plane accelerometer with fully differential gap-closing capacitance sensing electrodes *J. Micromech. Microeng.* **17** 1275–1280

[Wanner2012] Wanner A *et al* 2012 Seismic attenuation for the AEI 10 meter Prototype *Class. Quantum Grav.* accepted for publication in October 2012

[Ward2008] Ward R L 2008 DC readout experiment at the Caltech 40 m prototype interferometer *Class. Quantum Grav.* **25** 114030

[Webb1998] Webb S C 1998 Broadband seismology and noise under the ocean *Reviews of Geophysics* **36** (1) 105–142
http://www.agu.org/journals/rg/v036/i001/97RG02287/97RG02287.pdf

[Weber1960] Weber J 1960 Detection and generation of gravitational waves *Phys. Rev. Lett.* **117** (1)

[Weber1968] Weber J 1968 Gravitational-wave-detector events *Phys. Rev. Lett.* **20** (23) 1307–1308

[Weber1969] Weber J 1969 Evidence for discovery of gravitational radiation *Phys. Rev. Lett.* **22** (24) 1320–1324

[Weisberg2005] Weisberg J M *et al* 2005 Relativistic binary pulsar B1913+16: thirty years of observations and analysis *Astronomical Society of the Pacific* Conference Series **328** *Proc. Binary Radio Pulsars* 25–32 eds. Rasio F A and Stairs I H
http://arxiv.org/abs/astro-ph/0407149

[Weisberg2010] Weisberg J M *et al* 2010 Timing measurements of the relativistic binary pulsar PSR B1913+16 *Astrophys.J.* **722** 1030–1034
http://arxiv.org/abs/1011.0718

[Weiss1972] Weiss R 1972 Electromagnetically coupled broadband gravitational antenna *Quarterly progress report, research laboratory of electronics, MIT* **105** 54 (LIGO DCC: P720002-01-R)

[Westphal2012] Westphal T *et al* 2012 Design of the 10 m AEI prototype facility for interferometry studies *Appl. Phys. B* **106** 551–557

[Wielandt1982] Wielandt E and Streckeisen G 1982 The leaf-spring seismometer: design and performance *Bulletin of the Seismological Society of America* **72** (6) 2349–2367

[Wielandt2002] Wielandt E 2002 Seismic sensors and their calibration *IASPEI New manual of Seismological observatory practice (NMSOP)* **1&2** Ed. Bormann P (GeoForschungsZentrum Potsdam) Chap.5
http://de.scribd.com/doc/38063359

[Willke2006] Willke B *et al* 2006 The GEO-HF project *Class. Quantum Grav.* **23** S207–S214
http://iopscience.iop.org/0264-9381/23/8/S26/

[Willmore1966] Willmore P L 1966 Long period vertical seismograph (U.S. Patent 3,292,145)

[Winterflood1996] Winterflood J *et al* 1996 A long-period conical pendulum for vibration isolation *Phys. Lett. A* **222** (3) 141–147
http://dx.doi.org/10.1016/0375-9601(96)00619-6

[Winterflood1999] Winterflood J *et al* 1999 A long-period conical pendulum for vibration isolation *Phys. Lett. A* **263** 9–14
http://dx.doi.org/10.1016/S0375-9601(99)00715-X

[Winterflood-thesis] Winterflood J 2001 High performance vibration isolation for gravitational wave detection (PhD thesis, University of Western Australia) *LIGO Document Control Center* P020028

[Winterflood2002a] Winterflood J *et al* 2002 High performance vibration isolation using springs in Euler column buckling mode *Phys. Lett. A* **300** (2) 122–130
http://www.sciencedirect.com/science/article/pii/S037596010200258X

[Winterflood2002b] Winterflood J *et al* 2002 Mathematical analysis of an Euler spring vibration isolator *Phys. Lett. A* **300** (2–3) 131–139
http://www.sciencedirect.com/science/article/pii/S0375960102002591

[Wittel2011] Wittel H 2011 Active seismic isolation in GEO600 (poster 4) *Amaldi 9 & NRDA Conference, July 10-15 2011, Cardiff, UK*
http://www.amaldi9.org/abstracts/294/HolgerWittel.pdf

[Yamamoto2008] Yamamoto K *et al* 2008 Current status of the CLIO project *J. Phys.: Conf. Ser.* **122** 012002
http://iopscience.iop.org/1742-6596/122/1/012002

[Yang2008] Yang Y *et al* 2008 Characteristics of ambient seismic noise as a source for surface wave tomography G^3 *Journ. of Earth Science* **2** (2)
http://phys-geophys.colorado.edu/pubs/2008/Yang_noise_directivity.pdf

[Zöllner1873] Zöllner F 1873 Ueber eine neue Methode zur Messung anziehender und abstossender Kräfte *Ann. Phys.* **226** 131–134
http://onlinelibrary.wiley.com/doi/10.1002/andp.v226:9/issuetoc

Complete list of publications

[P1] Aasi J, . . . , Wanner A, . . . , Zweizig J (The LIGO Scientific Collaboration & The Virgo Collaboration) 2012 The characterization of Virgo data and its impact on gravitational-wave searches *Class. Quantum Grav.* **29** 155002
doi:10.1088/0264-9381/29/15/155002

[P2] Abadie J, . . . , Wanner A, . . . , Zweizig J (The LIGO Scientific Collaboration & The Virgo Collaboration) 2012 Search for gravitational waves associated with gamma-ray bursts during LIGO science run 6 and VIRGO science runs 2 and 3 *The Astrophysical Journal* **760** (1) 12
doi:10.1088/0004-637X/760/1/12

[P3] Abadie J, . . . , Wanner A, . . . , Zweizig J (The LIGO Scientific Collaboration) 2012 Implications for the origin of GRB 051103 from LIGO observations *The Astrophysical Journal* **755** (1) 2
doi:10.1088/0004-637X/755/1/2

[P4] Abadie J, . . . , Wanner A, . . . , Zweizig J 2012 First low-latency LIGO+Virgo search for binary inspirals and their electromagnetic counterparts *A&A* **541** A155
doi: 10.1051/0004-6361/201218860

[P5] Abadie J, . . . , Wanner A, . . . , Zweizig J (The LIGO Scientific Collaboration & The Virgo Collaboration) 2012 Implementation and testing of the first prompt search for gravitational wave transients with electromagnetic counterparts *A&A* **539** A124
doi: 10.1051/0004-6361/201118219

[P6] Abadie J, . . . , Wanner A, . . . , Zweizig J (The LIGO Scientific Collaboration & The Virgo Collaboration) 2012 All-sky search for gravitational-wave bursts in the second joint LIGO-Virgo run *Phys. Rev. D* **85** 122007
doi:10.1103/PhysRevD.85.122007

[P7] Abadie J, . . . , Wanner A, . . . , Zweizig J (The LIGO Scientific Collaboration & The Virgo Collaboration) 2012 Upper limits on a stochastic gravitational-wave background using LIGO and Virgo interferometers at 600-1000 Hz *Phys. Rev. D* **85** 122001
doi:10.1103/PhysRevD.85.122001

[P8] Abadie J, . . . , Wanner A, . . . , Zweizig J (The LIGO Scientific Collaboration & The Virgo Collaboration) 2012 Search for gravitational waves from intermediate mass binary black holes *Phys. Rev. D* **85** 102004
doi:10.1103/PhysRevD.85.102004

[P9] Abadie J, . . . , Wanner A, . . . , Zweizig J (The LIGO Scientific Collaboration & The Virgo Collaboration) 2012 Search for gravitational waves from low mass compact binary coalescence in LIGO's sixth science run and Virgo's science runs 2 and 3 *Phys. Rev. D* **85** (8) 082002
doi:10.1103/PhysRevD.85.082002

[P10] Abadie J, . . . , Wanner A, . . . , Zweizig J (The LIGO Scientific Collaboration & The Virgo Collaboration) 2012 All-sky search for periodic gravitational waves in the full S5 LIGO data *Phys. Rev. D* **85** 022001
doi:10.1103/PhysRevD.85.022001

[P11] Evans P A, . . . , Wanner A, . . . , Zweizig J 2012 Swift follow-up observations of candidate gravitational-wave transient events *The Astrophysical Journal Supplement Series* **203** (2) 28
doi:10.1088/0067-0049/203/2/28

[P12] Dahl K, . . . , Wanner A, . . . , Danzmann K 2012 Status of the AEI 10 m prototype *Class. Quantum Grav.* 29 (2012) 145005 (11pp)
doi:10.1088/0264-9381/29/14/145005

[P13] Tokmakov K V, . . . , Wanner A, and Hammond G 2012 A study of the fracture mechanisms in pristine silica fibres utilising high speed imaging techniques *Journal of Non-Crystalline Solids* **358** (14) 1699
doi:10.1016/j.jnoncrysol.2012.05.005

[P14] Wanner A *et al* 2012 Seismic attenuation for the AEI 10 m Prototype *Class. Quant. Grav.* **29** (24) 245007
doi:10.1088/0264-9381/29/24/245007

[P15] Westphal T, . . . , Wanner A, . . . , Danzmann K 2012 Design of the 10 m AEI prototype facility for interferometry studies *Appl Phys B* **106** (3) 551
doi:10.1007/s00340-012-4878-z

[P16] Abadie J, . . . , Wanner A, . . . , Zweizig J (The LIGO Scientific Collaboration & The Virgo Collaboration) 2011 Beating the spin-down limit on gravitational wave emission from the Vela pulsar *The Astrophysical Journal* **737** (2) 93
doi:10.1088/0004-637X/737/2/93

[P17] Abadie J, . . . , Wanner A, . . . , Zweizig J (The LIGO Scientific Collaboration & The Virgo Collaboration) 2011 Search for gravitational wave bursts from six magnetars *The Astrophysical Journal Letters* **734** (2) L35
doi:10.1088/2041-8205/734/2/L35

[P18] Abadie J, . . . , Wanner A, . . . , Zweizig J (The LIGO Scientific Collaboration) 2011 A gravitational wave observatory operating beyond the quantum shot-noise limit *Nature Physics Letters* **7** (12) 962
doi: 10.1038/NPHYS2083

[P19] Abadie J, . . . , Wanner A, . . . , Zweizig J (The LIGO Scientific Collaboration & The Virgo Collaboration) 2011 Search for gravitational waves from binary black

hole inspiral, merger, and ringdown *Phys. Rev. D* **83** (12) 122005
doi:10.1103/PhysRevD.83.122005

[P19E] Abadie J, . . . , Wanner A, . . . , Zweizig J (The LIGO Scientific Collaboration & The Virgo Collaboration) 2011 Erratum: Search for gravitational waves from binary black hole inspiral, merger, and ringdown [Phys. Rev. D 83, 122005 (2011)] *Phys. Rev. D* **86** (6)
doi:10.1103/PhysRevD.86.069903

[P20] Abadie J, . . . , Wanner A, . . . , Zweizig J (The LIGO Scientific Collaboration & The Virgo Collaboration) 2011 Directional limits on persistent gravitational waves using LIGO S5 science data *PRL* **107**(27) 271102
doi:10.1103/PhysRevLett.107.271102

[P21] Abadie J, . . . , Wanner A, . . . , Zweizig J (The LIGO Scientific Collaboration) 2010 First search for gravitational waves from the youngest known neutron star *The Astrophysical Journal* **722** (2) 1504
doi:10.1088/0004-637X/722/2/1504

[P22] Abadie J, . . . , Wanner A, . . . , Zweizig J (The LIGO Scientific Collaboration & The Virgo Collaboration) 2010 Search for gravitational-wave inspiral signals associated with short gamma-ray bursts during LIGO's fifth and VIRGO's first science run *The Astrophysical Journal* **715** (2) 1453
doi:10.1088/0004-637X/715/2/1453

[P23] Abadie J, . . . , Wanner A, . . . , Zweizig J (The LIGO Scientific Collaboration & The Virgo Collaboration) 2010 Predictions for the rates of compact binary coalescences observable by ground-based gravitational-wave detectors *Class. Quantum Grav.* **27** 173001
doi:10.1088/0264-9381/27/17/173001

[P24] Abadie J, . . . , Wanner A, . . . , Zweizig J (LIGO Scientific Collaboration) 2010 Calibration of the LIGO gravitational wave detectors in the fifth science run *Nuclear Instruments and Methods in Physics Research A* **624** (1) 223
doi:10.1016/j.nima.2010.07.089

[P25] Abadie J, . . . , Wanner A, . . . , Zweizig J (The LIGO Scientific Collaboration) 2010 Search for gravitational waves associated with the August 2006 timing glitch of the Vela pulsar *Phys. Rev. D* **83** (4) 042001
doi:10.1103/PhysRevD.83.042001

[P26] Abadie J, . . . , Wanner A, . . . , Zweizig J (The LIGO Scientific Collaboration & The Virgo Collaboration) 2010 Search for gravitational waves from compact binary coalescence in LIGO and Virgo data from S5 and VSR1 *Phys. Rev. D* **82** (10) 102001
doi:10.1103/PhysRevD.82.102001

[P27] Abadie J, . . . , Wanner A, . . . , Zweizig J (The LIGO Scientific Collaboration & The Virgo Collaboration) 2010 All-sky search for gravitational-wave bursts in the first joint LIGO-GEO-Virgo run *Phys. Rev. D* **81** (10) 102001
doi:10.1103/PhysRevD.81.102001

[P28] Dahl K, ..., Wanner A, ..., Danzmann K 2010 Towards a Suspension Platform Interferometer for the AEI 10m Prototype Interferometer *Journal of Physics: Conference Series* **228** 012027
doi:10.1088/1742-6596/228/1/012027

[P29] Goßler S, ..., Wanner A, ..., Danzmann K 2010 The AEI 10 m prototype interferometer *Class. Quantum Grav.* **27** (8) 084023
doi:10.1088/0264-9381/27/8/084023

[P30] Kawazoe F, ..., Wanner A, ..., Danzmann K 2010 Designs of the frequency reference cavity for the AEI 10m Prototype Interferometer *Journal of Physics: Conference Series* **228** 012028
doi:10.1088/1742-6596/228/1/012028

Acknowledgements

I would like to thank Prof. Karsten Danzmann, not only for the experience of working on the AEI 10 m Prototype project, which I joined in the very beginning as the first and only PhD student, but also for his courage to allow me to work in the same institute as my wife does, even though we were working in different working groups. I am grateful for the wonderful time at the AEI, which only was possible due to friendly working environment sustained by skilled and talented colleagues, and their resourceful supervisor Karsten Danzmann.
Many thanks go to Dr. Stefan Hild from University of Glasgow for being willing to read this thesis and come to Germany for the PhD defence.

I thank Stefan Goßler, the AEI 10 m Prototype project supervisor, and Harald Lück, our project attendant for not interfering with our daily work routine, but being open to any kind of questions and fruitful discussions.
I am honoured being taught by Alessandro Bertolini, who introduced the SAS concept to the AEI 10 m Prototype project and took always the time to discuss with me every issue I had during my work. Although he left the AEI before my thesis was finished, he always was remotely available for discussions and kept a friendly collaboration between the AEI and his new position at Nikhef in Amsterdam. I wish him and his family all the best in the Netherlands.
I am glad that I had the luck to work with friendly and cooperative colleagues. Thank you all for the amicable working environment. Special thanks go to Christian Gräf, Katrin Dahl, Michael Born, and Mirko Prijatelj for participation in our little control book-club which, even though was hard to maintain in parallel with the daily work, was fun to attend and learn together.
Cheers to the proof-readers of this thesis: Alessandro Bertolini, Riccardo DeSalvo, Stefan Goßler, Conor Mow-Lowry, Gerald Bergmann, Tobin Fricke, Gudrun Wanner, Michael Tröbs, Sönke Schuster, and those I forgot to mention. Their suggestions immensely improved the quality of this thesis. All remaining mistakes and typos are entirely my fault.
Finally, I salute my family for taking care of my children during the long and virtually never ending writing-phase of this thesis.

At last I feel obliged to express gratitude to the European Graduate College (EGC) and the Quantum Engineering and Space-Time Research (QUEST) excellence cluster for financial support.
The EGC seminars chaired by Prof. Eberhard Tiemann were a helpful forum to practice presentation skills. The seminars gave a wider view of scientific projects at different physics departments of the Leibniz Universität Hannover and beyond the university.
The EGC gave me the invaluable opportunity to make a six months visit in Glasgow,

where I had the chance to participate in the fused-silica fibre production and testing for Advanced LIGO, which culminated in a co-authorship in a publication [Tokmakov2012]. The time in Scotland was wonderful, mostly due to friendly and helpful Scots, like Kirill Tokmakov, Johanna Bogenstahl, and Ignacio Santiago.

Curriculum Vitae

PARTICULARS

Name: Alexander Wanner

Nationality: German

Date of birth: 08/12/1978

Place of birth: Rudny

Family status: married, two children

UNIVERSITY

12/2007 - 03/2013	PhD student at the Albert Einstein Institute in Hannover
02/2009 - 07/2009	Exchange semester at the Institute for Gravitational Research at the University of Glasgow, UK
08/2006 - 12/2007	Postgraduate research at the Institute for Microtechnology in Hannover
10/2000 - 08/2006	Studies of technical physics at the Universität Hannover *Graduated with Diploma*

SCHOOL

1999 – 2000	Military service in Rotenburg (Wümme)
1996 – 1999	Georg-Büchner Gymnasium Seelze *Graduated with Abitur*
1993 – 1996	Realschule Seelze *Graduated with Realschulabschluss*
1992 – 1993	Hauptschule Seelze
1985 – 1992	Gesamtschule Rudny